Temperature control for cell division: from microfluidics to AI

Pablo G. Salaverria Izaguirre

TESIS DOCTORAL UPF / 2019

Thesis co-supervisors

Dra. Isabelle Vernos, CRG

CELL AND DEVELOPMENTAL BIOLOGY PROGRAME, CRG

Dr. Jeremy Cramer, Cherry Biotech

R&D DEPARMENT, CHERRY BIOTECH

Dedication and acknowledgements

Primero de todo querría agradecer a mi familia, Ama, Aita, Natalia e Inigo, por todo el apoyo y cariño desde que me fui de casa en 2015 en busca de una carrera profesional. Gracias por las visitas tanto en Lincoln como en Rennes, sin vuestro apoyo no habría acabado la tesis. Espero que estéis orgullosos de mi. Eskerrik asko.

Después me gustaría agradecer a Wendy su apoyo, aliento y animo constante desde el día que hice la aplicación el stage de master en Cherry, cuando me traslade a Rennes, cuando me aceptaron en el doctorado y por supuesto durante estos 3 años, de los cuales 18 meses hemos podido compartirlos en juntos en Rennes. Gracias por permitirme que esta tesis nos quitara tiempo en pareja debido a mis viajes y que tú siempre me animaras a seguir, aunque hubiera dificultades. Yo he escrito esta tesis, pero sin tu aliento no habría sido capaz de hacerlo, gracias. MZ.

Ensuite, je voudrais tout d'abord remercier mes superviseurs au cours de ces trois années chez Cherry Biotech, Thomas, Jeremy et Pierre. Tout d'abord pour avoir eu l'occasion de travailler ici chez Cherry Biotech, puis de me soutenir, de m'encourager à aller mieux chaque jour et de m'aider à atteindre le meilleur de moi-meme. Un voyage incroyable avec beaucoup de belles histoires que nous partageons tous ensemble. J'espère pouvoir vous rendre tout ce que j'ai appris de vous.

Thank you to all my work colleagues during these three and a half years, Mathilde, Nadia, Damien, Denis, Brian, Julien, Pierre, Theo, Andreas, Charles, Blanca, Dario, Antoni, Matteo, Oussama, Mo, Melanie, Meriem, Betty, Shiva, Francois, Kevin, Giulia, Annise and more. I enjoy working, learning and sharing time with you all. Hell of a ride!

I would like also to thank to Isabelle Vernos as a co-supervisor from DivIDE network, for showing me how important is to be rigorous while reporting and explaining my work. I got great advice from you during our discussions and I hope I managed to reach what you expected from me when we first met.

Also, inside DivIDE, I would like to thank to Natalia, and the rest of the PI's for supporting me inside the academic community during these three years. I learnt a lot from the Pi's but also from theirs teams during my secondments at Thomas Muller, Phong Trang, Carsten Janke and Isabelle Vernos labs. Thank you also to my fellow colleagues in the consortium, I hope we all graduate as PhD after all the hard work we put during the project, specially during the organization of the conference. Special mention to Alejandra and Ivan, during our long microscopy night sessions when I was going to Barcelona. Both of you are big part of this thesis.

Finally, I am very happy for been able to complete this challenge in the best way I could with hard work and tenacity while overcoming difficulties, to end up giving everything I got until the last day. I am proud of my work and I hope that all of you who have been part of this thesis, each in its own way, feel proud of me

What's next for me? I do not know yet, but sky is the limit, and I am ready to take off!

Abstract (English)

This PhD thesis aimed to understand the impact of temperature at different levels (biology to physics) while performing live-cell imaging. A study and characterization of the role of the temperature during the cell division while using live-cell imaging on several biological models was done. Microfluidics was used to study it while accurately controlling the temperature on a microscope stage. Followed by characterizing a microscope setup to quantify the impact of different external factors on the sample temperature. Based on that, I built new microfluidic based devices able to control the sample temperature with high accuracy. Those devices were designed, manufactured and validated in collaboration with four research teams that used different biological models: *S. Pombe*, Hela-Kyoto cells, kidney cancer spheroids and *in vitro* microtubules. Finally, I developed an AI-based image classifier to study cell division, using data from samples thermalized by the accurate temperature control devices described above.

Abstract-Español

Esta tesis doctoral tuvo como objetivo comprender el impacto de la temperatura en diferentes niveles (biología o física) al realizar microscopia. Se estudio y se caracterizó la implicación de la temperatura aplicada la división celular de distintos modelos biológicos utilizando microscopia. Se utilizo la microfluidica para estudiarlo mientras se controlaba con precisión la temperatura en un microscopio. Se caracterizo un set de microscopia para cuantificar el impacto de diferentes factores externos en la temperatura de la muestra. Con ello, construí nuevos dispositivos microfluidicos capaces de controlar la temperatura de la muestra con precisión. Esos dispositivos fueron diseñados, fabricados y validados en colaboración con cuatro equipos de investigación que utilizaron diferentes modelos biológicos: *S. Pombe*, células Hela-Kyoto, esferoides de cáncer de riñón y microtúbulos *in vitro*. Finalmente, desarrolle un clasificador de imágenes usando inteligencia artificial para estudiar la división celular, utilizando imágenes adquiridas con el preciso control térmico descrito anteriormente.

Preface

This Industrial PhD thesis will be based in three different pillars that will put together all the work done at Cherry Biotech and at the laboratory of Prof. Isabelle Vernos, Prof. Phong Tran, Prof. Carsten Janke, Dr. Yanncik Arlot and Dr. J. Dumont since September 2016.

The first one is the technical research done inside the R&D team at Cherry Biotech, Here I managed to gather all the technical knowledge regarding the temperature control, building of microfluidics devices or the use of microscopy. I managed to create a test bench to characterize the impact of different factors on the sample temperature and at the same time use it to thermally calibrate different microfluidics devices. I developed my knowledge on how to manufacture microfluidic based devices from prototyping to the industrialization stage. All this knowledge allowed me to generate the technical core of this PhD thesis.

The second pillar was the interaction with the different biological laboratories inside the DivIDE and SpOC projects that helped me to evolve in my biological knowledge. I first needed to understand their approach and protocols in studying cell division to be able to provide them tools to go beyond current state of the art. Together, we designed and validated different devices, biological protocols and experiments that resulted on different tools.

The third pillar rely on the industrial dimension of this PhD thesis at Cherry Biotech. It has given me the possibility to acquire an entrepreneurship mindset. This meant to be able to do applied research trying to optimize all the process while aiming to put a product on the market that answer users' problems. In this case, I managed to do so as the ThermaFlow yeast edition device it is been thought to continue with industrialisation steps. With this mindset I managed to take advantage from a collaboration between Cherry Biotech and the Institut Jacques Monod in Paris. I started an innovative research line creating an artificial intelligence (AI)-based image classifier to process images from the 1st division of *C. elegans* embryos. This project was the first step of Cherry Biotech into the AI field as the company plans to apply this technology on its next product, the Cubix. This last pillar was summarized in the start-up culture of Cherry Biotech, that allowed me to innovate optimizing the resources, forcing me to be imaginative while developing a critical mindset and allowing me to learn new skills on a high working rhythm.

List of content

List of figures

List of tables

List of equations

Chapter 1, Introduction

1.1. Introduction to live-cell imaging

Live-cell imaging is an invaluable data source that helps on the development of knowledge of many fields related with the fundamental biology. It brings the possibility to observe different organisms in different physiological conditions allowing understanding how they behave, or which phenotypes do they present depending on different external (medium composition, environment temperature and gas concentration) and internal (cell division stage, cellular response to an inner stimuli or response to an sporadic gene mutation) parameters. All this is possible due to the latest technical improvements that increased both the time and spatial resolution.

For example, the confocal spinning disk coupled with the latest improvements regarding the different fluorescent tools opened a huge horizon of possibilities to keep getting increase the actual knowledge in the field of biology(1–4). However, there is no option to obtain relevant data if the key parameters that define a healthy phenotype are not properly controlled. In case of mammalian cells 37°C temperature with a gas concentration of at least, 75% of N_2, 20% of O_2 and 5% of CO_2. On the other hand, for *C. elegans,* the temperature range is between 15°C and 25°C depending on the developmental stage with no special gas requirements.

1.2. Main live-cell imaging techniques

From the technical point of view, live-cell imaging can be defined as the method to study living cells or species using time-lapse microscopy, which consists one obtaining sequenced images over a defined time period. The constant evolution of this technology from the beginning of the 20th century until today allowed scientists to acquire a deeper knowledge of biological functions or structures through the observation of cellular dynamics(5–8). The option to spot dynamic changes offers more insight regarding the inner machinery of a cell than a single frame obtained by imaging fixed cells. Furthermore, the spatial resolution gain using different fluorescent probes allows the observation of subcellular structures, proteins, different processes or molecular interactions. Finally, the majority of the techniques can be classified into two main groups: Transmission light microscopy and Fluorescent microscopy(9).

1.2.1. Transmission light microscopy (TLM)

The general definition of Transmission Light Microscopy (TLM), includes any technique where light passes from the source to the opposite side of the lens in order to distinguish morphological features of the sample.

The light path starts in the source where it can be polarized, light waves oscillates in one specific plane, or non-polarized, light waves oscillates in all the planes. The first one is used for sample where the non-homogeneity of the material does not allow all the light to go through the sample, therefore it is necessary to select that will for sure cross to the end. It reaches a condenser to focus on the sample while it gets as much illumination as possible. Once the light has overpassed the sample it arrives to the objective lens where

the image gets magnified. The final step consists on the getting the image into the ocular or the detector, for visualization or storage(5,7).

Inside TLM there different sub-techniques such as Bright-field, Dark-Field, Phase contrast or Differential interference contrast (DIC) microscopy, Figure 1. However it is necessary to point out that the spatial resolution of this type of imaging method is between 200-300nm (10–12).

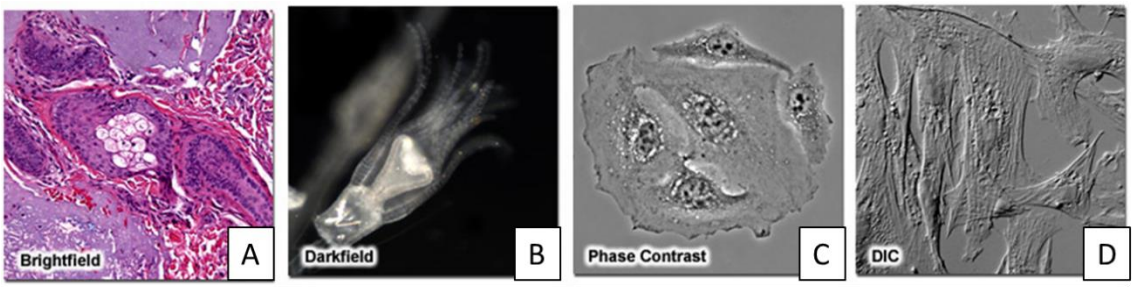

Figure 1,Example of the different sub-techniques inside the TLM. Bright-field(A), Dark-field(B), Phase contrast(C) and DIC(D)

1.2.1.1. Bright-field microscopy

Bright-field is the first technique presented here, and its key is that the contrast between the different parts of the sample is generated from the absorption of light by the different pigments in the sample. Those pigments can be either natural or added artificially following two steps, the first one, permeabilization, is a treatment for cells that using a mild surfactant allows large dye molecules because partially dissolves the cell membrane. Then fixation, preserves the cells or the tissue morphology by creating chemical bonds between proteins to increase their rigidity and the most used chemicals ae ethanol, methanol and picric acid. Finally, staining which is the process when the dye is placed in contact with the sample by immersion, meaning to immerge the sample on a dye such as Methylene blue, used to stain the cell nuclei.(13,14). This illumination method is based on the Köhler illumination principle(15–17), developed by August Köhler in 1893.

This technique requires the use of two iris diaphragms, a field one to direct the illumination beam towards eye for direct observation while the condenser one is used to direct the light beam to a camera or recording device. The role of the condenser is to focus the parallel rays over the sample allowing an even illumination field. An explanatory scheme can be observed Figure 2. The top row shows the illumination path starting from the light source (Figure 2-1), the condenser diaphragm (Figure 2-2), back focal plane of the objective lens (Figure 2-3) and the eyepoint (Figure 2-4). The bottom row presents the path of the sample image with the field diaphragm(Figure 2-A), sample(Figure 2-B), eyepiece(Figure 2-C) and camera or back of the eye(Figure 2-D).

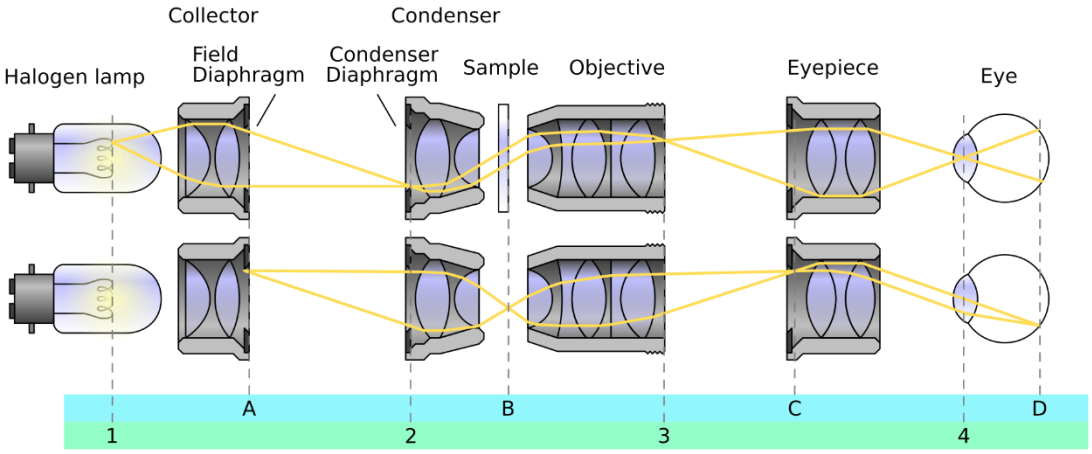

Figure 2, Scheme of the Köhler illumination

From the practical point of view, the main use of this microscopy technique involves the observation of stained or naturally pigmented specimens that have been prepared in slides, such as tissue or flat cell cultures, with a maximum penetration of 20µm(17,18).

1.2.1.2. Dark-field microscopy

Dark-field microscopy is a technique that generates the contrast between the different features of the sample and the background by the scattering of light from the sample as is illuminated from the side. The scattered light from the sample is detected by the objective lens and is seen with a dark background, which improves the contrast between different components of the sample(19–21). This technique does not require staining, but it needs a special opaque disc of 1 cm diameter underneath the condenser. This one acts by blocking most of the light from the illumination source. It is necessary to create the oblique illumination for darkfield microscopy as it can be seen in Figure 3. This image shows where the opaque disk, that stops the light, is placed into a bright-field microscope to produce images with dark background and higher contrast(22).

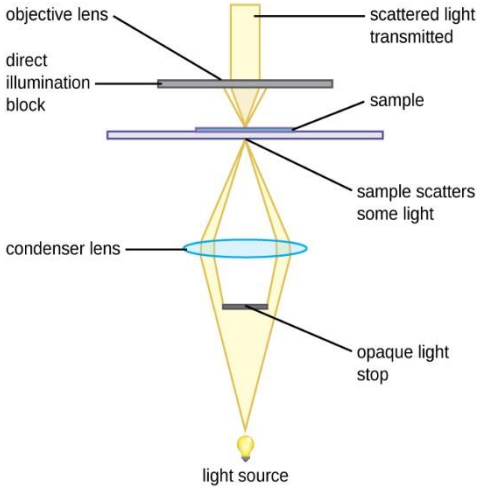

Figure 3, Scheme of the darkfield microscopy setup

This technique is mostly used at low magnifications, up to 100x but it is not recommended to be used with dry objectives, as light could enter in the path and disturb the final image. It is also very useful method to determine the motility of cultures or to find cells in suspension with a maximum sample thickness of 20µm (23,24).

1.2.1.3. Phase contrast microscopy

Phase contrast microscopy's main strength is using the refraction and interference of light provoked by structures in a specimen to generate high-contrast images with a higher resolution than the techniques mentioned before. It does not require any type of staining to get those features. This is possible because the sample is illuminated by a hollow cone of light that pass through a phase annulus in the condenser. In order to form altered wavelength paths, it is necessary to place an annular stop in the condenser, which at the end is what produces the annular cone of light, while the objective has a phase plate containing a phase ring. Finally, the light travels directly from the illuminator or light source, goes through the phase ring whereas light refracted or reflected by the specimen passes through the plate.

All this ends up making the waves travelling by the ring to be out of phase by one-half of a wavelength from those which end up in the plate. At the end, the interference generated from the different phases is what will create the contrast, between the sample and its background as it can be seen in Figure 4, where the annular stop is placed in the condenser producing a cone of light that focuses on the specimen (Figure 4-1), specimen refracts or reflects light(Figure 4-2), light travelling directly from the condenser lens and the one going through the specimen are out of phase when they pass by the objective and the phase plates(Figure 4-3) and finally the wavelengths that are in or out of phase either add together or cancel out each other(Figure 4-4). Along the process these are the different types of light: Illumination light(-red), diffracted light(Figure 4-yellow), un-diffracted light(Figure 4-blue) and combination of both (Figure 4-green).(25–30).

From the usability point of view the use of this technique improves the ones mentioned before but with a higher economic cost as it is necessary to add a condenser and higher resolution objectives to the microscope, but with a limited sample thickness of 20µm(29–31).

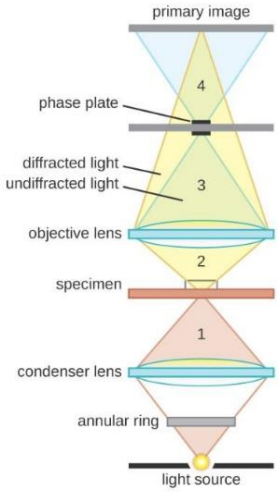

Figure 4, Scheme of the phase contrast setup

1.2.1.4. Differential Interference Contrast (DIC) microscopy

DIC microscopy is very similar to phase contrast in the sense that both use interference patterns to generate contrast between the different features or structures of the sample. In this case, two different polarized (different phase) lights beams are created and once they pass through the sample, their recombination makes it possible to have images with higher contrast that look like 3 dimensional images, without using any kind of staining technique(32,33).

Therefore, it is necessary to explain the extra components necessary to make this possible, as it can be seen in Figure 5. The first one is the Linear Polarizing filter which is placed between the light source and the condenser and is designed to produce the linear or plane-polarized light needed for the interference detection. Right after this piece the Wollaston filter(32,34–36) is placed to split the polarized light into two separates beams before it gets to the condenser. Those two light beams are known as specimen and reference beams. At the condenser the light is focused in the sample, pass through it, goes to an objective lens before arriving to 2nd Wollaston filter that recombines the light beams prior to arriving to the 2nd polarization filter that generates the differential interference that end up generating the enhance contrast.

From the usability point of view, this technique provides a 3-D like image to allows to study structural features and distinguish parts of the specimen that would not be possible unless using chemical staining. This improvement come with a higher economic cost than the previous methods as it is necessary to include two Wollaston filters and two polarizing ones(36–40).

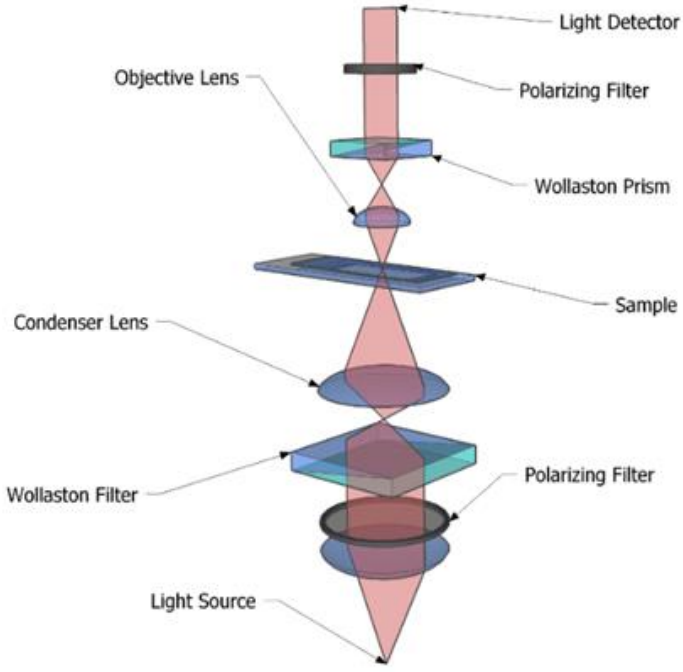

Figure 5, Scheme of DIC microscopy

A summary and comparation of the different techniques inside the TLM can be seen in Table 1.

Technique		Transmission Light microscopy (TLM)			
Sub-technique		Bright-Field microscopy (BFM)	Darkfield	Phase Contrast	Differential Interference Contrast (DIC)
Resolution	Temporal [ms]	Milliseconds			
	Spatial[µm]	0.2-0.3µm			
Principle to resolve the image		Absorption of light by different pigments of the sample that can be natural/artificial or immutable	Differentiation of the sample and the background by the scattering of light from the sample	Generation of contrast by using the refraction and interference of light provokes by different features of the sample	Generation of contrast by using polarized light to obtain 3D alike images
Main feature		Simplicity and usability	Useful to distinguish background/sample and motility	Higher contrast with no need of staining	Higher contrast with 3D alike images, with no need of staining
Main limitation		Necessity of using pigments/staining to enhance contrast	Only for immersion objective as dry could add distortion on the final image	Complex setup with high economic cost	Complex setup with high economic cost

Table 1, Summary and comparation of Transmission Light microscopy (TLM) techniques

1.2.2. Fluorescence microscopy

This type of microscopy relies on a physics principle where a molecule, while illuminating with a specific light wavelength, can absorbed the light and then emit a new light of a longer wavelength with less energy, therefore a different colour than the absorbed one, Figure 6. Knowing this, it is possible to attach those fluorophores, that normally are fluorescent proteins (FP) or decay dies to the different components of a sample or specimen in order to image them.

The base for this imaging method requires and excitation source, which is a light source at a specific wavelength. Optics for the excitation and collection part include the use of dichroic mirrors and filters, which some are polarizing ones. At the end it is necessary to observe or storage the image, therefore, high sensitive detectors such as CCD sensors, phot-multiplayers or CMOS cameras are needed(41).

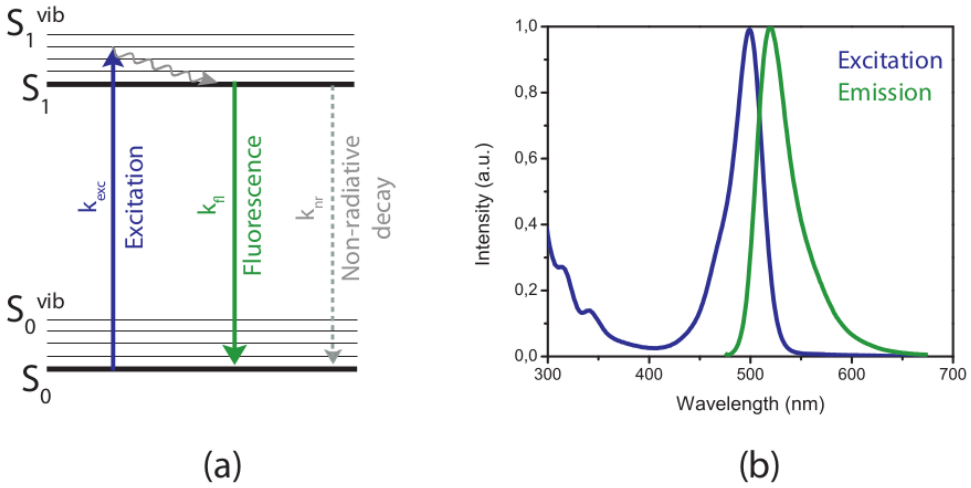

Figure 6, Schematic explanation of the fluorescent principle of excitation and emission. Scheme of the energy bands(a) and graph of the excitation and emission wavelength to intensity(b)

Something to consider while doing this type of microscopy is the phototoxicity and the photo-bleaching. In the first case, the excess of energy provided to the fluorophore causes the emissions of free radicals that can damage other parts inside the cells. On the other hand, when the fluorophore is not able to emit more energy because it has been saturated of excitation energy, photo-bleaching occurs.

Inside the fluorescence microscopy technique there are different approaches with different resolutions(42) such as epifluorescence microscopy (0.1-0.2µm), laser confocal and spinning disk microscopy (0.2-0.8µm). One step further are the techniques like Total Internal Reflection Fluorescence or TIRF(10nm) or super resolution ones such as Stochastic Optical Reconstruction microscopy or STORM (10nm) or Stimulated Emission Depletion or STED(50nm)(43–46). The last two are techniques can overcome the diffraction limit, which stablish that the minimal noticeable distance between two points follows the Abbe diffraction limit equation, Equation 1(47,48).

1.2.2.1. Epifluorescence microscopy

Epifluorescence microscopy is considered the simplest configuration of fluorescence microscope, and one of the most commonly used. The main configuration (Figure 7) consists on a broad spectrum light source that can be either a mercury arc lap(49) or a LED(50,51), which emits light in the visible spectrum with enough intensity or power to excite the fluorophores in the sample.

Prior to illuminate the sample is it necessary to set the excitation filter to select the band of wavelengths that will excite the fluorophore and combine it with a dichroic mirror that will transmit or reflect the wavelengths of light, allowing the separation of excitation and emission photons for the final observation.

An emission filter is included to separate the reflected light from the scattered one provided by the fluorescence of the sample. Finally, a sensitive imaging device or detector is placed to collect the photons at the image plane of the sample to be converted on a readable image or set of pixels. The maximum penetration of this microscopy techniques is around 25µm(48).

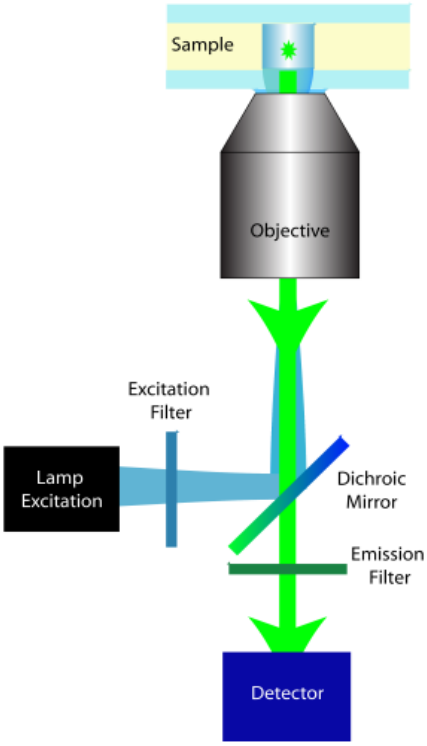

Figure 7, Scheme of the Epifluorescence microscopy setup

1.2.2.2. Laser confocal microscopy

The main improvement of this technique compared with the previous one is that it uses a collimated laser as light source, improving the axial resolution(52), allowing to obtain images of 3-dimensional structures by using optical sectioning. It also reduces the phot-bleaching of the fluorophore as it provides less energy than the widefield (52–54). The collimated laser is used as exciting source, focusing its light into a focal point of the sample. The light emitted by the sample passes by the dichroic mirror and the emission filter and it is focused into a pinhole aperture. This pinhole is placed before the objective and removes the out-of-focus light. This process improves the axial resolution as it only collects the emitted fluorescence from the focal plane. The complete process can be seen in Figure 8.

From the practical point of view, this technique allows to scan in the X-Y axis a plane of a sample in matter of seconds and to obtain a 3D reconstruction in minutes. This can be very useful for fixed samples with a maximum thickness of 100-200µm(48), but for live-cell imaging it could be too slow if the target is to observe dynamic events of a specimen(55–57).

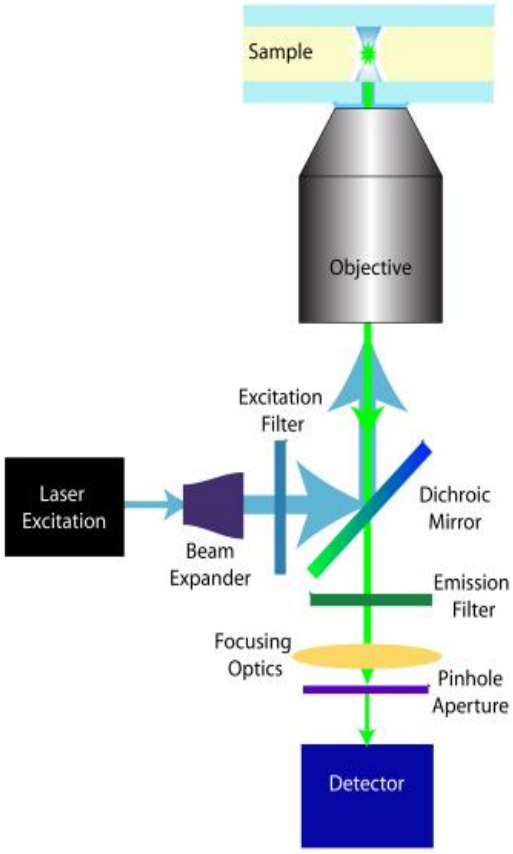

Figure 8, Scheme of the Laser Confocal microscopy setup

1.2.2.3. Spinning-disk confocal microscopy

Spinning-disk confocal microscopy is a technique that puts together capacity of the confocal microscopy to remove the out-of-focus light with the high sensitivity of the epifluorescence microscopy, as the fluorophore is excited and imaged at the same time from different points across the sample. The laser light source is defocused to a larger laser beam spot that is transformed into a lot of small focused laser beams by a the microlens array disk. Those laser beam spots pass through a dichroic mirror and then across a pinhole array disk, which is perfectly aligned to match each spot with a hole. Prior to the sample, the objective lens focuses all the spots in the correct focal plane. The microarray disk and the pinhole array disk are coupled and spin at 500-10000 rpm, so all the field of view is illuminated with one of the focused laser beam spots. Finally, the emission light generated from the focal plane of the sample is then re-focused by the objective lens back through the pinhole array and reflected off by the dichroic mirror getting to the camera(58–60). An scheme of this setup can be seen in the Figure 9(61).

This is a more complex setup than the previous ones but it improves a lot the collecting time, allowing the user to image very fast movements such as microtubules (MTs) movements inside living cells(62) or samples with a thickness between 30 and 50µm(48).

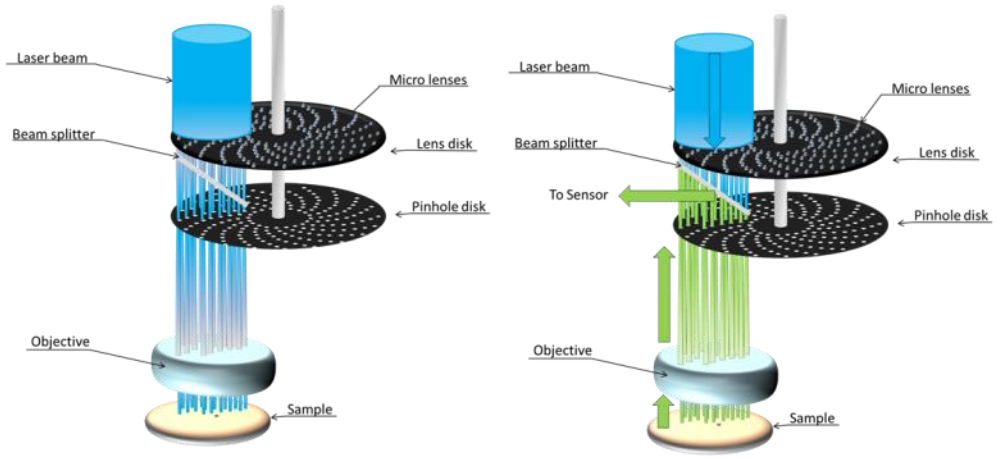

Figure 9, Spinning disk confocal microscopy scheme

1.2.2.4. Total Internal Reflection Fluorescence (TIRF) microscopy

This technique is based on the epifluorescence microscopy, but it takes advantage of the critical angle of light. Whenever light faces the interface between two transparent media with different refractive indexes, it will be both partially reflected and diffracted. There is a certain angle, so called critical angle of light, where the light is completely reflected, and an internal reflection occurs. This can only occur if the light goes from higher refractive index medium to a lower one, in case of the TIRF microscopy, from the glass dish or coverslip, with a refractive index of 1.52, to the sample, which is aqueous with an index of 1.33.

This ends up creating an evanescent wave or a near field wave, which decays exponentially but allows to penetrate around 10nm into the sample. The three main advantages of this method are that its reduces the background nose, increasing the signal-to-background ratio, there is not collection of out-of-focus fluorescence signal and that the amount of light that the sample is exposed to is much smaller than epifluorescence microscopy(41,63–65).

A summary and comparation of the different fluorescence microscopy techniques can be seen in Table 2.

Technique		Fluorescence microscopy			
Sub-technique		Epifluorescence	Laser confocal (LC)	Spinning-disk confocal (SDC)	Total inertial Reflection Fluorescence (TIRF)
Resolution	Temporal	Seconds			
	Spatial[µm]	0.1-0.2µm	0.2-0.8µm		0.01µm
Principle to resolve the image		Generation of contrast after exciting a fluorophore to obtain an image of a target feature or structure	Generation of contrast by using a laser to excite the fluorophore to obtain an image of a target feature or structure	Using the base of the confocal microscopy with the capacity of removing out-of-focus to improve the contrast of the image	Based on epifluorescence but creating an evanescent wave that penetrates 10nm into the sample and reduces the background noise and the out-of-focus collection
Main feature		Capacity to observe features and structures inside the cell	Capacity to obtain images with higher resolution and lower photobleaching	Less out-of-focus noise than standard LC with lower background noise	Out-of-focus fluorescence is minimized together with background noise
Main limitation		Limited resolution because of the diffraction limit, risk of photobleaching and phototoxicity	Limited resolution because of the diffraction limit and scanning speed	Limited resolution because of the diffraction limit, scanning speed much complex setup	Limited resolution because of the diffraction limit and the need to use a sample that is attached to the base/coverslips due to the limited penetration of this technique

Table 2, Summary and comparation of Fluorescence microscopy techniques

1.2.2.5. Super-Resolution microscopy

As it was introduces before, this type of fluorescence microscopy was created in order to overcome the diffraction limit defined by Abbe in 1873, which corresponds the minimal noticeable distance between two points, following Equation 1. The Abbe diffraction limits depends on the wavelength of the light(λ), the refractive index of the medium(n) and the angle of the converging spot (Θ), divided by two. Another limiting factor is the numerical aperture (NA), which could reach a maximum of 1.4 NA, giving an Abbe limit of λ/2NA. As an example, for the green light at 500nm, will present a limit of 0.25µm, which will provide a lateral resolution of 200nm and an axial of 500nm. Figure 10 shows

$$d = \frac{\lambda}{2n\sin\theta} = \frac{\lambda}{2\mathrm{NA}}$$

Equation 1, Diffraction limit equation of Abbe. Distance between points(d), wavelength of the light(λ), the refractive index of the medium(n) and the angle of the converging spot (Θ) and numerical aperture (NA)

visually the difference between resolution over and below the diffraction limit(43,44,66,67).

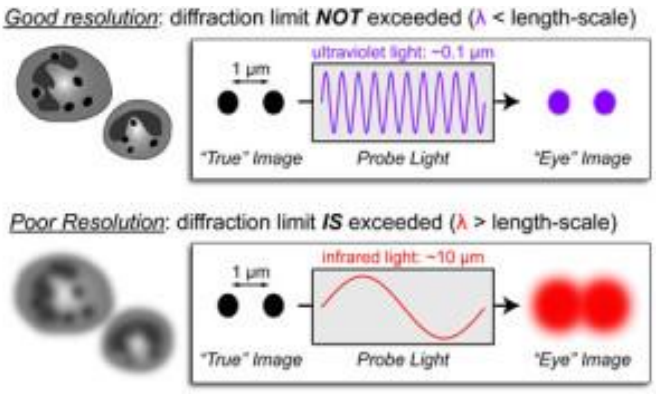

Figure 10, Explanation of the difference between resolution over and below the Diffraction limit of light

Therefore to overcome that limit there are different techniques such as the Stimulated Emission Depletion(STED) microscopy that is based on generating super resolution images by selectively deactivating fluorophores which minimizes the area of illumination and enhances the obtainable resolution, Figure 12 (68). This practise has a lateral resolution of 20-70nm and an axial of 40-150nm with a temporal resolution in the range of the milliseconds to seconds(69).

Another method is the Stochastic Optical Reconstruction microscopy or STORM, which uses sequential activation and time resolved location of fluorophores that are photoswitchables to obtain high resolution images, Figure 11(70,71)

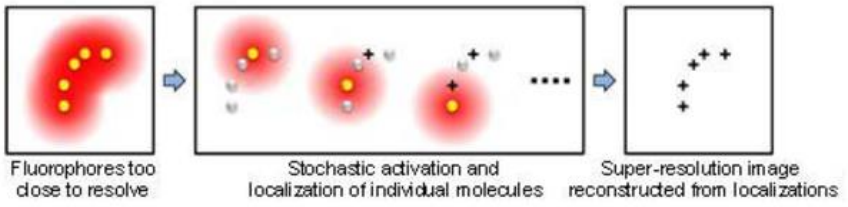

Figure 11, Scheme explaining the principle behind the STORM

Very similar to the STORM, there is the Photoactivated Localization microscopy (PALM), Figure 13 (72), which is a technique that uses fluorescent proteins that are optically highlighted to stochastically switch on a sub-population of molecules to obtain a sequential single-molecule readout. For those imaging methods the x-y resolution is in the range of 10 to 30 nm with an axial one of 10 to 75nm(69,73).

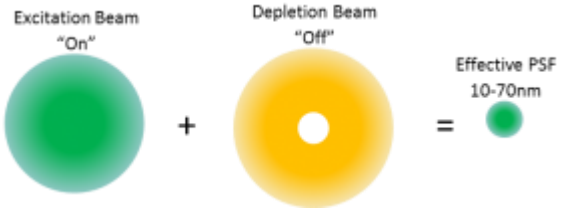

Figure 12, Scheme of the STED technique explained

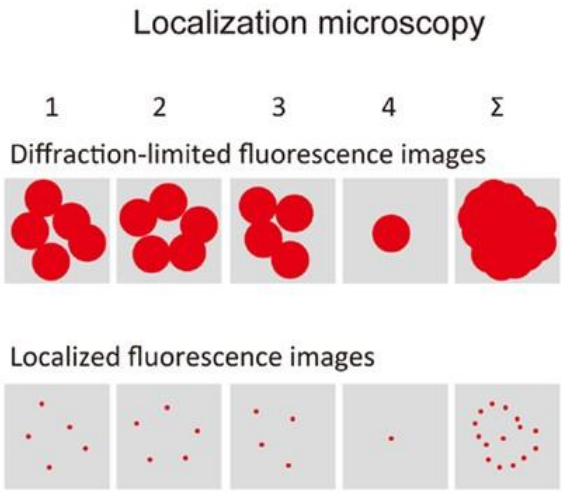

Figure 13, Scheme of the PALM method

A summary and comparation of the different techniques inside the super-resolution microscopy can be seen in Table 3.

Technique		**Super-Resolution microscopy**		
Sub-technique		Stimulated Emission Depletion (STED)	Stochastic Optical Reconstruction microscopy (STORM)	Photoactivated Localization microscopy (PALM)
Resolution	**Temporal**	Seconds	Minutes	
	Spatial[µm]	Lateral: 0.02-0.07µm Axial: 0.04-0.15µm Thickness: 20-80 µm	Lateral: 0.01-0.03µm Axial: 0.01-0.075µm Thickness: 20-80 µm	
Principle to resolve the image		Generation of super resolution images by selectively deactivate fluorophores which minimizes the area pf illumination and enhances the resolution	Generation of super resolution images by using sequentially activation and time resolved location of fluorophores that are photoswitchables	Localization of fluorophores that are optically highlighted by stochastically switching on a sub-group of molecules to obtain a sequential single-molecule readout
Main feature		High lateral resolution, overcoming diffraction limit	Highest lateral resolution among all the techniques	
Main limitation		Limited axial resolution and photobleaching if over exposition	Special fluorophores required and limited temporal resolution due to the different steps and the time to reconstruct the image	

Table 3, Summary and comparation of Super-Resolution microscopy techniques

As a conclusion of this section, live-cell imaging is one of the base s to gather biological knowledge by observation, but if the environment around the sample is not properly controlled and monitor, it will be hard to obtain reliable and repeatable data. Therefore, the next part will be focused on one of the main parameters that drives the close environment of the sample, the temperature.

1.3. Temperature from different points of view

Temperature and especially the one of the samples play a big role while doing live-cell imaging, but it is important to understand what means to thermalize at a certain temperature. Based on the point of view, temperature may have different meanings, from thermodynamics/physics to biology/biochemistry.

1.3.1. Temperature and heat, thermodynamic view

First, thermodynamics is the branch of physics that studies temperature and heat, along with their relation to energy, work, radiation or properties of matter. While temperature can be considered as the internal or kinetic energy of the total molecules that conform an object, heat is the amount of energy that flows from on body to another one due to their temperature difference. Then entropy is a measure of the molecular disorder or randomness of a system or the thermal energy of a system as itself(74–76).

Using this base, there are four basic principles or laws inside this field that need to be mentioned:

The zero law says that if two systems are each in thermal equilibrium with a third one, they will also be in equilibrium with each other. This statement refers to the fact that thermal equilibrium is an equivalence relation on the set of thermodynamic systems under observation.(74)

The first law expresses that the internal energy of an isolated system is constant. It refers to the conservation of energy that implies that the energy cannot be destroyed but only be transformed(74).

The second law implies that heat cannot spontaneously flow from a colder location to a hotter location. This one makes reference to the irreversibility of natural processes, and, in many cases, the tendency of natural processes to lead towards spatial homogeneity of matter and energy, and especially of temperature(74–76).

The third law says that as a system approaches absolute zero, all processes cease, and the entropy of the system reaches a minimum value. In this case, this law provides an absolute reference point for the determination of entropy at any other temperature(74–76).

1.3.1.1. Temperature

The temperature can be defined as the measure of kinetic energy of the molecules that make up an object or a volume of matter(74,75). Therefore, it is possible to measure that energy at different scales. In science the most used one is Kelvin (°K) as it is considered at 0° Kelvin there is absolute zero molecular motion inside that object or volume of matter. This scale is the one used to measure temperature of the nature but outside the range of the humans, e.g. the temperature of the sun is at 5778 °K in its surface(77–79).

Another scale is Celsius(°C) as it uses as reference the freezing(0°C) and boiling(100°C) points of water. Its relationship with Kelvin is based by the addition of 273 making 0°C equal to 273°K. This scale is commonly used to measure in the range of the human, e.g. 37°C is the average body temperature of a human being.

$$Tc = 5 \times \frac{(Tf - 32)}{9}$$

Equation 2, Conversion between Temperature in Celsius (Tc) and in Fahrenheit (Tf)

The last scale is Fahrenheit (°F) and it's the most commonly used in United States of America. It uses as reference the freezing and boiling temperatures of a mixture made of equals parts of ice and salt table being 0°F the freezing point and 212°F the boiling one. Its relationship with Celsius system follows the Equation 2.

1.3.1.2. Heat

Heat is physical quantification of the amount of energy that flows from on body to another one due to their difference in temperature. It is measured in Joules (J) as an international system unit. As a base, if two objects with different temperature are in contact the heat will flow the hotter one to the colder one until they reach an equilibrium meaning that both are at the same temperature. The heat transfer can occur in different ways, such as conduction, radiation or convection(74,80–83).

Conduction is a type of heat transfer that occurs between solid objects or materials, therefore there is none mass transfer because of all the energy is due to the vibration of atoms and free motion of electrons inside that object or medium. Due to this principle, metals are very good heat conductors as they contain many free electrons that can move freely. The difference of heat for this case can be expressed as Equation 3.

$$\Delta Q = KA\Delta t(\frac{\Delta T}{L})$$

Equation 3,Amount of heat equation. Amount of heat(∆Q), coefficient of thermal conductivity(k), area of contact(A), time interval(∆t), temperature difference(∆T) and distance between hot and cold bodies(L)

On the other hand, it is also important to know the resistance of the material to heat flow Equation 4.

$$R = \frac{L}{k}$$

Equation 4, Resistance of the material to heat flow equation. Distance between hot and cold bodies(L) and coefficient of thermal conductivity(k)

Another way to transfer heat is convection that mostly occurs between liquids and gases. In this case as the hot part of the fluid has a lower density than the cold one, the hot part flows upwards and while it transfers the heat. Thus, the heat is transferred due to the movement of a heated fluid. However, to express this phenomenon the difference of heat is expressed over time at Equation 5.

$$\Delta Q/\Delta t = qA\Delta T$$

Equation 5, Amount of heat(∆Q), over time(∆t). Coefficient of thermal convection(q), area(A), difference of temperature(∆T)

Finally, heat radiation is an electromagnetic radiation generated by the thermal motion of particles in all matter that has higher temperature than absolute 0°K. The motion of particle results in charge-acceleration that produces electromagnetic radiation. In order to quantify it is necessary to use the Stefan-Boltzmann constant (σ=5.67*10^-8) into Equation 6.

$$P = \sigma \epsilon A T^4$$

Equation 6, Heat radiate energy(P) equation. Stefan-Boltzmann Constant(σ), emissivity of the material(ϵ), area of emitting body(A) and absolute temperature in Kelvin(T)

1.3.2. Temperature from the biological/biochemistry point of view

The meaning of temperature from the biological point of view involves the understanding that every living organism needs a specific temperature range in order to survive. If the temperature is not the correct one, organism could be able to adapt, until a certain range, to avoid the water in their cells from turning ice or to avoid the denaturalization of metabolic enzymes with heat (84–87).

However, it is possible to divide the different organism in the nature according on how they regulate their body temperature. Endotherms generate most of the heat they need in order to keep a certain temperature and when the environment is below their body temperature, they increase the metabolic heat production to keep it constant and in the opposite case they sweat to remove the heat. Mammals and birds are part of this group. On the other hand, for ectotherms their body temperature is ambient dependant and the heat that their metabolism generates is not enough to change their body temperature, therefore they move towards the location whose temperature meets their needs. Most of the reptiles, fishes, amphibians and invertebrates are ectotherms(84–86).

Although, there is a response to temperature changes thermosensing mechanism that can act at different levels from nucleic acids to proteins and lipids. At transcriptional level, temperature can be sensed by the regulation of access of transcriptional machinery of DNA as it can be mediated by changes in DNA structure by a primary DNA sequence. E.g. in *Shigella*, the transcription of the *virF* virulence gene need the invaded host to be at least at 32°C. At lower temperature the machinery does not start, and the virus is not spread(88). The protein conformation is also temperature-dependant and it can be a way to an organism to react in response to an ambient temperature change, e.g thermosensitive mutants in *C. elegans* have proteins that are activated at a certain temperature like an on/off switch(89–91). Finally, temperature changes can affect protein activity indirectly due to the lipids in the membrane as their fluidity is temperature dependant(88,92–94).

1.4. Main techniques to measure temperature while doing live-cell imaging

Live-cell imaging goes from imaging single cells to tissue samples, therefore, to measure the temperature of those sample it is necessary to consider different features in order to choose the correct sensing technique. Although, for live cell imaging the most common used techniques can be based on resistance changes (Thermistors or RTDs), based on voltage changes (Thermocouples), based on thermochromic liquids, infrared thermography or a very recent technique that involve the use of themo-sensitive fluorescence molecules. Each of those techniques have their own strengths and weakness but all of them are relevant enough to be consider as techniques to measure the temperature of a biological sample while doing live-cell imaging.

1.4.1. Sensors based on resistance changes: Thermistors and Resistive Temperature Detectors (RTD)

This type of sensors measure temperature based on resistance changes. There are two different sub-types inside this group, thermistors(95–97) and Resistive Temperature Detectors (RTDs) (95,98,99), each of them with different features as it can be seen at Table 4.

1.4.1.1. Thermistors

Thermistors sensors are available in two different types: positive temperature coefficient (PTC) and negative temperature coefficient (NTC). The resistance in PTC increase with the temperature while with the NTC is the opposite. They are generally made from ceramic materials (oxides of nickel, manganese or cobalt) that are semiconductor materials sealed in glass or plastic, which provide them a very fast response to temperature changes. Thermistors are also considered passive resistive devices meaning that they only need a current to pass through in order to generate a measurable voltage output(100). In order to classify them, they are rated according to their resistive value at room temperature(25°C) and their time constant (time to react to a temperature change).

Along all the thermistors the most used ones are the NTC type sensors that follow Equation 7, Standard equation for NTC thermistor resistance as function of the temperature. Thermistor nominal resistance at 25°C(R_{25c}), thermistor material constant in Kelvin (β) and thermistor actual temperature in Celsius(T), which shows that the relationship between the resistance and the temperature is non-linear, and it depends on which type of materials are used in its manufacturing(101). The most used ones are 10Kohms sensors with a response time of 2-3seconds, with a measuring range of -40°C to 125°C, an accuracy of 0.5-1°C. The main strengths are the low cost, the durability and the adaptable size of this type of sensors while the main limitations are related with the non-linear resistance-temperature curve that requires a calibration and the slow response time in the range of 2-3seconds (102–104).

$$R_T = R_{25C} e^{\{\beta[(\frac{1}{T+273})-(\frac{1}{298})]\}}$$

Equation 7, Standard equation for NTC thermistor resistance as function of the temperature. Thermistor nominal resistance at 25°C(R_{25c}), thermistor material constant in Kelvin (β) and thermistor actual temperature in Celsius(T)

1.4.1.2. Resistive Temperature Detectors (RTD)

The other type of temperature sensors based on resistance are the Resistive Temperature Detectors (RTD) that are highly precise and accurate sensors made from high purity conducting metals such as platinum, nickel or copper. Among those materials, platinum is the most used one due to its high accuracy and it includes two types of sensors the PT-100 and the PT-1000.

The PT-100 sensors have a small circuit made of platinum that has a 100 ohms resistance at 0°C This one is the most used sensor and it has 4 wires/connections. Two of them to provide a small current and the other two to measure the voltage that will be then transformed to resistance that will lead to the temperature measurement as it can be seen at Figure 14. For example, the measurement current is normally around 1mA, if the resistance is 100 ohms, the voltage drop will be 0.1V over the resistance. For higher accuracy, it can reach +/-0.1°C the current can be decreases down to 0.1mA.

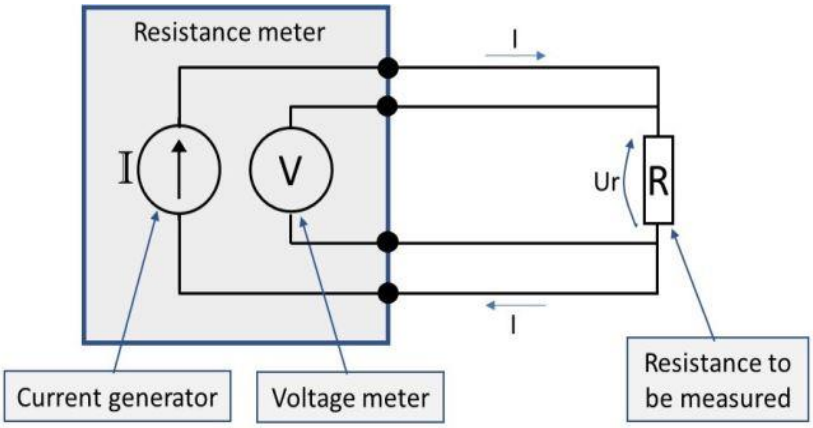

Figure 14,Scheme of a 4 wire PT-100 circuit. Voltage drop (Ur) and Current in amperes(I)

The second type, PT-1000 sensors have a resistance of 1000 ohms at 0°C and use the 2 wire/connection configuration as it can be seen at Figure 15. In this case the resistance is measured at the end of the two wires, making it less accurate than the previous configuration, as the current and the voltage are measured in the same circuit, including all the noise that was avoided before. It is more than enough if the desired accuracy is between 0.5°C-1°C.

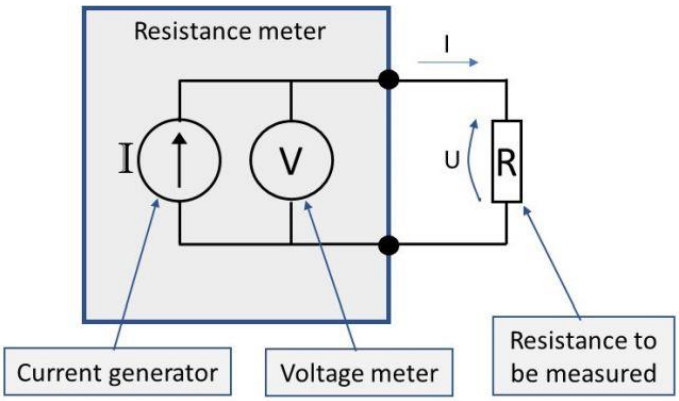

Figure 15, Scheme of a 2 wire PT-1000 circuit. Voltage drop(U) and Current in amperes(I)

As a summary, the strongest features of this sensor are the linear relationship between temperature-resistance, the high accuracy(+/-0.1°C) and stability. The only drawback is that it is a more expensive sensor compared with a thermistor and they require a special encapsulation due to their fragility (95,98,99,101).

Thermometer	Type of Measurement	Resolution		Temperature Range	Strength	Limitation
		Temporal[s]	Accuracy[°C]			
Thermistor-PTC-NTC	Resistance	2-3s	+/-0.5 to 1°C	-40°C to 125°C	Low cost Durable Small Size Stability	Need of calibration Slow response time
RTD	Resistance	100ms	+/-0.1	-200°C to +350°C	Linear output High accuracy and stability	High cost Fragile if not encapsulated

Table 4, Summary of resistance base temperature sensors

1.4.2. Sensors based on voltage changes

Thermocouples are thermo-voltage based thermometers that use the Seebeck effect of thermoelectric materials in order to measure the temperature(105–109). The voltage is measured at the two open ends (cold point) of the connection between two thermoelectric materials A and B (mostly metals). In case of a temperature change in the connection point (hot point) between material A and B will provoke a delta of voltage that follows the Equation 8. This equation includes the Seebeck coefficient that refers to the temperature-dependent property of the material used at the thermocouple, Figure 16(101,105–109).

$$\nabla V = -S(T)\nabla T$$

Equation 8, Equation of the thermoelectric effect. Gradient of Voltage(∇V), Seebeck coefficient(-S(T)) and gradient in temperature(∇T)

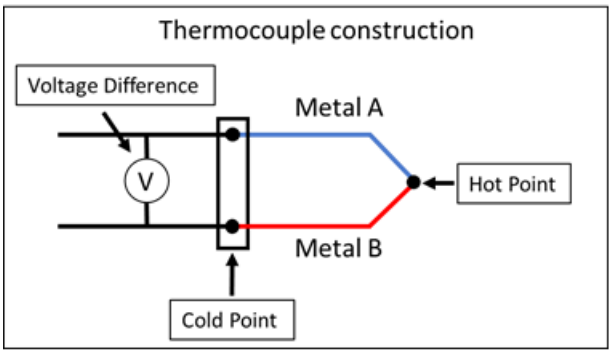

Figure 16, Scheme of the thermocouple construction

The reason to be the most used sensors as there is no need of any specific equipment or conversion. At the end, the main features are only dependant on the two-metal combination, as it can be seen at Table 5(110–117).

Type of Thermocouple	Material pair	Temperature range	Resolution		Strength	Limitation
			Accuracy[°C]	Time response[s]		
Type J	Iron/Constantan	0°C to 750°C	+/-1.1 to 2.2°C	1s	High resolution and range Low cost Small Size	Need of calibration Fragile if not encapsulated
Type K	Nickel Chromium/ Nickel Aluminium	-200°C to 1250°C	+/- 1.1°C to 2.2°C			
Type E	Nickel Chromium/ Constantan	-200°C to 900°C	+/-1 to 1.7°C			
Type T	Cupper/Constantan	-250°C to 350°C	+/-0.5°C to 1°C			

Table 5, Summary of the main features of the different type of thermocouples

1.4.3. Sensors based on Thermochromic Liquid crystals (TLC)

Another temperature measure technique involves the use of Thermochromic Liquid Crystal (TLC), which are liquid crystals that change their optical properties due to temperature. Outside the working range, the sensor is completely transparent because the crystal are in an amorphous state(101). Once it is thermalized inside the working range, the sensor will show a range of different colours, the rainbow of colours is known as colour play. This happens because the crystals are more structured and reflect the different wavelengths of light depending on the thermalization temperature(118).

The TLC can be made to display a colour change from -30°C up to 120°C. The lower limit depends on the crystallization and the glass formation while the upper one is subjected to the stability and lifetime of the device that include the TLC. The colour bandwidth can have a resolution from 0.1°C to 40°C, depending on the application as it could require a broad or a narrow bandwidth(118–124). A summary of the main features can be seen at Table 6.

For the moment the application of this type of temperature sensors did not only cover biological purposes but they have also been used in food industry to develop smart packaging(125–128).

1.4.4. Infrared thermography

Infrared technology can be used to measure the temperature as it is a non-invasive technique that provides more than a reduce amount of discreate points(129–134). This technique allows to observe the whole-field temperature of the sample as it monitors the thermal radiation of the heated objects, in our case sample of cells or tissues. The energy that is radiated from the surface of the sample depends on the emissivity, as dimensionless ratio it describes the amount of absorbed and reflected heat radiation emitted from a surface.

The thermic cameras can measure that heat radiation and calculate the temperature with an accuracy from 0.2°C to 2°C. The main advantages of the Infrared technology are related with the repeatability by decreasing the error between experiments and the possibility to observe the complete spectrum but for some setups a re-calibration might be needed as it is mentioned in Table 6(134).

Thermometer	Type of Measurement	Resolution		Temperature Range	Strength	Limitation
		Temporal[s]	Accuracy[°C]			
Thermochromic Liquid Crystals (TLC)	Temperature to colour bandwidth relationship	1s	+/-0.1 to 40°C	-30°C to 120°C	Easy to use and customize Affordable cost	Calibration needed Not suitable for large surface or objects
Infrared thermography	Heat radiation	1s	+/-0.2 to 2°C	0°C to 100°C	Possibility to observe the complete spectrum Repeatability between experiment	Re-calibration needed depending on the setup

Table 6, Summary of the main features of TLC and Infrared thermography

1.4.5. Fluorescence molecules-based sensors

There are four more techniques that include fluorescence to measure the temperature of the sample, but that are not commercialized yet. Those are fluorescent dyes, quantum dots, fluorescent polymeric thermometer and fluorescent based proteins as genetically encoded ratiometric fluorescent thermometer (gTEMP),Table 7.

1.4.5.1. Fluorescent dyes

The fluorescent dyes are used as semi-invasive technique to measure the temperature around and inside single cells(135–138). There is a direct relationship between the intensity of the fluorophore and the temperature(139). One approach is to combine a europium coordination entity composed of europium(III) coordinated to 4-[4,6-di(1H-indazol-1-yl)-1,3,5-triazin-2-yl]-N,N-diethylaniline and three 4,4,4-trifluoro-1-(thiophen-2-yl)butane-1,3-dione(EU-TTA), a synthetic dye, with nano-encapsulation of Poly(methyl methacrylate) or PMMA to protect the dye from pH changes(137). This technique is combined with fluorescent microscopy to obtain a read-out of the temperature at a specific location in the 3D space. It requires a calibration and a data post-processing to obtain the temperature in a field of view, which end up increasing the response time(135–138).

1.4.5.2. Quantum dots (QD)

Quantum dots(QD), are nanoparticles made of semi-conductor materials that emit fluorescence and that have been used to measure the temperature of living cells(140). The illumination properties of the QDs have temperature-dependent optical variations therefore the fluorescence intensity decreases while the heat goes up(140,141). This technique is considered as semi-invasive one as the it is biocompatible with living cells, but it requires to introduce the QDs in the target location, around or inside the cells(142–145).

1.4.5.3. Fluorescent polymeric thermometers (FPTs)

Fluorescent polymeric thermometers (FPTs) are another semi-invasive method used to measure the temperature around and inside single cells. The reason to use polyacrylamides such as Poly(N-isopropylacrylamide)(NIPAM) is that its structure changes due to temperature(146–150). The key point here is the phase transition of this polymers as it allows to have a very accurate response to a temperature change. The temperature range can be increased by synthesizing blocks of copolymers containing different polymers with different temperature sensitivities. If the size of the chain is too big the temperature sensitivity could be affected(151). At the end, the molecule was optimized by adding two more units and combine the thermosensitive unit (NIPAM) with a Hydrophilic unit, sulfonated polyacrylamide (SPA) and with a Fluorescents unit, N-{2-[(7-N,N-dimethylaminosulfonyl)-2,1,3-benzoxadiazol-4-yl](methyl)amino}ethyl-N-methylacrylamide(DBD-AA). It is necessary to use microinjection in order to place it close the target cells(151,152).

1.4.5.4. Fluorescent based proteins as genetically encoded ratiometric fluorescent thermometer (gTEMP)

Genetically encoded ratiometric fluorescent thermometer or gTEMP is an experimental technique that combines fluorescence proteins in order to measure the temperature around or inside a living organism. The team of Nakano et al.(153) checked for different fluorescent proteins combinations to improve its temperature sensitivity in order to develop a ratiometric thermometer(153–160).

The first fluorescent protein, Sirius, decreases it intensity by a 65% by increasing the temperature from 20°C to 65°C. On the other hand, mT-Sapphire only decreases by a 17% in the same range. This difference makes them compatible to be used a ratiometric fluorescent thermometer. These two proteins combined managed to get a sensitivity of 2.6%/°C in the 5°C to 45°C range after been calibrated from 32°C to 40°C. This technique was presented as a solution to image different living organisms, from inner part of the cells to complete embryos but requires a more in deep calibration in order start to use it as a standard temperature measurement technique, as it is in a very early development stage(153–160).

Thermometer	Type of Measurement	Resolution		Temperature Range	Strength	Limitation
		Temporal[s]	Accuracy[°C]			
Fluorescent dyes	Fluorescent intensity	30-60s	+/-0.05°C to 3°C	25°C to 90°C	Complete range reading	Calibration needed Slow time response
Quantum dots (QD)	Fluorescence intensity ratio	100ms	+/-0.1°C	-50°C to 130°C	Biocompatible Able to reach inside the cell	Need of special encapsulation and calibration
Fluorescent polymeric thermometers (FPTs)	Fluorescence lifetime	1s	+/-0.1 to 0.5°C	20°C to 49°C	Biocompatible Able to reach inside the cell	Need of special encapsulation and calibration
Genetically encoded ratiometric fluorescent thermometer (gTEMP)	Fluorescence intensity ratio	1s	+/-0.4°C	Characterized in the range of 5°C to 45°C	Wide range Fast response	Early stage of development with a complex protocol

Table 7, Summary of the features of fluorescent based temperature sensors

1.5. Main techniques to thermalize the sample while doing live-cell imaging

At this point, I will be reviewing different techniques that can be used to thermalize a sample while doing live-cell imaging. The first temperature controller for microscopy was patented back in 1940s(161) but it was not until 1980s(162–165) when researchers started to use them more and more on regular basis until today.

There are a wide variety of classifications, but I decided to divide them according on the approach they take in order to thermalize. The first group has a macro approach that involves thermalizing the stage in order to thermalize the sample. The second group has a micro one where the sample is thermalized more locally or even from the inside.

1.5.1. Macro approach to thermalization

Inside the macro approach group, I include the following technologies: incubation box, top stage incubators or Peltier elements. All of them thermalize the sample by thermalizing the surrounding environment that includes the microscope stage.

All these techniques have commercially available products in the market that can be purchase and used to thermalize samples while doing live-cell imaging. Their main features can be seen at Table 8.

1.5.1.1. Incubation box

This first technology has been in the market for more than 20 years now and it is a very well-known and reliable method to thermalize samples. It is normally composed by a transparent box that is normally made of plastic (plexiglass or PMMA) that is placed on top of the microscope stage creating a closed environment. There are connections to supply a thermalized mix of O2 and CO2 at the desired concentration. These kind of systems can thermalize the inner environment from the ambient temperature(20-22°C) up to 45°C, but it is possible to reach higher temperatures such as 60°C (166). The incubation boxes can provide homogeneous temperature in the sample location but they require long time (30 to 60min) to go from the ambient temperature up to the target one (167,168).

1.5.1.2. Top stage incubator

The second thermalization method is a more advanced and miniaturized version of the previous one, which is called top stage incubator and it was first patented in 1940s(161) but became more used after the 1980s(162–165). This is a more advanced incubator as it is generally adapted to host different type of cell culture plates as petri dish, multi-wells or single slides.

The thermalization using an incubation chamber has two different approaches. The simplest one uses the thermalized gas(O2+Co2) that fills the sealed environment giving the possibility to thermalize from ambient temperature up to 45-60°C, depending on the device features(169). The second option pre-thermalized uses water or any other liquid to thermalize the sample by flowing through a close circuit of metal that is in contact with

the sample plate thermalizing it, without contacting directly the cells(169) but with the possibly of thermalizing faster(35-°C per min) than the air based one(1-3°C per min).

1.5.1.3. Stage thermalization based on Peltier elements

The last method inside this group uses Peltier element in contact with a thermic conductive material that will end up thermalizing the cells plate, therefore the sample. Peltier elements or thermoelectric coolers are made of two types of semiconductors, N and P, which under a specific a current moves electric charges on the current direction Figure 17. They operate according to the Peltier effect that creates a temperature difference by heat transfer between two electrical junctions. A voltage is applied through the junction that creates a current. When the current goes in one direction of the junction, the heat goes all towards one part of the junction, increasing the temperature in one of the sides of the Peltier while cooling the other side(170–172).

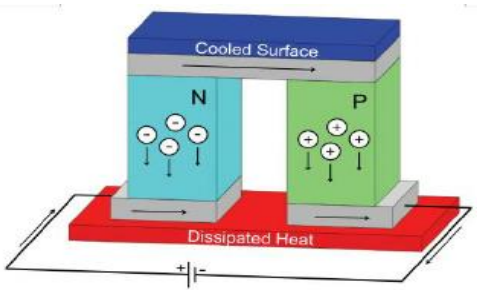

Figure 17, Scheme of the Peltier effect. Semiconductor type N(N), semiconductor type P(P)

Technique	Thermalizing method	Resolution		Temperature range	Strength	Limitation
		Temp to time response [°C/min]	Accuracy [°C]			
Incubation box	External air supply	0.21°C per min	+/-0.1-1°C	Ambient to 45°C-60°C	Stable and homogeneous temperature Gas and humidity control	Low time response Only over ambient temperature
Top stage Incubator	External air supply or liquid close circuit	Air base method 1-3°C per min Liquid base method 3-5°C per min	+/-0.1-1°C	Ambient to 45°C-60°C, depends on the model	Reduced version for incubation box with faster time response	Low time response Only over ambient temperature
Peltier element to thermalize stage	Thermal conductive	10-20°C per min	+/-0.1°C	Below ambient to 60°C with a complex setup	Accuracy Better control Fast response Possibility to go below ambient	Complex setup Need of a feedback loop

Table 8, Summary of the different macro approaches for sample thermalization

This setup allows a more accurate temperature control and gives the possibility to go below ambient temperature but it requires a more complex setup than the previous ones, such as a feedback loop to readjust the power of the Peltier in order to avoid overshooting (173–175). In this case the upper limits depends on the features of the Peltier element, but there are some that can reach up 200°C with a speed of 1°C per second(176–181).

1.5.2. Micro approach to thermalization

Inside this group there are different thermalization techniques that involve the use of microfluidics, microheaters or lasers. These methods allow to provide more localized thermalization and a more precise temperature control as it can be seen at Table 9(182).

1.5.2.1. Thermalization based in microfluidics

There is one commercially available product call based on combining externally pre-heated liquid and microfluidics (183–185). It uses a Peltier element to pre-thermalize a liquid that flows through a microfluidic chip in close loop. The microfluidic chips are made of a hard material that transfer/removes the energy from the sample that is in contact with the microfluidic chip through a glass coverslip. This multilayer setup allows to thermalize it to the desired temperature. Such a method requires a calibration as it does not use any sensor in the sample location to correct the temperature. It allows fast temperature switch (10s) and a range of 5°C to 45°C.

Another option is to use an approach developed first by Guijt et al(186) and then optimized by Maltezos et al.(187), which basically uses a chemical reaction to control the temperature of the sample inside a microfluidic channel. Two reagents, acetone and H2SO4 combines are used to heat or cool down the central channel that could host the sampling cells to be observed using live-cell imaging. The key here is to control the flow rate of the two reagents in order to control the chemical reaction and provide the good temperature to the sample. It could be possible to have a range from -10°C to 76°C with slopes of 1°C/second and an accuracy of between 0.5°C and 1°C(187–190).

1.5.2.2. Thermalization based in micro-heaters

There is one technique that is based in microelectronics technology that is the base of microheaters(191–194). Those components can be used in combination of metals or liquids to take advantage of their thermal conductivity property. The key point of those systems is that it is possible to calibrate them by establishing a relationship between the dissipated power (applied energy and resistance of the heater) and the temperature of the sample. Therefore, it is necessary to place a sensor in the sample location to monitor the amount of heat coming from the microheaters, which can work with less than 1W and very low voltage in order to heat up(192,193). In the case of liquid conductivity, a microheater can heat up the medium or liquid that is in contact with the sample in order to thermalize it (195,196).

In terms of features, a thermal time response can be between 10-20°C per second, with an accuracy of 0.2°C to 2°C and a range between ambient and 100°C depending on the setup and the heat capacity of the microheater(197–201).

1.5.2.3. Thermalization based in infrared (IR) lasers

The last method is the one that uses infrared(IR) and near-infrared(NIR) lasers to locally heat a sample while doing live-cell imaging (202). Those laser have the capacity to transfer energy to all the molecules under the focal spot and increase their temperature, e.g. using a wavelength of 1064nm a laser focused on a point can induce heat in a ratio of 1°C per 100mW of power(203). This method of generating heat with light has two main benefits: it is non-invasive and universally applicable, meaning that can be used in any type of cell or tissue(204). Depending on the application, it could require a more powerful laser setup as light is weakly absorbed in sample with thin cell membranes.

On the other hand, it is necessary to control the size of the laser spot as it could also rise the temperature of other parts than the surface ending with photodamage. In order to have a better control of the temperature, it is possible to use gold nanoparticles that absorb light in a more effective way than the molecules in the cell membrane(205–208).

Technique	Thermalizing method	Resolution		Temperature range	Strength	Limitation
		Temp to time response [°C/s]	Accuracy [°C]			
Microfluidic based system (CherryTemp)	Thermalization through a hard material	4°C per second	+/-0.1°C	5°C to 45°C	Stable and accurate temperature control	Calibration needed Complex setup
Microfluidic based system, chemical reaction	Thermalization based on thermal chemical reaction	1°C per second	+/-0.5°C to 1°C	-10°C to 76°C	Wide temperature range without electronics	Complex setup Hard to industrialize
Microheaters	Thermal conductivity	10-20°C per second	+/-0.2°C to 2°C	Ambient to 100°C	Easy to calibrate Low energy required, 1W	Only over ambient temperature
Laser based, IR and NIR	Heat based on light transfer	Spot location environment dependant, 1 to 10°C per second	+/-0.1°C to 1°C	Ambient to 100°C	Locale thermalization	Calibration needed

Table 9, Summary of the different micro approaches for sample thermalization

1.6. Parameters that can impact the sample temperature while doing live-cell imaging

There are many different factors that can affect the accuracy and stability of the sample temperature while doing live-cell imaging. The most important ones are the illumination, the laser power and the heat sink effect.

1.6.1. Illumination

Illumination can alter the sample temperature by heating up to the sample while doing live-cell imaging, especially techniques that using Transmission Light microscopy (TLM). The physics behind the heating is based on the magnification effect of the light when a light beam is focused on a very small area, all the illumination energy is transfer to heat in that spot, thus, increasing the temperature. Therefore, it is necessary to avoid illuminating the sample with a very powerful light source for long time on a very reduced area. As an example, there is an study reporting that microscopes illumination with a power of 300W had increased the brain tissue temperature in 1 to 2 ℃ while observation (209,210).

1.6.2. Laser power

As it has been mentioned here before, infrared laser can be used to locally heat sample areas while doing live-cell imaging in a range of 1°C per 100mW of power, therefore it is important to consider that while doing fluorescent microscopy the sample could be heated up while using lasers to generate the fluorescence.

In this case is important to understand the difference between the continuous and pulse configurations because the laser power and the illumination time play a big role in the heat transmission. Normally in the continuous illumination configuration, the power of the laser tends to be lower 50-100mW, than in the pulse one, 100-200mW. Those parameters combined with the exposition time will lead to the value of transmitted power per mm^2 per second, which provides the information about the amount of energy that it has been provided to an area of the sample during a certain period. The increase of temperature can be in the worst cases between 0.5°C to 1°C in an area of $1mm^2$, but this is very dependent on the type of sample/tissue and how the heat flows inside it(211–216).

1.6.3. Heat sink

The Heat sink is a physical phenomenon that occurs between two objects that are in contact or between one object an its environment. The heat sink is the transfer of energy, in this case of heat, between an object which it hotter to another one that is cooler in order to reach and equilibrium. This also occurs between an object and its environment but the time to reach an equilibrium tend to be much longer than in the previous case(217–221).

The heat sink occurs while doing live-cell imaging, especially when using immersion objectives that involve the use of oil or water. As an example, if the sample that is on a glass-slide at 37°C and is in contact via the immersion oil with the objective that is at room temperature, 20-25°C, due to the energetical difference the objective will start dragging energy/heat from the sample in order to reach an equilibrium where both are at

the same temperature or reduce the sample temperature by 2°C to 5°C after several hours. In the case of using dry objective the heat sink occurs with the stage and the surrounding environment so it could be that in the long-term(hours) the temperature of the sample could change due to changes in the stage or room temperature but those ones can be in a lower range of 0.5°C to 1°C after 10 hours of observation(222–224). A scheme of this phenomenon can be seen at Figure 18.

Another point to consider is the heat capacity of the materials of the different objects involved during this process because some of them can transfer very easily the heat like water or metals while others don't as they are isolating materials such as very dense oils or plastics (Polycarbonate or CoP). Some of the thermalizing systems take this into account during the calibration and the thermalization by monitoring the objective temperature. Some other system do not consider this at all, for example, the incubation boxes or try to mitigate it by using an objective heater to keep the objective temperature always at a certain temperature, normally closer to the sample one to reach the equilibrium as fast as possible and avoid drops in temperature(225–228).

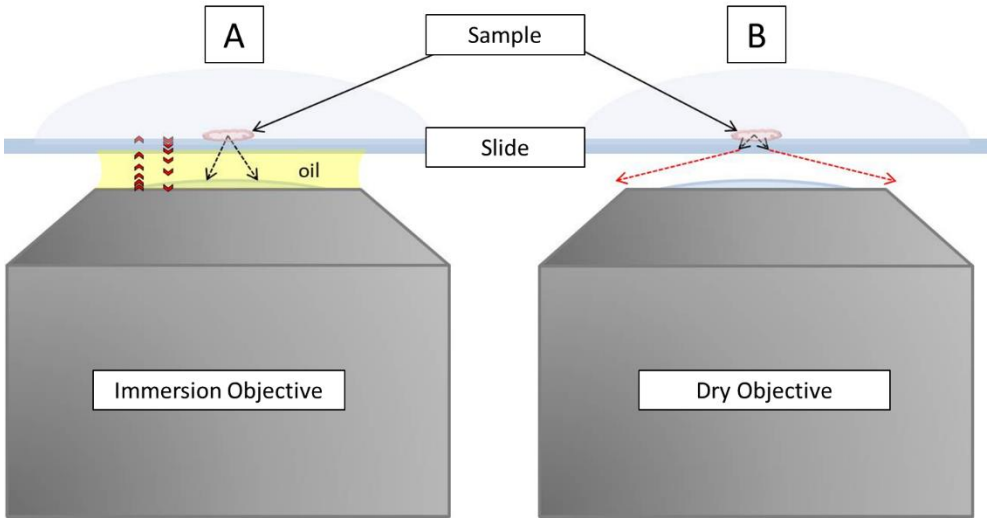

Figure 18, Scheme of the heat sink principle while using Immersion and Dry objectives

1.7. Implications in the sample while not proper temperature control

The implications can be divided in three major groups, image disruption, wrong biological phenotype and heat-shock or sample damage.

1.7.1. Image disruption

The image disruption is the first consequence of an issue with the temperature control, but it could be provoked by different factors, such as the image drift or the immersion liquid instability. The first one affects the focal plane because if the temperature increases the slide or the sample support device can expand by few micrometres altering the optical configuration. The same occurs if the temperature drops as the materials can contract. The drift can occur in the 3 axes, but it impact the image resolution more with the z-axis. Nevertheless, most of the microscopes nowadays have a re-focus feature that corrects this issue inside a range and with a defined frequency(229–233).

Another issue related with the lack of temperature control is the instability of the immersion liquid as most of them are done to work on a specific range, 20-25°C or 35-45°C(234), providing a specific refraction index. If the temperature changes or is outside those ranges, the liquid will have a different refraction index and will disturb the focal plane provoking imaging issues. Even if those liquids are prepared to work between ranges in the case of the water it cannot go below or close to 0°C as it could freeze and damage the objective. This kind of issues require to control very carefully the temperature and also to use the most suitable immersion liquids that work in the range of the sample temperature(235–237).

1.7.2. Phenotype disruption and sample damage

As it was introduced in the part 1.3.2 temperature plays a big role in the biology and if the thermalization is not properly done the observed phenotype can be different from the expected one.

As first example, the enzymatic activity of the cells is regulated by temperature as the enzymes have range of temperature at which they are functional and outside it they get denaturalized or degraded(238,239). Although, inside that range some enzymes are more efficient at specific temperatures while other stop completely their activity (240). There are also evidences that the active site is temperature dependent as it can change it conformation(241,242). Therefore, while doing live-cell imaging it is important to control the temperature as it is also possible to control the enzymatic activity of the studied phenotype(243–246).

Proteins are also temperature dependent entities. Their stability and capacity to trigger or stop certain mechanisms is dependant of the surrounding temperature. There are studies showing that the protein stability is different *in vivo* compared with what they observed *in vitro.* Those studies also show that the proteins are stable at different temperature *in vivo* and *in vitro.* There might be different reasons for that phenomena but the two more clear ones are first, that in the *in vivo* case there is an inner cell machinery in charge of the aggregation and folding, that is not present *in vitro*, where those processes become

thermodynamically dependent(247–250). The second reason is related with the inner cell temperature distribution, it could be that inside the cell the temperature could not be homogeneously distributed making the proteins stable only if they are at a certain location with an specific temperature, but this has not been validated yet(139,152,251–255).

Microtubules (MTs) are other example of temperature dependent structures as they can polymerize or depolymerize into monomers of tubulin due to temperature or because different inner cell mechanism. However, even if temperature could be the driving force it is necessary to understand if it is the only one or if it is inducing the action of other mechanism inside the cells. Those other mechanism could explain why some species are able to survive at very low temperatures and keep their MTs polymerized, e.g. Arctic anadromous fishes from the salmonid family or *Notothenia gibberifrons*(256–258) On the other hand, mammalian cells get most their MTs depolymerized by downing the temperature 20°C of its normal one(259,260). Microtubule-Based molecular motors are also temperature dependent as their transport speed can be reduced or increase due to temperature changes(261). All this together show how important is to control the temperature while observing MTs in live-cell imaging because a small variation in the comfort temperature of the sampling cells could affect their behaviour, resulting in observing a different phenotype from the aimed one(262–264).

At the cellular level the membrane stiffness is also temperature dependant and it can affect the cell permeability(265–267). The fatty acid tails of the phospholipids change their conformation depending on the temperature that is surrounding the cell, as those phospholipids have a range of temperature at which they can become more rigid or more fluidic. This capacity of change allows the cells to control the permeability and to adapt or react to it, if the conditions of the environment is not the most suitable one for them, being this mechanism a very important one for the survival of the cell against difficult situations(268–270).

As a summary, if the temperature of the sample is not properly controlled inside a specific range, it could happen that because of the temperature changes the cell in the sample could suffer a heat-shock that could end up on a irreversible cell damage. This kind of heat shocks can be due to both heat and cool, damaging the cells to an point of not recovery(271–275). This is why it is so important to have a correct temperature control while doing live-cell imaging.

1.8. Introduction to of AI for image classification

Artificial Intelligence (AI) can be used in combination with live-cell imaging for image classification and it represents the final application of this thesis.

Prior to go to the applications it is important to explain what Artificial Intelligence and all its subsets are such as Machine Learning (ML) and Deep Learning (DL) as it can be seen in Figure 19. The simplest definition of AI establishes it as a technique that enables machines to mimic human behaviour. Then Machine Learning is a subset of AI in which using statistics is possible to help a machine to improve with experience. Finally, Deep Learning is a subset of ML that takes care of the pure computational part connection different parts such as multi-layer neural networks.

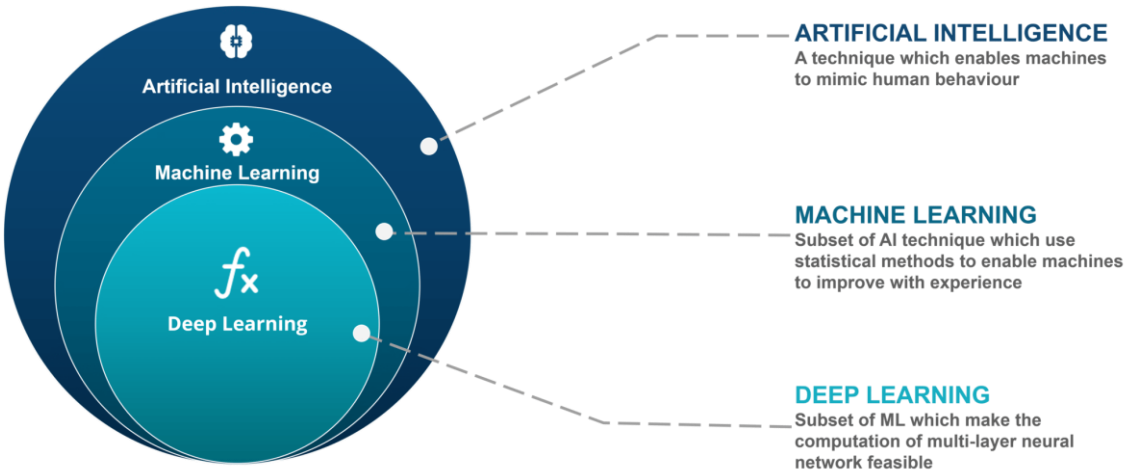

Figure 19, Illustration of the meaning of AI, machine learning and deep learning

1.8.1. AI brief history

The concept of AI was first introduced by Alan Turing during the 2nd World War when he and his team managed to "break" the code that was behind the encryption of the *Enigma* machine. According to him, if a machine could have a conversation with humans without the humans noticing that that is not human, the machine would win the "imitation game" be considered artificially "intelligent".

Later on, in 1956 John McCarthy organized the Dartmouth Conference, in which the term "Artificial Intelligence" was first used as it is used today. During the 1960s and 1970s computer science along with robotics and mathematics make the field to grow very fast until mid-1970s when it stopped. The period between mid-1970s to mid-1990s is commonly known as AI Winters due to the losing of momentum as the computers were not ready to work with the already developed algorithms as they were lacking on memory and computational power.

During the 2nd part of 1990s, AI start to gather the attention of the big companies, especially when IBM's Deep Blue defeated world chess champion, Garry Kasparov, becoming the first machine to beat a human. Since this event and thanks to the exponential improvement in computational power the field has continue growing specially in the last 15 years when Amazon, Google, Baidu or Tencent used AI based technology to gain

commercial advantage in order to process and predict what could be the final need of the user according to each individual profile.

Finally it is important to mention that thanks to the research performed over several years by Yoshua Bengio, Geoffrey Hinton and Yann LeCun, among other AI is what it is today(276).

1.8.2. Machine learning vs Deep learning

As it was introduced before Machine learning refers to technique that enables machines to learn by themselves using data and to make accurate predictions. It is just a subset of AI that is based on training algorithm so they can make the decision by themselves. This methodology normally requires a lot of data, high levels of computational power and time to obtain good results, if possible. Indeed, there are some cases in which the complexity of the algorithm could make very hard to obtain the good decision or prediction(277).

The ML based algorithms can be trained in two different ways, one is supervised, based on input and output data that can lead to classification or regression algorithms. The second one is unsupervised, where the algorithm itself will learn to make a classification based on the main features that it observed in the data set. This second group is normally used for clustering data Figure 20.

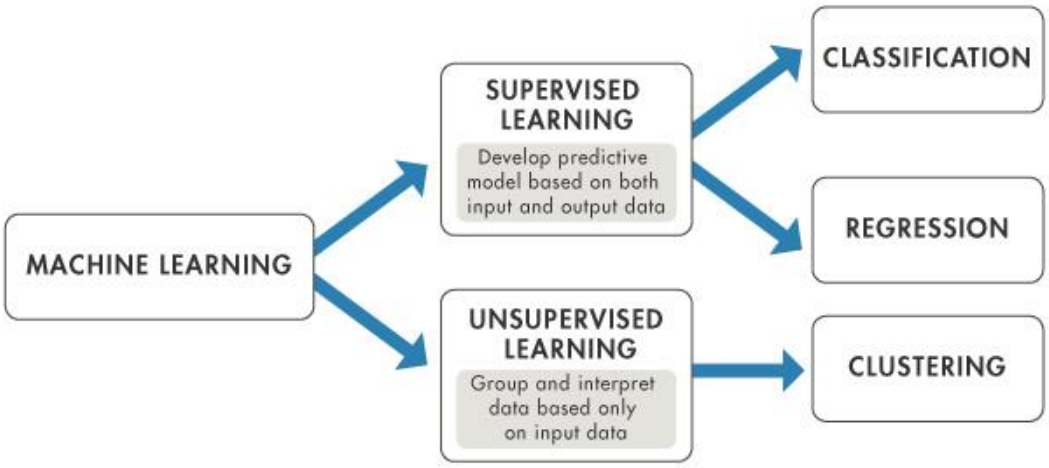

Figure 20,Machine learning types of learning scheme

On the other hand, deep learning is a subset of unsupervised ML that is inspired in the information processing pattern of the human brains that are able to identify patterns and classify different types of information(278,279). Whenever we receive new information, the brain tries to label it in order to understand it or to associate it with an already know concept. DL based algorithms can label by themselves the data prior to classify it. The main difference between ML and DL can be understand by Figure 21.

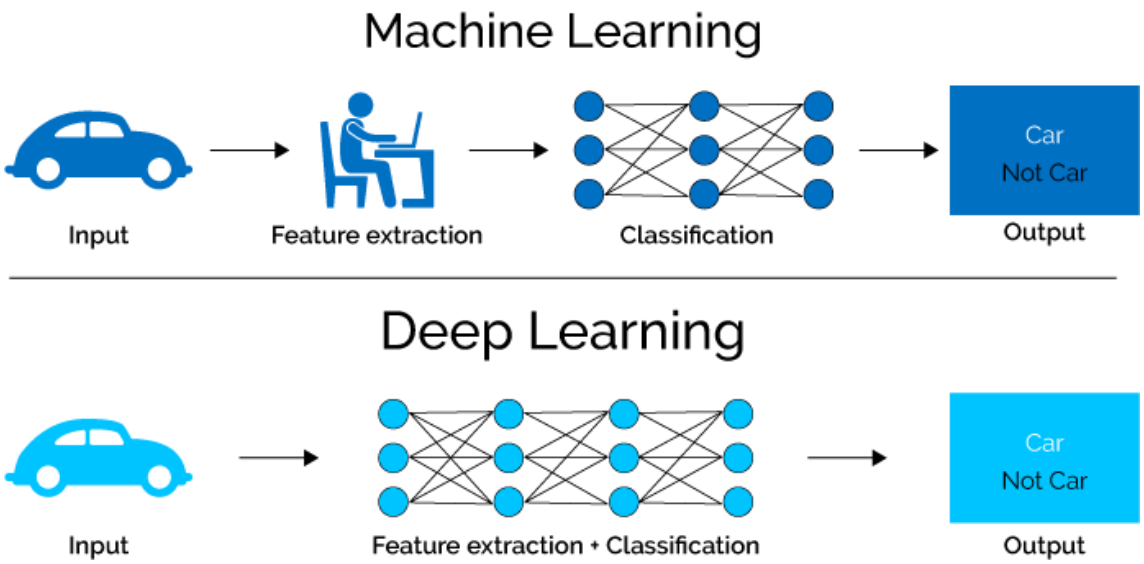

Figure 21, Illustration of the main difference between ML and DL

1.8.3. Examples of the image classification based on ML and DL

Now, there are different algorithms available to classify different types of images such as GoogLeNet, AlexNet or ResNet.

As a first example, AlexNet, which was a network developed by Alex Krizhevsky in 2012. This Neural Network competed in the ImageNet Large Scale Visual Recognition Challenge in 2012 archiving a top 5 error of 15.3% which was 10.8 percentage points lower than the runner-up. One of the keys of this network was the depth that allowed the high performance, which was computationally very expensive to run in a CPU but relatively feasible using GPU during the training process. It has 60 million parameters and 8 layers(280).

The second one, GoogLeNet, which was the winner of the ILSVRC 2014, at which it achieved a top-5 error of 6.67%. It is also known as Inception V1, as the researchers that developed it where the first ones to mention the concept of inception(281). This network used a CNN inspired by LeNet but with a novel element called inception module.

Finally, ResNet-152, which was the winner of the ILSVRC 2015, at which it achieved a top-5 error of 3.6%. It introduces the concept of skip connection to fit the input from the previous layer to then next one without any modification of the input allowing deeper networks. It is made of 152 layers and more than 60.2 million parameters.(282)

Chapter 2, Thermal Characterization of the microscope setup, from sensors to the microscope calibration using the CherryTemp

The second chapter will be focused on establishing a test bench to thermally characterize any microfluidic device or setup. It included the selection of different temperature sensors, the data shorting and the use of CherryTemp as stable, accurate and repeatable temperature source.

The construction of this test bench will be divided in the major parts:

- The thermal characterization of the temperature sensors
- The assembly of the setup (hardware and software)
- Presenting quantitative results of the impact in the sample temperature of different parameters surrounding the microscope setup

2.1. Different temperature sensor characterization

The first step was to thermally characterize different temperature sensors in order to monitor the temperature of the sample, the stage the objective and the room one(ambient). Each location possessed its own particularities (type of environment, working range, contact surface or size) thus, three different sensors were tested with the objective of finding which one of them would be the most suited one according to:

- Working environment: water, air or oil
- Working range: stable and accurate of at least +/-0.5°C
- Reactivity time: time to feel a change of temperature

All the tested sensors were compared with an RTD, PT-100 which was considered as golden-standard or reference sensor for this thermal characterization.

2.1.1. Specifications of tested sensors

Taking the requirements as a base I looked in the market for different sensors that could fit those needs and I selected three thermistors to be checked and one PT-100 to be used as reference or golden-standard.

Prior to present the characterisation of each sensor it was necessary to elucidate some concepts that drive their main features. All the thermistor sensors that were tested were resistance based, therefore the resistance to temperature relation followed the Steinhart-Hart equation(283,284), Equation 9. This complex equation using three resistance-temperature pairs of values to solve the equation and obtain the a, b and c values that provide the shape of the resistance-temperature curve of the sensor. The most common used temperatures are 0°C, 25°C and 85°C.

$$\frac{1}{T} = a + b\,\ln(R) + c\,(\ln(R))^3$$

Equation 9, Steinhart-Hart equation from resistance to temperature on thermistors. Thermistors coeficients(a,b,c), measured resistance(R) and measured temperature(T)

However, some sensor manufacturers provide the Beta value or $B_{25/85}$ as main feature of the thermistors. This Beta value came from a simpler equation, Equation 10, that represents the shape curve relationship between the resistance and the temperature using only two resistance-temperature points at 25°C and 85°C.

$$\beta = \frac{\ln(\frac{R_{T1}}{R_{T2}})}{(\frac{1}{T_1} - \frac{1}{T_2})}$$

Equation 10, Beta equation from resistance to temperature in thermistors. Beta value(ß) Resistance of temperature #1 and #2 (R_{T1} and R_{T2}) and Temperatures #1 and #2 (T_1 and T_2), where T_1 and R_1 are normally 25°C and 10K ohms.

Both equations were valid in order to calculate the temperature taking the resistance of the sensor, but the Steinhart-Hart equation is more complete as it covered a bigger range than the Beta one.

2.1.1.1. NTC thermistor from Vishay BC components

The 1st selected sensor was an NTC thermistor with the reference number NTCAIMME3 from Vishay BCcomponents. This sensor has a miniature insulated chip NTC thermistor mounted in a stainless steel (SS304) housing with a brass collar for sealed mounting and twin PVC insulated AWG#30 lead wire connection as it can be seen in Figure 22.

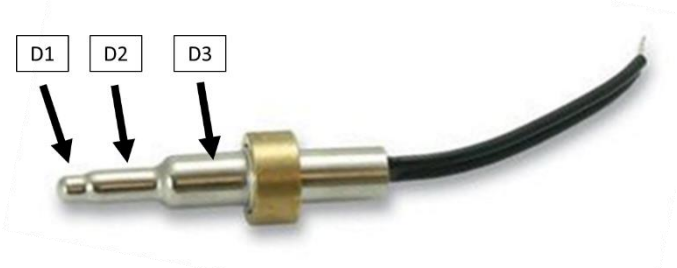

Figure 22, Example of the NTC thermistor from Vishay. 1st part diameter(D1), 2nd part diameter(D2) and 3rd part diameter(D3)

One of the keys to select this one was its size as the total length of the sensor was 23mm from the tip to the wire connection, and the different diameters from the tip:

- D1=2mm
- D2=2.5mm
- D3=3.9mm

All this combined present a small sensor able to be submerged in liquids or added in a flow circuit to measure the temperature of a liquid flowing. Together with this, the main features the NTC thermistor has R_{25} of 10K ohms, meaning that at 25°C the resistance was 10K ohms, with tolerance of +/-3%. Other key features of the sensor can be seen at Table 10.

Parameter	VALUE	UNIT
R_{25} or Resistance at 25°C	10K	Ω (ohms)
Tolerance on R_{25}	+/-3	%
Range of working temperature	-25 to +105	°C (Celsius)
Response time to 63.2% of ΔT, 25°C to 85°C	1.5	Seconds
Coefficient A for the S-H equation	1.1376^-3	-
Coefficient B for the S-H equation	2.3274^-4	-
Coefficient C for the S-H equation	0.9308^-7	-

Table 10, Summary of the main features of the NTC thermistor from Vishay

2.1.1.2. JT-sensor from Semitec

The 2nd selected sensor was an JT-sensor thermistor with the reference number 103-JT-025 from Semitec. This NTC sensor is encapsulated inside an insulation film of 25, 50, 75 or 100mm long and 0.5mm thick making it is perfect for small and thigh locations, Figure 23. The low mass of this sensor allow it to have a time response of 5 seconds from 25°C to 85°C but it can be shorter for smaller temperature ranges. A summary of the sensor specifications can be seen at Table 11.

Figure 23, Example of the JT-Sensor from Semitec

Parameter	VALUE	UNIT
R_{25} or Resistance at 25°C	10K	Ω (ohms)
Tolerance on R_{25}	+/-1	%
Range of working temperature	-50 to +125	°C (Celsius)
Response time to 63.2% of ΔT, 25°C to 85°C	5	Seconds
Coefficient A for the S-H equation	0.8047^-3	-
Coefficient B for the S-H equation	2.6631^-4	-
Coefficient C for the S-H equation	1.2329^-7	-

Table 11, Summary of the main specifications of the JT-sensor from Semitec

2.1.1.3. Omega sensor

The 3rd selected sensor was a self-adhesive patch sensor thermistor with the reference number SA2F-TH-44031-120 from Omega engineering. This NTC sensor is encapsulated inside a rubber that allows the connection to a copper based self-adhesive surface. The encapsulation is 35mm long, 12mm wide with a thickness of 2.5mm. Figure 24.

Figure 24, Example of the self-adhesive patch sensor from OMEGA

This sensor was ideal for surfaces as it had a self-adhesive patch in the sensing part. From the datasheet I extract the information available in the Table 12.

Parameter	VALUE	UNIT
R_{25} or Resistance at 25°C	10K	Ω (ohms)
Range of working temperature	-30 to +100	°C (Celsius)
Response time to 63.2% of ΔT, 25°C to 85°C	25	Seconds
Coefficient A for the S-H equation	1.0301^-3	-
Coefficient B for the S-H equation	2.3897^-4	-
Coefficient C for the S-H equation	1.5715^-7	-

Table 12, Summary of the main specifications of the self-adhesive patch sensor from Omega

2.1.1.4. RTD, PT-100 sensor from TC S.A.

For RTD, PT-100 I selected one from TC S.A. which is a French temperature sensor supplier. I selected model 16-1-2.5-4-15.5-CE1HT-R100-A-100 MM followed the measurements shown in the Figure 25.

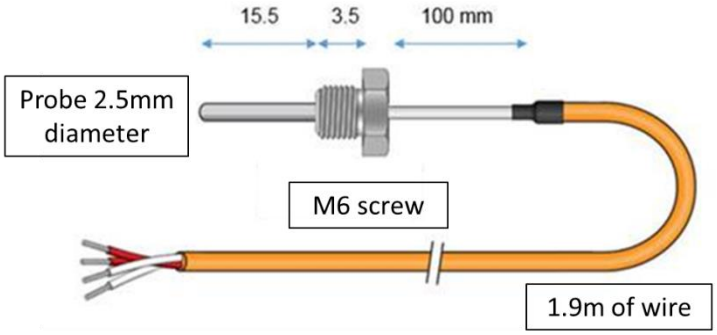

Figure 25, Scheme with the main dimensional specification of the RTD, PT-100 sensor from TC S.A.

All the previous sensors were thermistors while this one was an RTD which followed a different equation for the resistance-temperature curve. That equation was the Callendar-Van Dusen one(285–287), presented at Equation 11(A-B), with the two option according to the temperature range. Then, the main features of this type of sensor were specified at the Table 13.

Parameter	VALUE	UNIT
R_0 or Resistance at 0°C	100	Ω (ohms)
Alpha value or α	0.00385	1/°C
Accuracy	+/-0.1	°C
Range of working temperature	-200 to 850	°C (Celsius)
Response time to 63.2% of ΔT, 25°C to 85°C	1	Seconds
Coefficient A for the C-VD equation	3.9083^-3	1/°C
Coefficient B for the C-VD equation	-5.775^-7	1/(°C^2)
Coefficient C for the C-VD equation	-4.183^-12	1/(°C^4)

Table 13, Summary of the main specifications of the RTD, PT-100 sensor from TC S.A

A	$In\ the\ range\ of\ -200°C\ to\ 0°C, R_t = R_0[1 + At + Bt^2 + C(t-100)t^3]$
B	$In\ the\ range\ of\ 0°C\ to\ 850°C, R_t = R_0[1 + At + Bt^2]$

Equation 11, Callendar-Van Dusen equation for RTD, PT-100 according to the range. Coefficients (A, B, C), measured temperature(t), resistance at 0°C(R_0) and measured resistance (R_t)

2.1.2. Characterization setup, conditions and protocol

2.1.2.1. Characterization setup

As mentioned before the aim of the sensor's characterization was to find out which sensor would be the most suited one for the different locations. Each sensor was going to be assessed on the measurement of specific temperatures of the microscope setup and on their offset compared to the RTD, PT-100 (considered as reference). Additionally, different types of environmental conditions tested were:

- Air
- Water
- Oil

All of them tested at different temperature ranges:

- Ambient temperature (20-22°C)
- Over ambient temperature(>25°C)
- Below ambient temperature(<18°C)

The setup for the characterization included 3xJT-sensors, 3xNTC sensors, 1xOmega sensor and 2xRTD, PT-100 sensors, placed in a holding structure made of plastic with 10 slots. In order to fix their position and place them all at the same level, I decided to use polystyrene tubes that had a hole for the sensor to get in as it can be seen in Figure 26.

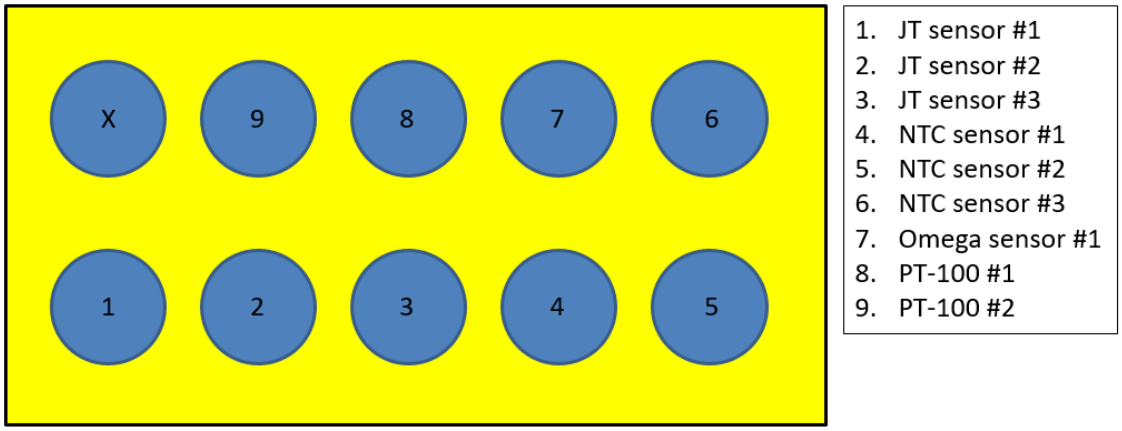

Figure 26,Scheme of the distribution of the different sensors in the holding structure

All the sensors were placed in a plastic structure following the scheme shown in the Figure 1 and connected with 2 meters of wire to an Agilent 34972A, a signal recorder from Keysight Technologies, in order to measure the resistance of each sensor and the temperature of the PT-100 sensors, following this order:

- **CH1:** 103-JT-sensor #1
- **CH2:** 103-JT-sensor #2
- **CH3:** 103-JT-sensor #3
- **CH4:** NTC Vishay #1
- **CH5:** NTC Vishay #2
- **CH6:** NTC Vishay #3
- **CH7:** Omega 44031 #0
- **CH8:** RTD, PT-100 #1, paired with **CH18**
- **CH9:** RTD, PT-100 #2, paired with **CH19**

NOTE #1: All the thermistors were 2-point connection sensors except the RTD, PT-100 that were 4-points ones.

NOTE #2: I only used one Omega 44031 due to the low stock availability of this type of sensors at the time of the experimentation.

2.1.2.2. Characterization condition

The conditions for the recording include three different mediums (air, water and oil) at three different temperatures ranges (ambient, below and over ambient). For the air condition, I placed the recording setup inside the fridge (below ambient), outside the fridge (ambient) and inside an empty kettle after heating up water (over ambient, decreasing to ambient).

For the water condition, the recording setup was placed inside a plastic box with water(0.5L) reaching the tip of the sensors and for the different temperatures it was placed inside the fridge (below ambient), outside the fridge (ambient) and with hot water after boiling it(100°C) using a kettle (over ambient, decreasing to ambient).

Finally, for the oil condition, I used regular microscopy oil, from Sigma-Aldrich, 56822-1L, inside the same plastic box of 0.5L volume. In this case, I only checked scenarios inside the fridge (below ambient) and outside the fridge(ambient).

2.1.2.3. Characterization protocol

For the data acquisition protocol, I recorded twice for 1h with a sample frequency of 10s. All the eight combinations between temperature range and medium were assessed using a programme based on MATLAB, release 2017b from MathWorks, Inc., Natick, Massachusetts, United States. The developed software include different modules such as settings for each type of sensor, adaptation of the Steinhart-Hart equation, data storage or communication with the Agilent 34972A an LXI Data Acquisition device from Keysight, Figure 27.

Figure 27, Image of the Agilent 34972A LXI Data Acquisition device from Keysight

2.1.3. Results of the characterization

The analysis of the results was separated in two parts. The first one was focused on the offset or different between the reference, RTD, PT-100 and each sensor. The second analysis aimed to determine if there was any intra-sensor deviation due to the different batch. As explained before, the target here was to identify which sensors had a working range inside the +/-0.5°C range for both analysed features.

2.1.3.1. Results from the air condition

In the air condition the analysis started from the higher temperature experiment towards the lower one analysing the mean difference between each sensor and the reference (inter-sensor offset), as well as the maximum and minimum deviation inside each sensor (intra-

sensor deviation) within the tested temperature range. The results can be seen in the Table 14.

As a recap, all the sensors fit inside the +/-0.5°C inter-sensor offset (1st column) threshold for air condition at the different temperatures. From the intra-sensor deviation (2nd column), the two values correspond to the maximum and minimum deviation between the sensors of the same type. Lastly, only the 103-JT-sensors present a bigger deviation but always below +/-0.5°C threshold.

Sensor	Air condition		
	Temperature range	Inter-sensor Offset(°C)	Intra-sensor Deviation(°C)
103-JT-sensor	46°C to 28°C	0.325°C	0.43°C to 0.22°C
NTC Vishay		0.14°C	0.186°C to 0.094°C
Omega 44031		0.326°C	NaN
RTD, PT-100		NaN	0.02°C
103-JT-sensor	21.8°C to 20.8°C	0.096°C	0.133°C to 0.059°C
NTC Vishay		0.126°C	0.186°C to 0.066°C
Omega 44031		0.328°C	NaN
RTD, PT-100		NaN	0.021°C
103-JT-sensor	7°C to 5.3°C	0.191°C	0.399°C to 0.01°C
NTC Vishay		0.173°C	0.258°C to 0.025°C
Omega 44031		0.06°C	NaN
RTD, PT-100		NaN	0.025°C

Table 14, Data summary of the results of the sensor characterization in the air condition at different temperatures ranges

2.1.3.2. Results from the water condition

In the air condition the analysis started from the higher temperature experiment towards the lower one analysing the mean difference between each sensor and the reference (inter-sensor offset), as well as the maximum and minimum deviation inside each sensor (intra-sensor deviation) within the tested temperature range. The results were summarized at Table 15.

Sensor	Water condition		
	Temperature range	Inter-sensor Offset(°C)	Intra-sensor Deviation(°C)
103-JT-sensor	85°C to 45°C	0.5193°C	0.106°C to 0.03°C
NTC Vishay		0.5°C	0.27°C to 0.13°C
Omega 44031		0.06°C	NaN
RTD, PT-100		NaN	0.022°C
103-JT-sensor	19°C to 16°C	0.161°C	0.476°C to 0.24°C
NTC Vishay		0.189°C	0.249°C to 0.12°C
Omega 44031		0.122°C	NaN
RTD, PT-100		NaN	0.025°C
103-JT-sensor	11°C to 7°C	0.075°C	0.056°C to 0.036°C
NTC Vishay		0.073°C	0.242°C to 0.103°C
Omega 44031		0.1653°C	NaN
RTD, PT-100		NaN	0.027°C

Table 15, Data summary of the results of the sensor characterization in the water condition at different temperatures ranges

As a recap, nearly all the sensor fit inside the +/-0.5°C inter-sensor offset (1st column) threshold for water condition except for the 103-JT-sensors at high temperatures. This was due to the low mass and small contact surface. Apart from that the deviation between the different sensors (2nd column) from the same batch was inside the expected range of +/-0.5°C.

2.1.3.3. Results from the oil condition

In the oil condition the analysis will follow the same steps than in the previous ones not including the over ambient temperature range, as mentioned before. The outcome of the analysis of the mean difference between each sensor and the reference (inter-sensor offset) and the maximum and minimum deviation inside each sensor (intra-sensor deviation) within the tested temperature range, were shown at Table 16.

Sensor	Oil condition		
	Temperature range	Inter-sensor Offset(°C)	Intra-sensor Deviation(°C)
103-JT-sensor	21.5°C to 21.1°C	0.09°C	0.08°C to 0.03°C
NTC Vishay		0.06°C	0.24°C to 0.115°C
Omega 44031		0.152°C	NaN
RTD, PT-100		NaN	0.027°C
103-JT-sensor	10°C to 5.5°C	0.653°C	0.091°C to 0.009°C
NTC Vishay		0.307°C	0.22°C to 0.095°C
Omega 44031		0.074°C	NaN
RTD, PT-100		NaN	0.12°C

Table 16, Data summary of the results of the sensor characterization in the oil condition at different temperatures ranges

As a final recap, at ambient temperatures, all the sensors had less variability than +/-0.5°C compared with the reference. This made much sense because oil was a denser liquid

compared with the water thus was more stable and less affectable to small temperature changes, especially in a short-ranges, 20-22°C.

At low temperatures, bigger differences in case of 103-JT-sensor could be explained again due to its low mass and small contact surface. Apart from that the rest of the sensors were within the +/-0.5°C in terms of offset and deviation.

2.1.4. Conclusion of the characterization

From this sensor characterization experiments I managed to extract some conclusion. The first one was related with the linearity and stability of the tested sensor, as all of them presented lower deviation than +/-0.5°C in all the conditions. This meant that all the selected sensors could be used several times in different conditions that the results should always be below that threshold. This led to the second conclusion that taking the off-set as reference all of them where within the +/-0.5°C threshold in most of the conditions. Altogether, allowed me to validate them all to be used at the test bench. However, an individual analysis was required.

The 103-JT-sensor could be perfectly used to monitor the temperature of a sample as it can fit in small location (0.5mm thickness) and it has a maximum offset of +/- 0.3°C on air. In case of water it was +/-0.56°C over 45°C, explainable due to the low mass and small contact surface of the sensing part. The sensor was placed in a big volume of liquid where big variations could be more relevant than at a small volume, which would be the case as it would be at the sample location.

In case of the NTC Vishay it could be easily used to monitor the temperature of different liquids (inside a microfluidic chip) as it had enough mass to not be affected by fast small changes and the overall offset was in its maximum 0.5°C (in water at high temperatures).

For the Omega 44031 sensor proved to be a very accurate sensor with a maximum offset of +/-0.32°C compared with the reference. Therefore, it would be used to monitor the temperature of the microscope stage.

The RTD, PT-100 deviation characterization showed that in its maximum point it could reach +/-0.12°C in the case of the oil at low temperatures while in the rest of the cases it oscillated between 0.027° and 0.02°C. Confronting its choice as reference.

Finally, in terms of time response $\Delta T_{25/85}$, time to sense a change from 25°C to 85°C, the values for each sensor were the following ones:

- RTD-PT100: 1s
- NTC Vishay: 1.5s
- 103-JT-sensor: 5s
- Omega 44031: 25s

As a summary the final location for each sensor at the test bench could be seen at the Table 17.

Sensor	Location	What to monitor?
RTD-PT-100	On top of the microscope	Room temperature
Omega 44031	Microscope stage or objective	Stage or objective temperature
103-JT-sensor	Sample location	Sample temperature
NTC Vishay	Inside microfluidic device	Thermalization liquid temperature

Table 17, Summary of the possible location at the test bench for the different characterized sensors

2.2. Characterization of the microscope setup using CherryTemp

Once the sensor characterization was done, the characterisation of the whole microscope setup was possible. Quantification pf the impact of different factors that could affect the sample temperature while doing live-cell imaging was the key driver of this setup. Depending on the type of microscopy configuration, dry or immersion objectives, the setup, the sensors and the culture device, the CherryTemp calibration needed to be adapted. The modifications were done to obtain more precise and reliable data as well as to quantify the key parameters impacting the final sample temperature.

In this part, I was going to cover the following points:

- Explanation of the thermalization technology behind CherryTemp
- Description of the setup, the characterization protocol and the results for each configuration (dry and immersion)
- In detail explanation of the different sub-factors that were addressed at each configuration
- Ranking of all the factors that end up affecting the sample temperature from higher to lower impact

All the previously mentioned steps were covered during this part of chapter 2.

2.2.1. Thermalization behind CherryTemp

The CherryTemp thermalization system, Figure 28, was first commercialized by Cherry Biotech, Rennes (France) in 2014 to allow thermalization while performing live-cell imaging of biological models. The first used models were yeast, then *C. elegans* until reaching *drosophila melanogaster* among others.

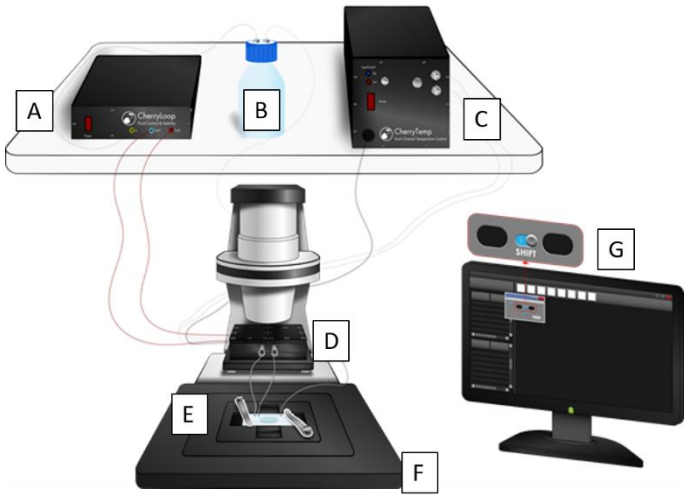

Figure 28, General scheme of the CherryTemp with the different components. CherryLoop (A), Fluidic Tank(B), CherryTemp (C), Heat-Exchanger module(D), Thermalization chip(E), chip insert to the microscope stage(F) and CherrySoft, software interface that controls the thermalization(G)

Some of the key features of this system were:

- Temperature range, from 45°C to 5°C but able to reach from 60°C to 0°C in special cases/setups
- Fast temperature switch between two different temperatures in 10 seconds or less
- Accuracy, +/-0.3°C in the sample location

The technology behind this features were the use of a microfluidic chip that allows to thermalize a sample using energy transfer through a hard surface(288).

First, the mounting of the sample was made of a sandwich between the thermalization chip Figure 28-E and Figure 29, and a glass coverslip. In order to protect the sample from squeezing a spacer was placed, which thickness can be adapted depending on the biological model. Then, the thermalization chip was a three layer microfluidic chip made of an 24x60x8mm PMMA block, Figure 29-A, a double-side tape layer that conformed the thermalization chamber, Figure 29-B and a glass coverslip(#3, 24x60mm). The thermalized chip had 2 input points, connected to the Heat Exchanger, Figure 28-D, and 1 output point, connected to the Fluidic Tank, Figure 28-B.

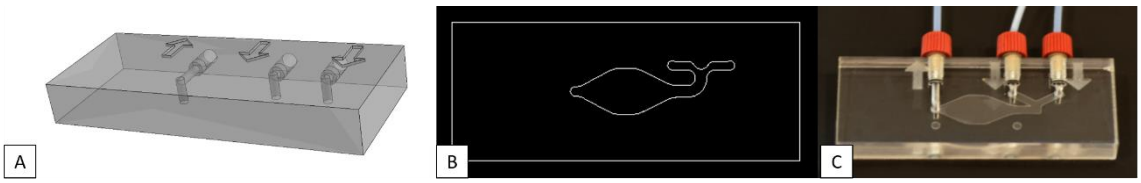

Figure 29,Thermalization chip. PMMA block 3D drawing(A), Thermalization chamber 2D drawing(B), Full chip assembly example(C)

The, the sample thermalization was based on two independent channels (Channel #1 and Channel #2) that had each of them one independent Peltier element allowing very accurate and stable temperature control. The working principle started with the thermalization liquid that circulated from a reservoir or Fluidic Tank, Figure 28-B, to the Heat-Exchanger module, where the Peltier elements were located. At this module, the thermalization liquid could be heated or cooled depending on the target temperature of each channel. Once the liquid reached the target temperature it could be quickly injected into the thermalization chip mounted with the sample on the microscope stage. Due to the small thermal mass (distance between the thermalization chip and the sample) the energy transfer could be very fast (10s or less). Finally, a feedback loop that continuously monitors the room temperature or the heat-sink in case of using immersion objective, provided the high accuracy of +/-0.3°C presented before. The algorithm behind this feedback loop was embedded on the CherrySoft, Figure 28-G, and it was able to calculate the heat-loss between the pre-thermalized liquid at the Heat-Exchanger module and the thermalization chip. Using as reference the selected sample temperature by the user, the CherryTemp tends to reduce this heat-loss in order to provide the most accurate and stable temperature as possible.

In the case that the user wanted to change the temperature from Channel #1 to Channe#2, it could be done by clicking on the CherrySoft that would activate a fluidic switch inside the CherryLoop. This would flow the thermalization liquid towards the Channel #2 at the Heat-Exchanger module to the thermalization chip, providing the selected temperature to the sample. This switch took 10 seconds or less, corresponding to the time for the liquid to flow from the Heat Exchanger to the thermalization chip. In addition, the

thermalization chip was placed on a chip insert that was adapted to the microscope stage, Figure 28-F.

2.2.2. Dry configuration characterization

The experiments for the characterization of dry configuration were performed at Cherry Biotech's Head Quarters in Rennes, France, during the summertime of 2018 with a warm room temperature(>25°C). The objective of this set of experiments was to quantify the impact of different factors in the sample temperature while building a ranking, from the higher to the lower impact.

2.2.2.1. Setup for the Dry configuration characterization

The material used for the Dry configuration characterization and the location of each component can be seen Figure 30. The detailed list is the following one:

CherryTemp from **Cherry Biotech,** to thermalize the sample:
- **Machine code:** TempoCell #2-E1533B118
- **Ambient sensor:** Omega 44031
- **Type of chip:** ThermaChip + AR-LSR-0.25-AR spacer
- **CherrySoft version:** 1.0.37 GeminiV1

Agilent 34972A from **Keysight,** to record the temperature of all the sensors:
- **103-JT-sensor:** to monitor the temperature of the sample
- **Omega 44031:** to monitor the temperature of the microscope stage
- **2x RTD, PT-100:** to monitor the temperature of the room at two locations, over the microscope and at the infinite.

Leica DM-IRBE microscope from **Leica:**
- **5x Dry objective**

R&D computer, to control the different software and to store the recorded data

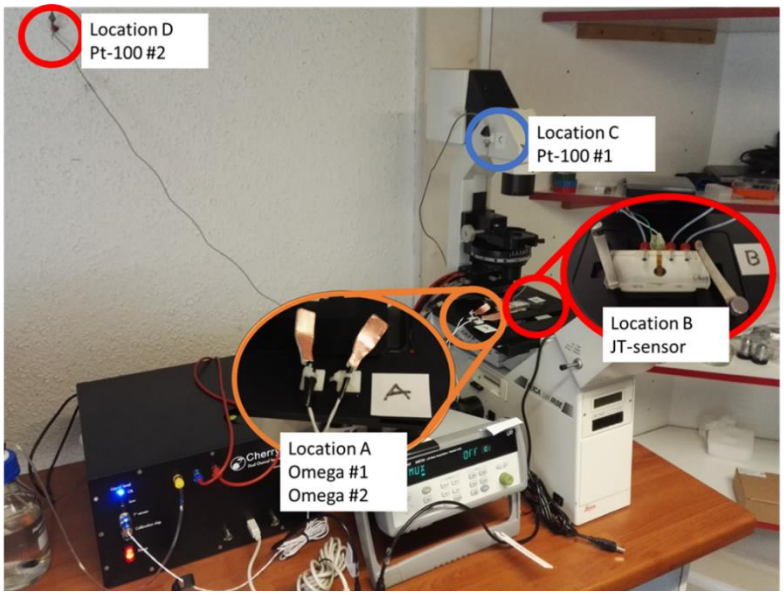

Figure 30, Dry configuration characterization setup with the location of the different sensors, devices and the microscope

NOTE #1: The AR-LSR-0.25-AR spacer which hosted the 103-JT-sensor(0.5mm thick) was made of a 3 layer lamination of AR-90880 tape(0.142m), 0.25mm liquid silicone robber, LSR, and AR-90880 tape(0.142mm), which makes a total of 0.543mm. The 2D design of the spacer can be seen at Figure 31.

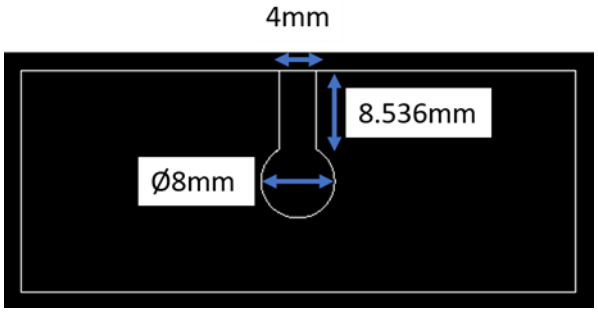

Figure 31, 2D design of the AR-LSR-0.25-AR spacer and the dimensions from the upper view

2.2.2.2. Dry configuration protocol

The protocol for the Dry configuration was divided in three major steps:

- Setup preparation
- CherrySoft and data recording settings
- Quantification of the impact of the room and the stage temperature over the sample one

For the preparation of the setup the requirements were that before starting the recording and the thermalization it was necessary to fill the chamber were the 103-JT-sensor was located with 50uL of distil water using a syringe. This step was necessary to prevent the formation of any air bubble to enter inside the chamber while performing the experiment. Indeed, an air bubble could disrupt the temperature measured by the 103-JT-sensor. Then the Omega 44031 sensor oversaw the monitoring of the stage temperature while the two RTD, PT-100 sensors were used to measure the ambient temperature.

NOTE #2: As an extra security, if the ambient temperature was higher than 30°C or below 18°C, the recording would be postponed until the temperature of the room fitted inside that threshold to avoid extreme conditions in the characterization that could generate outliers and disrupt the outcome.

For the thermalizing software settings, I built a thermalization sequence directly at the level of the Heat-Exchanger module in order to have in all the different experiments the same thermalization prior to reach the thermalization chip. This setting let the room temperature as the only variable capable to impact the sample temperature. The programmed temperature profile is available at Figure 32. Briefly, it started by started by thermalizing the sample with pre-heated liquid at 20°C for 10’ to go then to -5°C, 5°C, 15°C, 25°C, 37°C and 45°C. Between all the changes there was a 10’ at 20°C step to avoid over-heating the PMMA and remove any memory of the material that could generate a thermal inertia that could end up providing not real results.

From the recording settings, five cycles of 190 minutes each were done in order to generate enough data and the sampling frequency was 10s. All the recording was done using a MATLAB software that was based on the previous one used to characterize the different sensors.

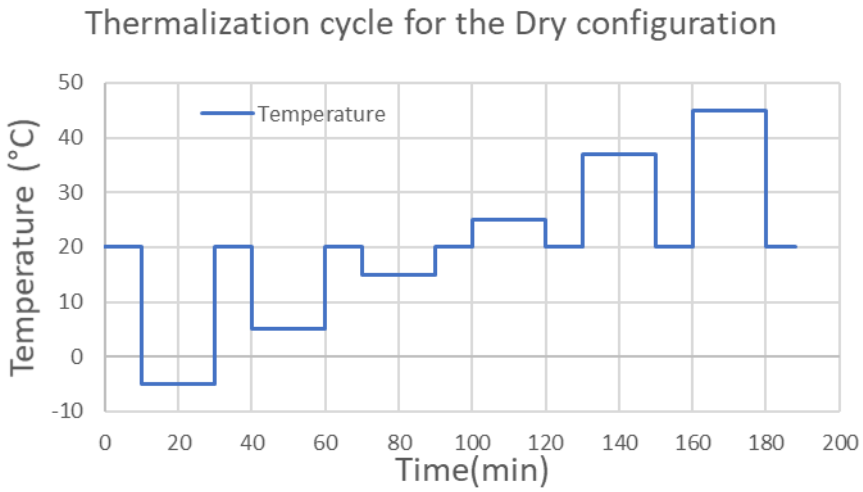

Figure 32, Scheme of the temperature evolution in the Heat Exchanger during the Dry configuration thermalization

NOTE: Prior to present the results it is necessary to mention that the data from the -5°C at the Heat Exchanger was removed from the final analysis because the difference of temperature between the room temperature, between 28°C and 24°C make it very hard for the chilling system of the CherryTemp to provide stable temperature during that step.

2.2.2.3. Dry configuration results

The obtained raw data was represented in the following variables:

- **Temperature of the Peltier (T_p):** corresponding to the temperature at the Heat-Exchanger module during the thermalizing cycles
- **Temperature of the stage (T_{st})**: measured temperature at the microscope stage with the Omega 44031 sensor (Location A)
- **Temperature of the sample (T_s):** measured temperature at the sample location with the 103-JT-sensor (Location B)
- **Temperature of the room #1 (T_{r1})**: measured temperature on top of the microscope with an RTD, PT-100 sensor (Location C)
- **Temperature of the room #2 (T_{r2})**: measured temperature on top of the microscope with an RTD, PT-100 sensor (Location D)

All this raw data was in absolute temperature and in order to compare between different experiment it was necessary to convert it to relative temperature in order to see the real effect of the room and stage temperatures on the sample one. The formula to convert the data to relative were presented at Table 18.

Relativization factor	Absolute temperature factor	Relative Temperature Equation
Temperature of the room #1 (T_{r1})	Temperature of the Peltier (T_{pA})	$T_{pR1}=T_{pA}-T_{r1A}$
	Temperature of the sample (T_{sA})	$T_{sR1}=T_{sA}-T_{r1A}$
Temperature of the room #2 (T_{r2})	Temperature of the Peltier (T_{pA})	$T_{pR2}=T_{pA}-T_{r2A}$
	Temperature of the sample (T_{sA})	$T_{sR2}=T_{sA}-T_{r2A}$
Temperature of the stage (T_{st})	Temperature of the Peltier (T_{pA})	$T_{pR3}=T_{pA}-T_{stA}$
	Temperature of the sample (T_{sA})	$T_{sR3}=T_{sA}-T_{stA}$

Table 18, Temperature relativization equations depending different factors such as room temperature or stage temperature.

All the previously mentioned variables allowed me to compare the data between experiments but in order to extract the impact of the different room temperatures (T_{r1} and T_{r2}) and the temperature of the stage (T_{st}) I created a new variable called Temperature impact in the sample (T_{is}) that was calculated as Equation 12. It was obtained for each relativization to quantify the impact of the different factors (room and stage temperature).

$$T_{is}= T_{pR}-T_{sR}$$

Equation 12, Temperature impact in the sample equation. This variable was obtained by making the difference between the Temperature of the Peltier in Relative (T_{pR}) and the Temperature of the sample in Relative (T_{sR})

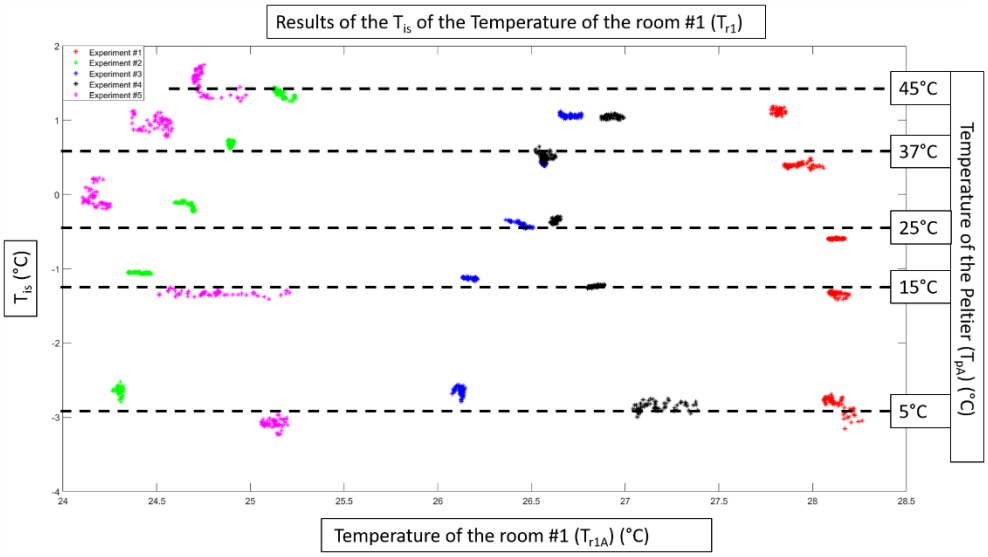

Figure 33, Results from the T_{is} calculation of the Temperature of the room #1(T_{r1A}). The left y- axis was the T_{is}, the x-axis was the Temperature of the room #1(T_{r1A}) in absolute temperature and the right y-axis was the (T_{pA}) to visualize the thermalization steps. Each colour represented one experiment.

At Figure 33, it was possible to observe that T_{is} followed a constant difference at each T_{pA} step, which was in absolute temperature for the visualization, without any impact from the temperature of the room #1 factor.

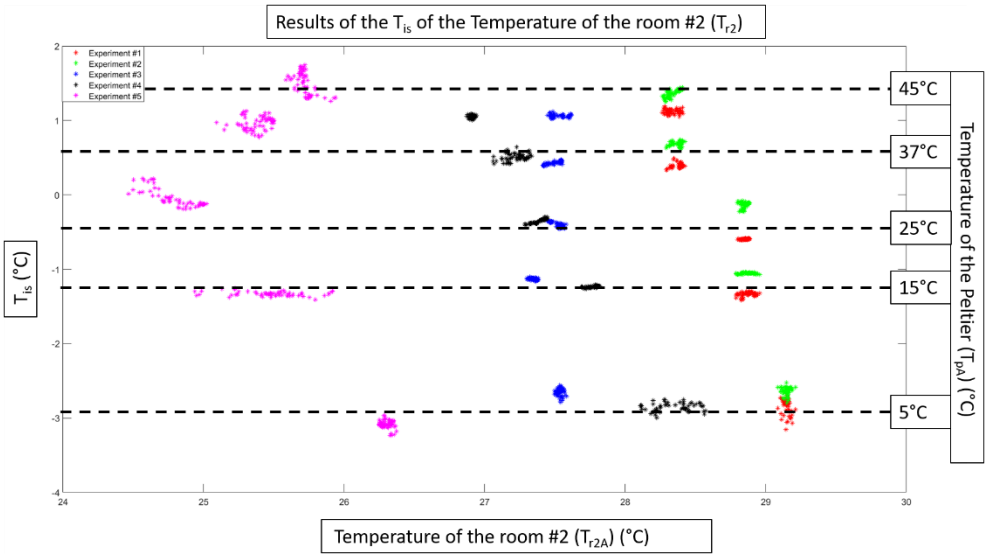

Figure 34, Results from the T_{is} calculation of the Temperature of the room #2(T_{r2A}). The left y- axis was the T_{is}, the x-axis was the Temperature of the room #2(T_{r2A}) in absolute temperature and the right y-axis was the (T_{pA}) to visualize the thermalization steps. Each colour represented one experiment.

At Figure 34 the obtained results showed that T_{is} followed again a constant difference at each T_{pA} step, without any impact from the temperature of the room #2 factor. The results of these two cases demonstrated that for the dry configuration, the impact of the room temperature is constant and measurable, therefore it can be quantified in order to adapt the thermalization to it.

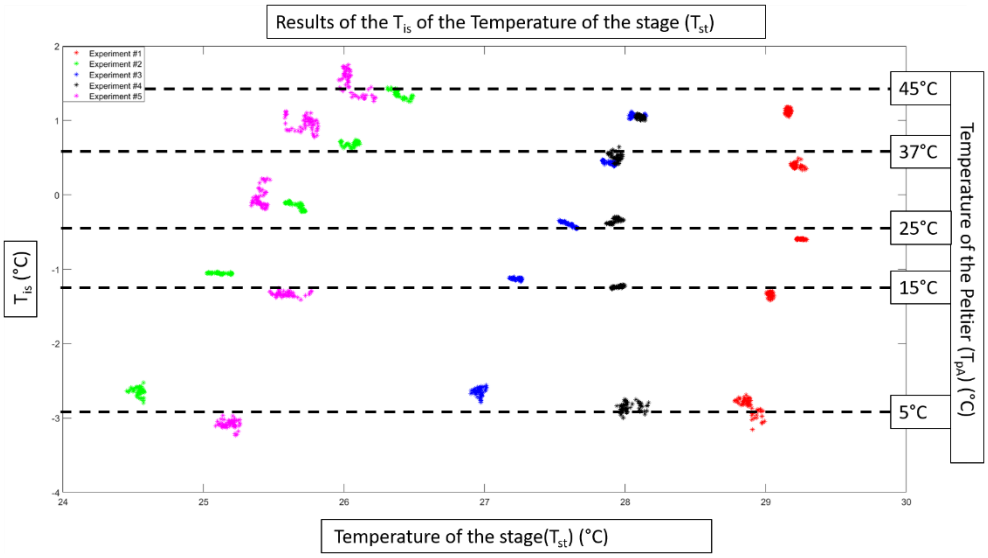

Figure 35, Results from the T_{is} calculation of the Temperature of the stage (T_{st}). The left y- axis was the T_{is}, the x-axis was the Temperature of the stage (T_{st})) in absolute temperature and the right y-axis was the (T_{pA}) to visualize the thermalization steps. Each colour represented one experiment.

Finally, in the case of the temperature of the stage $T_{st,}$ it did not impact at all the temperature of the sample as the T_{is} was again constant at the different T_{pA} steps, as presented at Figure 35. Consequently, it was possible to quantify the difference and use it in case of need for a thermalization using that value as reference.

2.2.3. Immersion configuration characterization

The experiments for the characterization of immersion configuration were performed during 2018 summertime at Cherry Biotech's Head Quarters in Rennes, France. The experimentation to characterize the impact of different factors on the sample temperature was divided in five groups/factors characterization:

- 2xRoom temperatures (on top of the microscope and at the infinite)
- Objective temperature
- Type of objective (sharp of flat tip)
- Z-distance between the sample and the different objectives
- Type of immersion liquid (oil vs water)

2.2.3.1. Setup for the Immersion configuration characterization

The material used for the Immersion configuration characterization was the following one and the location of each component can be seen at:

CherryTemp from **Cherry Biotech,** to thermalize the sample:

- **Machine code:** TempoCell #2-E1533B118
- **Ambient sensor:** Omega 44031
- **Type of chip:** ThermaChip + AR-LSR-0.25-AR spacer (same as in the Dry config)
- **CherrySoft version:** 1.0.37 GeminiV1

Agilent 34972A from **Keysight,** to record the temperature of all the sensors:

- **103-JT-sensor #1:** to monitor the temperature of the sample
- **103-JT-sensor #2:** to monitor the temperature of the stage close the sample
- **Omega 44031:** to monitor the temperature of objective
- **2x RTD, PT-100:** to monitor the temperature of the room at two locations, over the microscope and at the infinite.

Leica DM-IRBE microscope from **Leica:**

- **100x sharp tip immersion objective**
- **100x flat tip immersion objective**

R&D computer, to control the different software and to store the recorded data

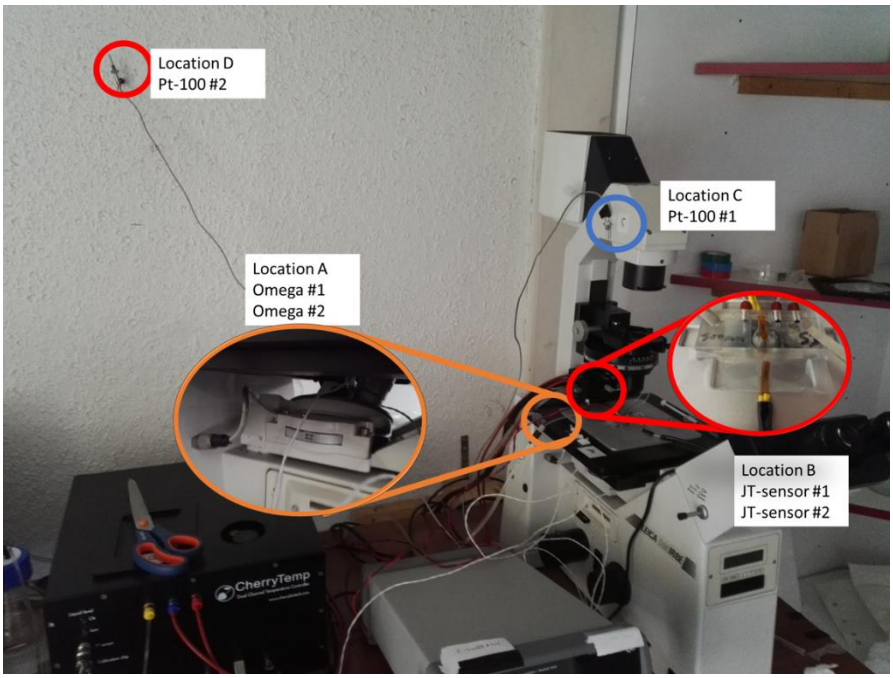

Figure 36, Immersion configuration characterization setup with the location of the different sensors, devices and the microscope

2.2.3.2. Immersion configuration protocols

There were different protocols in order to characterize the five different factors but all of them share the same thermalization steps and settings than the ones used with the dry configuration.

The preparation phase prior to characterize the impact on the sample temperature of the ambient, stage and objective temperature was the following one:

- The 100x sharp tip objective was placed at the microscope together with 3uL of immersion oil (S56822-50uL immersion oil from Sigma-Aldrich)
- The thermalization chip was assembled together with the AR-LSR-0.25-AR spacer and a glass coverslip #1.
- The chamber where the 103-JT-sensor #1 was located was filled with 50uL of distil water
- Thermalization chip assembly was placed on the chip insert on the microscope stage
- The objective was brought into contact with the bottom part of the assembly (glass coverslip), this point was considered at Z=0µm distance between the glass and the objective.

NOTE: As an extra security, if the ambient temperature was higher than 30°C or below 18°C, the recording would be postponed until the temperature of the room fitted inside that threshold to avoid extreme conditions in the characterization that could generate outliers and disrupt the outcome.

From the recording settings, five* cycles of 190 minutes each were done in order to generate enough data and the sampling frequency was 10s. All the recording was done using a MATLAB software that was based on the previous one for the dry configuration.

***NOTE:** During the recording of the experiment the experiment #4, the temperature of the objective rise over 30°C, therefore I decided to record a 6th experiment, to avoid extreme conditions but for the sake of the results I kept all the data.

In order characterize the impact of the type of objective and the Z-distance the protocol the preparation phase was the same one as presented before. The main difference was on the different type of recordings as once the five cycles at Z=0 µm were done two more at Z=-20µm and Z=-50µm were recorded. Finally, the objective was changed for the flat tip one and the 15 recordings repeated.

For the characterization of the impact of water as an immersion liquid, the preparation phase include distilled water instead of oil and I only used the 100x sharp tip objective because I wanted to compare just one variable Water vs Oil and not introduce more complexity by changing the type of objective. The used Z distance was Z= 0µm.

2.2.3.3. Immersion configuration results

In the case of the immersion configuration the obtained raw data was represented in the following variables:

- **Temperature of the Peltier (T_p):** corresponding to the temperature at the Heat-Exchanger module during the thermalizing cycles
- **Temperature of the objective (T_{obj})**: measured temperature at the objective with the Omega 44031 sensor (Location A)
- **Temperature of the sample (T_s):** measured temperature at the sample location with the 103-JT-sensor (Location B)
- **Temperature of the room #1 (T_{r1})**: measured temperature on top of the microscope with an RTD, PT-100 sensor (Location C)
- **Temperature of the room #2 (T_{r2})**: measured temperature on top of the microscope with an RTD, PT-100 sensor (Location D)

Relativization factor	Absolute temperature factor	Relative Temperature Equation
Temperature of the room #1 (T_{r1})	Temperature of the Peltier (T_{pA})	$T_{pR1=}T_{pA}-T_{r1A}$
	Temperature of the sample (T_{sA})	$T_{sR1=}T_{sA}-T_{r1A}$
Temperature of the room #2 (T_{r2})	Temperature of the Peltier (T_{pA})	$T_{pR2=}T_{pA}-T_{r2A}$
	Temperature of the sample (T_{sA})	$T_{sR2=}T_{sA}-T_{r2A}$
Temperature of the objective (T_{obj})	Temperature of the Peltier (T_{pA})	$T_{pR3=}T_{pA}-T_{obA}$
	Temperature of the sample (T_{sA})	$T_{sR3=}T_{sA}-T_{obA}$

Table 19, Temperature relativization equations depending different factors such as room temperature or objective temperature.

As it was presented before, all the data was in absolute values and in order to compare between different experiments it was necessary to relativize it. I used the same principle than in the dry configuration and obtained the equations that were summarized at Table 19. For the quantification of the impact I used the variable presented before Temperature impact in the sample (T_{is}).

I started the analysis of the results with the Figure 37. This figure represented the T_{is} values of the 6 different experiments (each with a different colour) against the room temperature #1(on top of the microscope). The horizontal lines showed the different thermalization steps. In the case of the dry configuration, the impact of the room temperature was quantifiable and linear as it increased the T_{is} value from being negative to positive as the room temperature increased. In this case, only in two experiments, #2 in green and #4 in dark blue, this linearity occurred. In the other four cases, the T_{is} started being positive and decreased as the room temperature increased but showing a parabolic shape instead of a linear curve. These was also the case for the room temperature #2 Figure 38, meaning that impact of the room temperature into the sample had not a direct relationship, or that it could be different types of relationship depending on other factors to be analysed such as the heat sink.

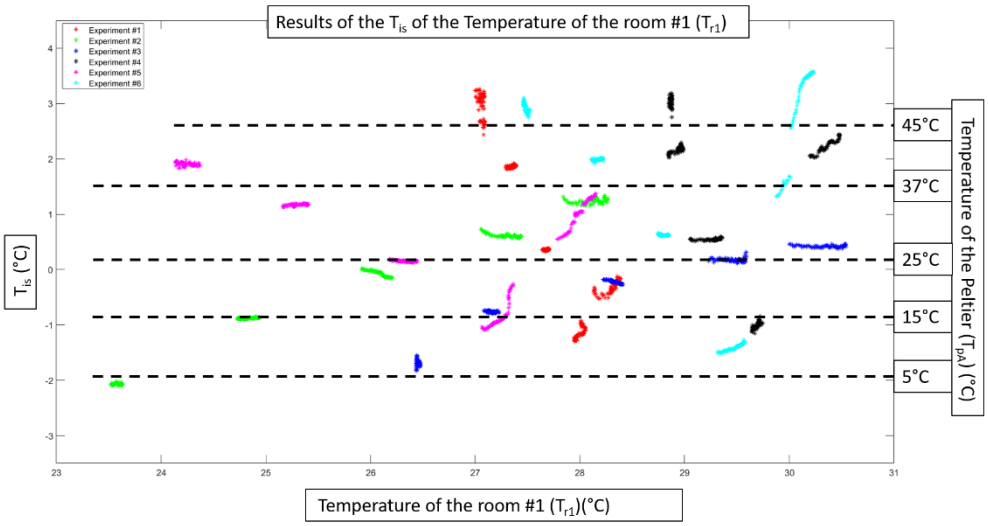

Figure 37, Results from the T_{is} calculation of the Temperature of the room #1(T_{r1A}). The left y- axis was the T_{is}, the x-axis was the Temperature of the room #1(T_{r1A}) in absolute temperature and the right y-axis was the (T_{pA}) to visualize the thermalization steps. Each colour represented one experiment of the immersion configuration.

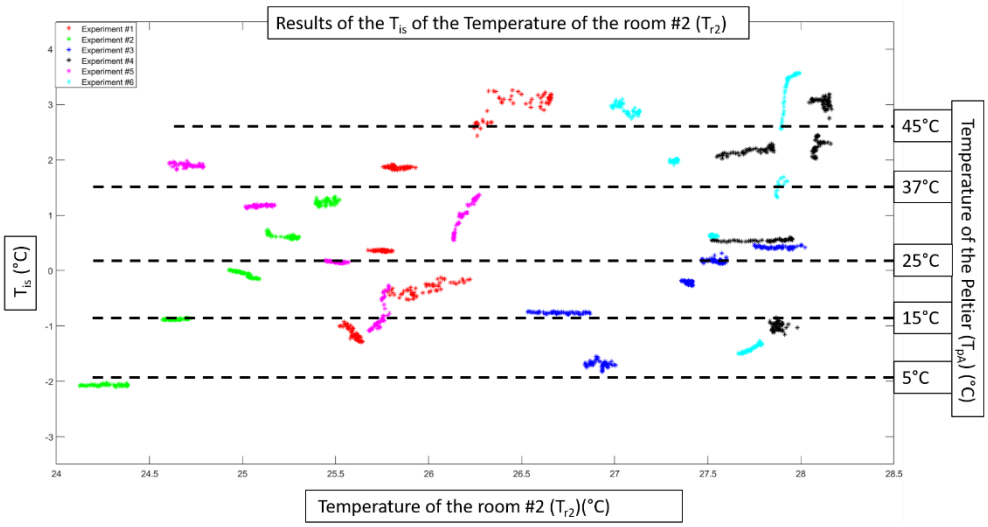

Figure 38, Results from the Tis calculation of the Temperature of the room #2(T_{r2A}). The left y- axis was the Tis, the x-axis was the Temperature of the room #2(T_{r2A}) in absolute temperature and the right y-axis was the (T_{pA}) to visualize the thermalization steps. Each colour represented one experiment of the immersion configuration

The next factor to be analysed was the impact of the objective temperature using the T_{is} and as it could be seen at Figure 39, again two of the experiments (#2 and #4) showed a linear evolution while the objective temperature increased. The other four experiments present similar parabolic trajectories, making not clear if it was possible to make a association between objective temperature and T_{is}. As it was mentioned before it could be the heat-sink was not the same in all the experiments even if the conditions were identical for all of them. This hypothesis could be probed by checking T_{is} difference between the two types of objectives as they would have for sure a different heat-sink due to the contact surface due to the tip, in one case sharp and small and the other one flat and bigger.

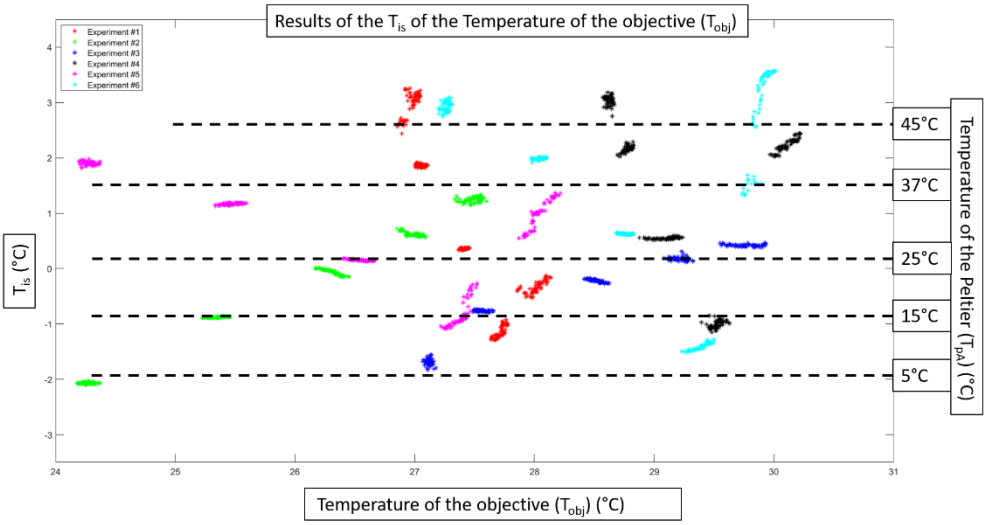

Figure 39, Results from the Tis calculation of the Temperature of the objective (T_{obj}). The left y- axis was the Tis, the x-axis was the Temperature of the objective (T_{obj}) in absolute temperature and the right y-axis was the (T_{pA}) to visualize the thermalization steps. Each colour represented one experiment of the immersion configuration

The second part of the results was focused on analysing the impact of the different types of microscopes objectives and the Z-distance. In order to ease the analysis, the sharp tip objective would be called Obj A and the flat one Obj B. For the comparation between them I took each Z distance compare the T_{is} of each of them at different T_p, at 5°C, 25°C and 45°C, all in relative using the extrapolation from the raw data.

For the Z=0µm, the results showed at Table 20, both objectives had different T_{is} with increment of the difference as T_p got higher. However, at Z=0µm the maximum difference was +0.65°C, that could be enough to validate the hypothesis that each objective had a different conformation of the heat-sink.

Z-Distance	Temperature of the Peltier (T_{pA})	T_{is} of Obj A	T_{is} of Obj B	Difference
0µm	5°C	6.24°C	6.13°C	+0.1°C
	25°C	0.9°C	0.63°C	+0.27°C
	45°C	8.04°C	7.39°C	+0.65°C

Table 20, Results from the different objectives comparation at Z=0µm

For the Z=-20µm, difference in the T_{is} was big enough in the extremes of the T_p to validate that the shape of the objective tip could impact the sample temperature, Table 21. Therefore, at a distance of -20µm both objectives would present a different heat-sink that could provoke a different heat transfer between the sample and the objective, providing a different thermalization.

Z-Distance	Temperature of the Peltier (T_{pA})	T_{is} of Obj A	T_{is} of Obj B	Difference
-20µm	5°C	7.81°C	5.95°C	+1.86°C
	25°C	0.94°C	0.66°C	+0.28°C
	45°C	9.37°C	7.27°C	+2.10°C

Table 21, Results from the different objectives comparation at Z=-20µm

Finally, the data from the Z=-50µm, confirmed the hypothesis that both objectives had different heat-sink just because of the shape of the tip due to the big difference in T_{is} between them.

Z-Distance	Temperature of the Peltier (T_{pA})	T_{is} of Obj A	T_{is} of Obj B	Difference
-50µm	5°C	7.87°C	5.6°C	+2.02°C
	25°C	0.94°C	0.60°C	+0.34°C
	45°C	9.32°C	6.8°C	+2.52°C

Table 22, Results from the different objectives comparation at Z=-20µm

On the other hand, the impact of the Z distance showed different result for each objective Table 23. In case of the Obj A, the big difference appeared when moving from Z=0µm to Z=-20µm as the delta of T_{is} was at least 1.33°C in the thermalization extremes. Then the difference from Z=-20µm to Z=-50µm was lower than 0.1°C. This could be due to the surface of contact of the oil at different Z-distance that could modify the heat-sink conformation, been more noticeable from 0µm to -20µm than this one to -50µm.

In case of the Obj B or the flat tip objective, the differences were smaller while the big change was between -20µm and -50µm. Again, the surface of contact between the oil, the

sample and the objective could be impacting the final sample temperature and the Z-distance played a big role on this.

Type of Objective	Temperature of the Peltier (T_{pA})	T_{is} at Z=0µm	T_{is} difference at Z=-20µm	T_{is} difference at Z=-50µm
Obj A	5°C	6.24°C	+1.57°C	+1.63°C
	25°C	0.9°C	+0.04°C	+0.04°C
	45°C	8.04°C	+1.33°C	+1.28°C
Obj B	5°C	6.13°C	-0.18°C	-0.53°C
	25°C	0.63°C	+0.03°C	-0.03°C
	45°C	7.39°C	-0.12°C	-0.59°C

Table 23, Results from the different Z distance comparation for each objective separately.

Finally, for the difference between the oil and the water, using the data of the Obj A at Z=0 µm, the T_{is} for each liquid and its difference was presented at Table 24. The difference was clear as the T_p increased proving that the immersion liquid could end up impacting the sample temperature. The reason behind this could be that during the heat-sink, the thermal-bridge between the sample coverslip, the immersion liquid and the objective transfer the heat on a different way due to the difference in the liquid heat capacity. It this case, distil water had a heat capacity of 1 cal/gram°C and immersion oil, (mainly mineral oil) had a heat capacity of 0.4 cal/gram°C, meaning that the water was able to transfer more heat with lower volume.

Z-Distance	Temperature of the Peltier (T_{pA})	T_{is} of Oil	T_{is} of Water	Difference
0µm	5°C	6.24°C	7.22°C	-0.98°C
	25°C	0.9°C	2.29°C	-1.39°C
	45°C	8.04°C	11.8°C	-3.76°C

Table 24, Results from the comparation between water and oil as immersion liquid

2.2.4. Conclusions from the thermal characterization of the microscope setup

As a conclusion for dry condition, the impact of the room and the stage temperatures was the same as the T_{is} followed a predictable trend. Knowing this it was possible to counterbalance the effect of both factors via a feedback loop system. Therefore, for dry configuration either the room temperature or the stage one had a controllable impact.

In the case of the immersion condition, the results were more complex to analyse as there were up to five factors that could impact the temperature of the sample. The type of immersion liquid was the factor that could impact more as the heat capacity of the immersion liquid played a big role on the heat-sink. Then the thermal-bridge of the heat-sink could also be affected by the Z-distance and the shape of the objective tip, been both of them critical factors to be consider during the thermalization. Following with the temperature objective could be a summary of the impact of the different factors mentioned before, being the heat-sink the one that caused the different trends presented at Figure 39. Finally, the room temperature did not show any direct relationship to the sample temperature that could be measured or controlled.

Chapter 3, Context and needs of each biological model used to develop new microfluidic devices

Knowing which are the factors that could influence the sample temperature while doing live-cell imaging, it was necessary to decipher the needs and requirements for the different biological models used in this thesis. Biological experiments have been conducted in two different projects: DivIDE and SpOC.

3.1. DivIDE project

The DivIDE project was part of the H2020 program, as an International Training Network, under Marie Skłodowska Curie grant with the number H2020-MSCA-ITN-2015-675737. The objective of this research network was to investigate the principles and the mechanism behind cell division and to reproduce them in vitro with synthetic approaches. All the research was performed by 11 Early Stage Researchers (ESR) that were all PhD students.

Key for the cell division is the mitotic spindle, a structure whose main duty is the separation of chromosomes. The spindle is made of microtubules (MT), molecular motors, and MT-binding factors, some of which very complex. The mitotic spindle is the one of the cellular structures that best represents the ability of biological matter to self-organize though arrays of dynamic protein-protein interactions. It rapidly assembles when cells enter mitosis, and it disassembles, after sister chromatid separation and mitotic exit. The complexity and dynamic behaviour of the mitotic spindle captures the imagination of synthetic biologists and modellers.

This project was founded in 2015 and it has been working since September 2016 until October 2019 and it involved 11 European institutions of which 6 were academic labs or universities:

- Centre for Genomic Regulation (CRG) in Barcelona, Spain
- Institute Curie in Paris and Orsay, France
- Francis Crick Institute in London, United Kingdom
- Max Planck Institute of Molecular Physiology in Dortmund, Germany
- Dresden University of Technology (TUD), in Dresden, Germany
- European Molecular Biology Laboratory (EMBL) in Heidelberg, Germany

And 5 companies:

- Eugin Clinics in Barcelona, Spain
- Lead Discovery Centre GmBH (LDC) in Dortmund, Germany
- Cherry Biotech in Rennes, France
- Elvesys in Paris, France
- Surfrender, Netherlands

At the end all these partners aimed to research around cell division with different approaches. My specific objectives in this project as an ESR at Cherry Biotech, was to provide the necessary tools that involve temperature control and perfusion at the microscope stage. There were three major collaborations that required specific adaptations of the CherryTemp temperature controller to add new features for each

specific biological model. Those collaborations involve the following models: yeast, mammalian cells and MTs in vitro.

Inside the DivIDE project, all the researchers agreed that temperature is a key factor for the cell division as it can impact the MT's polymerization state, altering the cell division cycle. Therefore, all the partners understood that in order to obtain the more reliable data from the experiments it was necessary to have an accurate temperature control, and that is why I used CherryTemp to thermalize the different biological models.

3.1.1. Yeast Model

The laboratory of Prof. Phong Tran at the Institute Curie in Paris worked with yeast, *S. Pombe* as their biological model to study cell division. His team was interested in understanding how cell polarity and cell division are managed by the cytoskeleton. Their previous studies in *S. Pombe* showed that bundles of MTs can direct new sites of actin-dependent polarized cell growth and that MTs oversee organizing the mitotic spindle for the chromosome segregation. The architecture and the dynamics of the cytoskeleton are influenced by associated proteins such as motors and bundlers, and regulatory proteins such as kinases and phosphatases. Their long-term goal is to understand the molecular mechanisms by which these proteins function and establish potential evolutionary conservation between yeast and man(289,290).

Their plan has 3 parts:

- To identify the molecular components of the cell shape and cell division pathways
- To define the interactions of known (and newly discovered) cytoskeletal proteins and their roles in the cell polarity and division
- To develop and apply advanced optical imaging analysis, and nanotechnology methods to the yeast

For many years they have been using CherryTemp as temperature controller to manage their thermosensitive mutants or to have accurate and stable temperature while doing live-cell imaging. To push further his investigation, Prof. Phong Tran had the need of a microfluidic device that could allow him to go beyond with his thermosensitive mutant's yeast. This species allowed him to trigger specific phenotypes changing the temperature of the sample, but their new interest was to use different drugs to replicate the phenotypes observed using temperature control.

In order to do so, it was necessary to first coat the surface of a chamber, a cavity where the cells were placed in order to thermalize and observe them during the experimentation. For the yeast model the treatment for the surface involved the use of Lectin, a type of protein that recognize and bind specific carbohydrates found on the surfaces of cells, allowing to immobilize them on specific surfaces. Once the cells were attached inside the chamber it would be possible to have medium perfusion at the microscope stage with temperature control.

After discussing with him, we agreed about the following main technical requirements:

- One microfluidic device compatible or Add-on of the CherryTemp
- Microfluidic chamber of 50-100µL of volume
- All materials must be biocompatible, non-absorbent and transparent

- Possibility to perfuse different reagents, first manually with the option to connect it to an automatic system in the future
- Possibility to make more than one experiments per device

Taking all those requirements into consideration, together with Prof. Phong Tran, we designed two experiments to validate the possible device, one based on cells perfusion and temperature control, while the second one was more focused on the drug perfusion protocols.

The first one consisted on coating the surface of the chamber using Lectin and then introduce *S. Pombe* cells that could get attached to the surface of the chamber. Then using, the temperature control of the CherryTemp to depolymerize and repolymerize MT switching from 25°C to 8°C and then back to 25°C while doing live-cell imaging.

The second one included the coating and the injection part but also the perfusion of a MT depolymerizing drug, called carbendazim or MBC, a molecule capable of disrupt the dynamic stability of MTs during the cell division(291,292). The used concentration was 50ug/uL. That drug, injected at 25°C, could depolymerize the MTs in 5', presenting the same phenotype than with the temperature.

3.1.2. Mammalian cells Model

The laboratory of Prof. Isabelle Vernos at the CRG in Barcelona worked with HeLa-Kyoto cells as their biological model to study cell division, more specifically the mitotic spindle. The research in her laboratory targets to understand the role of the microtubule network in the cell organization and function. In order to address this, they study different microtubule-associated proteins (MAPs) and their regulation (Kinases, phosphatases and the small GTPase Ran during M-phase). Their long-term goal is to understand how the self-organization of cellular components results in the morphogenesis of dynamic molecular machines. Now their main focus is on the bipolar spindle in mitosis and meiosis, which is one of those self-organized structures(293–296).

In order to contextualize, during the cell division, the mitotic spindle is formed and is composed of three different types of MTs fibres: kinetochore (297–299), polar (300–302) and aster (303–305). All of them emanate from the centrosome and their duty is to pull and push the sister chromatids part towards opposite spindle poles Figure 40.

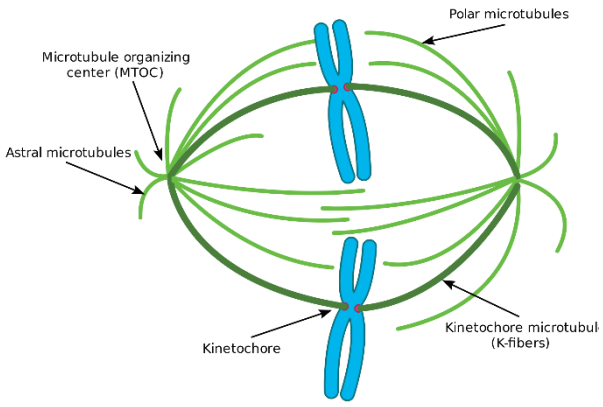

Figure 40, Scheme of the mitotic spindle and the different types of MTs

The team of Prof. Isabelle Vernos needed of a microfluidic device composed of two parts: one where the mammalian cells could be seeded until they reach confluency and a second one that could provide temperature control and perfusion (medium renewal or drug injection). The need of this device was related with the re-growth experiments where the MT's of a mammalian cell are depolymerized by temperature or drugs and then recovered to observe their re-growth or re-adjustment using live-cell imaging.

These type experiments aimed to understand the dynamics of this process and how different components inside the cell react to different conditions. Therefore, the main technical requirements for her adaptation were the followings:

- One microfluidic device with one disposable part and one fix compatible with the CherryTemp
- A cell chamber with a glass base to seed the cells
- Working volumes of 400 to 500 µL in the complete device
- All materials must be biocompatible, non-absorbent and transparent
- Possibility to perfuse different reagents, first manually with the option to connect it to an automatic system in the future

Considering those requirements, together with the team of Prof. Isabelle Vernos, we designed two different experiments to validate the possible device before moving to more complex protocols and setups.

The first experiment started with the optimization of the cell seeding protocol on the cell chamber, in terms of quantity of cells, surface area and time to reach confluency. Once that protocol was optimized, the second part involve the assembly of the two parts of the device and the medium renewal steps, all of which to be performed under the hood. With these two parts ready, the next step is on the microscope stage where the device should be able to perform a complete re-growth experiment using just temperature. Beginning by imaging MTs at 37°C, then go down to 4°C until all of them were depolymerized and then going back to 37°C to observe the re-polymerization without collapse or death cells.

The second experiment required the optimization of the medium renewal and the drug injection protocol on the microscope stage with the objective of using nocodazole, at MT's depolymerizing drug. The aim of this second experiment was to perform the same re-growth experiment but instead of using temperature, take advantage of the effect of a drug to obtain a very similar phenotype.

3.1.3. MTs *in vitro* model

The laboratory of Prof. Carsten Janke at the Institute Curie in Orsay, Paris, worked with an *in vitro* MT's assay to study cell division, more specifically the role of the tubulin on the assembly of those microtubules. His target was to decipher the role of the different types of tubulin, the different combinations and their impact on the MT's, therefore on the cell division. As context, MTs are formed by two components, a pair of protein dimers, α-tubulin and β-tubulin, which are very similar and conserved proteins. Tubulins is highly subjected to a big variety of post-translational modification, which end up providing a fast and reversible mechanism to diversify MTs function inside the cell.

His team was focused on studying the mechanism and functional roles of these modifications by using multidisciplinary approach that includes biochemistry, biophysics

and structural biology. The final goal is to find the correlation between the different post-translational modifications and possible pathologies in humans (306–308).

Therefore, Prof. Carsten Janke was interested on having a microfluidic device that could allow him and his team to perform *in vitro* experiments with MTs with temperature control and medium perfusion. The need of this device was related with two different types of scientific questions involving TRIF microscopy. One of their aims was to find at which temperature the MTs stop growing in presence of tubulin, meaning that they stop being functional. This could explain some post-translational modification in some brain diseases, assumed to be linked with MT stability impairment. The second part was to discover the affinity of different microtubule-associated proteins (MAPs) and different types of MTs with different tubulin configuration.

The main technical requirements for his adaptation were the followings:

- One microfluidic device compatible or Add-on of the CherryTemp
- A cell chamber with a maximum volume of 50 µL, due to the low volume of the different reagents used in *in vitro* experiments
- Working volumes of 400 to 500 µL in the complete device
- All materials must be biocompatible, non-absorbent, transparent and compatible with TIRF microscopy
- Possibility to perfuse different reagents, first manually with the option to connect it to an automatic system in the future

Considering those requirements, together with the team of Prof. Carsten Janke, we designed two different experiments to validate the possible device before moving to more complex protocols and setups.

The first experiment started with the optimization of the MT's seeding protocol on the cell chamber, in terms of quantity of coating (Kinesin) and the time for it to dry. Then, concentration of GMPCPP MT seeds from where the MTs would grow once adding the tubulin into the *in vitro* chamber. Once that protocol was optimized, the second part involve the observation on the microscope stage of which is the minimum temperature at which the MTs keep growing in presence of different type of tubulin. Some of the tubulin was considered as wild type and others as mutants (linked to brain diseases). This part required the screening of different types of tubulin and the determination of a testing temperature profile to find out the minimum temperature.

The second experiment involved the seeding of two different types of MTs with different tubulin configuration and to quantify the affinity of different MAPs to each of the combinations. This was considered as a first part of a more complex set of experiments as a big quantity of microfluidic devices could be needed to obtain enough data from the screening of the different combinations.

3.2. SpOC project

The SpOC (Spheroids On-a-Chip) project was part of the Région Bretagne transfer de technologies, a technology transfer project under the Britany Region grant programme. This project aimed at cultivating kidney cancer cells spheroids for at least 5 days in a microfluidic device that ensures the micro-environment control of the culture. My contribution, as part of Cherry Biotech R&D team was to design the microfluidic device, and in collaboration with the Institute de Genetique & Development de Rennes (IGDR), applied it to the drug development. The project was granted in January 2017 and it lasted between June 2017 until June 2018.

The reason of selecting a 3D cell culture model instead of a 2D one was due to the fact that 90% of the drug development processes fail, been most of them based on 2D cell cultures models (309,310). Even if those 2D models could provide large amount of data on a non-expensive way, they did not represent the complexity of the human body, particularly a tumour growth. Therefore, there was an urgent need for more physiologically relevant and realistic models to better predict drug effects, specially the adverse ones. The new model could substitute the 2D cell culture during the *in vitro* testing in the early phase of the drug development(311,312).

3.2.1. Spheroid-3D cell culture Model

The laboratory of Dr. Yannick Arlot at the IGDR in Rennes, France, was focused on the Von Hippel Lindau (VHL) disease(313–315). This disease was categorized as a rare autosomal-dominant hereditary neoplastic one associated with germline loss-of-function mutations of the VHL gene. People affected by this illness may develop both benign and malignant tumours including clear-cell renal cell carcinoma (ccRCC), retinal angioma, cerebellar and spinal hemangioblastoma, pheochromocytoma and pancreatic cancers. They investigate the functions of VHL gene in the process of tumorigenesis. The VHL gene product (pVHL) was also involved in multiple biological processes such as cell growth, differentiation, cell motility and response to hypoxia. They started working with 2D cell cultures but promptly moved to 3D cell culture models as their gene expression profiles as they considered them closer to the real complexity of the human body (313–315).

Therefore, Dr. Yannick Arlot was looking for the development of a microfluidic device that could host spheroids made of 786-O kidney cancer cells, with a diameter of 200µm. The objective of the project was to keep them alive for at least 5 days, for which temperature control and perfusion for the medium renewal could be needed.

The main technical requirements for her adaptation were the followings:

- One microfluidic device compatible or Add-on of the CherryTemp
- A cell chamber with a minimum thickness of 200µm to avoid smashing the spheroids
- Working volumes of 400 to 500 µL in the complete device
- All materials must be biocompatible, non-absorbent, transparent and preventing cells to attach in the base, so no glass
- Possibility to perfuse different reagents, first manually with the option to connect it to an automatic system in the future

Considering those requirements, together with the team of Dr. Yannick Arlot, we designed an experimental protocol to validate microfluidic device before moving to more complex protocols that involve the use of different drugs.

The aim of that experiment was to keep spheroids inside the microfluidic device for at least 5 days, avoiding the collapse of the spheroid. The first step was to find a way to place the spheroids in the microfluidic device, without damaging the 3D structure, and preventing them to move too much inside the culture chamber. Then to keep the 3D shape of the spheroids. Therefore, the optimization of the medium renewing protocol was crucial to remove the dead cells as it could lead to an internal apoptosis or cell migration that could risk the structural integrity of the 3D cell culture. Once validated, the testing of anti-migration drugs was discussed. These drugs has all shown anti-migration properties in 2D models, a comparative effect between 2D and 3D models has then been achieved.

3.3. Conclusion about the context and the needs of each biological models

As a conclusion of this chapter, the entire needed device have, as common base, the thermalization chip of the CherryTemp, which was adapted for each specific model. Although, the iterative process that has been done during the different projects have results in obtaining more robust devices.

Once agreed on the required specification, the next step was to conceive, design and characterize each of them along with other included in different projects of the R&D team inside Cherry Biotech.

Chapter 4, Conception, design and characterization of the different microfluidic devices

4.1. State of the art in Microfluidics

The state of the art of the microfluidic field can be divided according to 3 major axes: materials, manufacturing techniques and applications.

Microfluidics is a multidisciplinary science field involving the development of the technology to control fluids at the micro-scale. It is at the convergence of physics, engineering, biochemistry or material science. The term itself was first introduced in the 90s related with the development of Micro Electro Mechanical Systems (MEMS), which were made up of components in the range of 1 to 100µm, aiming at increasing the power of the microprocessors but also to ease their fabrication (316,317).

Nowadays, microfluidics is emerging as the breakthrough technology that can help the development and discovery in different fields such as biology, chemistry, micro-electronics or even optics. The exponential increase of the field is mainly due to the improvements in materials science that allowed using a wide range of materials with new micro-fabrication techniques adapted for new applications.

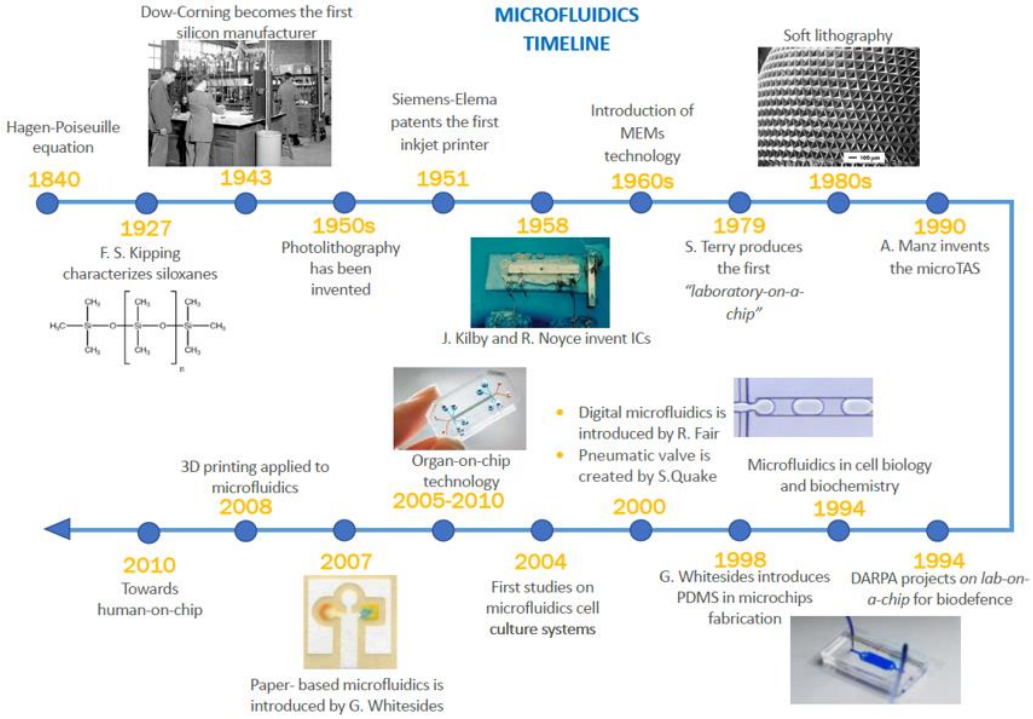

Figure 41, Timeline of the microfluidics history from 1840s until today

4.1.1. Main materials used in microfluidics

The growth of the microfluidic field could be due to different factors been the discovery of new materials on of the most important ones, thanks to the material sciences field researchers. The most used ones have been silicon, glass, epoxy, thermoplastics, elastomers or tapes, among others.

Silicon was the first material used as in the 80s-90s, all the MEMS were based on this material but presented a big drawback, it was not transparent so it could not be used for microscopy related applications(318–320). However it is still used as base material for microfabrication specially in techniques related with soft-lithography or electro deposition(321).

Therefore, researchers moved to glass because of its excellent optical properties and low-fluorescence background. It is also highly resistant to different chemicals and inert for most of the biological reagents. In most of the cases it is used as a proof-of-concept or prototyping but not for mass production due to its high cost compared with any plastic(321,322).

Polydimethylsiloxane (PDMS) was introduced in the field in the late 90s and it is still one of the most used materials due to its versatility and low-cost (100-150€/kg. It presents excellent optical properties for normal fluorescence microscopy and it is also gas permeable. In cases of very high mechanical compliance it can present channel deformation. It can evaporate and absorb small molecules (323). Related to some biological applications: the compliance property provokes mechanical deformation under high stress, and this can be a problem specially when culturing cells that require a specific shear force for long periods of time. The absorption properties discards it as material eligible for devices related with drug testing, particularly when using hydrophobic compounds, making it very unpredictable for experiments with this type of compounds(321–327).

SU-8 is an epoxy-based material used in photolithography allowing to build complex 3D structures from a liquid resin. It was discovered in the 1970s by scientists at General Electric(328) and commercialized under the EPON® SU-8 registered trademark of Shell Chemical Company. It is a negative photoresist, meaning that its structures changes (hardens) when exposed to electromagnetic radiation (UV-light). This process provides a material that is highly stable from the mechanic, thermal and chemical point of view. However, the process can generate internal stress making it hard to handle but not fragile. It can be deposed and patterned from a nanometre thickness to millimetres films using either lithography or laser ablation. It is an excellent material for making master mould. It has been commonly used for hot-embossing for thermoplastic devices or for injection moulding(328–333).

The next materials are the thermoplastics that include polycarbonate (PC)(334), polystyrene (PS)(335,336), polymethylmethacrylate (PMMA)(337) or cyclic olefin copolymer (COC)(338,339). Most of the thermoplastics are used as bulk material for the fabrication of microfluidic devices due to their low-cost, transmission of light in the UV/optical range, biocompatibility, chemical inertness and achievable glass transition temperature (Tg, temperature at which the plastic pass from solid to liquid state). Among all of them, PMMA is the most used one due to it its low-cost and possibility to generate

microstructures on its surface using UV light. Then PS has been used for long time in the biological field, especially for the fabrication of culture dishes thanks to its biocompatibility. Finally, COC is best thermoplastic regarding light transmission and the closest one to glass, while PMMA is one the most used one due to its low-cost, possibility to be mould injected and CNC milled. Therefore it is a very attractive solution for optical microfluidic devices as an alternative to glass(340–344).
Elastomers(345–347) and liquid silicon rubbers (LSR)(347–349) are polymers that by definition are viscoelastic and able to regain their shape after deformation. They are available at low-cost, are optically transparent and present a great biocompatibility which make them usable for proteins, cells or tissue applications. They are normally manufactured after lamination but they can follow a similar process like the PDMS that involves curing(350).

The final material is tape that can be laminated and stacked in independently cut layers which once bounded together can form microfluidics devices. This is a very versatile material to build microfluidic circuits while bounding together different materials with the only drawback of the cutting resolution(50-200µm) that for some applications may not be small enough(351,352).

4.1.2. Main fabrication methods used in microfluidics

The main manufacturing techniques, are moulding, casting, laser ablation, lamination and 3D printing(353,354)

4.1.2.1. Moulding as fabrication method for microfluidics

Moulding as the first technique can be divided three sub-types: replica moulding, injection moulding and hot embossing, as it can be seen at Figure 42.

4.1.2.1.1. Soft lithography-based moulding

The first sub-technique was first introduced by Xia and Whitesides in 1998 and requires the use of soft photolithography to generate silicon and photoresist moulds(355). Soft photolithography is a technique that allows generating microstructures over a silicon disk. The first step is to design a mask, then place it over a resin coated silicon disk. Depending on the type of mask (negative or positive) the resin can get cured or get removed.

After this, by electrodeposition it is possible to place different metals (gold, platinum, nickel or cupper) to generate a micro 3D structure that could act later as a microfluidic channel. This technique allows to build the so-called master fabrication mould, Figure 42, based on a silicon disk. Then any liquid-set polymer such as PDMS can be casted and cured to generate a microfluidic device from the master fabrication mould. For very high resolutions (lower than 10µm) it is necessary to use a clean room. Finally, device can be treated with plasma for the bonding with different materials such as glass.

4.1.2.1.2. Injection moulding

The second sub-technique, injection moulding for microfluidics was first developed in the 1980s and it grew until today, to become a common fabrication method using different thermoplastics. The process starts by melting the thermoplastic inside a compressible chamber, then two halves of the mould are compressed, which creates a mould cavity, Figure 42. At this point the thermoplastic is injected at a specific rate in order to fill all the cavity while it is still liquid prior to cooling it down. The last part consists on removing the piece from the mould. Depending on the production life of the mould or the number of pieces that it will reproduce it can be done in silicon for short batches or metal for industrial scale. The mould is normally milled using a computer numerical control (CNC) or a laser but there are some companies that 3D prints it, with very good results(356,357). Finally, the main advantages of this technique is the possibility of high-throughput, cost-efficient and precise production with the only drawback of a very high starting investment, in the order of thousands of euros for the metal moulds(353,358,359).

4.1.2.1.3. Hot embossing moulding

Hot embossing is the last sub-technique inside this group. This method uses thermoplastics that become viscous liquid at certain temperature, that are shaped pressuring it under the heated master fabrication mould, Figure 42. The process starts by placing a thermoplastic film between two mould inserts. Then the mould chamber is compressed and heated while evacuating all the air inside creating a cast of the mould. Prior to remove the piece, the mould is cooled down. This method presents some advantages over the injection as the stress in the material is reduces as the thermoplastic liquid does not stay for long in liquid while heated. It also avoids the shrinkage of the cast while cooling, allowing to fabricate more delicate pieces(360). The main limitations are

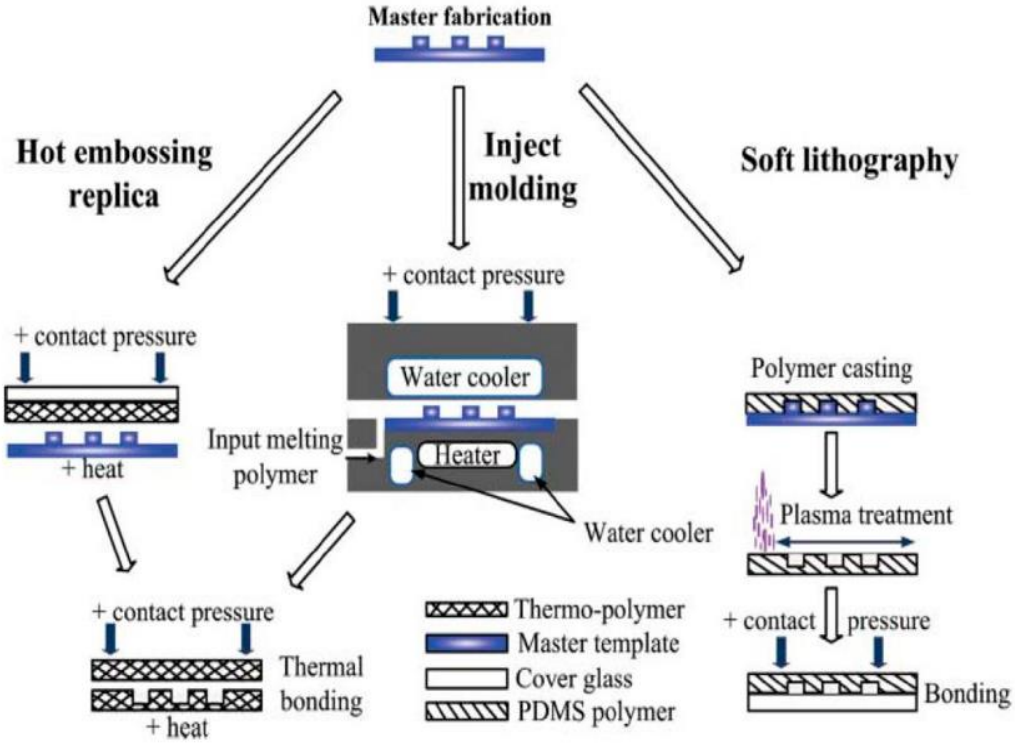

Figure 42, Scheme with the different moulding methods for microfluidics fabrication

that it can only use thermoplastics and that it is quite complex to generate 3D structures(360–363).

4.1.2.2. Laser abrasion as fabrication method for microfluidics

The next major fabrication method includes the use of a Laser in order to fabricate microfluidic devices. The most used one is the CO_2 laser due to its relatively low-cost. It has a 10.6µm wavelength and it able to perform direct ablation on surface of different materials such as PMMA, PS, COC or glass. The working principle is that the energy of the laser is focused over the surface of the material, melting it down resulting on a Gaussian-like profile microchannel which width and depth can be controlled with the applied power of the laser.

The main advantages of this techniques are that it is straightforward with a relative low-cost and that the ablation is purely thermal, which makes it compatible with most of the thermoplastics and glass. As a drawback, the microchannel can have a very rough inner surface, requiring further treatment, apart from the melted material that is deposed in both sides of the microchannel. It has a resolution of 50-80µm, which might not be enough for some applications(364–368).

4.1.2.3. 3D printing as fabrication method for microfluidics

Another fabrication technique is 3D printing which is a layer-by-layer manufacturing technology where a new layer of material is added on top of the previous one. It is commonly used for prototyping or to build different moulds for other techniques, such as hot-embossing or injection moulding. There are two main sub-techniques that are the most used ones, fused deposition moulding (FDM)(369,370) and stereolithography(SL)(371,372).

4.1.2.3.1. Fused deposition moulding (FDM)

FDM is the most used method as it is based on the extrusion that combined with a nozzle print different layer of 2D planes one on top of each other. The material is melted in the nozzle and then extruded onto the already printed layer where it binds before cooling. It is considered as the low-cost approach, as it has been widely commercialized, some are available at a starting price of $200(373). It can directly print on PC, acrylonitrile butadiene styrene (ABS) or PS or print multi-material objects, been one of them, the sacrificial material that acts as structural reinforcement during the printing, then is removed using solvent(374).

The resolution of this technique can reach 100µm which could be enough for some applications. The main drawbacks are related with the usage of materials that are not fully transparent and the fabrication time that can reach several hours(375–377).

4.1.2.3.2. Stereolithography (SL)

The stereolithography (SL) 3D printing method is a classic fast prototyping technique that works through an optical process that builds layer by layer. It is a widely used method to create fine features very fast as it uses a bath of resins that is polymerized using UV light. The working principle is based on using a focused light-emitted diode (LED) laser and a scanning Galvano-mirror to cure spots at the surface of the bath. This technique also presents two options to expose the photopolymer to the light. One of the approaches, so called "free surface", Figure 43-A, requires that the height of the bath to be the height of the structure while the light comes from the top while the stage foes down. The second option "constrained surface", Figure 43-B, is the most used one as it avoids potential contamination and formation oxides that can inhibit the polymerization. The light comes from the bottom while the stage goes up, requiring less material in the process. The most used materials are PDMS, Fluorinated ethylene propylene (FEP) and glass(378–381).

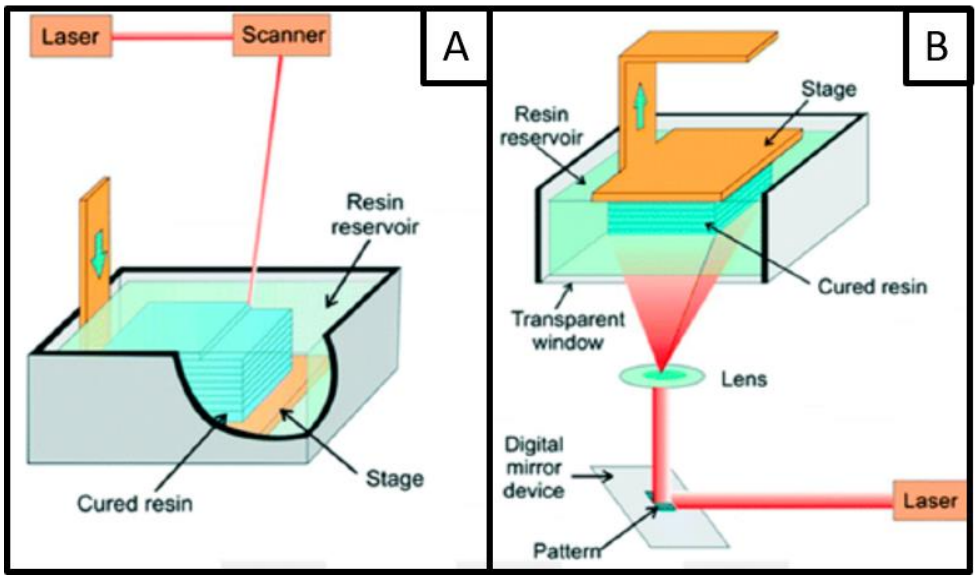

Figure 43, Stereolithography 3D printing scheme. Free surface stereolithography setup, that cures from the top surface of the resin (A) Constrained surface stereolithography setup, that cures from the bottom of stage through a transparent window(B)

4.1.2.4. Tape lamination as fabrication method for microfluidics

The final fabrication method that I will cover is related with the lamination of tapes in combination with different materials. This technique is very versatile as it allows to easily build any microfluidic circuit using tape and any thermoplastic or glass. The only cost comes from the cutting of the tape and from the tape itself. For the cutting a plotter can be used or a CO_2 laser but it is necessary to characterize the tape to avoid burning it while cutting as well as the emission of toxic fumes. This method is used for bounding different materials together as there are double-side tapes with different adhesive properties on each side. The main limitations are related with the durability of those tape and the maximum achievable resolution, which normally is between 50-200µm(382–386).

4.1.3. Main applications for microfluidic devices

Since the discovery of the PDMS the applications for the microfluidic devices have connected different fields such as biochemistry and material science or bioengineering and microscopy. Those connections are because it is a multidisciplinary field with a lot of opportunities. The most used applications nowadays are related with 3D cell culture, the organ-on-chip and lab-on-a-chip.

3D cell culture it has become a trend thanks to the latest improvements in the microfluidics field developing devices that can be used as high-throughput method for drug screening. Most of the actual 2D models lack complexity compared with the patients, therefore it was necessary to develop a more complex biological model. Thanks to the new 3D cell culture or tissue models, it is possible to access to cell-cell and cell-extracellular matrix interactions, to spatial migration, cellular growth and differentiation or even to patterning(387). Using microfluidics devices, it is possible to control the size of a tumour spheroid using just the design of a cell culture chamber geometry thanks to micro-engineering methods to manufacture cell microarrays in 3D shapes. At the end, those 3D cellular models mimic the cell-cell interactions that are characteristic from the *in vivo* models making them a more complete cell culture reference model(387–390).

An evolution of the 3D cell culture model inside the microfluidics field is to combine them with environmental control that includes, temperature, gas and fluid/medium. This evolution is called organ-on-chip and it is presumed to represent an alternative to animal testing for the drug development industry. The principle is basically to recreate a human organ function using cells from a patient in order to test a drug efficacy and the possible occurrence of side-effects before using it on the patient. At the moment there are different models for different organs such as lung(391–393), liver(394–396), kidney(397–399) or gut(400–402).

Another use for microfluidics is lab-on-a-chip (LOC), as it takes the advantage of handling low volumes to perform analysis and biochemical detections with a future target in diagnostics. The final aim is to develop a portable diagnostic system with integrated pumps, electrodes, valves and microelectronics, like a miniaturized version of the insulin test that are currently used(403,404). Another application of this technology is on pathogen detection for the food industry were some of the bacteria can be lethal for the human body, therefore a fast and low-cost test is required, and LOC can provide it(405–408).

4.2. Microfluidic adaptation for different biological models

Using the state of the art of microfluidics, the knowledge inside the R&D department of Cherry Biotech and the requirements for each biological model I come together with a solution for each model, the ThermaFlow device line. There was also one more adaptation that needed to be done inside other Cherry Biotech's projects called Cubix.

However, it needed to be mentioned that the base for all the devices presented here was the ThermaChip from the CherryTemp device, Figure 44.

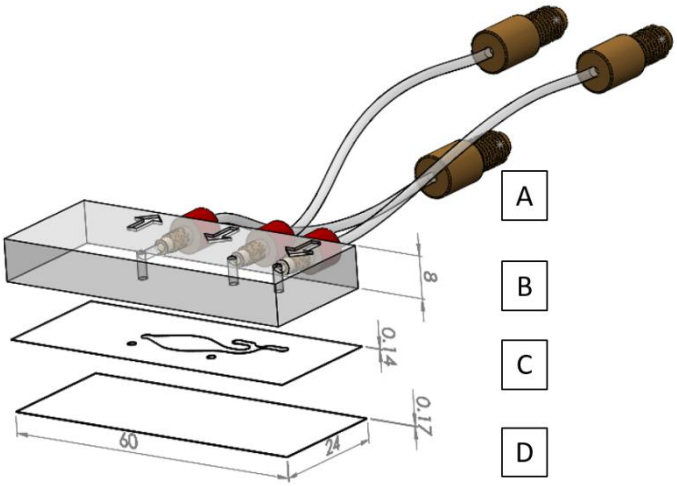

Figure 44, 3D drawing of the Thermachip for the CherryTemp. Fluidic connectors(A), PMMA manifold of 8mm thick(B), thermalization chamber of a double-side tape, 0.14mm thick (C) and closing glass coverslip, 0.17mm(D)

4.2.1. Microfluidic device for yeast model

Inside the collaboration with Pr. Phong Trang's laboratory at the Institute Curie, Paris, we developed together the following device that aimed to be compatible with S. Pombe a yeast model used to study cell division inside the project DivIDE.

4.2.1.1. Conception, design and materials

The main requirements for this device, which were explained at the 3rd chapter, included the need to be compatible with CherryTemp for the temperature control and to have a microfluidic chamber of at least 50µL. I used the thermalization chip of the CherryTemp as basis for the development of this new microfluidic device, Figure 44. I performed all the modifications in the design together with the selection of the new materials.

The thermalization part was made of three pieces: the manifold, the thermalization chamber and the plastic coverslip. The manifold was a PMMA block of 24x60x8mm (ZEG-MED – Design, Poland) with three thread holes on the side for the fluidic connectors. It has been modified by adding two holes passing through the manifold thickness for the perfusion. They have been separated by 45mm and with an 8mm diameter upper hole and a thread of 4.2mm for M5x0.8 connectors, as it can be seen at Figure 45-A. The second layer was a thermalization chamber made of double-side tape of 24x60x0.144mm (ARseal™ 90880; Adhesives Research Inc, Ireland) that had two

holes that match the one on the PMMA for the perfusion, of 6mm diameter, Figure 45-B. All the cutting was done using a microblade plotter (CE6000-40, Graphtec Corp, Tokyo, Japan).The third layer was a plastic coverslip made of Rinzl, a plastic vinyl of 24x60x0.28mm (72261-60, Rinzl coverslip, Electron Microscopy Sciences, USA) with two added holes of 6mm diameter for the perfusion. This coverslip provided the thermal conduction from the thermalization chamber towards the cell chamber and it also allows the perfusion, Figure 45-C.

The perfusion part was made of two parts, the cell chamber, Figure 45-D, and the closing coverslip, Figure 45-E. The first one made of two layers of double side tape of 24x60x0.144mm (ARseal™ 90880; Adhesives Research Inc, Ireland) laminate one over the other and cut using a microblade plotter (CE6000-40, Graphtec Corp, Tokyo, Japan). The total area and volume inside this chamber were 190.06mm^2 and 54.73µL. The last layer which closes the perfusion circuit is made of #1 24x60mm glass coverslip (Menzel-Glaser B.V &Co. KG. Germany).

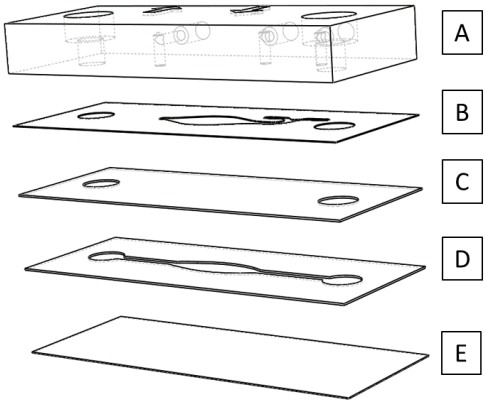

Figure 45, Explode view of the ThermaFlow yeast model. PMMA manifold of 8mm thick(A), thermalization chamber of a double-side tape, 0.14mm thick (B), Rinzl plastic coverslip, 0.28mm thick(C), cell chamber for the yeast, 0.28mm thick(D)and closing glass coverslip, 0.17mm(E)

The perfusion circuit was made of 5 different elements, Figure 46. The first one was a sealing O-ring, OR-5X1.5-FPM90-5x8x1.5mm (123Roulement, France) that was placed in the outlet point of the PMMA block, Figure 46-A. Then the M5x.8 Thread with 1/4" Hex to 200 Series Barb, 1/16" (1.6 mm) ID Tubing, Animal-Free Natural Polypropylene connector (Nordson Medical, US), Figure 46-B, was placed to seal the chamber prior to connect a 150mm Peroxide-Cured Silicone Tube, 1/16"ID X 1/8"OD tube (Cole-Parmer Int. Comp. US), Figure 46-C, and a Female Luer Lug Style to Classic Series Barb, 1/16" (1.6 mm) ID Tubing, White Nylon connector (Nordson Medical, US) connector, Figure 46-D. Finally, a 1mL Luer Slip Terumo Syringe (Terumo Interventional Systems, US), Figure 46-E, acted as a manual negative pressure generator to allow the liquid to enter in the system.

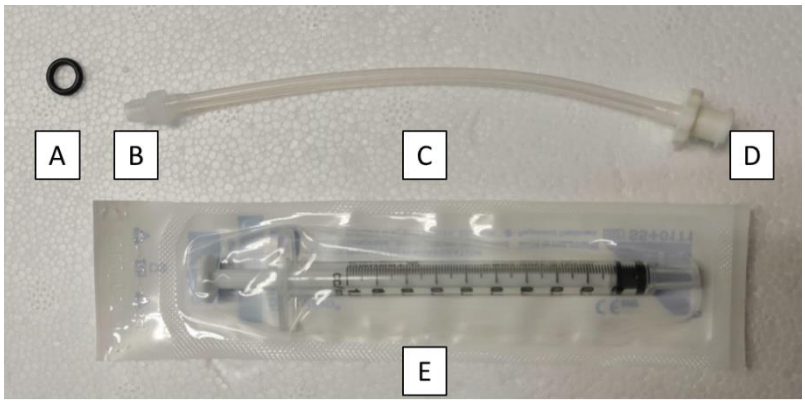

Figure 46, Picture of the perfusion circuit. Sealing O-ring(A), M5x.8 Thread with 1/4" Hex to 200 Series Barb, 1/16" (1.6 mm) connector(B), Peroxide-Cured Silicone Tube, 1/16"ID X 1/8"OD tube(C), Female Luer Lug Style to Classic Series Barb, 1/16" (1.6 mm)(D) and 1mL Luer Slip Terumo Syringe(E)

4.2.1.2. Assembly process and perfusion protocol

Prior to assemble anything it was necessary to sterilize all the parts with 90% ethanol and at least 15' under UV light.

The assembly process for the devices with all the pieces manufactured started by assembling the thermalization part which included the PMMA block, the thermalization chamber and the plastic coverslip. The first step was to attach the plastic coverslip and the thermalization chamber, which was a layer made of double-side tape, making sure that the holes for the perfusion are aligned. For the alignment I manufactured an insert made of plastic with a cavity of 24x60x5mm to align all the different layers. Then this piece was attached to the PMMA block and pressed using a roller to remove all the bubbles. This part should stay untouched for at least 24 hours, the time for the adhesive part of the tape to stabilize, especially because the flow at the thermalization chamber (4.5mL/min) could dis-attach it.

The perfusion part was then attached to the previously described thermalization part right before starting the experimentation. The cell chamber layer was attached to the plastic coverslip of the thermalization part using the alignment insert and closed using the glass coverslip.

The perfusion connection was done starting from the O-ring, then the M5x.8 thread connector and the tubing of 150mm long with the final female Luer connector for the syringe.

The perfusion protocol for this device was based on placing the injection liquid on the inlet well/hole and applying negative pressure with the syringe, introducing the liquid inside the cell chamber.

4.2.1.3. Thermal calibration

The calibration protocol for the ThermaFlow device yeast edition for dry and immersion(oil) configurations can be found at the Annex #1-Standard ThermaFlow Dry and Immersion modes calibration. However, the results from that calibration provide two different fitting curves and different thermalization equations, one for dry and another one for immersion(oil). The fitting curves were the results of plotting the applied temperature at the Peltier (Tp) and the temperature of the sample (Ts) during the calibration process. These temperatures were relativized, meaning that the ambient (Ta), dry mode, and the objective (Tobj), immersion mode, temperatures were subtracted to both Tp and Ts, in order to compare between experiments, no matter the influence of external factors. From those curves, I extracted the thermalization equations that showed the relationship between the Ts, Tp and Ta or Tobj, that allowed me to control the Ts for both modes.

The dry mode calibration was performed in the range of 5°C to 45°C providing a fitting curve with an equation like Equation 13 and an average error inside the range of +/- 0.14°C.

$$T_s=0.86*(T_p-T_a)-0.0038+T_a$$

Equation 13, ThermaFlow dry configuration fitting curve. Temperature of the sample (Ts), temperature of the Peltier (Tp) and temperature of the ambient (Ta)

On the other hand, for the immersion mode calibration, the range was the same, 5°C to 45°C providing a different fitting curve like Equation 14 and an average error inside that range of +/-0.3°C.

$$T_s=0.3488*(T_p-T_{obj})-0.8413+T_{obj}$$

Equation 14, ThermaFlow immersion configuration fitting curve. Temperature of the sample (Ts), temperature of the Peltier (Tp) and temperature of the objective (Tobj)

4.2.2. Microfluidic device for mammalian cells model

Thanks to the collaboration with Prof. Isabelle Vernos laboratory at the CRG, Barcelona, we managed to create together a new device with a specific protocol that aimed to be compatible with HeLa-Kyoto cells, mammalian cells model used to study cell division inside the project DivIDE.

4.2.2.1. Conception, design and materials

The main requirements for this device, which were explained at the 3rd chapter, included the need to be compatible with CherryTemp for the temperature control, to have a working volume of at least 400µL and two parts, one fixed and another disposable where to seed the cells. Taking the thermalization chip of the CherryTemp as base and their cell seeding protocols, we developed it and made some modification in the materials.

The thermalization part was the same than the one for the yeast model, made of three pieces: the manifold, the thermalization chamber and the plastic coverslip, Figure 47-A-B-C.

The perfusion part was again made of two parts, the cell chamber, Figure 47-D, and the closing coverslip, Figure 47-E. The first one made of two layers of double side tape of 24x60x0.144mm (ARseal™ 90880; Adhesives Research Inc, Ireland) laminate one over the other and cut using a microblade plotter (CE6000-40, Graphtec Corp, Tokyo, Japan). The total area and volume inside this chamber were 298mm^2 and 85.82µL. Figure XX-D. The last layer which closes the perfusion circuit is made of #1 24x60mm glass

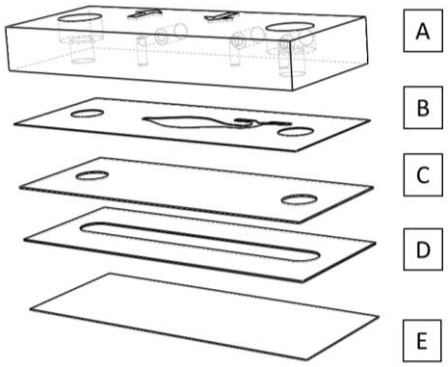

Figure 47, Explode view of the ThermaFlow mammalian cells model. PMMA manifold of 8mm thick(A), thermalization chamber of a double-side tape, 0.14mm thick (B), Rinzl plastic coverslip, 0.28mm thick(C), cell chamber for the mammalian cells, 0.28mm thick(D)and closing glass coverslip, 0.17mm(E)

coverslip (Menzel-Glaser B.V &Co. KG. Germany). Figure 47**.** At the end the total volume of the full perfusion circuit is 572 µL, considering the both holes and the cell chamber.

Finally, the perfusion circuit was the same than the one used in the yeast model, Figure 46.

4.2.2.2. Assembly process and perfusion protocol

Prior to assemble anything it was necessary to sterilize all the parts with 90% ethanol and at least 15' under UV light.

The assembly process for the devices with all the pieces manufactured started by assembling the thermalization part which included the PMMA block, the thermalization chamber and the plastic coverslip. The first step was to attach the plastic coverslip and the thermalization chamber, which was a layer made of double-side tape, making sure that the holes for the perfusion are aligned. For the alignment I manufactured an insert made of plastic with a cavity of 24x60x5mm to align all the different layers. Then this piece was attached to the PMMA block and pressed using a roller to remove all the bubbles. This part should stay untouched for at least 24 hours, the time for the adhesive part of the tape to stabilize, specially because the flow at the thermalization chamber (4.5mL/min) could dis-attach it.

The perfusion part was then attached separately as the cells were first seeded in the cell chamber and then assembled to the thermalization part. The cell chamber was first attached to the glass coverslip and left untouched for 24 hours prior to add any biological reagent.

The perfusion connection was done starting from the O-ring, then the M5x.8 thread connector and the tubing of 150mm long with the final female Luer connector for the syringe.

The perfusion protocol for this device was based on placing the injection liquid on the inlet well/hole and applying negative pressure with the syringe, introducing the liquid inside the cell chamber

4.2.2.3. Thermal calibration

This device together with the yeast and the MT's models presented the same materials and layers thickness, therefore the calibration was the same for the three of them. The fitting curves and the thermal equations end up been the same for the three of them. Therefore, the data from the thermal calibration can be found at the Annex #1-Standard ThermaFlow Dry and Immersion modes calibration.

4.2.3. Microfluidic device for MT *in vitro* model

Together with the laboratory of Prof. Carsten Janke at the Institute Curie, Paris-Orsay we developed a new device suitable for *in vitro* experiments with MTs, in order to study cell division inside the project DivIDE.

4.2.3.1. Conception, design and materials

The main requirements for this device, which were explained at the 3rd chapter, included the need to be compatible with CherryTemp for the temperature control, to have a cell chamber of less than 50µL and the possibility to manually handle very small volumes. two parts, one fixed and another disposable where to seed the cells. Taking the thermalization chip of the CherryTemp as base and their cell seeding protocols, we developed it and made some modification in the materials.

The thermalization part was the same than the one for the yeast and the mammalian cells models, made of three pieces: the manifold, the thermalization chamber and the plastic coverslip, Figure 48-A-B-C.

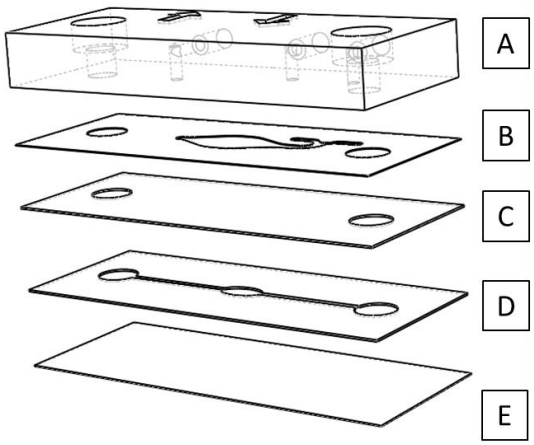

Figure 48, Explode view of the ThermaFlow MTs model. PMMA manifold of 8mm thick(A), thermalization chamber of a double-side tape, 0.14mm thick (B), Rinzl plastic coverslip, 0.28mm thick(C), cell chamber for the in vitro MTs, 0.28mm thick(D)and closing glass coverslip, 0.17mm(E)

The perfusion part was also made of two parts, the cell chamber, Figure 48-D, and the closing coverslip, Figure 48-E. The first one made of two layers of double side tape of 24x60x0.144mm (ARseal™ 90880; Adhesives Research Inc, Ireland) laminate one over the other and cut using a microblade plotter (CE6000-40, Graphtec Corp, Tokyo, Japan). The total area and volume inside this chamber were 108mm^2 and 31.1µL. Figure XX-D. The last layer which closes the perfusion circuit is made of #1 24x60mm glass coverslip (Menzel-Glaser B.V &Co. KG. Germany). At the end the total volume of the full perfusion circuit is 572 µL, considering the both holes and the cell chamber.

The perfusion circuit was made of 5 different elements, Figure 49. The first one was a sealing O-ring, OR-5x1.5-FPM90 (123Roulement, France), Figure 49-A, that was placed in the outlet point of the PMMA block. Then a metallic thread connector, M5x0.8 (M-5AU-4, SMC, US), with an ID of 1.6mm, Figure 49-B, was placed to seal the chamber prior to connect it to a 150mm PTFE tubing, 0.5mmID X 1.6mm OD tube (008T16-50-20, Kinesis, Cole-Parmer Int. Comp. US), Figure 49-C, together with a heat-shrink tubing

of 2mm ID and 25mm long (Alpha wire via RS, UK) to fix the tube to the metallic connector.

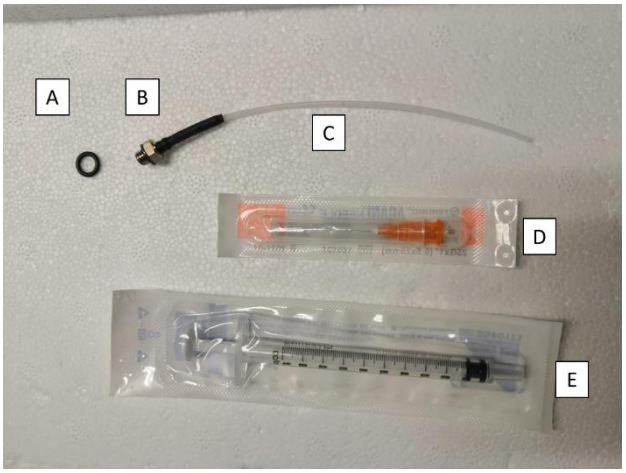

Figure 49, Picture of the perfusion circuit for the ThermaFlow MTs edition. Sealing O-ring(A), M5x.8 metallic thread connector(B), PTFE tubing, 0.5mm ID X 1.6mmOD(C), 25G1", Luer 0.5x25mm needle (D) and 1mL Luer Slip Terumo Syringe(E)

The final part include a needle(25G1", Luer 0.5x25mm, Terumo Interventional Systems, US), Figure 49-D, that was introduce 15mm inside the Teflon tube and a 1mL Luer Slip Terumo Syringe (Terumo Interventional Systems, US), Figure 49-E, acted as a manual negative pressure generator to allow the liquid to enter in the system.

4.2.3.2. Assembly process and perfusion protocol

Prior to assemble anything it was necessary to sterilize all the parts with 90% ethanol and at least 15' under UV light.

The assembly process for the devices with all the pieces manufactured started by assembling the thermalization part which included the PMMA block, the thermalization chamber and the plastic coverslip. The first step was to attach the plastic coverslip and the thermalization chamber, which was a layer made of double-side tape, making sure that the holes for the perfusion are aligned. For the alignment I manufactured an insert made of plastic with a cavity of 24x60x5mm to align all the different layers. Then this piece was attached to the PMMA block and pressed using a roller to remove all the bubbles. This part should stay untouched for at least 24 hours, the time for the adhesive part of the tape to stabilize, specially because the flow at the thermalization chamber (4.5mL/min) could dis-attach it.

The perfusion part was then attached to the thermalization part right before starting the experimentation. The cell chamber layer was attached to the plastic coverslip of the thermalization part using the alignment insert. The last part was closed using the glass coverslip.

The perfusion connection was done starting from the O-ring, then the M5x.8 thread that was connected to the PTFE tube. The needle was introduced 15mm into PTFE tube prior to connect it to the syringe via the Luer connector.

The perfusion protocol for this device was based on placing the injection liquid on the inlet well/hole and applying negative pressure with the syringe, introducing the liquid inside the cell chamber while removing any air could remain inside the cell chamber.

4.2.3.3. Thermal calibration

As it was mentioned before, this device together with the yeast and the mammalian cells models presented the same materials and layers thickness, therefore the calibration was the same for the three of them. The fitting curves and the thermal equations end up been the same for the three of them. Therefore, the data from the thermal calibration could be found at the Annex #1-Standard ThermaFlow Dry and Immersion modes calibration.

4.2.4. Microfluidic device for spheroids, 3D cell culture model

Inside the SpOC project, the target was to develop a microfluidic device that could allow the team of Dr. Yannick Arlot to observe spheroid alive after 5 days. Together using the microfluidics experience at Cherry Biotech and their knowledge regarding the culture of kidney cells to obtain spheroids, we engineered a microfluidic device capable to achieve that target of 5 days.

4.2.4.1. Conception, design and materials

The main requirements for this device, which were explained at the 3rd chapter, included the need to be compatible with CherryTemp for the temperature control, to have a cell chamber with a minimum thickness of 200µm to avoid smashing the spheroids once the device was assembled and the possibility to manually renew the medium without disturbing the spheroid with shear-stress or high flows. It was designed to be in two parts, one fixed and another disposable where spheroids were placed and trapped. Taking the thermalization chip of the CherryTemp as base and their spheroid handling protocols, we developed it and made some modification in the materials.

The thermalization part was again made of three layers: the manifold, the thermalization chamber and the plastic coverslip, Figure 50-A-B-C.

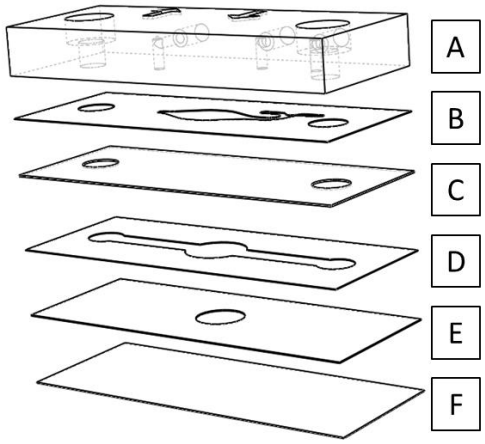

Figure 50, Explode view of the ThermaFlow 3D cell culture model. PMMA manifold of 8mm thick(A), thermalization chamber of a double-side tape, 0.14mm thick (B), Rinzl plastic coverslip, 0.28mm thick(C), perfusion channel layer, 0.14mm thick(D), cell chamber layer, 0.149mm thick(E), and the closing COC coverslip, 0.24mm thick(E)

In this case, the perfusion part was made of three layers, the perfusion channel, the cell chamber and the closing coverslip. The perfusion channel was a layer of double side tape of 24x60x0.144mm (ARseal™ 90880; Adhesives Research Inc, Ireland) with an area of 254.10mm^2 and a volume of 36.6µL. The cell chamber was made of lamination of a mono-tape 24x60x0.05mm(9793R; 3M Adhesives and tapes, USA) and a double side tape 24x60x0.144mm (ARseal™ 90880; Adhesives Research Inc, Ireland) with a chamber of 8 mm diameter, an area of 50.24mm^2 and a volume of 9.74 µL. The difference in height between the perfusion channel and the cell chamber created a 0.194mm step to trap and immobilized the spheroids inside that cell chamber. The closing coverslip was a

24x60x0.24mm coverslip of Cyclicolefin Copolymer (COC) (TOPAS®, Germany, provided by Microfluidic ChipShop GmbH, Germany). This material was selected because its excellent optical properties(409,410), its low molecules/drug absorption (411,412), and its capability to prevent cell adhesion(413–416). All the materials were cut using a microblade plotter (CE6000-40, Graphtec Corp, Tokyo, Japan). The total volume of all the perfusion circuit was 497µL considering the both holes, the perfusion channel and the cell chamber.

All the perfusion was done manually by using a 200µL pipette to introduce the medium and to remove it, the flow was passive due to gravity difference between the inlet hole and the outlet.

4.2.4.2. Assembly process and perfusion protocol

Prior to assemble anything it was necessary to sterilize all the parts with 90% ethanol and at least 15' under UV light.

The assembly process for the devices with all the pieces manufactured started by assembling the thermalization part which included the PMMA block, the thermalization chamber and the plastic coverslip. The first step was to attach the plastic coverslip and the thermalization chamber, which was a layer made of double-side tape, making sure that the holes for the perfusion are aligned. For the alignment I manufactured an insert made of plastic with a cavity of 24x60x5mm to align all the different layers. Then this piece was attached to the PMMA block and pressed using a roller to remove all the bubbles. This part should stay untouched for at least 24 hours, the time for the adhesive part of the tape to stabilize, especially because the flow at the thermalization chamber (4.5mL/min) could dis-attach it.

The perfusion part was assembled independently, by first attaching the cell chamber to the COC coverslip and then the perfusion channel layer on top of the previous ones. Then once the spheroid was placed in the cell chamber the whole device was assembled using an alignment insert, as mentioned before in this chapter.

4.2.4.3. Thermal calibration

The protocol for the ThermaFlow device spheroid edition for dry configurations can be found at the Annex #2-ThermaFlow Spheroid Dry mode calibration. The result of that calibration provided one fitting curve with a thermal equation available from 5°C to 45°C, Equation 15. This calibration presented an average error of +/-0.13°C.

$$T_s=0.8812*(T_p-T_a)-0.6095+T_a$$

Equation 15, ThermaFlow dry configuration fitting curve for spheroids. Temperature of the sample (Ts), temperature of the Peltier (Tp) and temperature of the ambient (Ta)

4.3. Heat stage development for Cubix

During the development these microfluidic devices, other projects inside the R&D team of Cherry Biotech require some adaptation in order to build a new temperature controller based on microfluidics. The project was inside the Cubix development, a new product inside Cherry Biotech's portfolio that aims to provide a device to keep biological samples alive for more than 5 days. Inside it, the temperature control was a must have in terms of stability and accuracy, especially for a 24 multi-well from Falcon, US.

4.3.1. Main requirements

As part of an R&D project leaded by Antoni Homs-Corbera, the CTO of Cherry Biotech, I took advantage of the knowledge and processes previsuly generated during my PhD to design, manufacture and thermally characterize the heat-stage. got the assignment of designing, manufacturing and thermally characterize the heat-stage. The thermalization needed to be based on microfluidics, as it offer more stability, the capacity to go below ambient temperature. Therefore, it should be compatible with the CherryTemp device. The main requirements were the following ones:

- Be able to thermalize a 24 Multi-well of Falcon (Corning, US)
- Be compatible with the stage of the Leica DM-IRBE microscope
- Have a fluidic circuit to use as radiator coupled with CherryTemp to thermalize the samples
- Have dedicated space for temperature control sensors to monitor the temperature of the sample
- Be compatible with the fluidic manifold designed by Matteo Boninsegna from the R&D team at Cherry Biotech, to provide the enriched gas

Taking this in consideration, I designed 3 different pieces for this adaptation: heat stage base, the sealing rubber and heat stage top, Figure 51.

Figure 51, Explode view of the heat stage. Heat stage base(A), sealing rubber(B) and heat stage top(C).

4.3.2. Design and Materials for the different parts

The first piece was heat-stage top, Figure 51-A. that together with the next ones it was made to seal the fluidic part and distribute the heat alongside the piece. It contained 70 holes for the screws that were in the heat-stage base and to fit with M3x10 screws (#965IT3010 from BAFA, France). The dimensions of this piece were bigger compared with the base one, 160.07x202.23mm and it also contained two levels, the main one of 5mm and the bottom one of 0.8mm. There were four spaces for reference temperature sensors to monitor the stage temperature while thermalizing using the CherryTemp and four holes to place tweezers to press the top closing part against the fluidic part and seal it. The piece was made in aluminium and manufactured by Protolabs, UK. Figure XX-C

The sealing rubber was the part that would assure the thermalization liquid circulating around the piece would not leak at all. Its main features were its 2mm thickness and that it was made of FKM rubber. It was rectangular, 189.23x147.09mm with an inner cut of 149.23x107.09mm. The difference between the external and the internal perimeter was 20mm in all the piece, Figure 51-B. IT was manufactures by F.elastomers, a company from France.

The heat-stage base, Figure 51-C, was a two levels piece, the lower one to fit into the Leica DM-IRBE microscope stage and the top one to host the fluidic circuit. The lower part was a square base of 149.70mm of lateral side and 3mm high. The top part was all a fluidic circuit with one inlet and one outlet points compatible with ¼ -28 UNF connector. There were 70 holes for screws (M3x0.5) to seal the fluidic part with an average distance of 17mm between each other. It also had 24 holes on the base to host a 24 Multi-well with a contact base of 0.5mm thickness to allow the imaging, as it was visible from the upper view, Figure 52. At the end the total thickness of the piece was 10.6mm of which 7.6mm were for the top part and 3 for the base. The piece was manufactured in Aluminium by Protolabs, a prototyping company in UK.

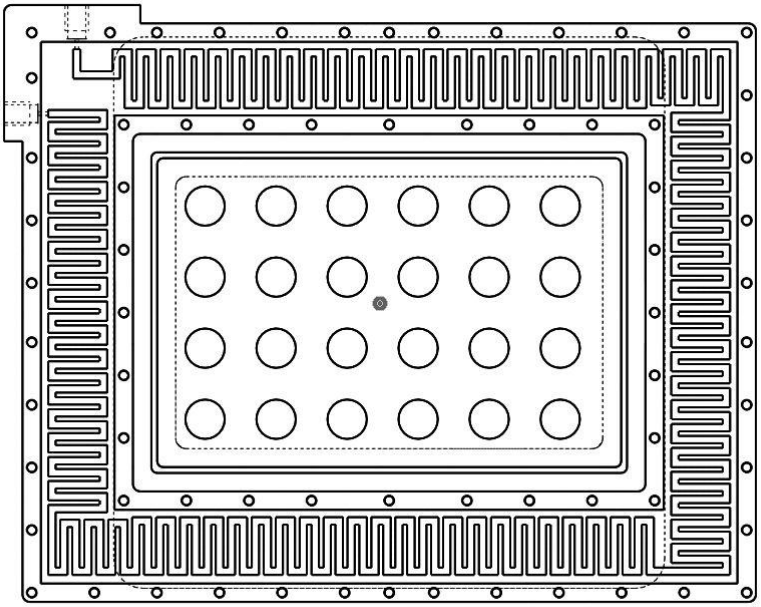

Figure 52, Upper view of the heat-stage base

4.3.3. Thermal calibration of the heat-stage

The protocol for the heat-stage calibration can be found at the Annex #3-Heat-Stage calibration. The outcome of that calibration provided a new equation, Equation 16, in order to use the CherryTemp and provide 36.5°C stable in the D row of the 24 Multi-wells. The reason behind targeting the D row was that the samples were placed in that row while the A, B, C rows were used as reservoirs.

$$Ts = \frac{(-5 * Ta + 30 - Tp)}{-6}$$

Equation 16, Heat-stage fitting curve. Temperature of the sample (Ts), temperature of the Peltier (Tp) and temperature of the ambient (Ta)

However, during the calibration it was necessary to perform a thermal mapping to understand the temperature at the different wells and at the same time to check if any of them could be too high or too low that could affect the properties of the medium in that well. The outcome of that thermal mapping can be seen at Figure 53, showing the big discrepancy between the different rows, specially row A and D.

In terms of stability and accuracy this setup helped at the first version of the Cubix, as a fast prototype but a new direction has been taken, using a resistance Kapton to thermalize. This new option provided more even temperature requiring less equipment, been cheaper than using a complete CherryTemp but with the drawback of not been able to thermalize below ambient temperature. However, the protocol to characterize the temperature of the different well of the 24 multi-well has been based on the one used for this version.

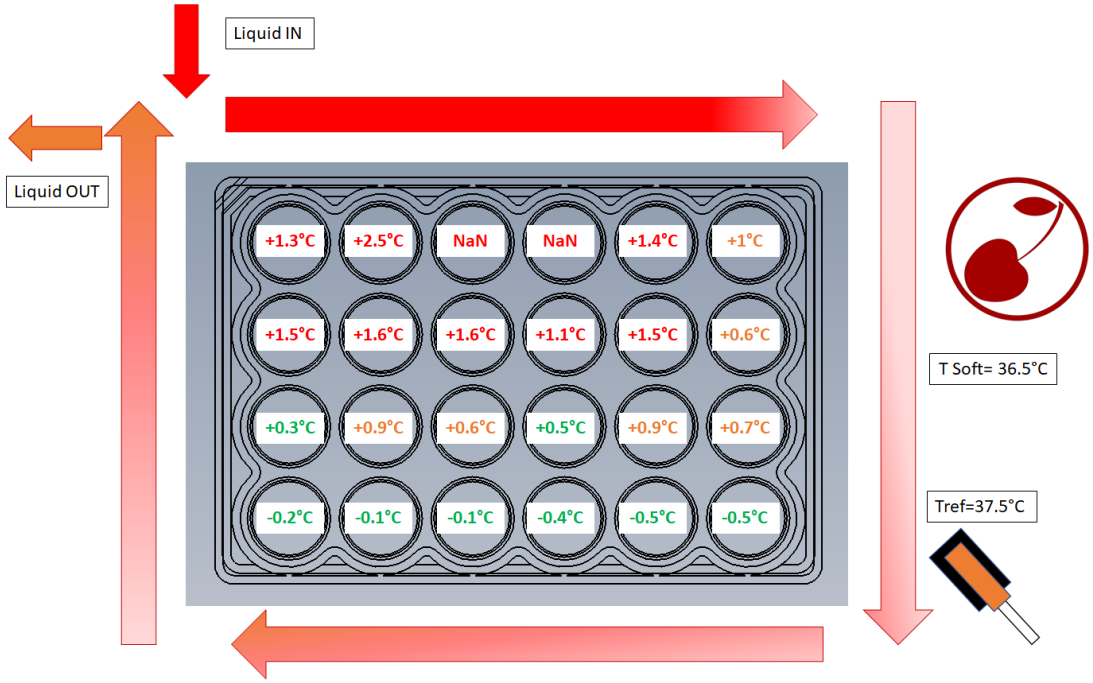

Figure 53, Heat map of the heat-stage while thermalizing the 24 Multi-well. The reference wells during the calibration were the D row. In red the wells with a difference higher than +/-1°C with the reference. In orange the ones with a difference between +/-1°C and +/-0.5°C. In green the ones with a difference lower than +/-0.5°C. The arrows show the path of the thermalized circuit.

Chapter 5, Results of the biological proof-of-concepts performed with the different models

This chapter will present the different biological protocols developed for each specific microfluidic device adapted for the different biological models. Then each microfluidic device will have a validation experiment or a proof-of-concept that will lead to results such as images or specific phenotypes. Based on this biological validation, the future of the device will be decided at the company level, either to integrate a product line or need further industrialisation process.

5.1. Biological validation of the Yeast model

As it was mentioned in chapters 3&4, Prof. Phong Tran's collaboration leaded to the development of the ThermaFlow yeast edition chip, and thanks to that partnership we managed to industrialize it and sell it as a commercial product. The first user and client of this product was Prof. Erfei Bi from the Cell and Developmental Biology department at the Perelman School of medicine inside the University of Pennsylvania, United States of America.

Prior to that together with the team of Prof. Phong Tran, we designed two different biological experiments as proof-of-concept for the microfluidic chip. The experimentation was divided in two different parts, the first one covered the validation of the temperature features, while the second one targeted the perfusion one. All the biological experimentation were performed at Prof. Phong Trang's laboratory at the Institute Curie, Paris, France. The imaging system used was an Inverted Spinning Disk Confocal Roper/Nikon coupled with a CCD 1392x1040 CoolSnap HQ2 camera. The used objective was CFI Plan Apo VC oil, with a Numeric Aperture of 1.4 and WD of 0,23.

5.1.1. Temperature validation experiment

The biological model used by Prof. Phong Tran was a yeast, *S. Pombe,* which is a eukaryote cell extensively studied in the field of cell division due to its simplicity, short generation time (2-4 hours) and availability of thermo-sensitive mutant(417–421). In such biologically engineered model, some proteins are temperature dependant, therefore depending on the temperature of the specimen they can be functional or not. For example, microtubules are proteins made of tubulin monomers in charge of the cell division process and that for the *S. Pombe* needed to be at 25°C to be polymerized and stable. If the temperature drops those MTs start to depolymerize and can stop the cell cycle(422).

The validation experiment for the temperature aimed to replicate the depolymerization of microtubules (MTs), naturally temperature dependant proteins that are key for the cell division(189). The temperature profile was the following one, 25°C for 5', then 8°C for 10', to end up going back to 25°C to observe the repolymerization. All this using the ThermaFlow device connected to the CherryTemp for the thermalization. The biological model were *S. Pombe* cells from Rnd1Δ:URA GFP-Atb2:Kan Ase1Δ:Hph strain with the GFP tagged at the Atb2 tubulin gene.

The temperature validation required the performance of the following steps:
Sterilization part:

- All the components of the ThermaFlow were previously cleaned with Ethanol 90% and sterilized using UV light for at least 15'

Lectin coating of the cell chamber:

- A pipette to inject 200µL of Lectin solution (20µL of Lectin (2mg/ml) and 180µL of sterile MiliQ water) was prepared
- Using the inlet point, the Lectin solution was injected while sucking from the syringe until filling all the cell chamber
- It was left for 15' at room temperature under the hood
- As much as Lectin solution as possible was removed using the syringe
- It was left again to dry for 15' at room temperature leave it to dry for 15' more

Cell injection step:

- A pipette to inject 200µL of cell and medium was prepared
- Using the inlet point, the cell's solution was injected while sucking from the syringe until filling all the cell chamber
- The cells were ready to be imaged or stored until the experimentation

Medium renewal step:

- A pipette to inject 200µL of fresh medium was prepared
- Using the inlet point, the fresh medium was injected while sucking using the syringe until filling all the cell chamber
- These steps were repeated at least 3x times to make sure that all the old medium is removed

Thermalization step:

- A ThermaFlow device with the cells was placed on the microscope stage with 100x oil objective
- It was connected to the CherryTemp using the Immersion configuration
- Thermalized at 25°C while looking for the target *S. Pombe* cells using the Immersion configuration
- Once founded, imaged for 5' to make sure that the MTs are present
- The temperature was reduced to 8°C and the sample imaged for 10' while the MTs depolymerized
- The last step was to rise back the temperature to 25°C to validate that the MTs were re-polymerizing

A temperature profile of this experiment can be seen at Figure 54.

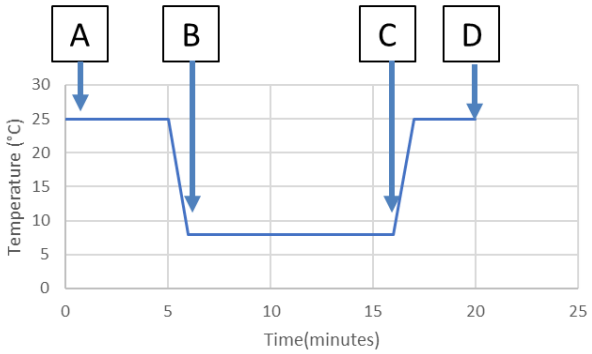

Figure 54, Temperature profile of the ThermaFlow yeast edition during the temperature validation. Image obtained at T=1min (A), image after 6'(B), image after 16'(C) and image after 21'(D)

As it can be seen at Figure 55-A, the were more than ten *S. Pombe* cells in the selected field of view that was thermalized at 25°C. After 5' of imaging, the temperature was reduced to 8°C, Figure 55-B for 10'. After this time, it was possible to notice that the majority of the MTs were depolymerized, Figure 55-C, just before increasing back the temperature to 25°C, Figure 55-D, for 5', were the MTs were repolymerized. The presented images were the ones selected from a pull of a set of 5 experiments.

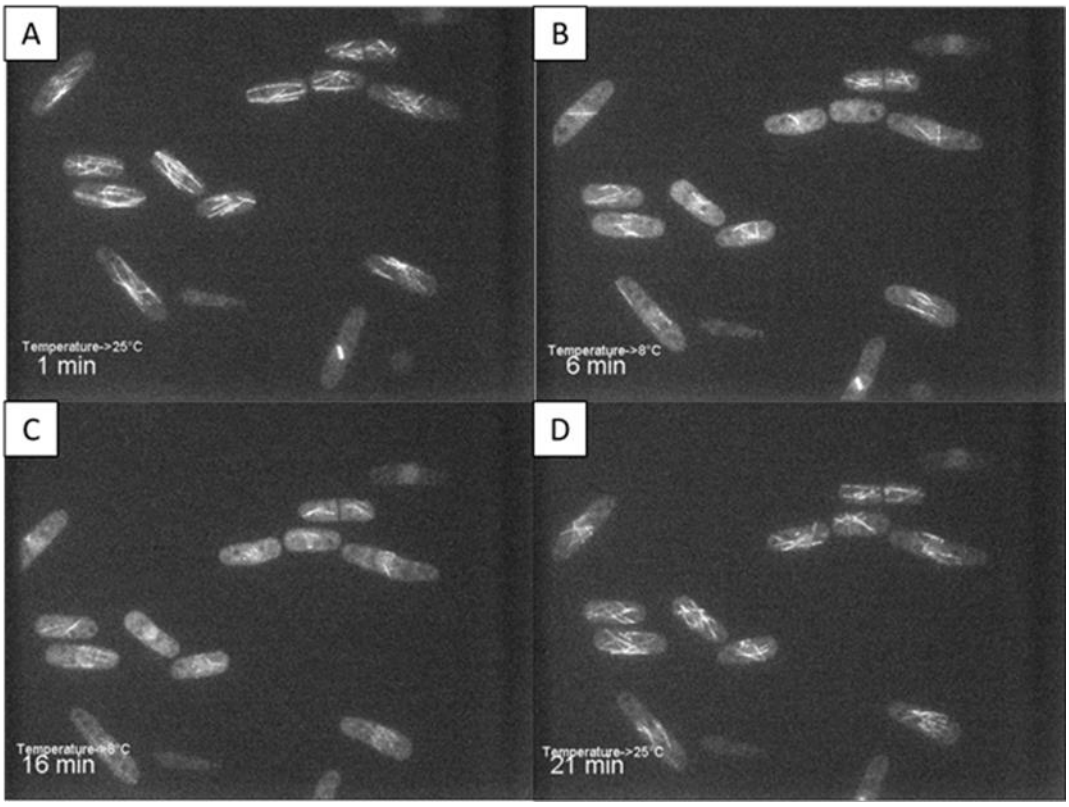

Figure 55, Temperature control validation experiment for MTs depolymerization using ThermaFlow yeast edition and 100x objective. Sample yeast at 25°C (A), sample temperature decreased to 8°C (B) sample at 8°C after 10' (C) and sample at 25°C after 5' (D). Note: the tubulin at MTs was tagged with GFP fluorophore

These results demostrated the proof-of-concept regarding the capacity of ThermaFlow yeast edition to control the sample temperature while doing live-cell imaging with a biological sample as *S. Pombe* using CherryTemp.

5.1.2. Perfusion validation experiment

Once the temperature control was validated, it was necessary to validate the perfusion feature. As it was mentioned in chapter 3, we decided to use Carbendazim or MBC, which is a molecule that suppresses MTs dynamic instability during cell division. Therefore, the expected phenotype once the drug was perfused to the cells was to observe the depolymerization of the MTs inside the *S. pombe* cells.

The experimental plan followed these steps:
Sterilization part:

- All the components of the ThermaFlow were previously cleaned with Ethanol 90% and sterilized using UV light for at least 15'

Lectin coating of the cell chamber:

- A pipette to inject 200µL of Lectin solution (20µL of Lectin (2mg/ml) and 180µL of sterile MiliQ water) was prepared
- Using the inlet point, the Lectin solution was injected while sucking from the syringe until filling all the cell chamber
- It was left for 15' at room temperature under the hood
- As much as Lectin solution as possible was removed using the syringe
- It was left again to dry for 15' at room temperature leave it to dry for 15' more

Cell injection step:

- A pipette to inject 200µL of cell and medium was prepared
- Using the inlet point, the cell's solution was injected while sucking using the syringe until filling all the cell chamber
- The cells were ready to be imaged or stored until the experimentation

Medium renewal step:

- A pipette to inject 200µL of fresh medium was prepared
- Using the inlet point, the fresh medium was injected while sucking from the syringe until filling all the cell chamber
- These steps were repeated at least 3x times to make sure that all the old medium is removed

Thermalization and imaging:

- A ThermaFlow device with the cells was placed on the microscope stage and connected to the CherryTemp
- Thermalized at 25°C while looking for the target *S. Pombe* cells
- Once founded, imaged for 5' to make sure that the MTs are present

The temperature profile of this validation experiment can be seen Figure 56.

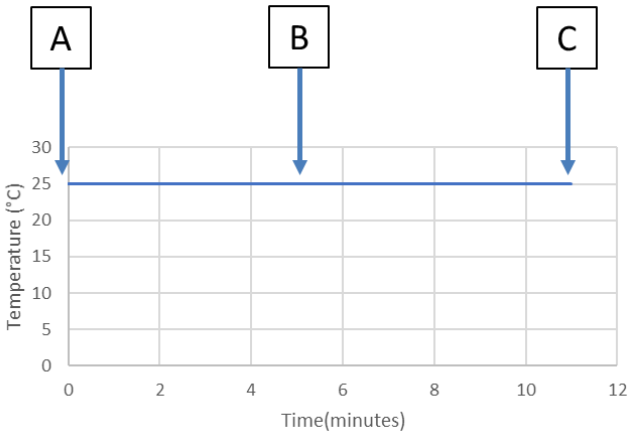

Figure 56, Temperature profile of the ThermaFlow yeast edition during the perfusion validation. Image taken at T=0min(A), T=5min(B) and T=11min(C)

MBC perfusion step:

- A pipette to inject 200µL of an MBC+medium solution at 50µg/µL concentration of MBC
- Using the inlet point the MBC solution was injected while sucking from the syringe until the cell chamber was filled
- Observation was done for 10' in order to validate that the MTs were depolymerizing

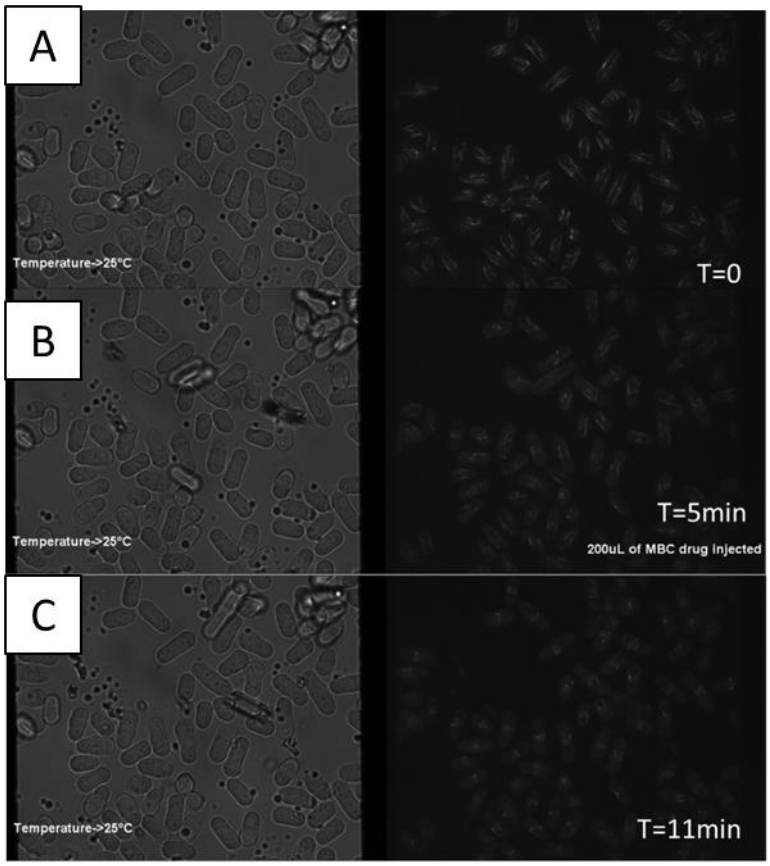

Figure 57, Perfusion validation experiment for MTs depolymerization using ThermaFlow yeast edition and a 100x objective. Sample yeast at 25°C (A), sample at 25°C after adding the MBC solution(B) sample at 25°C 6' after adding the MBC solution (C). Note: the tubulin at the MTs were tagged with GFP fluorophore.

As it can be seen at Figure 57-A, the were more than twenty *S. Pombe* cells in the selected field of view that was thermalized at 25°C. After 5' of imaging, the MBC solution was injected following the protocol previously mentioned, and it was possible to observe a MTs depolymerization Figure 57-B. After six minutes of drug incubation most of the MTs were depolymerized, proving that the drug entered in the cells and acted. It also demonstrated that the perfusion capacity of the presented device combined with the developed protocol worked. Again, the presented images were selected from a set of 5 experiments under the same conditions.

These results demonstrated the proof-of-concept regarding the capacity of ThermaFlow yeast edition to control the sample temperature while doing live-cell imaging with a biological sample as *S. Pombe using* CherryTemp and to perfuse drugs on the sample. These results allowed Cherry Biotech to start commercializing this device inside the CherryTemp and perfusion pack having the laboratory of Prof. Erfei Bi as first real user.

5.2. Biological validation of the Mammalian cells model

As it was mentioned before in chapters 3&4, thanks to a collaboration between the Prof. Isabelle Vernos laboratory and Cherry Biotech, we developed a ThermaFlow mammalian cells edition device. In this case the biological model were Kyoto-HeLa cells with the tubulin tagged with GFP and DNA with m-cherry.

The experimentation was divided in two different parts, the first one covered the validation of the temperature features, while the second one targeted the drug perfusion and the temperature control combined. All the experimentation was performed at the CRG, Barcelona, Spain.

5.2.1. Temperature validation experiment

Inside the research on the cell division field, MTs play a big role as key proteins that lead different structures and dynamics inside the cell. For the team of Isabelle Vernos, their most used biological model were Kyoto-HeLa cells because as mammalian cells. Their study of the MTs involve the understanding of the different mechanisms that trigger their actions, which structures could be affected after a disruption and how is the rearrangement after that.

A set of experiments was designed to validate the ThermaFlow device that we developed together. Its ability to thermalize the sampled cells while doing live-cell imaging was the primary focus. However, prior to any experimentation, a protocol to seed the Kyoto-HeLa cells on the cell chamber and the assembly of the ThermaFlow device was developed with Alejandra Laguillo Diego and Ivan Zadra, two PhD students at Prof. Isabelle Vernos Laboratory.

The protocol followed these steps:
Sterilization part:

- All the components of the ThermaFlow were previously cleaned with Ethanol 90% and sterilized using UV light for at least 15’

Cells preparation and seeding on the cell chamber:

- Kyoto-HeLa cells were seeded on a standard petri-dish, 100x15mm using 10mL of DNEM medium.
- Between the 10th and the 15th passage, once the cells reached confluency, we took apart $2.2x10^6$ cells per 1mL of medium on 10mL falcon.
- We diluted that concentration on a 10mL falcon with fresh DNEM medium
- 2x cell chambers were placed on standard petri dish prior to place 1mL of the cell’s solution on them
- Finally, 9mL of Fresh DNEM medium was added for the cells to grow in the incubator (37°C, 5% CO2) for at least 12h or until reaching confluency

ThermaFlow device assembly

- One cell chamber was taken from the petri dish and placed on a chip insert for the alignment
- 80µL of fresh DNEM medium were added prior to remove the liner using a tweezer

- ThermaFlow thermalization part was placed on top and press it for 1’ in order to seal the cell chamber
- A pipette of 500µL of DNEM medium + HEPES (20µM) was prepared to keep the pH stable
- Using the inlet point, the fresh medium was injected while sucking from the syringe until filling all the cell chamber with fresh medium

For the validation of the temperature control feature of the ThermaFlow device mammalian cell edition, we decided to perform a MTs re-growth experiment. This experiment aim to find metaphase cells at 37°C, then depolymerize the MTs using temperature(4°C) and the observe the re-growth while rising back to 37°C. The protocol for this was the following one:

Thermalization step:

- A ThermaFlow device with the cells was placed on the microscope stage and connected to the CherryTemp
- Thermalized at 37°C while looking for cells in metaphase using the Immersion configuration of the CherryTemp
- The temperature was reduced to 20°C for 10’ and then to 4°C for 10’ more, using the Dry configuration of the CherryTemp and removing the objective from the contact of the sample
- After that time, the objective was placed back in contact with the sample and the temperature was risen to 37°C.

NOTE: It was necessary to make the 20°C step to not thermally shock the cells with a change of 29°C in 10’. We also switch from the Immersion mode to the Dry one because the CherryTemp system was not able to keep the 4°C for Immersion mode due to the objective and room temperatures that were over 25°C. The consequence of this was that we lose time resolution in order to observe the depolymerization of the MTs.

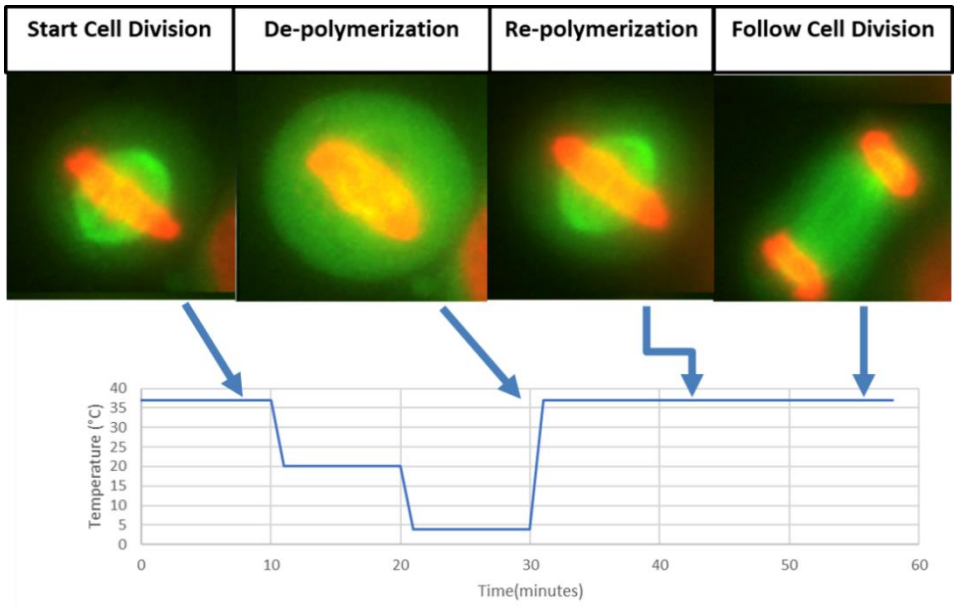

Figure 58, 1st HeLa-Kyoto regrowth experiment in the Leica DMI6000B microscope with a 63x objective. 1st image, metaphasic spindle at 37ºC, 2nd image, after decreasing the temperature sequentially to 20°C and 4°C, most of the MTs were de-polymerize, 3rd image, once increased back to 37°C, most of the MTs re-polymerized and 4th image, the cell end up segregating after 55’ . Note: the MTs were tagged with GFP and the DNA with m-cherry fluorophore.

For the thermalization validation was first tested using 63x objective on an epifluorescence Leica DMI6000B microscope, using a Leica DFC9000GT camera and the LAS X software from Leica, Germany. The results for this first experiment can be seen in the Figure 58, presenting one cells obtained from a set of 7 experiments. The observed cell was metaphase cell that completed a re-growth experiment using just temperature variation (37°C, 20°C and 4°C) and managed to complete the cell division afterwards. Even if the epifluorescence microscope provide very good resolution it only allowed us to obtain few pictures before photo-bleaching the image. Another drawback was the un-possibility to obtain different positions during the experiment as the stage did not allow to perform multi-position in the x-y axes.

Considering all the previous points, we decided to move to another microscope, the Andor Dragonfly Spinning Disk confocal module on a Nikon Eclipse Ti2 microscope. This different setup allowed us to obtain more images at high resolution, without photo-bleaching the cells and obtain different images using multi-positioning.

Using a 63x objective, performed four sets of experiments following the previously mentioned temperature cycle. From all of them recorded cells we selected the ones presented at Figure 59. There were four cells at different stages of the cell division. we managed to observe four different cells at different cell division stages. In the sample cases #1, #2 and 4#, after the 20°C and 4°C steps it was possible to observe that the MT's were depolymerized. In case of sample #3, the aster MTs were still present after the thermal cycle. Reason behind this could be that the cell was in anaphase, a very advanced stage of the cell division, were the aster MTs are more resistance to depolymerize as cell is close to finish the cell division(423–425).

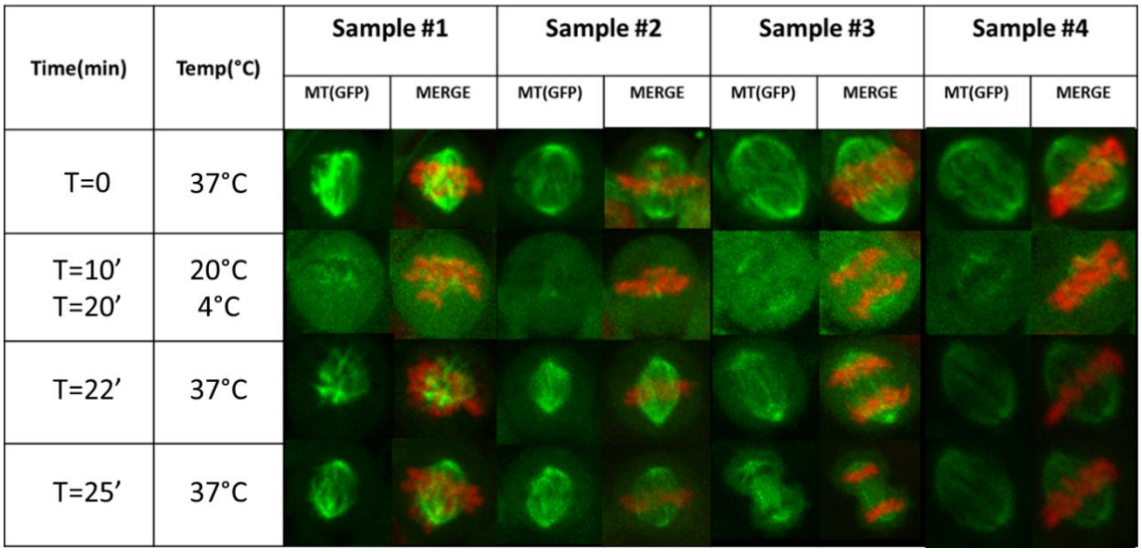

Figure 59, 2nd HeLa-Kyoto regrowth experiment in the Andor Dragonfly Spinning Disk confocal module on a Nikon Eclipse Ti2 microscope with a 63x objective. Four different cells in the same ThermaFlow device, imaged only the GFP (left column) and merged GFP and DNA (right column). 1st row, at time zero and 37°C, 2nd row, after two steps of 10' each at 20°C and 4°C, 3rd row, 2' after rising to 37°C and 4th row, 5' after rising to 37°C.

5.2.2. Perfusion validation experiment

Once the temperature featured was demonstrated, we planned another experiment using Nocodazole, at 2uM, which is an antineoplastic agent capable of blocking the polymerization of MTs, and then remove it from the cells by renewing the medium. Both experiments were performed at the Andor Dragonfly Spinning Disk confocal module on a Nikon Eclipse Ti2 microscope using a 63x objective.

In order to study the dynamics of the mitotic spindle, sometimes it is necessary to stop or inhibit some processes to understand its global structure. Therefore, using Nocodazole to depolymerize the MTs and then remove it by renewing the medium could provide information about the dynamic stability of the MTs and their rearrangement after the re-polymerization. If the perfusion feature is validated it could provide a new tool for studying cell division.

The protocol for the perfusion followed the same steps than the previous one but with a different thermalization, as at this time during all the experimentation the sample was at 37°C. The perfusion protocol had two parts, the Nocodazole perfusion and the medium renewal to remove the drug.

Nocodazole perfusion step:

- A pipette to inject 500µL of a Nocodazole + DNEM with HEPES (20µM) at 2µM concentration of Nocodazole was prepared
- Using the inlet point the Nocodazole solution was injected while sucking from the syringe until the 500µL were perfused through the ThermaFlow
- Nocodazole was incubated for 40’ with image acquisition every 1’

For the washout we used for each part of Nocodazole solution 3xPBS parts and 3xDNEM+HEPES solutions parts, the steps were the following:

Nocodazole washout step:

- A 2mL Eppendorf with 1.5mL of PBS and another one with 1.5mL of DNEM+HEPES (20µM) solution were prepared.
- Using 500 µL all the PBS and the DNEM+HEPES solution were perfused while sucking from the syringe

The results of this experiment were obtained from a set 4 experiments where we selected one cell to illustrate the results as it can be seen at Figure 60. This cell showed that using the perfusion protocol presented before it was possible to depolymerize MTs using drugs. This new protocol could be the base for researchers to test different drugs on their sample while performing live-cell imaging under a temperature-controlled environment.

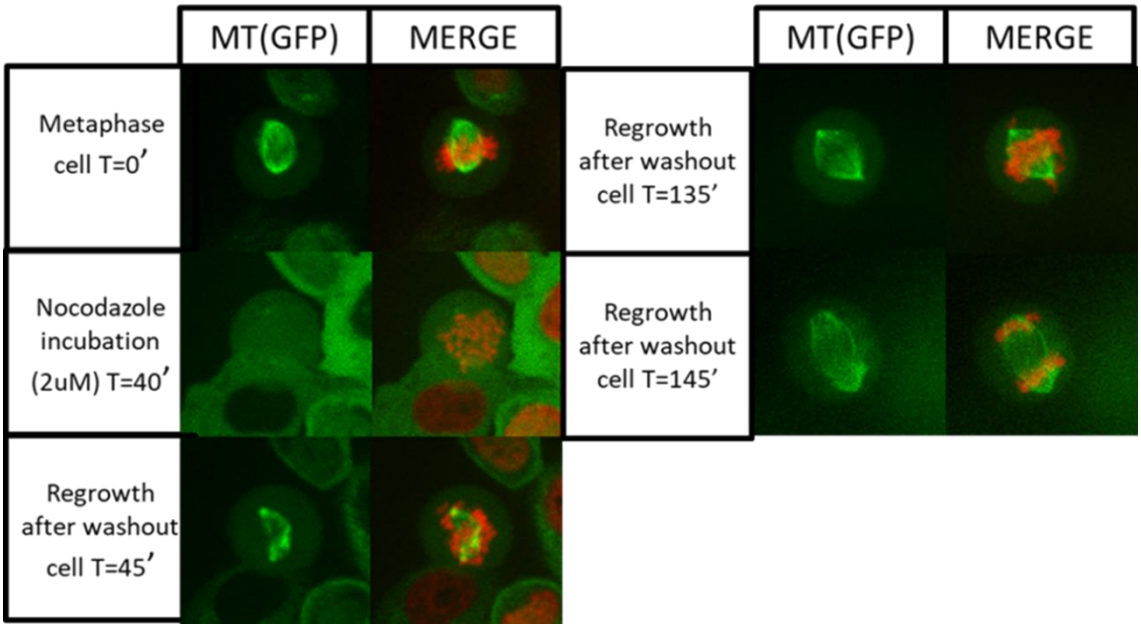

Figure 60, HeLa-Kyoto cells at the Nocodazole perfusion experiment in the Andor Dragonfly Spinning Disk confocal module on a Nikon Eclipse Ti2 microscope with a 63x objective. One cell at metaphase inside a ThermaFlow device, imaged only the GFP (left column) and merged GFP and DNA (right column). 1st image, metaphase cell at t=0, 37°C and before perfusing the Nocodazole solution. 2nd image, the cell after 40' of incubation at 37°C with the Nocodazole solution. 3rd image, MTs re-growing after the Nocodazole washout step. 4th image, the cell 90' after the washout continuing the cell cycle. 5th image, the cell 100' after the washout finishing the cell cycle.

5.2.3. Combination of temperature and perfusion, validation experiment

Once the temperature and the perfusion features were validated, we combine temperature control and drug perfusion to obtain a more complete view of the usability of the device. In this experiment, we targeted the mitotic spindle and decided to first depolymerize the MTs using temperature, then perfused S-trityl-L-cysteine (STLC), which is a molecule capable of inhibiting Eg5, a key protein on keeping the bipolar mitotic spindle(426). After the perfusion, we increased the temperature back to 37°C and check if the Kyoto-HeLa cells develop a bi-polar or a mono-polar spindle due to the effect of the STLC. Finally, using the wash-out protocol, we aimed to remove all the STLC from the cells and observe them recovering the bi-polar spindle in order to continue the cell cycle.

The protocol for this experiment was divided in three parts, the thermalization step, the STLC perfusion step and the STLC washout step. The temperature profile can be seen at Figure 61. The experiment steps were the following ones:

Thermalization step:

- A ThermaFlow device with the cells was placed on the microscope stage and connected to the CherryTemp
- Thermalized at 37°C while looking for cells using the Immersion configuration of the CherryTemp software
- The temperature was reduced to 20°C for 10' and then to 4°C for 10' more, using the Dry configuration of the CherryTemp and removing the objective from the contact of the sample
- Once the MTs were depolymerized the STLC was perfused.

- After that the perfusion, the objective was placed back in contact with the sample and the temperature was risen to 37°C.
- The sample was thermalized at 37°C while

NOTE: It was necessary to make the 20°C step to not thermally shock the cells with a change of 29°C in 10'. We also switch from the Immersion mode to the Dry one because the CherryTemp system was not able to keep the 4°C for Immersion mode due to the objective and room temperatures that were over 25°C. The consequence of this was that we lose time resolution in order to observe the depolymerization of the MTs.

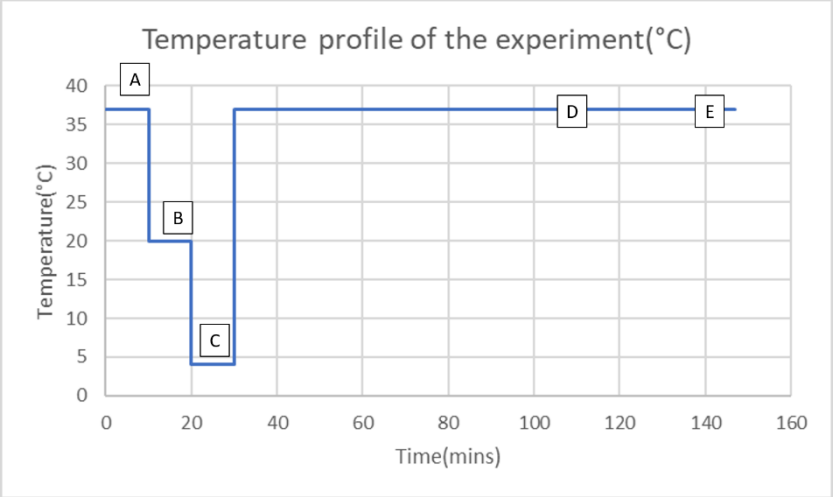

Figure 61, Temperature profile of the STLC experiment. Start of the experiment with sample temperature at 37°C in immersion mode to search for the cells(A), reduce to 20°C in dry mode by removing the objective for 10'(B), reducing to 4°C for 10' more before perfusion the STLC and rising back to 37°C(C), washout of the STLC drug after 80' of incubation which corresponded with 110' after starting the experiment(D), end of the experiment at 140'(E)

STLC perfusion step:

- A pipette to inject 500µL of an STLC+DNEM with HEPES (20µM) at 10µM concentration of STLC was prepared
- Using the inlet point the STLC solution was injected while sucking from the syringe until the 500µL were perfused through the ThermaFlow
- STLC was incubated for 80' with image acquisition every 1'

For the washout we used for each part of STLC solution 6xDNEM+HEPES solutions parts, the steps were the following:

- A 2mL Eppendorf with 1.5mL of DNEM+HEPES (20µM) solution was prepared.
- Using 500 µL all the DNEM+HEPES solution were perfused while sucking from the syringe

This experiment was performed 3 times with multiples cells imaged. An example of what we observed was in the Figure 62, where the first image was a cell without MTs due to the cold treatment(10' at 20°C and 10' at 4°C). Before rising the temperature back at 37°C, while the sample was at 4°C the STLC was perfused and incubated for 80'. We observed different phenotypes but the one that we hypothesized was to obtain monopolar spindles after 80's of STLC incubation. After the incubation time following the washout protocol we managed to observe that the cells were recovering the bi-polar spindle and end-up dividing.

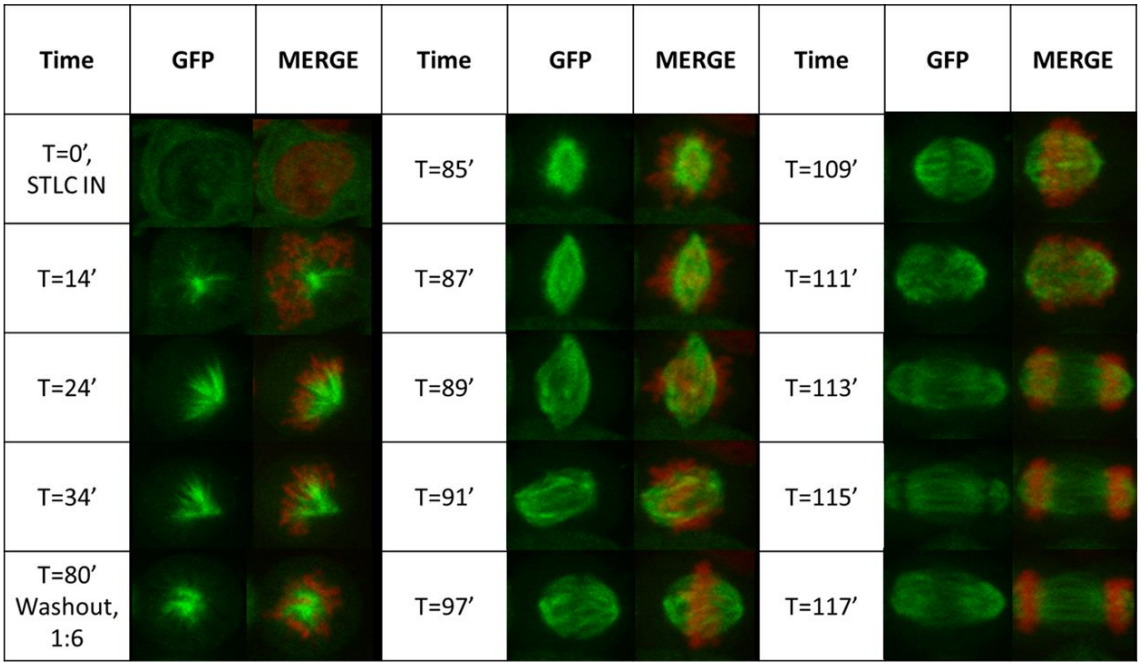

Figure 62, STLC perfusion and temperature experiment with Kyoto-HeLa cells in the Andor Dragonfly Spinning Disk confocal module on a Nikon Eclipse Ti2 microscope with a 63x objective. One cell at metaphase inside a ThermaFlow device, imaged only the GFP (left column) and merged GFP and DNA (right column).

Although, we observed two different phenotypes during this experimentation. The first one, where cells that does not develop a mono-polar spindle, Figure 63, while in the second one it passed from a bi-polar to mono-polar and again to bi-polar due to the effect of the STLC, Figure 64.

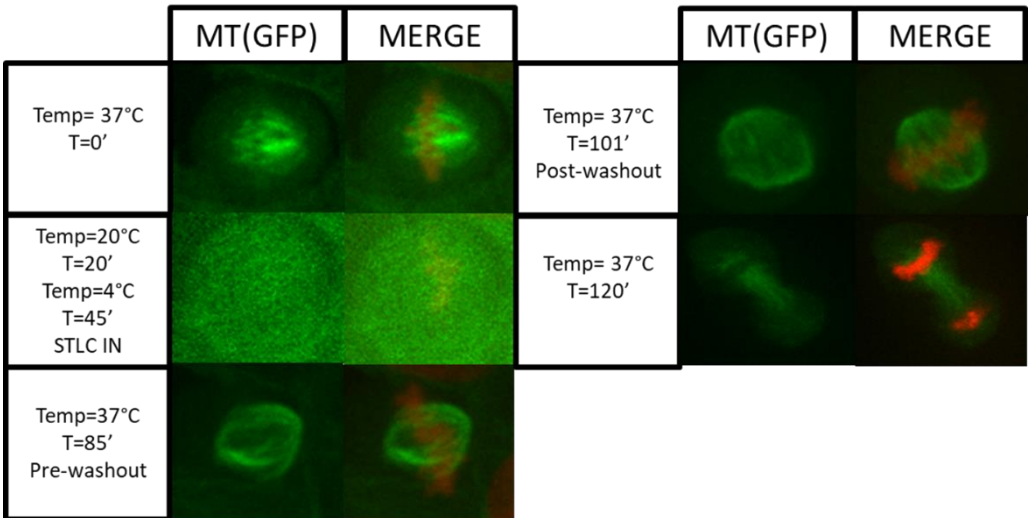

Figure 63, Phenotype #1 of STLC perfusion and temperature experiment with Kyoto-HeLa cells in the Andor Dragonfly Spinning Disk confocal module on a Nikon Eclipse Ti2 microscope with a 63x objective. One cell at metaphase inside a ThermaFlow device, imaged only the GFP (left column) and merged GFP and DNA (right column).

These differences on the phenotype could be due to moment of the cell cycle when the cell was contacted by the STLC drug. Depending of the cell division phase, the inhibition of Eg5 could no longer be possible, therefore the bi-polar spindle will remain. This first hypothesis will be further investigate using the developed device.

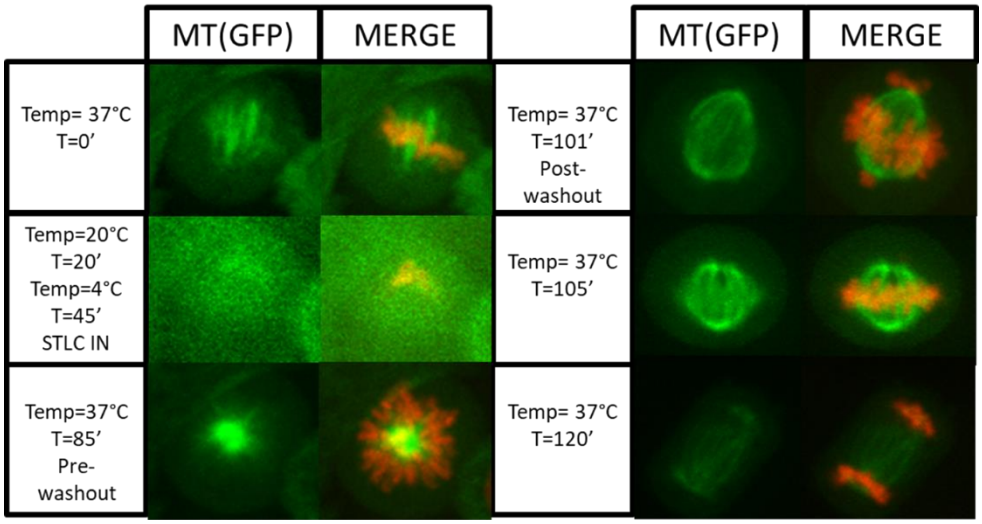

Figure 64, Phenotype #2 of STLC perfusion and temperature experiment with Kyoto-HeLa cells in the Andor Dragonfly Spinning Disk confocal module on a Nikon Eclipse Ti2 microscope with a 63x objective. One cell at metaphase inside a ThermaFlow device, imaged only the GFP (left column) and merged GFP and DNA (right column).

Therefore, as a conclusion in the ThermaFlow mammalian cells edition features, temperature control, perfusion and the combination of both were validated and ready to be industrialized in order to be commercialized as Cherry Biotech's products as an add-on to the CherryTemp.

5.3. Biological validation of the *in vitro* MT's model

As it was mentioned before in chapters 3&4, thanks to a collaboration between the Prof. Carsten Janke laboratory and Cherry Biotech, we developed a ThermaFlow *in vitro* edition device. In this case the biological model were MTs formed of different types of tubulin.

The experimentation was divided in two different parts, the first one covered the validation of the temperature features, while the second one targeted the perfusion. All the device development was done at Cherry Biotech headquarters and the biological experimentation at Carsten Janke's Laboratory in the Institute Curie Orsay, Paris. The microscopy technique used was based on TIRF microscopy, using a 100x objective and immersion oil on a Nikon Eclipse Ti spinning disc-TIRF microscope.

During all the process I received the support of Jijumon A.S. a PhD student from Carsten Janke's team that is also part of the DivIDE project.

5.3.1. Temperature validation experiment

According to the latest research performed at Prof. Carsten Janke's laboratory, some mutations in the tubulin of MTs made them more resistant to lower temperatures. This mutation might be one of the causes of some brain diseases. Such mutant MTs can keep polymerizing at a lower range outside their ideal temperature of 37°C. Therefore, can be used as an original model to validate the temperature control the de device. Taking this as an objective, we developed a protocol for injecting the MTs inside the *in vitro* chamber of the ThermaFlow device and to perfuse the different reagents necessary to perform the experiment. Finally, we designed a thermalization protocol to find out which was the limit temperature at which the different MTs stop polymerizing.

For this experimentation the used MTs were divided in two groups, beta tubulin mutants and alpha tubulin mutants, Figure 65, of which one of each group were controls and the rest mutants.

Beta Tubulin Mutants
EB3-2A-hTubA1B
EB3-2A-hTubA1B_mut1
EB3-2A-hTubA1B_mut2
EB3-2A-hTubA1B_mut3
EB3-2A-hTubA1B_mut4

Alpha Tubulin Mutants
EB3-2A-hTUBB2A
mEB3-GFP-2A-hTubB2B_mut1
mEB3-GFP-2A-hTubA1B_mut5

Figure 65, List of different type of MTs based on their alpha or beta mutation. Controls(green) and mutants(red)

Taking those types, we developed a protocol to perfuse them inside the ThermaFlow device, following those steps:
Sterilization part:

- All the components of the ThermaFlow were previously cleaned with Ethanol 90% and sterilized using UV light for at least 15'
- The glass coverslips were sterilized by placing them in Ethanol-Acetone, 50-50% solution and dried suing a Bunsen flame.

ThermaFlow device assembly step:

- The glass coverslip was attached to the ThermaFlow device using an insert to align it.
- The perfusion part with the tubes and the syringe were assembled

Kinesin coating of the *in vitro* chamber step:

- A pipette to inject 50µL of Kinesin solution (500nM) was prepared
- Using the inlet point, the Kinesin solution was injected while sucking from the syringe until filling all the cell chamber
- It was left for 5' at room temperature under the hood for it to act on the glass surface

At this point it was necessary to inject the GMPCPP MT seeds from where the MTs would grow once adding the tubulin into the *in vitro* chamber.

Injection of the GMPCPP MT seeds step:

- A pipette to inject 50µL of GMPCPP MT seeds solution (to have 5-10 per field of view) was prepared
- Using the inlet point, the GMPCPP MT seeds solution was injected while sucking from the syringe until filling all the cell chamber

All the previous steps were done under the hood, so the next steps were done directly at the microscope stage. Anyway, prior to perfuse the tubulin it was necessary to flush 100µL of buffer to remove the seeds that did not attached to the coated glass surface.

Injection of the tubulin step:

- A pipette to inject 100µL of buffer solution (BRB80 buffer 1X) was prepared
- Using the inlet point, the buffer solution was injected while sucking from the syringe until filling all the cell chamber
- A pipette to inject 50µL of the selected tubulin solution (0.24mg/mL) was prepared
- Using the inlet point, tubulin solution was injected while sucking from the syringe until filling all the cell chamber

The objective of these set of experiments was to obtain the polymerization limit temperature for different tubulin strains and their stability. Therefore, we designed a thermalization protocol to obtain that information using the ThermaFlow *in vitro* edition chip. Starting at 37°C to make sure that the MTs are growing, we will sequentially reduce the temperature to 30°C, 25°C and 20°C, taking 4' on each one. Once at 20°C we would rise the temperature to 23°C, 25°C, 28°C, 30°C, 33°C and finally 37°C. All the steps would take 4', while the last one could last more just to validate the recovery of the polymerization as it can be seen at the Figure 67.

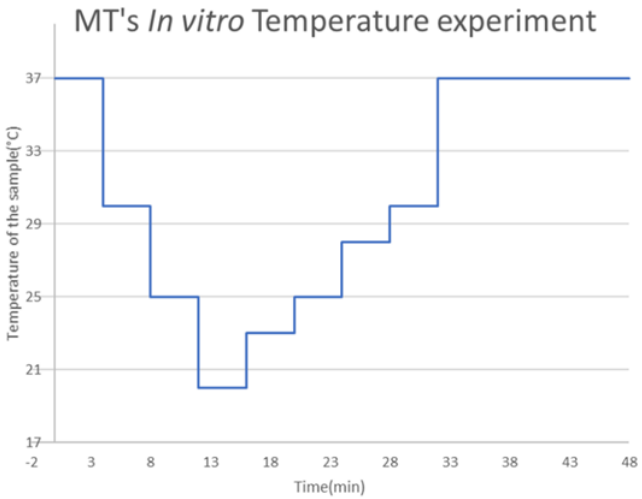

Figure 67, Thermalization protocol for the MTs stability experiment

The results of this experiment were not fully available yet as the team of Prof. Carsten Janke was still performing screening to determine which was the real polymerization blocking temperature for each of the tubulin strains. An example of how the outcome of the experiment was available at Figure 66.

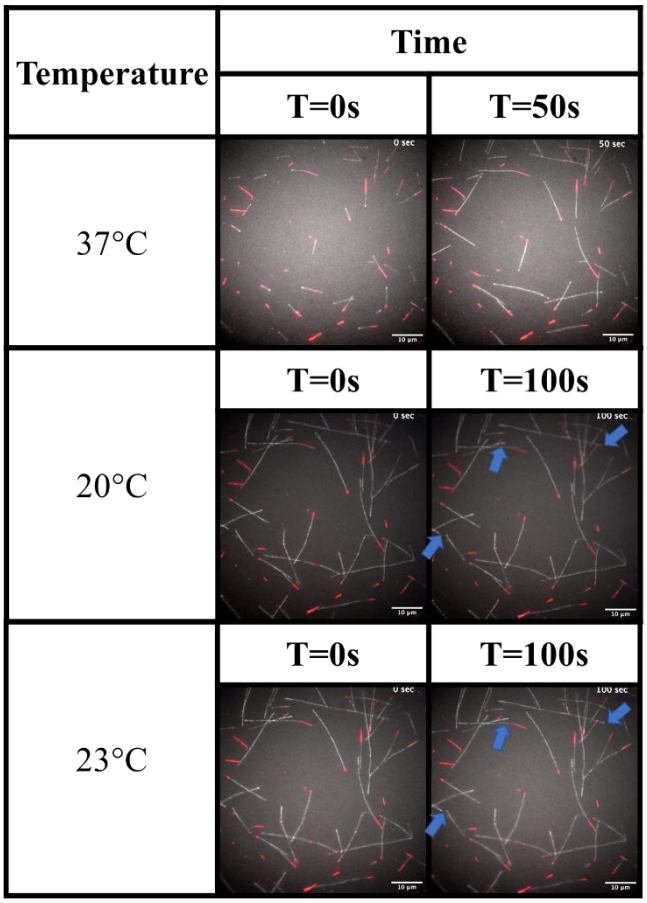

Figure 66, Example of the temperature validation experiment using a X1360 mutant tubulin in vitro. In red the GMPCPP MT seeds while in white the selected tubulin of which the MTs growth. The first line show the initial growing at 37°C, while the second one stopped completely the polymerization at 20°C. the third line showed that at 23°C the polymerization was back in the indicated points (blue arrows). The images were obtained using a 100x objective and immersion oil on a Nikon Eclipse Ti spinning disc-TIRF microscope, while the scale was 10µm

Nevertheless, the first preliminary results available can be observed at Figure 68 where the three experiments performed with the wild type tubulin control from the alpha tubulin(green) showed that the MTs start re-polymerizing at 28°C. For the mutant N° 1360 it was at 23°C while for the 1362 and 1363 it was at 25°C. These preliminary results indicated that the stability could be affected by the assembly of the mutant tubulin, as Prof. Carsten Janke's team hypothesised. However, further investigations were necessary to finish the screening and to have the complete data set to validate it or not. Anyway, the complete protocol developed due to this collaboration in order to work with MTs on *in vitro* conditions was validated.

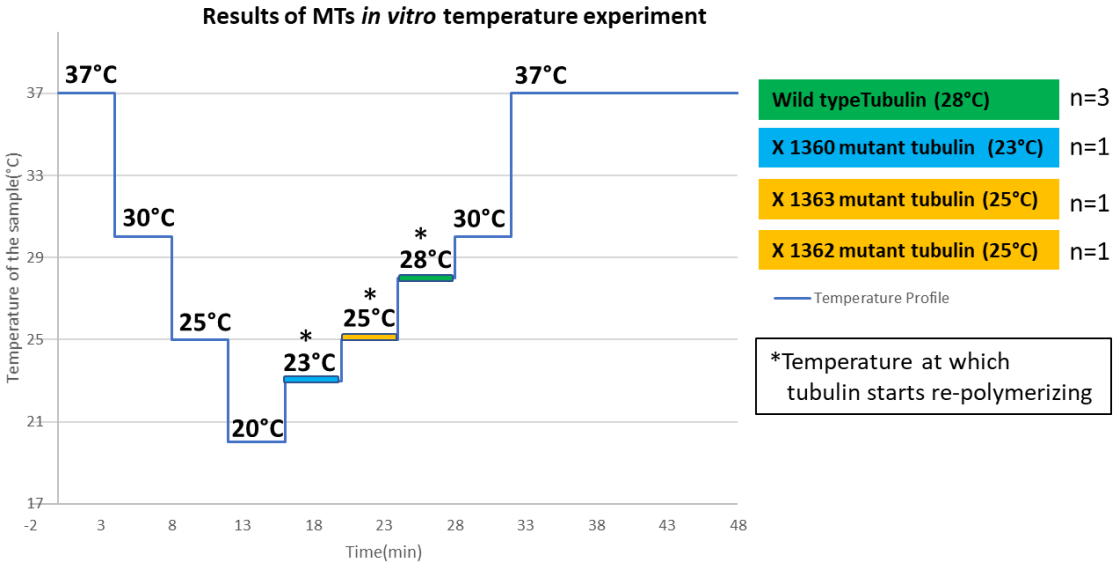

Figure 68,Preliminary results of the MTs in vitro temperature experimentation

5.3.2.Perfusion validation experiment

The second experiment aimed at validating the perfusion feature as the target was to quantify the affinity of different types of Microtubule Associate Proteins (MAPs), Figure 69, toward different types of MTs, built with different types of tubulin (alpha or beta mutations). The experimental plan was to have two different types of MTs growing inside the *in vitro* chamber before injecting a specific type of MAP to quantify its affinity for one type of MT or another.

MAPs to be tested	
Tau 3R	EML 3
Tau 4R	EML 4
Syntaphilin A	EML 5
Syntaphilin C	EML 6
EML 1	CSAP
EML 2	CFAP

Figure 69, List of the MAPs to be tested using the ThermaFlow in vitro edition device

The developed protocol followed these steps:
Sterilization part:

- All the components of the ThermaFlow were previously cleaned with Ethanol 90% and sterilized using UV light for at least 15'
- The glass coverslips were sterilized by placing them in Ethanol-Acetone, 50-50% solution and dried suing a Bunsen flame.

ThermaFlow device assembly step:

- The glass coverslip was attached to the ThermaFlow device using an insert to align it.
- The perfusion part with the tubes and the syringe were assembled

Kinesin coating of the *in vitro* chamber step:

- A pipette to inject 50µL of Kinesin solution (500nM) was prepared
- Using the inlet point, the Kinesin solution was injected while sucking from the syringe until filling all the cell chamber
- It was left for 5' at room temperature under the hood for it to act on the glass surface

At this point it was necessary to inject the two different types of GMPCPP MT seeds from where the MTs would grow once adding the tubulin into the *in vitro* chamber.

Injection of the GMPCPP MT seeds step:

- Two pipettes to inject 50µL of GMPCPP MT seeds solution (to have 5-10 per field of view) was prepared
- Using the inlet point, the type A GMPCPP MT seeds solution was injected while sucking from the syringe until filling all the cell chamber
- Then the type B GMPCPP MT seeds solution was injected while sucking from the syringe until filling all the cell chamber

As mentioned before, all the previous steps were done under the hood, so the next steps were done directly at the microscope stage. Anyway, prior to perfuse the tubulin it was necessary to flush 100µL of buffer to remove the seeds that did not attached to the coated glass surface.

Injection of the buffer and the two types of tubulin step:

- One pipette to inject 100µL of buffer solution (BRB80 buffer 1X) was prepared
- Using the inlet point, the buffer solution was injected while sucking from the syringe until filling all the cell chamber
- Two pipettes to inject 50µL of the two selected tubulin solutions (0.24mg/mL) was prepared
- Using the inlet point, the type A tubulin solution was injected while sucking from the syringe until filling all the cell chamber
- Then, the same was done using the type B tubulin solution.

Thermalization step:

- A ThermaFlow device with the cells was placed on the microscope stage and connected to the CherryTemp, the oil was placed on the 100x objective using TIRF microscopy
- Thermalized at 37°C while looking for cells using the Immersion configuration of the CherryTemp

Injection of the MAPs step:

- One pipette to inject 50µL of MAPs solution (concentration) was prepared
- Using the inlet point, the buffer solution was injected while sucking from the syringe until filling all the cell chamber

At this point, using TIRF microscopy the selected MTs were observed for 10' in order to quantify the affinity of the MAPs for each type of MTs depending on the tubulin type. Together with Jijumon A.S. we managed to fine tune this protocol in order to make it repetable for his experiments, as it will be necessary for him to check multiple combinations of tubulins and MAPs.

NOTE: At the moment of writing this manuscript, the experiments were still on going and the results were not yet available. However, the developed protocol was validated by Prof. Carsten Janke's team as a fast way to perform live-cell imaging experiment while doing screening. Once the preliminary results will be available, they will be introduced as Annex.

5.4. Biological validation of the Spheroid/3D cell culture model

As it was mentioned before in chapters 3&4, inside the SpOC project and together with the team of Dr. Yannick Arlot from the IGDR, we developed a protocol to culture kidney cancer spheroids for 5 days.

5.4.1. Spheroid formation, transfer and viability validation

The spheroids were made of 786-O kidney adenocarcinoma cells from ATCC, LGC Standards, UK. The protocol to form the spheroids followed these steps:

Spheroids formation step:

- The 786-O cells were seeded and expanded (P10) in RPMI-1640 medium (GibcoTM-Life Technologies) supplemented with 10% foetal calf serum (FCS) and 1% penicillin/streptomycin (PS) at 37°C with 5% CO2
- The spheroids were formed by seeding 5000 cells/well in a 96 Multi-well plate for 3 days until they reach a diameter up to 200 µm
- To prevent cell adhesion to the bottom of the 96 Multi-well plate, this was previously coated with Poly (2)-hydroxyethyl metacrylate) (Sigma Aldrich – Merck, Germany)

Once the spheroids were formed it was necessary to recover them and place them on the ThermaFlow device in order to start the 5 days experimentation. The steps were the following:

Spheroids recovery step:

- After three days, using a pipette with the tips cut in order to avoid damaging them, 6 spheroids were recovered one by one and transferred to a 1.5mL Eppendorf
- Together with 1.5mL of RPMI-1640 medium, the 6 spheroids were centrifuged (3min, 250G force) to push them to the bottom of the Eppendorf
- Again, using a pipetted with a cut tip, all of them were resuspended in 25µL of RPMI-1640 medium supplemented with 10% of FCS and 1% of PS

Prior to transfer the spheroids to the ThermaFlow it was necessary to sterilize the device and to prepare the thermalization part and the cell chamber to host the spheroids. The main steps were the following ones:

Sterilization part:

- All the components of the ThermaFlow were previously cleaned with Ethanol 90% and sterilized using UV light for at least 15’

Spheroids transfer and ThermaFlow assembly step:

- Up to 6 spheroids suspended in 25µL of medium were transferred from the Eppendorf to the cell chamber that was placed on a insert to ease the alignment for the assembly
- At this point, the liner of the perfusion channel was removed and the thermalization part was placed on top, pressed for 1’
- Finally, 475µL of RPIM-1640 medium were injected using a pipette directly in on of the inlets of the manifold, the flow was gravity driven and in 5’ it would fulfil the cell chamber and the perfusion channel with medium.

After these steps, the spheroids were placed on the incubator at 37°C, 5% CO_2 until the observation at a Leica DNRIM microscope with a 10X objective. Samples were kept at 37° C during the imaging using a CherryTemp with the Dry configuration.

For the medium renewal protocol, after different iterations the final version followed these steps:

Medium renewal protocol steps:

- The RPIM-1640 medium was pre-thermalized at 37°C prior to separate 1.2mL of it on 1.5mL Eppendorf.
- Using a pipette, 200µL of old medium were removed while perfusing 400µL of fresh medium.
- Due to the gravity after 30-60s the new medium pushed towards the output the old medium
- The previous step was repeated two more times until flashing all the 1.2mL of fresh medium.
- These steps was performed every 12h in order to keep the spheroids on a healthy state.

Following this protocol, we performed a 5 days experiment aiming to keep the structure of the spheroids after that. However, before deciding the outcome of the experiment we established a criterion to classify the state of the different spheroids at each given time. We classified them in three groups? according to the aspect of their surface and their spherical shape; The first group presented a healthy state, Figure 70-A, when surface was smooth; the second as unstable state, Figure 70-B, when showing sign of cell migration and the last one as collapsing state, Figure 70-C, when losing the spherical shape.

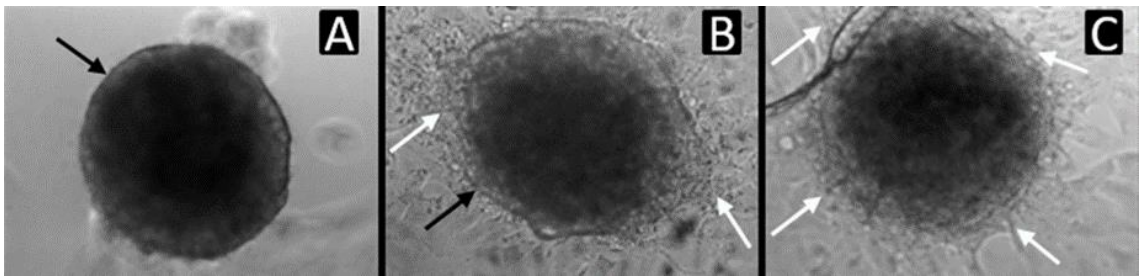

Figure 70, Qualitative spheroids viability assessment. 786-O spheroids were classified in three different states: Healthy State (A) in the absence of cells migration (white arrow) and clear and continuous edge (black arrow); Unstable State (B) in the presence of cells migration and discontinuous but clear edge; Collapsing State (C) in the presence of massive cell migration and complete absence of the edge

In this experimentation six different spheroids were placed on ThermaFlow device monitored and images at different endpoints (3h, 8h, 23h, 29h, 48h, 57h, 73h, 81h and 96h). A recap of state of the spheroids was summarized at Table 25 and the raw images presented at Figure 71.

Spheroid	Day#1		Day #2		Day #3		Day #4		Day #5
ID	T=3	T=8	T=23	T=29	T=48	T=57	T=73	T=81	T=96
#1									
#2									
#3									
#4									
#5									
#6									

Table 25, Viability assessment of six spheroids from day 1 to day 5. Spheroids viability was checked at selected endpoints; manual medium renewal (red stripped lines) was performed every 12 hours. Green = Healthy State; Yellow = Unstable State; Orange=Collapsing

As a summary, we could resume that 6 spheroids were properly loaded and trapped inside the chamber. Spheroids were immobilized allowing a clear identification among the time Table 25. After 96 hours using our discontinuous medium renewal, four out of six spheroids were in Healthy State; one was in the Unstable State and another in Collapsing State, as it can be seen in Figure 71. After 23 hours three spheroids entered in an Unstable State, two of them recovered after renewing the medium after 81 hours and one end up in the Collapsing State after 96 hours.

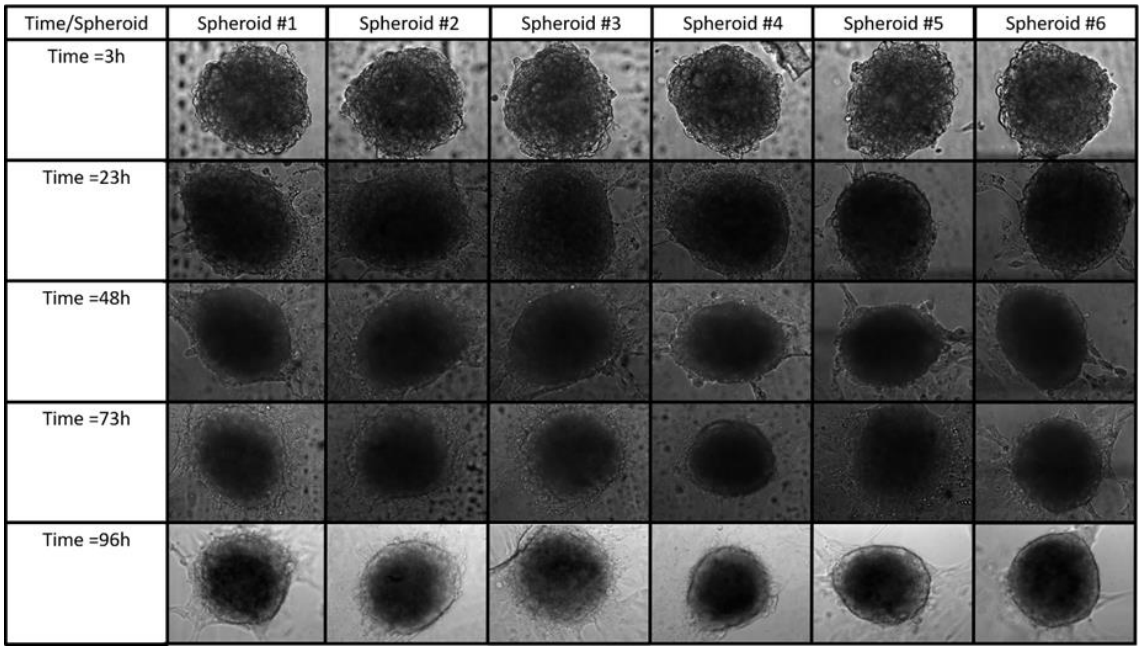

Figure 71, Follow-up of all the spheroids during the viability assessment. Overview of all the spheroids (#1-6) during the viability test at the times, 3h, 23h, 48h, 73h and 96h.

We could conclude that using the discontinuous and manual perfusion approach that we adopted, it was possible to preserve 66% of spheroids viable up to 5 days, allowing to perform long term observations on the microscope stage. Therefore, we could validate the protocol here presented as a first step to develop more complex protocols that could include the use of enriched gas or drug perfusion.

Chapter 6, Proof-of-concept combining AI for image classification

As it was introduced briefly in chapter 1, Artificial Intelligence (AI) can be a very useful tool to speed up process that could requires hours of human time but second of computing time. In this line, Cherry Biotech and the institute Jacques Monod in Paris, started a collaboration project on January 2019 to apply AI for image classification of biological samples. This project allowed me to close the story of my thesis as I started developing technology to image samples in the microscope, it will end by processing those images using different algorithms. Ultimately, using the improved robustness of image generation provided by CherryTemp on temperature sensitive model and the AI algorithm on development, we aim at reducing both the variability and the processing time following optical readout acquisition.

6.1. Context of the project

Inside the collaboration project, the laboratory of Dr. J. Dumont oversaw providing data from their *C. elegans* embryos experiments while myself start the development of an algorithm to classify the provided data according to different features and to release a desktop app by July 2019. We firstly aimed at automatizing the already existing manual lab protocol.

6.1.1. Biological context of the project

Dr. J. Dumont was one of the first users of the CherryTemp and it has been using it for nearly 3 years in order to control the temperature while performing live-cell imaging of *C. elegans* embryos. At the moment of the collaboration, his team was studying the difference between controls and mutants during the 1st embryotic division focusing on features such as the distance between the centrosome, the cell perimeter and the cell area, and shape, Figure 72.

His actual hypothesis was that by modifying the genomic sequence of a *C. elegans* embryo gene, the previously mentioned features should be affected at different levels compared with the controls.

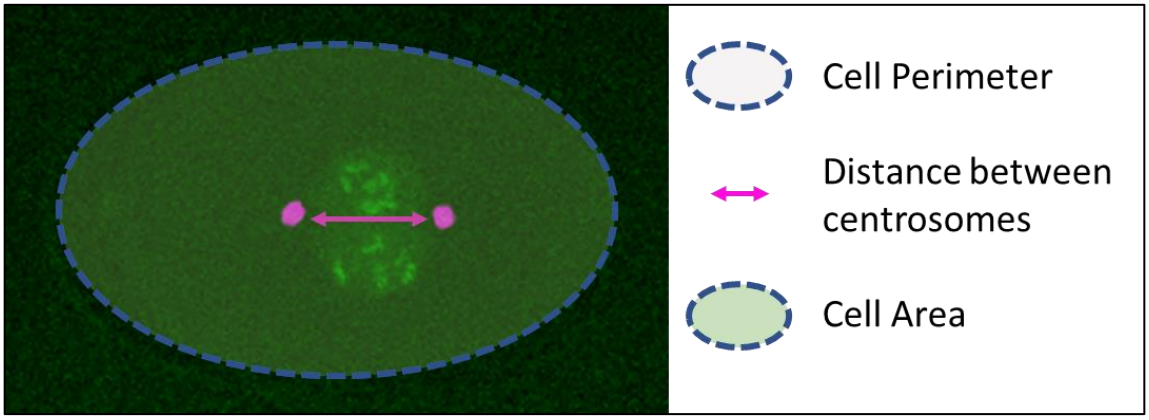

Figure 72, Example of a C. elegans embryo during the 1st division. Main features of interest for J. Dumont's team, cell perimeter (blue dots ellipse), centrosome distance (pink arrows) and cell area (blue dots and green ellipse).

6.1.2. Technical context of the project

From the technical point of view the objective of this project was to solve a pain that the team of Dr. J. Dumont had. In order to demonstrate his theory, his team imaged 42 controls cells and 25 mutants' cells trying to relate the mutation with a distortion in the embryotic division. The analysis of the data took them more than 2 months of a laboratory technician manually labelling data, one by one.

The role of Cherry Biotech inside this project was to develop a software able to perform the following tasks: extract the desired features(centrosome distance, cell area and cell perimeter) from the data, perform a sorting and training an AI algorithm to label each image according to some pre-stablished features.

This first AI project also opened the Cherry Biotech's long-term project to include AI technology inside Cubix and more generally inside its life science instruments.

Therefore, using the data provided by Dr. J. Dumont and under the supervision of Dr. Antoni Homs, the CTO of Cherry Biotech, on January 2019 I began the development of the software for the image labelling according to the different pre-established features.

6.2. Project outline: available data, steps, deadlines and deliverables

As it was mentioned before the main objective of this collaboration project was to develop a tool that could ease and speed up the analysis of different features from images of *C. elegans* embryo entering their 1st division. The project was divided into two phases: image classification and phenotype classification. The first phase was done during this PhD thesis while the second one will be continued by Cherry Biotech's R&D team.

The data provided by Dr. J. Dumont included images of 42 experiment with control data, and images of 25 experiments with DNA modified samples. The main feature for this dataset was the distance between the centrosomes Figure 73-A. The distance was the key to analyse if the cell division followed a linear ascending pattern (Figure 73-B) like in the control cases or if first shrinks and then growths like in the cases of mutations (Figure 73 -C).

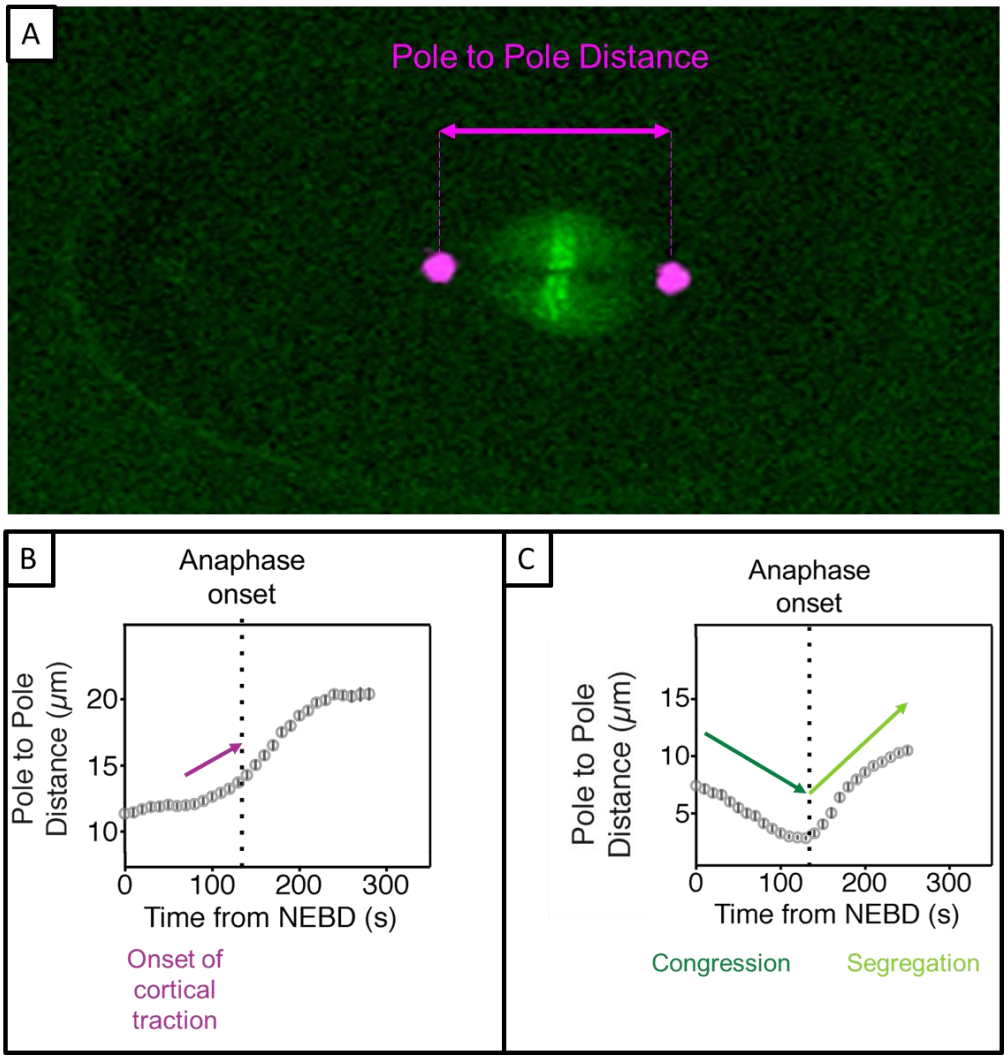

Figure 73, Example of the first C. elegans embryo division and the distance between poles/centrioles (A), evolution of the pole to pole distance during the 1st division on a control example(B) and the evolution on a mutated example(C), images provided by J. Dumont

Knowing what we got and what we were looking for, we planned the following steps, deadlines and deliverables:

Steps->Phase #1-Image classification:
- **Feature extraction:** distance between centrosomes
- **Data classification:** from raw data to data sorting
- **Data augmentation:** generation of new data to homogenise the training set
- **Train, valid and test split:** separate into train, validation and test datasets
- **Convolutional Neural Network (CNN) algorithm:** training, validation and testing
- **Algorithm deployment:** build standalone application

Deadlines:
- **Feature extraction:** February 2019
- **Data classification:** March 2019
- **Data augmentation:** March 2019
- **Convolutional Neural Network (CNN) algorithm:** June 2019
- **Algorithm deployment:** V1 July 2019, V2 September 2019

Deliverables:
Standardized protocols by September 2019:
- Feature extraction using ImageJ
- Data shorting
- Trained algorithm to classify images according to their centrosome distance
- Standalone app able to process experiment to extract the distance over time.

6.3. Image classification development, phase #1

As it was mentioned before, the collaboration project was divided in two phases, the first one covering the image classification algorithm while the second one will be focused on the phenotype classification. At this point, the steps, process and results of the phase #1 will be summarized, starting from the feature extraction until the standalone app deployment.

6.3.1. Feature extraction

The first step was to develop a standardize protocol to extract the desire feature, distance between centrosomes, from all the raw data prior to label each single frame. The raw data provided by the Dr. J. Dumont had two different data sets with images of different *C. elegans* embryos making the 1st division. The first data set contained images of 42 experiments of control samples labelled as JCC56 control. The second one contained 25 images of mutation samples labelled as JCC56 gpr-1*2(RNAi).

In order to have a standardized protocol it was necessary to add some filtering and remove the data that could be considered as artefacts or noise during the Neural Network training. Therefore, the first filter consists on removing all the experiments that include more than 1 cell in the same field of view. These reduced the available datasets to 36 controls experiment and 16 mutant ones. After these, we performed the extraction of the distance between the two centrosomes on an easy, repeatable and fast way. I iterate with different software's that had image segmentation, but I end up using Fiji from ImageJ (https://imagej.net/Fiji) to extract the position of each centrosome and MATLAB, release 2019a from MathWorks, Inc., Natick, Massachusetts, United States.

Using the Fiji software:

- Merge the different channels of each image in .tiff, using the RGB channel tool
- Track each of the centrioles during all the image sequence, using the Manual tracking tool
- Save the x-y coordinates for each centriole at each image sequence into a .csv file
- Save each of the frame of the image sequence into a .png file

Using MATLAB software:

- Pair each frame with the name of the experiment and the frame number
- Calculate the distance of each frame using the x-y coordinates
- Assign the distance to each individual frame
- Classify each frame according to the distance from 0 to 250
- Save each frame to each destination folder according to the previous classification

All the steps presented before were summarized at Figure 74.

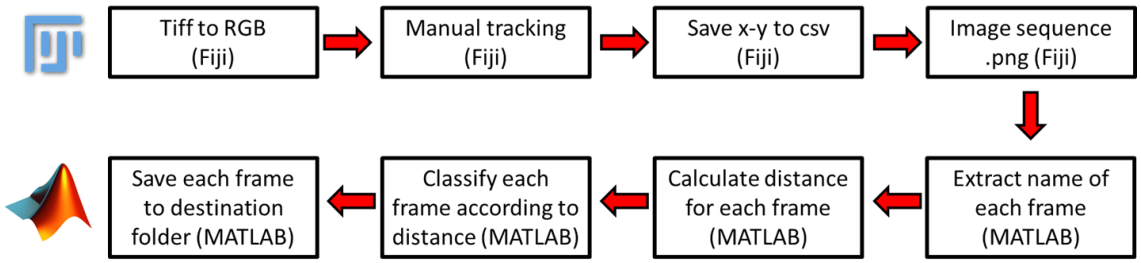

Figure 74, Diagram with the different steps of the feature extraction protocol for the distance between centrosomes

6.3.2. Image classification

The 2nd step include the preliminary analysis of the labelled data and the sorting of it in order to avoid future issues during the Neural Network training. The raw data obtained from the feature extraction provided 1609 different images classified on 22 different distance between 20 and 125 pixels, with steps of 5 pixels. The distance groups with less data were in the extremes, all below 10 images. The distribution of the raw data grouped by distance can be seen at Figure 75-A, while a table with the exact number for each is available at Figure 75-B.

A

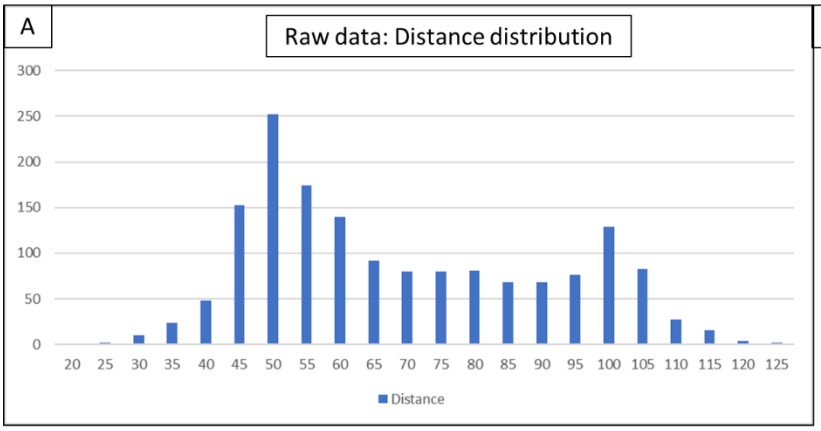

B

Distance	N° per distance
20	1
25	2
30	10
35	24
40	48
45	152
50	252
55	174
60	140
65	92
70	80
75	80
80	81
85	68
90	68
95	76
100	129
105	83
110	27
115	16
120	4
125	2
Total	1609

Figure 75, Visualization of the raw data obtained after the labelling. Graphic distribution of the number of images per distance group(A), Table with the exact number of images per distance group(B)

After checking that there was a possibility to introduce noise in the training due to the low number of images in the distance groups, 20, 25, 120 and 125 that could affect the final classification accuracy. This was because in order to learn the features of a specific group the more different images of that group the better for the algorithm to learn. In this case having all less than 4 images, it was going to be very hard for the algorithm to properly classify these types of images. Therefore, I decided to remove them from the training data set.

A

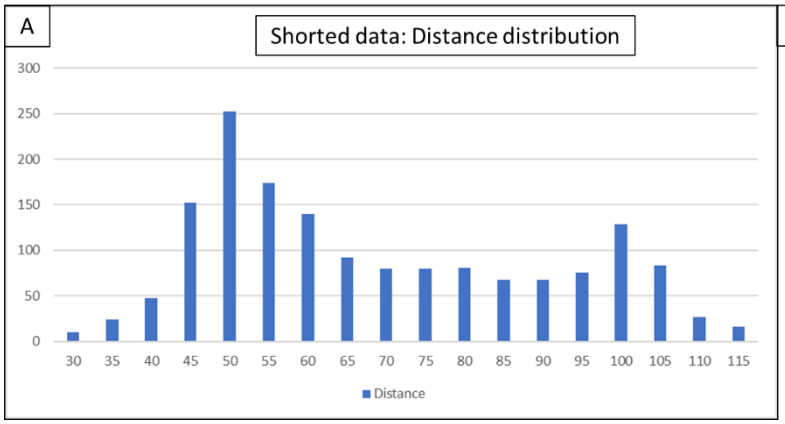

B

Distance	N° per distance
30	10
35	24
40	48
45	152
50	252
55	174
60	140
65	92
70	80
75	80
80	81
85	68
90	68
95	76
100	129
105	83
110	27
115	16
Total	1600

Figure 76, Visualization of the shorted data obtained after the image classification. Graphic distribution of the number of images per distance group(A), Table with the exact number of images per distance group(B)

I ended up with a total of 1609 images, distributed in 18 different groups, with a maximum of 252 and a minimum of 10 per distance group. The new distribution and exact number are available at Figure 76.

6.3.3. Data augmentation

Prior to start any training it was necessary to generate more data in order to have the same number of images per group so the training could be homogeneous for the algorithm. There were different options to perform this augmentation from a raw image Figure 77-A, starting from the vertical flip, Figure 77-B, and horizontal flip, Figure 77-C. These methods only provide one augmented image each while combined they generate up to four new images.

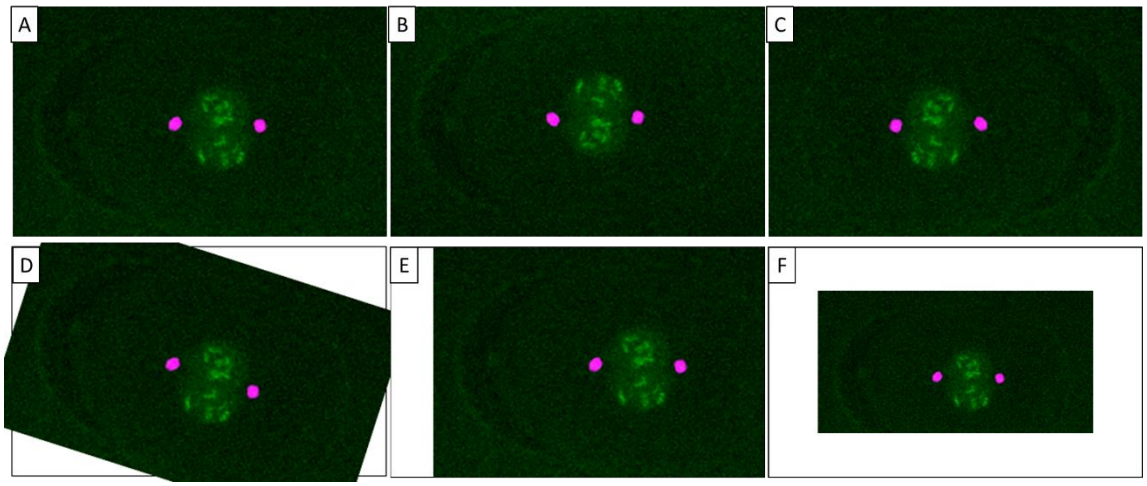

Figure 77, Example of data augmentation techniques. Raw image(A), vertical flip(B), horizontal flip(C), Rotation(D), x-y translation(E) and scaling or zooming(F)

On the other hand, image rotation provides up to 360 augmented images, one per each degree of rotation, Figure 77-D. Another option is to translate the image, Figure 77-E, in the x-y axes, but this option could remove some information for the image if the image size needed certain dimensions. As a final option it is possible to scale or zoom, Figure 77-F the image in order to have the same image but at different scale.

Among all the techniques mentioned before, I decided to use rotation as I needed to generate plenty of new images from the ones that I selected after the sorting. The target was to generate at least 3600 images per distance group for the training, which end up been a total of 64800 images, that were also resize to 520x696 pixels to have all a coming base. However, not all the distance groups required the same rotation as it can be seen at Table 26.

Distance	N° per distance	End rotation	Rotation interval
30	10	360	1
35	24	150	2
40	48	75	4
45	152	24	15
50	252	15	24
55	174	21	17
60	140	26	13
65	92	40	9
70	80	45	8
75	80	45	8
80	81	45	8
85	68	53	6
90	68	53	6
95	76	48	7
100	129	28	12
105	83	44	8
110	27	134	2
115	16	225	1

Table 26, Summary of the data augmentation using rotation settings.

The end rotation meant which was the final rotation point while the rotation interval represented the separation in degrees between each rotation. As an example, for the distance group of 30 pixels, there were 10 images that needed to be rotate 1° at a time 360 times in order to reach the 3600 images target that I mentioned before.

6.3.4. Train, valid and test split for the training

Once all the dataset distribution was homogenous, it was necessary to separate the data into different group of the training. The first separation was to segment each distance intow two groups of 1800 images, as the GPU power available at Cherry Biotech did not allow me to train sets of 3600 images at once. The second segmentation involve the separation between training and testing data sets. Taking the literature(427,428) and the diagram at Figure 78 as reference I did the following separation:

- Training dataset 90%-> 1620 images out of 1800
    - Pure training data 70%->1134 images
    - Validation data 30%-> 486 images
- Test dataset 10%-> 180 images out of 1800

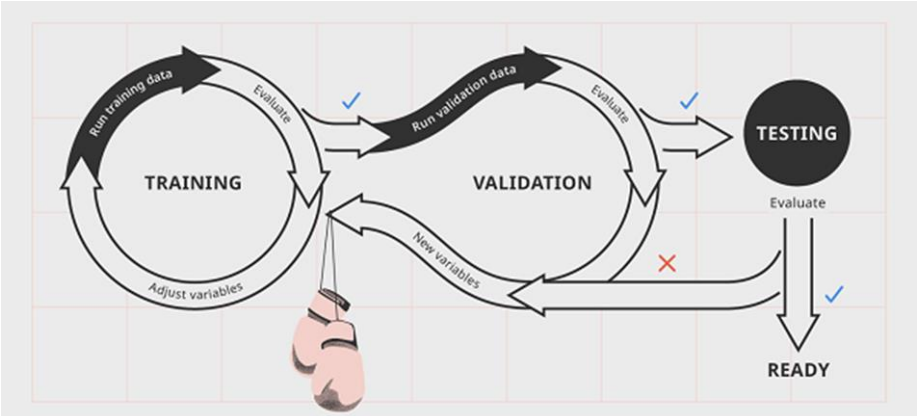

Figure 78, Diagram of the training, validation and testing cycle of a dataset using Neural Networks

This separation allowed me to perform a two-step training, allowing me to save computing time, to adjust more precisely the hyperparameters of the Convolutional Neural Network and to obtain a more stable training with available computing power at Cherry Biotech.

6.3.5. Convolutional Neural Network (CNN) algorithms

As it was mentioned in the Chapter 1, there were different generations of CNN algorithms already trained to classify images developed by AI scientists and companies such as Google or OpenAI. Therefore, I selected three different algorithms from different generations Table 27, AlexNet (2012), GoogLeNet (2014) and ResNet-101, the 101 layers version of ResNet (2015) and performed transfer learning. This process consisted on adapting an already pre-trained CNN and adapt the final 3 layers to match the desired output, in this case to classify the data between the 18 different distance groups. All this was done using the MATLAB deep learning toolbox that allowed to download the different pre-trained CNN and adapted them for the transfer learning.

Network	Depth	Size	Parameters (Millions)	Image Input Size	Developed by	Year
AlexNet	8	227 MB	61	227-by-227	Alex Krizhevsky	2012
GoogLeNet	22	27 MB	7	224-by-224	Google	2014
ResNet101	101	167 MB	44.6	224-by-224	Kaiming He	2015

Table 27, Summary of the main features of the used CNN, AlexNet, GoogLeNet and ResNet101

6.3.5.1. Key concepts for CNN training and optimizing features

Prior to explain the CNN training and the different steps performed it was necessary to define the meaning of some complex technical concepts as the following ones:

- **Mini-Batch:** hyperparameter that determines the size of a subset of the training set.
- **Iteration:** each evaluation of the gradient using a Mini-Batch at which the algorithm takes one step towards minimizing the loss function.
- **Loss/Cost function:** function to be optimized e.g. the sum of squared errors over your training set using Stochastic Gradient Descent with Momentum (SGDM)
- **Stochastic Gradient Descent with Momentum (SGDM):** method used to solve the loss function that oscillate along the path of the steepest descent towards the optimum

and it adds a momentum value to the result to get updated while decreasing the oscillation, Equation 17.

- **Epoch:** hyperparameter that covers one full pass of the training algorithm over the entire training set using Mini-Batches.
- **Learning rate**: hyperparameter that determines if a newly acquired information substitutes old information.
- **Validation frequency:** number of iterations between evaluation of the validation metrics.
- **Weight**: hyperparameters that while calculating the output of an operation the input is multiplied by a value(weight) that conditions the results. It needs to be initiated to a number different to zero to avoid dead neurons in the CNN.
- **Biases:** while calculating the output of an operation the result from the multiplication of the input and the weight is added or subtracted by a value(bias) that leads to the result.

$$\theta_{\ell+1} = \theta_\ell - \alpha \nabla E(\theta_\ell) + \gamma(\theta_\ell - \theta_{\ell-1}),$$

Equation 17, Stochastic Gradient Descent with Momentum (SGDM) equation. Iteration number(ℓ), α>0 learning rate(α>0), parameter vector(θ), loss function (E(θ)) and contribution of the previous gradient step to the current iteration(γ)

The second part covered the optimization of the training and which featured needed to be considered in order to obtain the best results as possible. The outcome from the training provide these five features plus the outcome of the test process.

- **Training time:** time for the training to be completed-> shorter as possible
- **Train max accuracy:** max value of accuracy during the training->higher as possible
- **Train loss function value:** value of the loss function during the training->lower as possible
- **Validation max accuracy:** max value of the accuracy after the training while performing the validation step->higher as possible
- **Validation loss function value:** value of the loss function after the training while performing the validation step->lower as possible
- **Test accuracy:** after both training and validation, accuracy in the classification of images in the test data set
    - **Target=90%**
    - **Ideal >95%**

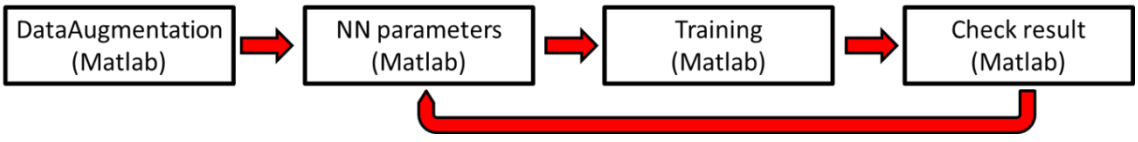

Figure 79, Convolutional Neural Network training diagram

Therefore, the training process, Figure 79, aimed to optimize these features using different settings divided in three phases. Phase #1 used the 1st dataset with the training settings #1, Table 28, to build a solid base while doing the training.

Settings #1						
Test Number	**MiniBatch Size**	**Epochs**	**Learning rate**	**Valid Frequency**	**Iterations per epoch**	**Total iterations**
trainedNet1	**48**	10	**0.001**	45	**425**	4250
trainedNet2				100		
trainedNet3		20		45		8500
trainedNet4				100		
trainedNet5		30		45		12750
trainedNet6				100		
trainedNet7		60		45		25500
trainedNet8				100		
trainedNet9		66		45		28050
trainedNet10				100		

Table 28, Summary of the training setting #1 for the training phase #1

The best trained network of this first batch in terms of validation accuracy and loss function was used for the phase #2. In this phase that CNN was re-trained with the same dataset but increasing the validation frequency, training settings #2, Table 29, to speed up the training and achieving a higher accuracy. together with the training settings #2 aiming to reach the highest validation accuracy prior to check the test accuracy. Again, the best trained CNN in terms of validation accuracy and loss function was used for the phase #3. In this final phase, the 2nd dataset was used

Settings #2						
Test Number	**MiniBatch Size**	**Epochs**	**Learning rate**	**Valid Frequency**	**Iterations per epoch**	**Total iterations**
trainedNet10	**48**	10	**0.001**	100	**425**	4250
trainedNet20				200		
trainedNet30		20		100		8500
trainedNet40				200		
trainedNet50		30		100		12750
trainedNet60				200		
trainedNet70		60		100		25500
trainedNet80				200		
trainedNet90		66		100		28050
trainedNet100				200		

Table 29, Summary of the training setting #2 for the training phase #2 & #3

6.3.5.2. Results from training with AlexNet

The best results from the training with AlexNet from the phase #1 managed to reach the values presented in Table 30. On the other hand, the evolution of the accuracy and the loss function is presented at Figure 80, able to reach 77.75% and 0.5736 respectively.

Phase #1							
Test Number	Result	Time	TrainAccuracyMax	TrainLossMin	ValidAccuracyMax	ValidationLossMin	Test Accuracy
trainedNet1	49.57%	05:25:30	60.42%	1.25	52.56%	1.3	50.34%
trainedNet2	51.65%	03:52:20	64.58%	1.15	51.65%	1.2	52.96%
trainedNet3	61.93%	16:11:10	70.83%	0.95	61.93%	1.05	62.75%
trainedNet4	57.96%	07:24:21	72.91%	0.892	60.95%	0.9592	58.64%
trainedNet5	66.68%	15:53:36	75.00%	0.8161	67.47%	0.8038	66.08%
trainedNet6	63.23%	12:05:55	72.91%	0.7891	65.59%	0.8472	63.21%
trainedNet7	74.99%	32:56:40	83.33%	0.6112	75.12%	0.6163	74.97%
trainedNet8	74.04%	23:17:06	85.42%	0.5827	75.44%	0.6137	75.03%
trainedNet9	75.67%	36:18:37	83.33%	0.5332	77.05%	0.5648	74.85%
trainedNet10	76.50%	24:45:45	85.41%	0.5717	76.49%	0.5736	77.75%

Table 30, Results from the phase #1 training with AlexNet

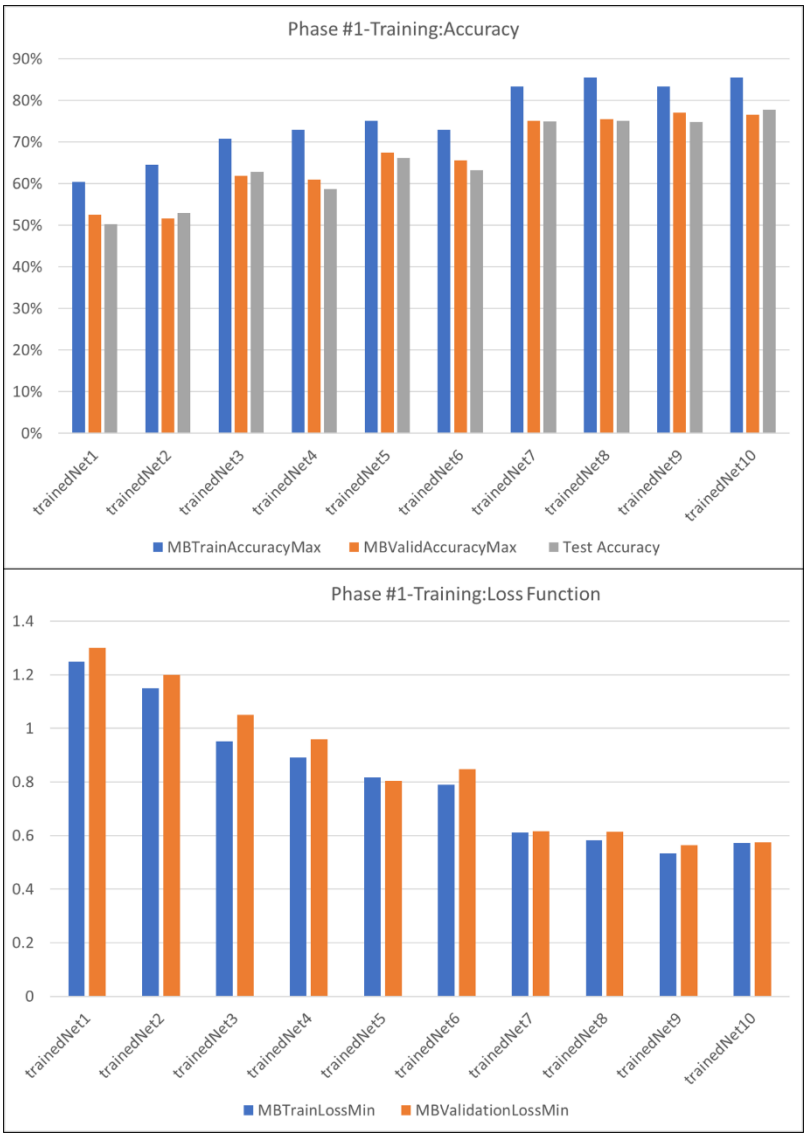

Figure 80, Graphic representation of the phase #1 training with AlexNet. Results of the training in terms of accuracy (Upper part) and results in terms of loss function value (lower part)

Phase #2							
Test Number	Result	Time	TrainAccuracyMax	TrainLossMin	ValidAccuracyMax	ValidationLossMin	Test Accuracy
trainedNet10	75.90%	00:59:43	85.41%	0.5532	77.09%	0.564	77.31%
trainedNet20	75.34%	00:49:05	85.41%	0.5035	77.51%	0.546	76.23%
trainedNet30	75.38%	01:58:38	89.58%	0.502	79.30%	0.509	75.56%
trainedNet40	77.77%	01:45:46	85.41%	0.4974	78.39%	0.5236	78.55%
trainedNet50	77.51%	03:18:16	91.66%	0.4204	80.80%	0.4794	77.44%
trainedNet60	78.53%	02:41:14	89.58%	0.3821	80.31%	0.4846	78.86%
trainedNet70	81.37%	06:07:48	91.66%	0.3594	83.32%	0.4114	81.82%
trainedNet80	80.38%	04:51:07	93.75%	0.3203	83.32%	0.4103	80.71%
trainedNet90	82.97%	06:37:19	93.75%	0.315	83.63%	0.3995	82.77%
trainedNet100	82.24%	05:58:22	91.66%	0.3477	84.37%	0.3907	83.78%

Table 31, Results from the phase #2 training with AlexNet

For the phase #2, I used trainedNet10 which was the best one from phase #1 and applied the settings #2 in the same dataset. Table 31 showed the obtained results while the evolution of the training in terms of accuracy and loss function is available at Figure 81, where trainedNet100 managed to reach max value of accuracy of 83.78% with a loss function value of 0.3907 in its lowest.

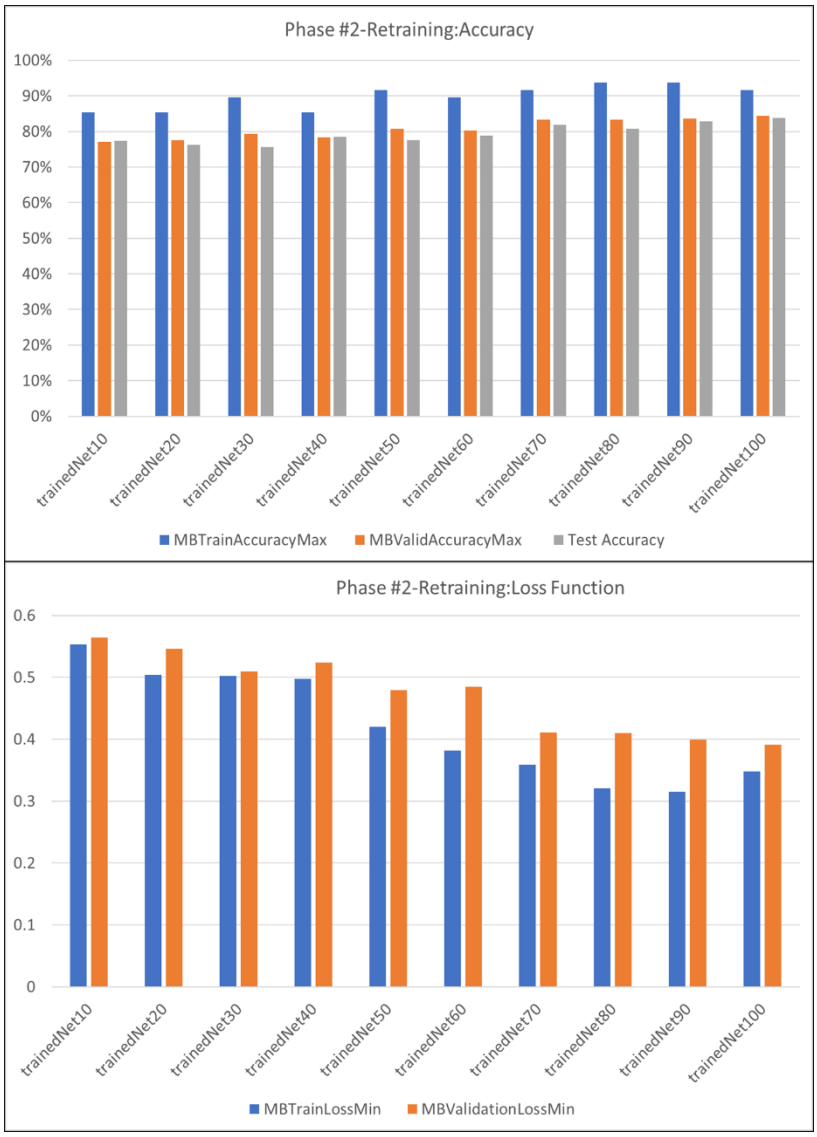

Figure 81, Graphic representation of the phase #2 training with AlexNet. Results of the training in terms of accuracy (Upper part) and results in terms of loss function value (lower part)

Finally, using the trainedNet100 from phase #2, I applied the settings #2 for the phase #3 on the 2nd dataset and obtained the results Table 32.The evolution of the training in terms of accuracy and loss function is available at Figure 82 where trainedNet1001 managed to reach max value of accuracy of 87.03% with a loss function value of 0.3057 in its lowest. Nevertheless, this was not enough taking the previously mentioned target of 90% accuracy.

Phase #3							
Test Number	Result	Time	TrainAccuracyMax	TrainLossMin	ValidAccuracyMax	ValidationLossMin	Test Accuracy
trainedNet101	84.09%	01:02:24	89.58%	0.3472	84.08%	0.3941	85.33%
trainedNet201	83.41%	00:55:50	89.58%	0.3036	84.01%	0.4024	83.79%
trainedNet301	84.02%	01:59:39	91.66%	0.3439	85.68%	0.367	84.53%
trainedNet401	84.88%	01:45:33	93.75%	0.3287	84.87%	0.3797	85.55%
trainedNet501	83.84%	03:14:38	93.75%	0.2887	85.29%	0.3651	84.96%
trainedNet601	84.39%	02:42:36	95.83%	0.2982	85.41%	0.3677	85.18%
trainedNet701	83.02%	07:02:30	97.91%	0.2	87.46%	0.3116	85.06%
trainedNet801	85.56%	05:00:04	93.75%	0.2766	86.19%	0.3442	86.48%
trainedNet901	86.31%	07:40:55	93.75%	0.3023	87.89%	0.3087	86.91%
trainedNet1001	86.88%	05:43:12	93.75%	0.2857	86.96%	0.3057	87.03%

Table 32, Results from the phase #3 training with AlexNet

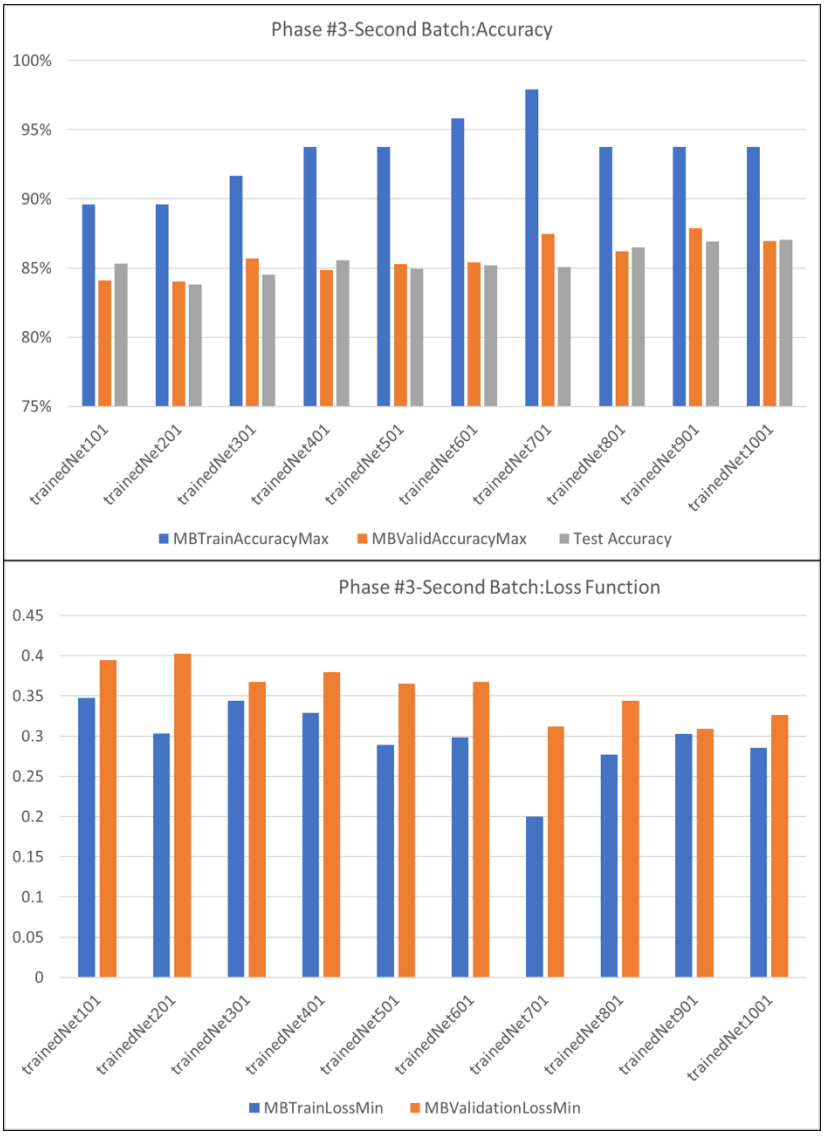

Figure 82, Graphic representation of the phase #3 training with AlexNet. Results of the training in terms of accuracy (Upper part) and results in terms of loss function value (lower part)

6.3.5.3. Results from training with GoogLeNet

The 2nd CNN used was GoogLeNet and the results from the phase #1, training on the 1st dataset with the settings #1. The results of the training were summarized at Table 33. On the other hand, the evolution of the accuracy and the loss function is presented at Figure 83, able to reach 86.2% and 0.272 respectively.

Phase #1							
Test Number	Result	Time	TrainAccuracyMax	TrainLossMin	ValidAccuracyMax	ValidationLossMin	Test Accuracy
trainedNet1	63.34%	02:19:50	72.92%	0.85	63.34%	0.8	64.57%
trainedNet2	57.52%	01:33:58	68.75%	0.8	63.12%	0.74	58.73%
trainedNet3	73.27%	04:38:16	79.17%	0.73	73.27%	0.62	75.15%
trainedNet4	72.03%	03:07:39	79.17%	0.695	72.43%	0.596	74.23%
trainedNet5	76.90%	07:02:28	83.33%	0.54	78.81%	0.43	77.19%
trainedNet6	76.49%	04:45:22	85.42%	0.52	78.36%	0.39	76.85%
trainedNet7	85.04%	14:32:37	89.58%	0.45	87.48%	0.37	85.52%
trainedNet8	80.51%	10:02:05	95.83%	0.3388	87.64%	0.2991	80.99%
trainedNet9	85.27%	16:42:07	91.66%	0.3591	88.28%	0.277	86.02%
trainedNet10	85.86%	11:18:05	93.75%	0.3094	88.43%	0.2722	86.20%

Table 33, Results from the phase #1 training with GoogLeNet

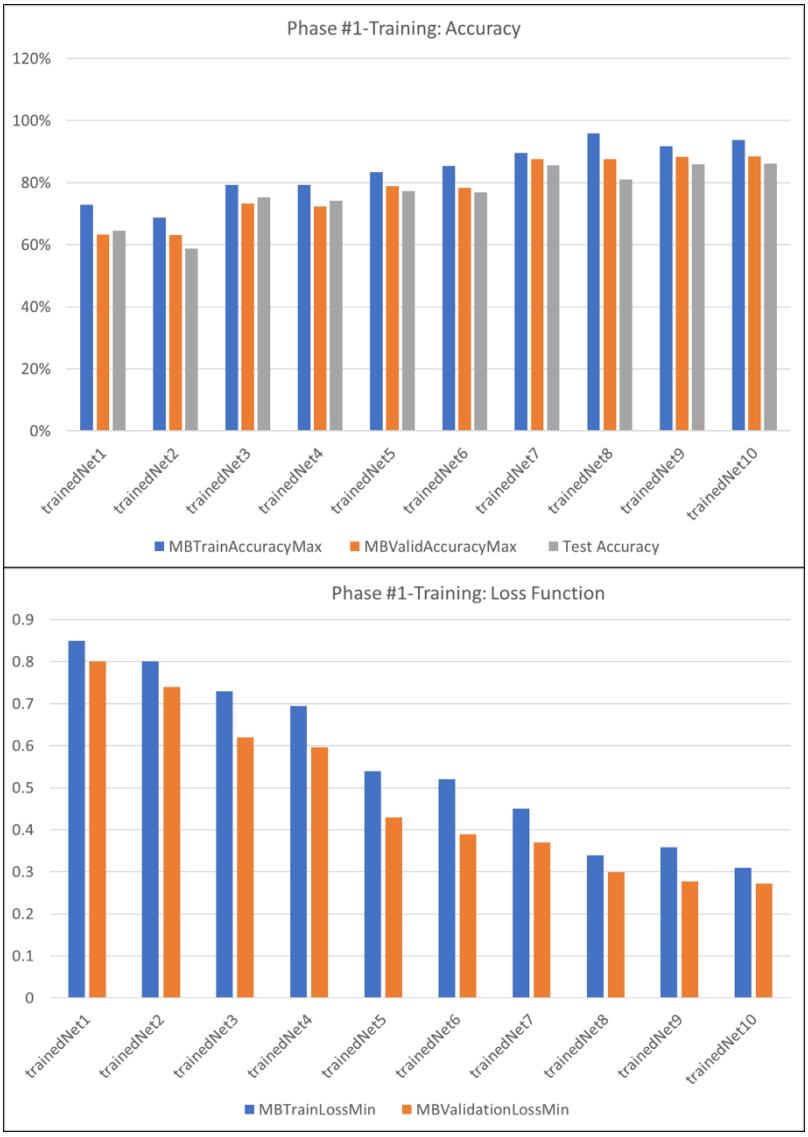

Figure 83, Graphic representation of the phase #1 training with GoogLeNet. Results of the training in terms of accuracy (Upper part) and results in terms of loss function value (lower part)

For the phase #2, I used trainedNet10 which was the trained network with best results from phase #1 and applied the settings #2 in the 1st dataset. Table 34 showed the obtained results while the evolution of the training in terms of accuracy and loss function is available at Figure 84, where trainedNet100 managed to reach max value of accuracy of 93.52% with a loss function value of 0.1392 in its lowest

Phase #2							
Test Number	Result	Time	TrainAccuracyMax	TrainLossMin	ValidAccuracyMax	ValidationLossMin	Test Accuracy
trainedNet10	90.59%	01:34:30	95.83%	0.3251	90.59%	0.2365	89.44%
trainedNet20	88.23%	01:17:47	93.75%	0.3335	89.19%	0.2613	87.10%
trainedNet30	90.56%	03:03:41	95.83%	0.1781	91.88%	0.2052	90.25%
trainedNet40	91.82%	02:34:51	93.75%	0.2677	91.81%	0.2015	91.48%
trainedNet50	89.92%	04:41:21	97.91%	0.2172	92.27%	0.1805	89.01%
trainedNet60	91.07%	03:55:02	93.75%	0.2308	92.26%	0.1906	90.34%
trainedNet70	93.52%	09:19:39	97.91%	0.1475	93.99%	0.1495	93.02%
trainedNet80	94.22%	07:41:28	97.90%	0.1534	94.21%	0.1429	93.02%
trainedNet90	93.90%	10:25:49	97.91%	0.1843	94.36%	0.1391	93.40%
trainedNet100	93.51%	08:43:27	97.91%	0.1705	94.29%	0.1392	93.52%

Table 34, Results from the phase #2 training with GoogLeNet

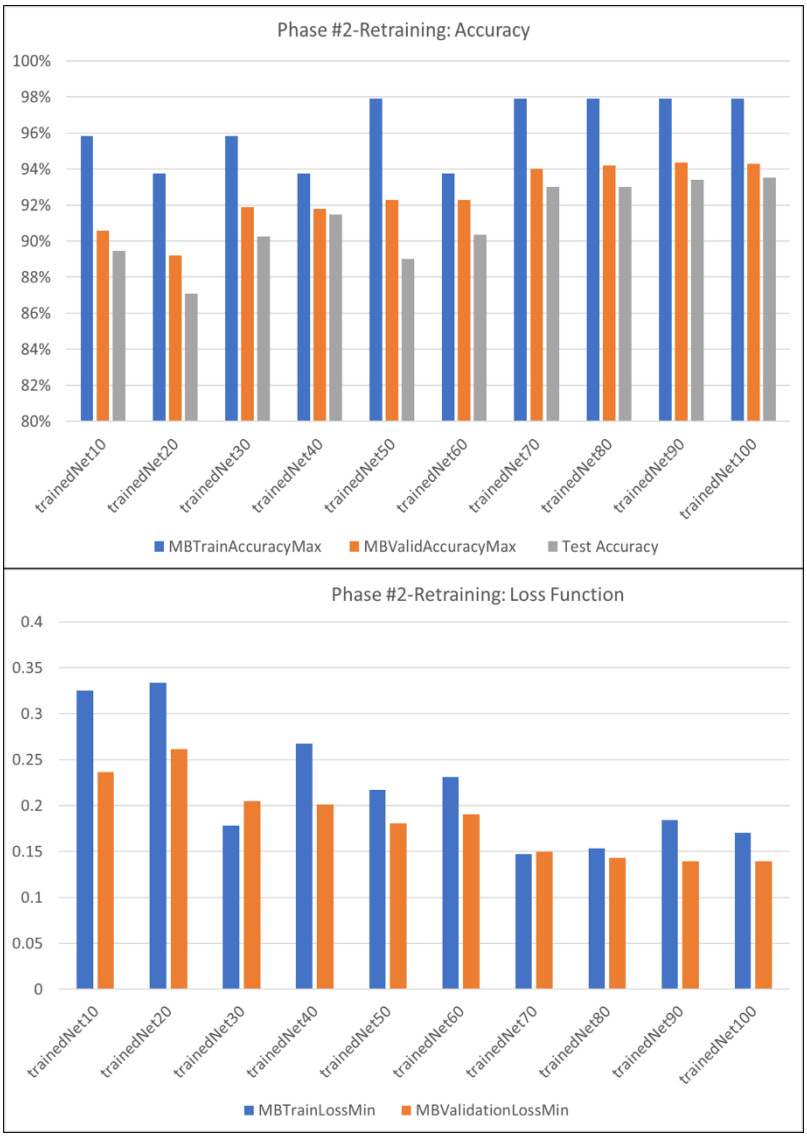

Figure 84, Graphic representation of the phase #2 training with GoogLeNet. Results of the training in terms of accuracy (Upper part) and results in terms of loss function value (lower part)

For the final phase #3, I took trainedNet100 from phase #2, I applied the settings #2 for the phase #3 on the 2nd dataset and managed to reached the target as it can be seen in Table 35. The evolution of the training in terms of accuracy and loss function is available at Figure 85 where trainedNet1001 managed to reach max value of accuracy of 96.11% with a loss function value of 0.09 in its lowest. This was so far the only trained CNN able to reach the ideal target of >95%.

Phase #3							
Test Number	Result	Time	TrainAccuracyMax	TrainLossMin	ValidAccuracyMax	ValidationLossMin	Test Accuracy
trainedNet101	92.07%	01:38:16	95.83%	0.1833	94.38%	0.1433	92.09%
trainedNet201	93.52%	01:21:33	95.83%	0.148	94.59%	0.1361	93.08%
trainedNet301	93.02%	03:09:57	95.83%	0.1662	95.10%	0.1229	93.45%
trainedNet401	94.55%	02:39:46	97.91%	0.1693	94.76%	0.1319	94.75%
trainedNet501	93.13%	04:46:17	97.91%	0.1399	95.23%	0.1234	93.14%
trainedNet601	94.57%	03:56:23	97.91%	0.1171	94.98%	0.1234	94.75%
trainedNet701	96.11%	09:49:36	100.00%	0.1106	96.11%	0.099	96.05%
trainedNet801	95.37%	07:54:20	97.91%	0.1141	96.05%	0.1015	95.74%
trainedNet901	95.88%	10:42:58	97.91%	0.0887	95.88%	0.1037	95.74%
trainedNet1001	95.99%	08:52:38	100.00%	0.0796	96.39%	0.0945	96.11%

Table 35, Results from the phase #3 training with GoogLeNet

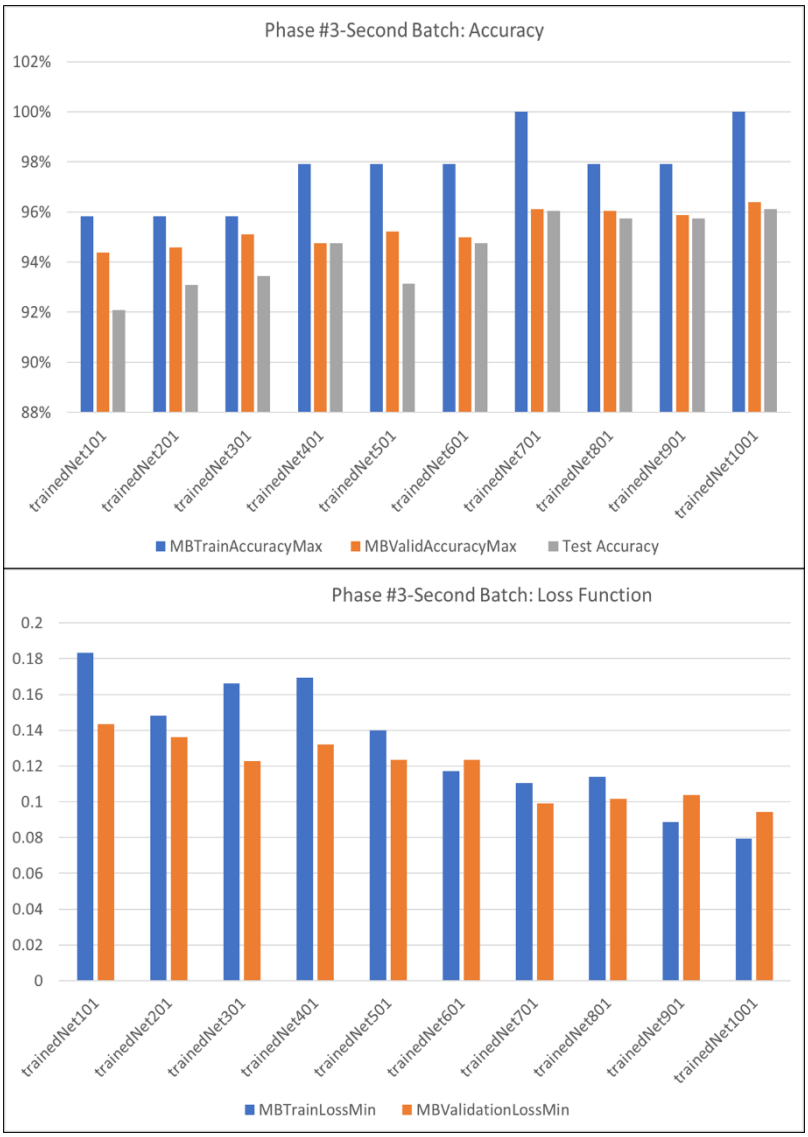

Figure 85, Graphic representation of the phase #3 training with GoogLeNet. Results of the training in terms of accuracy (Upper part) and results in terms of loss function value (lower part)

6.3.5.4. Results from training with ResNet-101

The 3rd CNN used was ResNet-101, the 101 layers version of ResNet and the results from the phase #1, training on the 1st dataset with the settings #1 were not the expected ones. The computing power available at Cherry Biotech did not support the 3rd iteration of the training and collapsed. The reason for this was due to the depth in layers of this CNN that saturated the memory of the GPU. I tried to compute the training in the couple using Amazon Web Services together with MATLAB cloud but the price for the computing hours and the storage data was 50€ per hour of renting. After discussing with Antoni Homs and Jeremy Cramer, we decided to stop the training of ResNet at this point. The preliminary results can be seen at Table 36 and Figure 86.

Phase #1							
Test Number	Result	Time	TrainAccuracyMax	TrainLossMin	ValidAccuracyMax	ValidationLossMin	Test Accuracy
trainedNet1	72.75%	31:29:32	100.00%	0.2103	68.91%	0.7431	72.19%
trainedNet2	70.42%	19:38:23	100.00%	0.2947	68.86%	0.7475	71.17%
trainedNet3	0.00%	00:00:00	0.00%	0	0.00%	0	0.00%
trainedNet4	0.00%	00:00:00	0.00%	0	0.00%	0	0.00%
trainedNet5	0.00%	00:00:00	0.00%	0	0.00%	0	0.00%
trainedNet6	0.00%	00:00:00	0.00%	0	0.00%	0	0.00%
trainedNet7	0.00%	00:00:00	0.00%	0	0.00%	0	0.00%
trainedNet8	0.00%	00:00:00	0.00%	0	0.00%	0	0.00%
trainedNet9	0.00%	00:00:00	0.00%	0	0.00%	0	0.00%
trainedNet10	0.00%	00:00:00	0.00%	0	0.00%	0	0.00%

Table 36, Results from the phase #1 training with ResNet-101

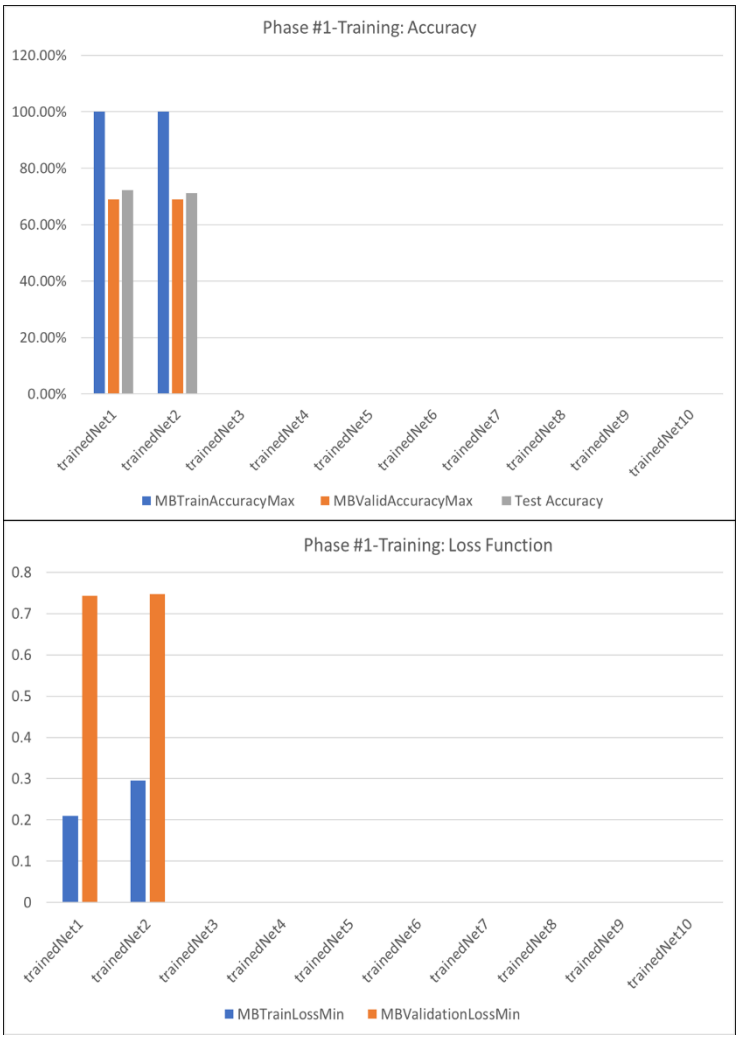

Figure 86, Graphic representation of the phase #1 training with ResNet-101. Results of the training in terms of accuracy (Upper part) and results in terms of loss function value (lower part)

6.3.5.5. Conclusion from the CNN algorithms training

Each of the trained CNN algorithms presented a challenge as it was necessary to make some modifications in the code in MATLAB in order to make them work with used datasets.

6.3.5.5.1. Conclusion from the AlexNet algorithm training

Starting with AlexNet, the main requirements from this network was that the image input needed to be 227x227 pixels and that the outcome needed to be changes to the new 18 distance categories. The used hardware for this training was an Asus laptop (AsusTeK Computer, Inc. Taiwan) R558U model with an Intel(R) Core™ i5-6200 CPU @ 2.30 GHz-2.40 GHz, with 8 GB of RAM. The operating system was a Windows 10, 64-bits. The GPU used for the training was a GeForce 920MX from Nvidia (Nvidia Corporation, USA). The key values from the recap from the training with AlexNet were the following:

Phase #1
- **Total training time:** 153 hours and 25 minutes
- **Maximum Test accuracy achieved:** 77.75%
- **Minimum loss function value:** 0.5648

Phase #2
- **Total training time:** 29 hours and 8 minutes
- **Maximum Test accuracy achieved:** 83.78%
- **Minimum loss function value:** 0.3907

Phase #3
- **Total training time:** 31 hours and 24 minutes
- **Maximum Test accuracy achieved:** 87.03%
- **Minimum loss function value:** 0.3057

As a conclusion, the training using AlexNet did not reach the target of 90%, that due to the deadline contains I decided to stop the training. Nevertheless, this training process allowed me to optimize the MATLAB code to be optimum during the data saving process after the training.

6.3.5.5.2. Conclusion from the GoogLeNet algorithm training

Following with the GoogLeNet, hardware used for the training of this CNN was an assembly tower computer by Cooler Master, Co. Ltd, Taiwan. It had an Intel(R) Core™ i7-4790 CPU @ 3.60 GHz-3.60 GHz, with 8 GB of RAM. The operating system was a Windows 10, 64-bits while the GPU used for the training was a GeForce GTX 1050 Ti from Nvidia (Nvidia Corporation, USA). The only adaptations required for this CNN were to re-scale the input images to 224x224 pixels in order to fit with the image classification and to adapt the output to 18 distances groups. As it was presented with the previous CNN, the key values from the training were the following ones:

Phase #1

- **Total training time:** 63 hours and 44 minutes
- **Maximum Test accuracy achieved:** 86.20%
- **Minimum loss function value:** 0.272

Phase #2

- **Total training time:** 44 hours and 34 minutes
- **Maximum Test accuracy achieved:** 93.52%
- **Minimum loss function value:** 0.1391

Phase #3

- **Total training time:** 45 hours and 59 minutes
- **Maximum Test accuracy achieved:** 96.11%
- **Minimum loss function value:** 0.09

In order to conclude, the training using GoogLeNet achieved both the initial target of 90% and the ideal one of >95%, reaching 96.11%. This score makes it this algorithm the ideal one to be introduced in the standalone application prior to the final deployment.

6.3.5.5.3. Conclusion from the ResNet-101 algorithm training

Finally, for the training of the ResNet-101 the hardware was the one used for the training of the GoogLeNet. The input and output adjustments were the same, 224x224 and 18 as the ones performed for the GoogLeNet algorithm. As it could have been in the results part, due to the lack of computational power I was not able to complete the full training with this CNN, therefore the maximum values obtained did not reach the targeted threshold, therefore I discard this one.

6.3.6. Algorithm deployment: build standalone application

Once the training was finished and the results from the different algorithms compared, I decided to implement the trainedNet1001 from GoogLeNet inside the standalone application built using MATLAB app designer toolbox from the 2019a release following the AGILE methodology for software development, following the Figure 87. This methodology was first mentioned by Dr William Royce in 1970 as a perfect example of how to manage and develop large software systems(429).

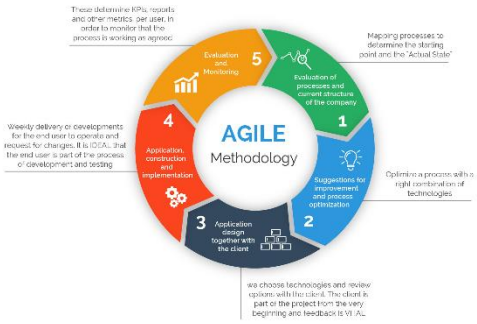

Figure 87, Scheme of the Agile methodology for software development

The basis was that a software need to be developed like a product on an assembly line. Each of the steps need to be completed before moving to the next one but before the developers needed to have all the requirements prior to start the process. Then the architecture and the designs, followed by the code followed with iterations with the end-user.

In this case, I got the main requirements from Dr. J. Dumont during a meeting in January and from that I developed all the User Interface as it can be seen at Figure 88. This was the version 1.0, but it will change once I will get the feedback from the final user after the meeting in September 2019.

The user guide for this version 1.0, it is available at the Annex #4-Distance extraction app UI.

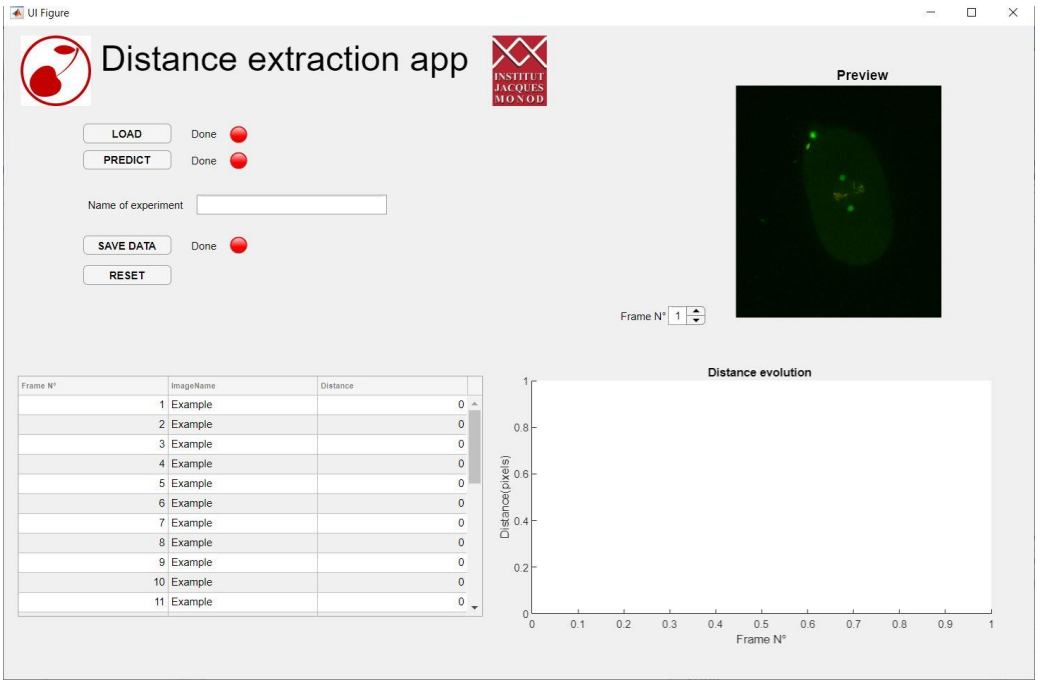

Figure 88, Main view of the standalone application for the image classification and the distance extraction built using MATLAB app designer

6.4. Conclusion from the AI proof-of-concept

As a conclusion for this chapter, I can say that I managed to develop a full AI project from 0 to 1. Starting from the feature extraction of the raw data, followed by the sorting and classification, to the training and final deployment application. This project is not close at all as once the final user get to use it and start to generate feedback it will evolve but for what concerns this PhD thesis, the project is closed.

From the part of Cherry Biotech AI department, this is not only the first step into the AI field but a clear proof-of-concept that with the actual resources, technical and personal, we are able to build tools that could help researchers or to be included inside the Cubix as an additional feature, combined with the image acquisition and the signal processing.

Chapter 7, Discussion of the Thesis

Inside the discussion chapter I would cover all the different results presented and compare the expectations with the actual results.

The results of the dry configuration characterization in Chapter 2 showed that it was possible to quantify the impact of the room temperature (on top of the microscope and at the infinite) and the one of the stage on the sample temperature. The relationship between the sample temperature and the room temperature is simpler than expected in view of the complexity of phenomena involved. These results also proved that the T_{is} relationship with the T_p was direct. This was because if the T_p was below the room or stage temperatures the T_{is} was negative and then turned positive as the T_p overcome the two factors temperature.

This direct relationship was not present in the immersion configuration characterization where more complex factors were impacting the sample temperature. In this setup the heat-sink play a big role as the thermal-bridge between the sample coverslip, the immersion liquid (oil or water) and the objective could be altered by many different factors. The one that had a bigger impact was the type of immersion liquid as the heat capacity of each liquid change completely the capability of the thermal bridge to transfer the thermal energy.

On a second level the most impactful parameters were the distance between the sample and the objective, what I called Z-distance and the shape of the objective tip. These two together modified the thermal bridge generating a different heat-sink at a time. It can be counterbalance knowing which could be the maximum distance that could really impact the sample temperature, e.g. for the sharp tip objective it was from 0µm to -20µm with a T_{is} difference of +1.33°C while for the flat tip objective was between -20µm and -50µm with a difference of -0.47°C in the T_{is}.

On a third level, there was objective temperature that did not show any direct relationship that could be quantified as at the end the impact of the heat-sink was driving its temperature. Nevertheless, for the calibration if the temperature of the objective could be properly monitored and the other parameters controlled the heat-sink could be monitored using it as reference.

As a recap, the temperature of the room did not directly impact in the temperature of the sample, but it could in the cases of extreme temperatures (+30°C or <18°C) or very fast temperature changes. In that circumstances the equilibrium of the hat-sink between the objective, the immersion liquid and the sample coverslip could be altered for a fraction of time until reaching a new equilibrium.

As continuation, this knowledge could be directly applied expanding the way the CherryTemp systems controls the temperature of the sample. At the moment, it uses one feedback loop, monitoring the ambient temperature (dry configuration) or the objective temperature (immersion configuration) but it could be possible to add a second one monitoring the stage temperature or the temperature of the sample introducing a JT-sensor but modifying the actual ThermaChip. All these ideas were proposed and are been considered by the R&D team of Cherry Biotech.

The results presented at the Chapter 4, the ones related with the calibration of the different microfluidic devices showed how relevant was the characterization made at Chapter 2. The reason of this was that knowing the impact that the different parameters could make on the sample temperature helped into the building of the calibration for each specific developed device. However, there was room to improve that calibration by integrating a temperature sensor on the microfluidic device in order to monitor the temperature very close to the sample, but this would complicate the industrialization of the device later-on. For the moment, the presented calibration method was able to thermalize the sample with an accuracy of +/-0.3°C.

In terms of design, conception and manufacturing process of the different microfluidic devices, it followed the Agile methodology. The reason for this was that as an industrial PhD and been in a start-up I needed to use this type of methodology in order to deliver a finalized device as fast as possible to the end-user. The presented devices come after several discussions with the different collaborators because they were parts of the conception, as their inputs were vital in the design decision process. Finally, the implementation aimed to reduce to the maximum the possible frictions regarding the usability of the different devices.

Nevertheless, the results of the biological validation demonstrated that the different devices were able to deliver the features for what they were conceived. The yeast model end-up been the most used device as the team of Prof. Erfei Bi in Philadelphia had been using this device for more than 2 years. All the suggestions made by them during the different stages of the development end up been useful to ease their usability and allow them to generate robust results with straight-forward protocols.

The mammalian model validation was complicated as it was necessary to develop a protocol for the seeding of the cells that end-up been useful but not the best solution. The reason for this was that on a later project inside the R&D team at Cherry Biotech, the Therma35 was developed. This was a thermalization chip made to fit on 35mm petri-dish, which for mammalian cells was the perfect solution because most of the seeding protocols were already adapted for this culture dish. On the other hand, the possibility to observe two different phenotypes in the case of the temperature and STLC experimentation, highlight that this device was able to provide biologically relevant data. However, further investigation will be needed to decipher the exact mechanism behind this result.

The spheroids project was a complete challenge as it included the use of a new material, CoP that required a new thermal calibration, the adaptation of the manufacturing process and a modification of the seeding protocol compared with the initial idea of the project. Anyway, the results validate the projects objective and open a collaboration partnership with the team of Dr. Yanncik Arlot. The knowledge regarding 3D cell culture will fit perfectly with the development of Cubix, which is new platform developed by the R&D team of Cherry Biotech, aiming to control the full environment of any biological model while doing image acquisition and processing. The adaptation of microfluidic device for 3D cell culture that could fit with the Cubix it will be possible using the knowledge (design, materials and protocols) generated during the SpOC project.

The *in vitro* model adaptation was a success from the protocol point of view, as we, Jijumon A.S. and me, figure it using our combined experience on microfluidics and *in vitro* experimentation. The only drawback was that in order to generate enough data to

present it here, Jijumon needed at least 6 more months starting from May 2019, therefore they were not included here. However, it has been considered that the new device could allow them to continue a set of experiments that before was not possible and to open new research paths such as the screening of different MAPs with different MTs strains, in order to quantify the affinity of the MAPs.

Results for the CubiX heating stage cannot be presented here for the same reasons as biological validation are currently ongoing. This project allowed me to apply all the knowledge generated from the thermal characterization and the different microfluidics calibration for a combine device, to work with very tight deadline and to deal with supplier to deliver the final version of the temperature controller.

Finally, regarding the proof-of-concept combining Artificial intelligence for image classification, the results could be analysed regarding the different steps: data labelling, data shorting, algorithm training and application building.

The key output from the data labelling step was that I developed protocol to extract the distance between the centrosome on a standard way. It was the most efficient solution as it was fast, simple and clean as I managed to label 1609 images in 9h. Then the data shorting step end up saving a lot of time as the distribution between the 18 different distance group was more uniform after removing the 4 groups that had less than 2 images per set. This step was critical because the dataset of 1609 images first and then 1600 was relatively small but in the next iteration of the development I assumed that the team of Dr. J. Dumont could easily provide 2 or 3 times that number of images. This collaboration allowed Cherry Biotech to make the first steps towards the AI that would be used in the Cubix in order to manage different types of data (imaging, genomics and proteomics) for the assessment and why not discovery of different phenotypes while culturing the samples.

Chapter 8, Conclusion

As a final conclusion, I would like summary all the knowledge, experience and skills that I got from this Industrial PhD.

From the technical point of view and the research performed at the R&D team of Cherry Biotech, I learn how to be innovative while developing a strong technical base. I learnt from my supervisor, Dr. Jeremy Cramer, how important is the temperature control while doing live-cell imaging. He also showed me how microfluidics combined with electronics can support the microscopy to obtain robust and reliable results while having a very accurate and stable temperature control.

From the scientific point of view, all the experimentation performed at the different laboratories, but especially the ones performed at the CRG with my supervisor Prof. Isabelle Vernos, helped to understand the reasoning behind the scientific mindset and how important is to be structured, with a clear hypothesis to be validated or not, before starting any experiment. This learning process allowed me to expand my mindset and to be more critic with myself while organizing my experiments in order to obtain the best from them while understanding the results.

From the entrepreneurship point of view, I got the chance to make the Industrial PhD on a growing start-up, while doing research. I learnt a lot from my work colleagues, especially about team building and communication but also how important is to have clear goals and a clear organisation. I got the chance to collaborate with all the departments inside the company which helped me to have a global view and to understand the big picture. All the skills that I gain during these three years allowed me to growth both personally and professionally, to become a more complete person. These was possible thanks to the culture of the Cherry Biotech that embrace the individual to get the best version of itself while been a key player for the team. Everyone is important for the team while the team needs the best version of everyone.

As final conclusion, these experience closes a journey of three years where I learnt everyday many things from science to communication passing from team building or even management, while I was building new entrepreneurial and scientific mindset of doing applied research to bring new products to the market and improve experience of the final end-user.

Bibliography

1. Frigault MM, Lacoste J, Swift JL, Brown CM. Live-cell microscopy - tips and tools. J Cell Sci [Internet]. 2009 Mar 15 [cited 2018 Nov 6];122(Pt 6):753–67. Available from: http://www.ncbi.nlm.nih.gov/pubmed/19261845
2. Wang Y, Shyy JY-J, Chien S. Fluorescence Proteins, Live-Cell Imaging, and Mechanobiology: Seeing Is Believing. Annu Rev Biomed Eng [Internet]. 2008 Aug [cited 2018 Nov 6];10(1):1–38. Available from: http://www.annualreviews.org/doi/10.1146/annurev.bioeng.010308.161731
3. Chyan WPDMI of T. Fluorogenic probes for live-cell imaging of biomolecules. 2018 [cited 2018 Nov 6]; Available from: https://dspace.mit.edu/handle/1721.1/118216
4. Specht EA, Braselmann E, Palmer AE. A Critical and Comparative Review of Fluorescent Tools for Live-Cell Imaging. Annu Rev Physiol [Internet]. 2016 Feb 10 [cited 2018 Nov 6];79(1):93–117. Available from: http://www.annualreviews.org/doi/10.1146/annurev-physiol-022516-034055
5. Thorn K. A quick guide to light microscopy in cell biology. Mol Biol Cell [Internet]. 2016 Jan 15 [cited 2018 Nov 13];27(2):219–22. Available from: http://www.ncbi.nlm.nih.gov/pubmed/26768859
6. Bright-Field Microscopy [Internet]. 2009 [cited 2019 Mar 18]. Available from: http://www.ipfdd.de/fileadmin/user_upload/nm/stamm/Praktikum/8_Light_Microscopy.pdf
7. Walker-Daniels J. Live Cell Imaging Methods Review. Mater Methods [Internet]. 2012 Jul 23 [cited 2018 Nov 13];2. Available from: http://www.labome.com/method/Live-Cell-Imaging-Methods-Review.html
8. McCann T. Live Cell Imaging: An Industrial Perspective. In: Methods in molecular biology (Clifton, NJ) [Internet]. 2010 [cited 2018 Nov 13]. p. 47–66. Available from: http://www.ncbi.nlm.nih.gov/pubmed/19957123
9. Ettinger A, Wittmann T. Fluorescence live cell imaging. Methods Cell Biol [Internet]. 2014 [cited 2018 Nov 13];123:77–94. Available from: http://www.ncbi.nlm.nih.gov/pubmed/24974023
10. Xia Y, Petti C, Williams MA, DeBolt S. Experimental approaches to study plant cell walls during plant-microbe interactions. Front Plant Sci [Internet]. 2014 Oct 14 [cited 2018 Nov 16];5:540. Available from: http://journal.frontiersin.org/article/10.3389/fpls.2014.00540/abstract
11. Bright Field Microscopy. In: Biomedical Image Analysis Recipes in MATLAB® [Internet]. Chichester, UK: John Wiley & Sons, Ltd; 2015 [cited 2018 Nov 16]. p. 215–89. Available from: http://doi.wiley.com/10.1002/9781118657546.ch6
12. Trimby PW, Prior DJ. Microstructural imaging techniques: a comparison between light and scanning electron microscopy. Tectonophysics [Internet]. 1999 Mar 15 [cited 2018 Nov 16];303(1–4):71–81. Available from: https://www.sciencedirect.com/science/article/pii/S0040195198002637
13. Drey LL, Graber MC, Bieschke J. Counting unstained, confluent cells by modified bright-field microscopy. Biotechniques [Internet]. 2013 Jul [cited 2019 Mar 18];55(1):28–33. Available from: http://www.ncbi.nlm.nih.gov/pubmed/23834382
14. Salinas J, Sánchez-Serrano JJ. Arabidopsis protocols [Internet]. Humana Press; 2006 [cited 2019 Mar 18]. 469 p. Available from: https://books.google.fr/books?id=TnDH-UvwhTAC&pg=PA271&lpg=PA271&dq=brightfield+microscopy+pigmentation+addition+protocol&source=bl&ots=vB8HnqFXit&sig=ACfU3U0RszIXhMKNi6kQu-ZR8l-Ubim6cg&hl=en&sa=X&ved=2ahUKEwju2M3iuovhAhVDxxoKHQOlBrcQ6AEwDHoECAEQAQ#v=onepage&q=brightfield microscopy pigmentation addition protocol&f=false
15. Chen E, Guo T. Modified Köhler illumination for LED-based projection display. Displays [Internet]. 2014 Apr 1 [cited 2018 Nov 14];35(2):84–9. Available from: https://www.sciencedirect.com/science/article/pii/S0141938214000183
16. Attota RK. Step beyond Kohler illumination analysis for far-field quantitative imaging: angular illumination asymmetry (ANILAS) maps. Opt Express [Internet]. 2016 Oct 3 [cited 2018 Nov 13];24(20):22616. Available from: https://www.osapublishing.org/abstract.cfm?URI=oe-24-20-22616
17. BENNER G, PROBST W. Köhler illumination in the TEM: Fundamentals and advantages. J Microsc [Internet]. 1994 Jun 1 [cited 2018 Nov 13];174(3):133–42. Available from: http://doi.wiley.com/10.1111/j.1365-2818.1994.tb03461.x
18. Bagnell © C Robert. Chapter 8 Bright Field Types of Specimens for Bright Field

Microscopy [Internet]. [cited 2019 Mar 18]. Available from: https://www.med.unc.edu/microscopy/files/2018/06/lm-ch-8-bright-field.pdf
19. Gnerucci A, Romano G, Ratto F, Centi S, Baccini M, Santosuosso U, et al. Statistical detection of nanoparticles in cells by darkfield microscopy. Phys Medica [Internet]. 2016 Jul 1 [cited 2019 Mar 18];32(7):938–43. Available from: https://www.sciencedirect.com/science/article/pii/S1120179716301193
20. Gnerucci A, Faraoni P, Romano G, Fusi F. Unstained cell imaging: Morphological insights from coupled fixation and darkfield microscopy. Acta Histochem [Internet]. 2019 Feb 1 [cited 2019 Mar 18];121(2):248–52. Available from: https://www.sciencedirect.com/science/article/pii/S0065128118302307
21. Gray P. Handbook of basic microtechnique [Internet]. 3d ed. New York: McGraw-Hill; 1964 [cited 2019 Mar 18]. Available from: https://www.worldcat.org/title/handbook-of-basic-microtechnique/oclc/250679
22. 2.3: Instruments of Microscopy - Biology LibreTexts [Internet]. [cited 2018 Nov 16]. Available from: https://bio.libretexts.org/TextMaps/Microbiology/Book%3A_Microbiology_(OpenStax)/02%3A_How_We_See_the_Invisible_World/2.3%3A_Instruments_of_Microscopy
23. Darkfield Microscopy [Internet]. [cited 2019 Mar 18]. Available from: https://www.microscopeworld.com/t-darkfield_microscopy.aspx
24. Darkfield Illumination | MicroscopyU [Internet]. [cited 2019 Mar 18]. Available from: https://www.microscopyu.com/techniques/stereomicroscopy/darkfield-illumination
25. Chen M, Tian L, Waller L. 3D differential phase contrast microscopy. Biomed Opt Express [Internet]. 2016 Oct 1 [cited 2018 Nov 16];7(10):3940. Available from: https://www.osapublishing.org/abstract.cfm?URI=boe-7-10-3940
26. Chen M, Kanade T. Detect Cells and Cellular Behaviors in Phase Contrast Microscopy Images. Med Image Recognition, Segmentation Parsing [Internet]. 2016 Jan 1 [cited 2019 Mar 18];485–514. Available from: https://www.sciencedirect.com/science/article/pii/B9780128025819000214
27. Grah JS, Harrington JA, Koh SB, Pike JA, Schreiner A, Burger M, et al. Mathematical imaging methods for mitosis analysis in live-cell phase contrast microscopy. Methods [Internet]. 2017 Feb 15 [cited 2019 Mar 18];115:91–9. Available from: https://www.sciencedirect.com/science/article/pii/S1046202317300518
28. Rohde M. Microscopy. Methods Microbiol [Internet]. 2011 Jan 1 [cited 2019 Mar 18];38:61–100. Available from: https://www.sciencedirect.com/science/article/pii/B9780123877307000048
29. Phase Contrast Microscopy - Introduction | Olympus Life Science [Internet]. [cited 2019 Mar 18]. Available from: https://www.olympus-lifescience.com/en/microscope-resource/primer/techniques/phasecontrast/phase/
30. Introduction to Phase Contrast Microscopy | MicroscopyU [Internet]. [cited 2019 Mar 18]. Available from: https://www.microscopyu.com/techniques/phase-contrast/introduction-to-phase-contrast-microscopy
31. Liu Z, Tian L, Liu S, Waller L. Real-time brightfield, darkfield, and phase contrast imaging in a light-emitting diode array microscope. J Biomed Opt [Internet]. 2014 Oct 1 [cited 2019 Mar 19];19(10):106002. Available from: http://biomedicaloptics.spiedigitallibrary.org/article.aspx?doi=10.1117/1.JBO.19.10.106002
32. Kozminski KG. Chapter 38 High-Resolution Imaging of Flagella. Methods Cell Biol [Internet]. 1995 Jan 1 [cited 2019 Mar 19];47:263–71. Available from: https://www.sciencedirect.com/science/article/pii/S0091679X08608195
33. Pluta M. Nomarski's DIC microscopy: a review. In: Pluta M, Szyjer M, editors. International Society for Optics and Photonics; 1994 [cited 2019 Mar 19]. p. 10–25. Available from: http://proceedings.spiedigitallibrary.org/proceeding.aspx?articleid=1005240
34. Differential Interference Contrast - How DIC works, Advantages and Disadvantages [Internet]. [cited 2019 Mar 19]. Available from: https://www.microscopemaster.com/differential-interference-contrast.html
35. Xia Y, Petti C, Williams MA, DeBolt S. Experimental approaches to study plant cell walls during plant-microbe interactions. Front Plant Sci [Internet]. 2014 Oct 14 [cited 2019 Mar 19];5:540. Available from: http://journal.frontiersin.org/article/10.3389/fpls.2014.00540/abstract
36. Xiomara Bautista Rozo L. Phase estimation for Differential Interference Contrast

microscopy [Internet]. [cited 2019 Mar 19]. Available from: https://tel.archives-ouvertes.fr/tel-01576339v2
37. Ishmukhametov RR, Russell AN, Wheeler RJ, Nord AL, Berry RM. A Simple low-cost device enables four epi-illumination techniques on standard light microscopes. Sci Rep [Internet]. 2016 Feb 8 [cited 2019 Mar 19];6:20729. Available from: http://www.ncbi.nlm.nih.gov/pubmed/26853732
38. Differential Interference Contrast - Comparison of Phase Contrast and DIC Microscopy | Olympus Life Science [Internet]. [cited 2019 Mar 19]. Available from: https://www.olympus-lifescience.com/en/microscope-resource/primer/techniques/dic/dicphasecomparison/
39. Koos K, Molnár J, Kelemen L, Tamás G, Horvath P. DIC image reconstruction using an energy minimization framework to visualize optical path length distribution. Sci Rep [Internet]. 2016 Sep 25 [cited 2019 Mar 19];6(1):30420. Available from: http://www.nature.com/articles/srep30420
40. Centonze Frohlich V. Phase contrast and differential interference contrast (DIC) microscopy. J Vis Exp [Internet]. 2008 Aug 6 [cited 2019 Mar 19];(17). Available from: http://www.ncbi.nlm.nih.gov/pubmed/19066508
41. M. J. Advanced-Microscopy Techniques for the Characterization of Cellulose Structure and Cellulose-Cellulase Interactions. In: Cellulose - Fundamental Aspects [Internet]. InTech; 2013 [cited 2019 Mar 20]. Available from: http://www.intechopen.com/books/cellulose-fundamental-aspects/advanced-microscopy-techniques-for-the-characterization-of-cellulose-structure-and-cellulose-cellula
42. Resolution | MicroscopyU [Internet]. [cited 2019 Mar 19]. Available from: https://www.microscopyu.com/microscopy-basics/resolution
43. Willig KI, Kellner RR, Medda R, Hein B, Jakobs S, Hell SW. Nanoscale resolution in GFP-based microscopy. Nat Methods [Internet]. 2006 Sep 1 [cited 2019 Mar 19];3(9):721–3. Available from: http://www.nature.com/articles/nmeth922
44. Klar TA, Jakobs S, Dyba M, Egner A, Hell SW. Fluorescence microscopy with diffraction resolution barrier broken by stimulated emission. Proc Natl Acad Sci U S A [Internet]. 2000 Jul 18 [cited 2019 Mar 19];97(15):8206–10. Available from: http://www.ncbi.nlm.nih.gov/pubmed/10899992
45. Waters JC. Live-Cell Fluorescence Imaging. In 2013 [cited 2019 Mar 19]. p. 125–50. Available from: https://linkinghub.elsevier.com/retrieve/pii/B9780124077614000063
46. Ettinger A, Wittmann T. Fluorescence live cell imaging. In: Methods in cell biology [Internet]. 2014 [cited 2019 Mar 19]. p. 77–94. Available from: http://www.ncbi.nlm.nih.gov/pubmed/24974023
47. So S, Kim M, Lee D, Nguyen DM, Rho J. Overcoming diffraction limit: From microscopy to nanoscopy. Appl Spectrosc Rev [Internet]. 2018 Apr 21 [cited 2019 Jun 11];53(2–4):290–312. Available from: https://www.tandfonline.com/doi/full/10.1080/05704928.2017.1323309
48. Thorn K. A quick guide to light microscopy in cell biology. Mol Biol Cell [Internet]. 2016 Jan 15 [cited 2019 Jun 11];27(2):219–22. Available from: http://www.ncbi.nlm.nih.gov/pubmed/26768859
49. Aswani K, Jinadasa T, Brown CM. Fluorescence Microscopy Light Sources. 2012 [cited 2019 Mar 20]; Available from: https://doi.org/10.1017/S1551929512000399
50. Rehman M, Ullah S, Bao Y, Wang B, Peng D, Liu L. Light-emitting diodes: whether an efficient source of light for indoor plants? Environ Sci Pollut Res [Internet]. 2017 Nov 4 [cited 2019 Mar 20];24(32):24743–52. Available from: http://www.ncbi.nlm.nih.gov/pubmed/28980183
51. Mubaid F, Kaufman D, Wee T-L, Nguyen-Huu D-S, Young D, Anghelopoulou M, et al. Fluorescence microscope light source stability. Histochem Cell Biol [Internet]. 2019 Feb 14 [cited 2019 Mar 20]; Available from: http://www.ncbi.nlm.nih.gov/pubmed/30767050
52. Singh A, Gopinathan KP. Confocal microscopy: A powerful technique for biological research [Internet]. Vol. 74, Current Science. Current Science Association; [cited 2019 Mar 20]. p. 841–51. Available from: https://www.jstor.org/stable/24101088
53. Satsoura D, Leber B, Andrews DW, Fradin C. Circumvention of fluorophore photobleaching in fluorescence fluctuation experiments: a beam scanning approach. Chemphyschem [Internet]. 2007 Apr 23 [cited 2019 Mar 20];8(6):834–48. Available from: http://www.ncbi.nlm.nih.gov/pubmed/17394281
54. St Croix CM, Shand SH, Watkins SC. Confocal microscopy: comparisons, applications, and problems. 2005 [cited 2019 Mar 20]; Available from: www.BioTechniques.com

55. De Luca GMR, Breedijk RMP, Brandt RAJ, Zeelenberg CHC, de Jong BE, Timmermans W, et al. Re-scan confocal microscopy: scanning twice for better resolution. Biomed Opt Express [Internet]. 2013 [cited 2019 Mar 20];4(11):2644–56. Available from: http://www.ncbi.nlm.nih.gov/pubmed/24298422
56. Waddell A, Star P, Guitera P. Advances in the use of reflectance confocal microscopy in melanoma. Melanoma Manag [Internet]. 2018 Jun [cited 2019 Mar 20];5(1):MMT04. Available from: http://www.ncbi.nlm.nih.gov/pubmed/30190930
57. Nwaneshiudu A, Kuschal C, Sakamoto FH, Rox Anderson R, Schwarzenberger K, Young RC. Introduction to Confocal Microscopy. J Invest Dermatol [Internet]. 2012 Dec [cited 2019 Mar 20];132(12):1–5. Available from: https://linkinghub.elsevier.com/retrieve/pii/S0022202X15355536
58. Stehbens S, Pemble H, Murrow L, Wittmann T. Imaging Intracellular Protein Dynamics by Spinning Disk Confocal Microscopy. In: Methods in enzymology [Internet]. 2012 [cited 2019 Mar 21]. p. 293–313. Available from: http://www.ncbi.nlm.nih.gov/pubmed/22264541
59. Maddox PS, Moree B, Canman JC, Salmon ED. Spinning disk confocal microscope system for rapid high-resolution, multimode, fluorescence speckle microscopy and green fluorescent protein imaging in living cells. Methods Enzymol [Internet]. 2003 [cited 2019 Mar 21];360:597–617. Available from: http://www.ncbi.nlm.nih.gov/pubmed/12622170
60. Gräf R, Rietdorf J, Zimmermann T. Live cell spinning disk microscopy. Adv Biochem Eng Biotechnol [Internet]. 2005 [cited 2019 Mar 21];95:57–75. Available from: http://www.ncbi.nlm.nih.gov/pubmed/16080265
61. Spinning disk confocal microscopy: go live | Cherry Biotech [Internet]. [cited 2019 Mar 21]. Available from: https://www.cherrybiotech.com/scientific-note/microscopy/introduction-to-spinning-disk-confocal-microscopy
62. Spinning Disk Confocal Microscopy Application Note Optical Sectioning Out-of-Focus Light [Internet]. [cited 2019 Mar 21]. Available from: http://www.leica-microsystems.com/science-lab/confocal-microscopy/
63. Sydor AM, Czymmek KJ, Puchner EM, Mennella V. Special Issue: Quantitative Cell Biology Super-Resolution Microscopy: From Single Molecules to Supramolecular Assemblies. Trends Cell Biol [Internet]. 2015 [cited 2019 Mar 21];25(12):730–48. Available from: http://dx.doi.org/10.1016/j.tcb.2015.10.004
64. Martin-Fernandez ML, Tynan CJ, Webb SED. A “pocket guide” to total internal reflection fluorescence. J Microsc [Internet]. 2013 Oct [cited 2019 Mar 21];252(1):16–22. Available from: http://www.ncbi.nlm.nih.gov/pubmed/23889125
65. Fish KN. Total internal reflection fluorescence (TIRF) microscopy. Curr Protoc Cytom [Internet]. 2009 Oct [cited 2019 Mar 21];Chapter 12:Unit12.18. Available from: http://www.ncbi.nlm.nih.gov/pubmed/19816922
66. Super-resolution microscopy [Internet]. [cited 2019 Mar 21]. Available from: https://www.nature.com/collections/vvfdnjgfrj
67. The Diffraction Barrier in Optical Microscopy | MicroscopyU [Internet]. [cited 2019 Mar 21]. Available from: https://www.microscopyu.com/techniques/super-resolution/the-diffraction-barrier-in-optical-microscopy
68. S. J, A. J. Advanced Optical Imaging of Endocytosis. In: Molecular Regulation of Endocytosis [Internet]. InTech; 2012 [cited 2019 Mar 21]. Available from: http://www.intechopen.com/books/molecular-regulation-of-endocytosis/advanced-optical-imaging-of-endocytosis
69. Sydor AM, Czymmek KJ, Puchner EM, Mennella V. Special Issue: Quantitative Cell Biology Super-Resolution Microscopy: From Single Molecules to Supramolecular Assemblies. Trends Cell Biol [Internet]. 2015 [cited 2019 Mar 22];25(12):730–48. Available from: http://dx.doi.org/10.1016/j.tcb.2015.10.004
70. Hess ST, Girirajan TPK, Mason MD. Ultra-high resolution imaging by fluorescence photoactivation localization microscopy. Biophys J [Internet]. 2006 Dec 1 [cited 2019 Mar 21];91(11):4258–72. Available from: http://www.ncbi.nlm.nih.gov/pubmed/16980368
71. Henriques R, Mhlanga MM. PALM and STORM: What hides beyond the Rayleigh limit? Biotechnol J [Internet]. 2009 Jun 1 [cited 2019 Mar 21];4(6):846–57. Available from: http://doi.wiley.com/10.1002/biot.200900024
72. Habuchi S. Super-Resolution Molecular and Functional Imaging of Nanoscale Architectures in Life and Materials Science. Front Bioeng Biotechnol [Internet]. 2014 Jun 12 [cited 2019 Mar 22];2:20. Available from: http://journal.frontiersin.org/article/10.3389/fbioe.2014.00020/abstract

73. Maglione M, Sigrist SJ. Seeing the forest tree by tree: super-resolution light microscopy meets the neurosciences. Nat Neurosci [Internet]. 2013 Jul 25 [cited 2019 Mar 22];16(7):790–7. Available from: http://www.ncbi.nlm.nih.gov/pubmed/23799471
74. Karim AM. Fundamentals of Engineering Thermodynamics 5th Edition - By (Michael J. Moran & Howard N. Shapiro) [Internet]. [cited 2019 May 20]. Available from: https://www.academia.edu/30805355/Fundamentals_of_Engineering_Thermodynamics_5th_Edition_-_By_Michael_J._Moran_and_Howard_N._Shapiro_
75. Ziegler H. An introduction to thermomechanics. North-Holland Pub. Co.; 1983.
76. Onsager L. Reciprocal Relations in Irreversible Processes. I. Phys Rev [Internet]. 1931 Feb 15 [cited 2019 May 20];37(4):405–26. Available from: https://link.aps.org/doi/10.1103/PhysRev.37.405
77. Phillips KJH. Guide to the sun. Cambridge University Press; 1992. 386 p.
78. Journal GK-TA, 1938 undefined. The Magnitude of the Sun, the Stellar Temperature Scale, and Bolometric Corrections. adsabs.harvard.edu [Internet]. [cited 2019 May 20]; Available from: http://adsabs.harvard.edu/full/1938ApJ....88..429K
79. Kuhn JR, Libbrecht KG, Dicke RH. The Surface Temperature of the Sun and Changes in the Solar Constant [Internet]. Vol. 242, Science. American Association for the Advancement of Science; [cited 2019 May 20]. p. 908–11. Available from: https://www.jstor.org/stable/1701970
80. Stewart GR. Measurement of low-temperature specific heat. Rev Sci Instrum [Internet]. 1983 Jan 4 [cited 2019 May 20];54(1):1–11. Available from: http://aip.scitation.org/doi/10.1063/1.1137207
81. Lachenbruch AH. Crustal temperature and heat production: Implications of the linear heat-flow relation. J Geophys Res [Internet]. 1970 Jun 10 [cited 2019 May 20];75(17):3291–300. Available from: http://doi.wiley.com/10.1029/JB075i017p03291
82. Abhat A. Low temperature latent heat thermal energy storage: Heat storage materials. Sol Energy [Internet]. 1983 Jan 1 [cited 2019 May 20];30(4):313–32. Available from: https://www.sciencedirect.com/science/article/pii/0038092X8390186X
83. Siegel R, Sparrow EM, Hallman TM. Steady laminar heat transfer in a circular tube with prescribed wall heat flux. Appl Sci Res [Internet]. 1958 Sep [cited 2019 May 20];7(5):386–92. Available from: http://link.springer.com/10.1007/BF03184999
84. Clarke A, Rothery P. Scaling of body temperature in mammals and birds. Funct Ecol [Internet]. 2007 Oct 29 [cited 2019 May 20];0(0):071029083929001-??? Available from: http://doi.wiley.com/10.1111/j.1365-2435.2007.01341.x
85. Hiebert SM, Noveral J. Are chicken embryos endotherms or ectotherms? A laboratory exercise integrating concepts in thermoregulation and metabolism. Adv Physiol Educ [Internet]. 2007 Jan [cited 2019 May 20];31(1):97–109. Available from: http://www.physiology.org/doi/10.1152/advan.00035.2006
86. Cannon B, Nedergaard J. Nonshivering thermogenesis and its adequate measurement in metabolic studies. J Exp Biol [Internet]. 2011 Jan 15 [cited 2019 May 20];214(2):242–53. Available from: http://jeb.biologists.org/cgi/doi/10.1242/jeb.050989
87. Ahlgren G. Temperature Functions in Biology and Their Application to Algal Growth Constants. Oikos [Internet]. 1987 Jun [cited 2019 May 20];49(2):177. Available from: https://www.jstor.org/stable/3566025?origin=crossref
88. Sengupta P, Garrity P. Sensing temperature. Curr Biol [Internet]. 2013 Apr 22 [cited 2019 May 20];23(8):R304-7. Available from: http://www.ncbi.nlm.nih.gov/pubmed/23618661
89. O'Rourke SM, Carter C, Carter L, Christensen SN, Jones MP, Nash B, et al. A survey of new temperature-sensitive, embryonic-lethal mutations in C. elegans: 24 alleles of thirteen genes. PLoS One [Internet]. 2011 Mar 1 [cited 2019 May 20];6(3):e16644. Available from: http://www.ncbi.nlm.nih.gov/pubmed/21390299
90. Argon Y, Ward S. Caenorhabditis elegans fertilization-defective mutants with abnormal sperm. Genetics [Internet]. 1980 Oct [cited 2019 May 20];96(2):413–33. Available from: http://www.ncbi.nlm.nih.gov/pubmed/7196361
91. Lowry J, Yochem J, Chuang C-H, Sugioka K, Connolly AA, Bowerman B. High-Throughput Cloning of Temperature-Sensitive Caenorhabditis elegans Mutants with Adult Syncytial Germline Membrane Architecture Defects. G3 (Bethesda) [Internet]. 2015 Aug 26 [cited 2019 May 20];5(11):2241–55. Available from: http://www.ncbi.nlm.nih.gov/pubmed/26311651
92. O'Brien WJ, Frerman FE. The effect of temperature and membrane lipid composition on the rate of beta-oxidation by Escherichia coli. Biochim Biophys Acta [Internet]. 1980 Jan

18 [cited 2019 May 20];617(1):20–7. Available from: http://www.ncbi.nlm.nih.gov/pubmed/6986174
93. van Dooremalen C, Ellers J. A moderate change in temperature induces changes in fatty acid composition of storage and membrane lipids in a soil arthropod. J Insect Physiol [Internet]. 2010 Feb [cited 2019 May 20];56(2):178–84. Available from: http://www.ncbi.nlm.nih.gov/pubmed/19835878
94. Murata N, 10s DA. Membrane Fluidity and Bemperature Perception' [Internet]. Vol. 11, Plant Phvsiol. [cited 2019 May 20]. Available from: https://www.ncbi.nlm.nih.gov/pmc/articles/PMC158550/pdf/1150875.pdf
95. Desmarais R. How To Select And Use The Right Temperature Sensor Presented at the 1996 Heat Processing Conference [Internet]. 1996 [cited 2018 Aug 16]. Available from: http://www.foxanddole.com/Temperature Sensor Selection Guide.pdf
96. Kamat RK, Naik GM. Thermistors – in search of new applications, manufacturers cultivate advanced NTC techniques. Sens Rev [Internet]. 2002 Dec 14 [cited 2018 Aug 16];22(4):334–40. Available from: https://www.emeraldinsight.com/doi/10.1108/02602280210444654
97. Tong A. Improving the accuracy of temperature measurements. Sens Rev [Internet]. 2001 Sep 14 [cited 2018 Aug 16];21(3):193–8. Available from: https://www.emeraldinsight.com/doi/10.1108/02602280110398044
98. Childs PRN, Greenwood JR, Long CA. Review of temperature measurement. Rev Sci Instrum [Internet]. 2000 Jul 31 [cited 2018 Aug 16];71(8):2959. Available from: https://aip.scitation.org/doi/10.1063/1.1305516
99. Radetić R, Pavlov-Kagadejev M, Milivojević N. The Analog Linearization of Pt100 Working Characteristic. SERBIAN J Electr Eng [Internet]. 2015 [cited 2018 Aug 16];12(3):345–57. Available from: http://www.doiserbia.nb.rs/img/doi/1451-4869/2015/1451-48691503345R.pdf
100. Liu G, Guo L, Liu C, Wu Q. Evaluation of different calibration equations for NTC thermistor applied to high-precision temperature measurement. Measurement [Internet]. 2018 May 1 [cited 2018 Aug 16];120:21–7. Available from: https://www.sciencedirect.com/science/article/pii/S0263224118300939
101. Ross-Pinnock D, Maropoulos PG. Review of industrial temperature measurement technologies and research priorities for the thermal characterisation of the factories of the future. Proc Inst Mech Eng Part B J Eng Manuf [Internet]. 2016 May 6 [cited 2018 Aug 16];230(5):793–806. Available from: http://journals.sagepub.com/doi/10.1177/0954405414567929
102. Feteira A. Negative Temperature Coefficient Resistance (NTCR) Ceramic Thermistors: An Industrial Perspective. J Am Ceram Soc [Internet]. 2009 May [cited 2018 Aug 16];92(5):967–83. Available from: http://doi.wiley.com/10.1111/j.1551-2916.2009.02990.x
103. Kulkarni A, Patrascu M, van de Vijver Y, van Wensveen J, Pijnenburg R, Nihtianov S. Investigation of long-term drift of NTC temperature sensors with less than 1 mK uncertainty. In: 2015 IEEE 24th International Symposium on Industrial Electronics (ISIE) [Internet]. IEEE; 2015 [cited 2018 Aug 16]. p. 150–5. Available from: http://ieeexplore.ieee.org/document/7281460/
104. Hardal G, Price BY. Aging Behaviour in Ni0.5CoxMn2.5−xO4 (x = 0.5, 0.8 and 1.1) Thermistors. In Springer, Cham; 2017 [cited 2018 Aug 16]. p. 85–9. Available from: http://link.springer.com/10.1007/978-3-319-51382-9_10
105. Geballe TH, Hull GW. Seebeck Effect in Silicon. Phys Rev [Internet]. 1955 May 15 [cited 2018 Aug 16];98(4):940–7. Available from: https://link.aps.org/doi/10.1103/PhysRev.98.940
106. Uchida K, Takahashi S, Harii K, Ieda J, Koshibae W, Ando K, et al. Observation of the spin Seebeck effect. Nature [Internet]. 2008 Oct 9 [cited 2018 Aug 16];455(7214):778–81. Available from: http://www.nature.com/doifinder/10.1038/nature07321
107. Mora-Ventura B, González G, González FJ. Fabrication and thermal analysis of micro thermocouples for energy harvesting. In: Al-Jassim MM, Bermel P, editors. Thermal Radiation Management for Energy Applications [Internet]. SPIE; 2017 [cited 2018 Aug 16]. p. 16. Available from: https://www.spiedigitallibrary.org/conference-proceedings-of-spie/10369/2273274/Fabrication-and-thermal-analysis-of-micro-thermocouples-for-energy-harvesting/10.1117/12.2273274.full
108. Pollock D. Thermocouples [Internet]. Routledge; 2018 [cited 2018 Aug 16]. Available from: https://www.taylorfrancis.com/books/9780203735824

109. Goldsmid HJ. The Thermoelectric and Related Effects. In Springer, Berlin, Heidelberg; 2016 [cited 2018 Aug 16]. p. 1–7. Available from: http://link.springer.com/10.1007/978-3-662-49256-7_1
110. Van Herwaarden AW, Sarro PM. Thermal sensors based on the seebeck effect. Sensors and Actuators [Internet]. 1986 Nov 12 [cited 2018 Aug 17];10(3–4):321–46. Available from: https://www.sciencedirect.com/science/article/pii/0250687486800531
111. Kasap S. THERMOELECTRIC EFFECTS IN METALS: THERMOCOUPLES [Internet]. Thermoelectric Effects in Metals. 1997 [cited 2018 Aug 17]. Available from: http://educypedia.karadimov.info/library/Thermoelectric-Seebeck.pdf
112. Zhang M. Research and Implement of Thermocouple Sensor and Microcontroller Interface. In: 2010 International Conference on Multimedia Technology [Internet]. IEEE; 2010 [cited 2018 Aug 17]. p. 1–3. Available from: http://ieeexplore.ieee.org/document/5630931/
113. Yang JC-Y, Clarke DW. Control using self-validating sensors. Trans Inst Meas Control [Internet]. 1996 Jan 2 [cited 2018 Aug 17];18(1):15–23. Available from: http://journals.sagepub.com/doi/10.1177/014233129601800103
114. Yang JC-Y, Clarke DW. A self-validating thermocouple. IEEE Trans Control Syst Technol [Internet]. 1997 Mar [cited 2018 Aug 17];5(2):239–53. Available from: http://ieeexplore.ieee.org/document/556028/
115. Iwanaga S, Toberer ES, LaLonde A, Snyder GJ. A high temperature apparatus for measurement of the Seebeck coefficient. Rev Sci Instrum [Internet]. 2011 Jun [cited 2018 Aug 17];82(6):063905. Available from: http://aip.scitation.org/doi/10.1063/1.3601358
116. Zhou Y, Yang D, Li L, Li F, Li J-F. Fast Seebeck coefficient measurement based on dynamic method. Rev Sci Instrum [Internet]. 2014 May [cited 2018 Aug 17];85(5):054904. Available from: http://aip.scitation.org/doi/10.1063/1.4876595
117. Danisman K, Dalkiran I, Celebi FV. Design of a high precision temperature measurement system based on artificial neural network for different thermocouple types. Measurement [Internet]. 2006 Oct 1 [cited 2018 Aug 17];39(8):695–700. Available from: https://www.sciencedirect.com/science/article/pii/S0263224106000595
118. Cesconeto RB, Rodrigues A, Dal-Bó AG, Dias Filho NL, Rocha MR da, Frizon TEA, et al. Evaluation of a Thermochromic Liquid Crystal for Use as a Temperature Sensor for Components of Electrical Systems. Mater Res [Internet]. 2017 May 22 [cited 2018 Aug 17];20(suppl 2):130–6. Available from: http://www.scielo.br/scielo.php?script=sci_arttext&pid=S1516-14392017000800130&lng=en&tlng=en
119. Guan Y, Zhang L, Wang D, West JL, Fu S. Preparation of thermochromic liquid crystal microcapsules for intelligent functional fiber. Mater Des [Internet]. 2018 Jun 5 [cited 2018 Aug 21];147:28–34. Available from: https://www.sciencedirect.com/science/article/pii/S0264127518302090
120. Puccetti G, Rossi M, Morini GL, Kähler CJ. Sensitivity to shear stress of non-encapsulated thermochromic liquid crystal (TLC) particles for microfluidic applications. Microfluid Nanofluidics [Internet]. 2016 Jan 7 [cited 2018 Aug 21];20(1):19. Available from: http://link.springer.com/10.1007/s10404-015-1694-x
121. M. Seredyuk †, Ana B. Gaspar *,‡, V. Ksenofontov †, S. Reiman †, Y. Galyametdinov §, W. Haase ǁ, et al. Room Temperature Operational Thermochromic Liquid Crystals. 2006 [cited 2018 Aug 21]; Available from: https://pubs.acs.org/doi/abs/10.1021/cm052632w
122. Ireland PT, Jones T V. The response time of a surface thermometer employing encapsulated thermochromic liquid crystals. J Phys E [Internet]. 1987 Oct [cited 2018 Aug 21];20(10):008. Available from: http://stacks.iop.org/0022-3735/20/i=10/a=008?key=crossref.f8fc27f6b55b0efde2cc7d2e11430c95
123. Smith CR, Sabatino DR, Praisner TJ. Temperature sensing with thermochromic liquid crystals. Exp Fluids [Internet]. 2001 Feb 6 [cited 2018 Aug 17];30(2):190–201. Available from: http://link.springer.com/10.1007/s003480000154
124. Abdullah N, Abu Talib AR, Jaafar AA, Mohd Salleh MA, Chong WT. The basics and issues of Thermochromic Liquid Crystal Calibrations. Exp Therm Fluid Sci [Internet]. 2010 Nov 1 [cited 2018 Aug 17];34(8):1089–121. Available from: https://www.sciencedirect.com/science/article/pii/S0894177710000683
125. Vanderroost M, Ragaert P, Devlieghere F, De Meulenaer B. Intelligent food packaging: The next generation. Trends Food Sci Technol [Internet]. 2014 Sep 1 [cited 2018 Aug 21];39(1):47–62. Available from:

https://www.sciencedirect.com/science/article/abs/pii/S092422441400137X
126. Ghaani M, Cozzolino CA, Castelli G, Farris S. An overview of the intelligent packaging technologies in the food sector. Trends Food Sci Technol [Internet]. 2016 May 1 [cited 2018 Aug 21];51:1–11. Available from: https://www.sciencedirect.com/science/article/abs/pii/S0924224415301382
127. Jakovljević M, Lozo B, Klanjšek Gunde M. Packaging added value solutions by Thermochromic Liquid Crystal-based printed labels. [cited 2018 Aug 21]; Available from: https://www.ingentaconnect.com/content/ist/nipdf/2016/00002016/00000001/art00082
128. Sage I. Thermochromic liquid crystals. Liq Cryst [Internet]. 2011 Nov [cited 2018 Aug 21];38(11–12):1551–61. Available from: http://www.tandfonline.com/doi/abs/10.1080/02678292.2011.631302
129. Vollmer M, Möllmann K-P. Infrared thermal imaging : fundamentals, research and applications.
130. Benayas A, del Rosal B, Pérez-Delgado A, Santacruz-Gómez K, Jaque D, Hirata GA, et al. Nd:YAG Near-Infrared Luminescent Nanothermometers. Adv Opt Mater [Internet]. 2015 May 1 [cited 2018 Aug 21];3(5):687–94. Available from: http://doi.wiley.com/10.1002/adom.201400484
131. Jones BF, Plassmann P. Digital infrared thermal imaging of human skin. IEEE Eng Med Biol Mag [Internet]. 2002 Nov [cited 2018 Aug 21];21(6):41–8. Available from: http://ieeexplore.ieee.org/document/1175137/
132. Kastberger G, Stachl R. Infrared imaging technology and biological applications. Behav Res Methods, Instruments, Comput [Internet]. 2003 Aug [cited 2018 Aug 21];35(3):429–39. Available from: http://www.springerlink.com/index/10.3758/BF03195520
133. Theriault DH, Fuller NW, Jackson BE, Bluhm E, Evangelista D, Wu Z, et al. A protocol and calibration method for accurate multi-camera field videography. J Exp Biol [Internet]. 2014 Jun 1 [cited 2018 Aug 21];217(Pt 11):1843–8. Available from: http://www.ncbi.nlm.nih.gov/pubmed/24577444
134. Curran A, Klein M, Hepokoski M, Packard C. Improving the accuracy of infrared measurements of skin temperature. Extrem Physiol Med [Internet]. 2015 Sep 14 [cited 2018 Aug 21];4(Suppl 1):A140. Available from: http://extremephysiolmed.biomedcentral.com/articles/10.1186/2046-7648-4-S1-A140
135. Hsiao WW-W, Hui YY, Tsai P-C, Chang H-C. Fluorescent Nanodiamond: A Versatile Tool for Long-Term Cell Tracking, Super-Resolution Imaging, and Nanoscale Temperature Sensing. Acc Chem Res [Internet]. 2016 Mar 15 [cited 2018 Aug 21];49(3):400–7. Available from: http://pubs.acs.org/doi/10.1021/acs.accounts.5b00484
136. Cui Y, Song R, Yu J, Liu M, Wang Z, Wu C, et al. Dual-Emitting MOF⊃Dye Composite for Ratiometric Temperature Sensing. Adv Mater [Internet]. 2015 Feb 1 [cited 2018 Aug 21];27(8):1420–5. Available from: http://doi.wiley.com/10.1002/adma.201404700
137. Oyama K, Takabayashi M, Takei Y, Arai S, Takeoka S, Ishiwata S, et al. Walking nanothermometers: spatiotemporal temperature measurement of transported acidic organelles in single living cells. Lab Chip [Internet]. 2012 Apr 3 [cited 2018 Aug 21];12(9):1591. Available from: http://xlink.rsc.org/?DOI=c2lc00014h
138. Suzuki M, Tseeb V, Oyama K, Ishiwata S. Microscopic detection of thermogenesis in a single HeLa cell. Biophys J [Internet]. 2007 Mar 15 [cited 2018 Aug 21];92(6):L46-8. Available from: http://www.ncbi.nlm.nih.gov/pubmed/17237208
139. Okabe K, Sakaguchi R, Shi B, Kiyonaka S. Intracellular thermometry with fluorescent sensors for thermal biology. Pflügers Arch - Eur J Physiol [Internet]. 2018 May 4 [cited 2018 Jul 25];470(5):717–31. Available from: http://www.ncbi.nlm.nih.gov/pubmed/29397424
140. Mokari T, Rothenberg E, Popov I, Costi R, Banin U, Li JJ, et al. Selective Growth of Metal Tips onto Semiconductor Quantum Rods and Tetrapods. Science (80-) [Internet]. 2004 Jun 18 [cited 2018 Aug 22];304(5678):1787–90. Available from: http://www.ncbi.nlm.nih.gov/pubmed/15205530
141. Maestro LM, Rodríguez EM, Rodríguez FS, la Cruz MCI, Juarranz A, Naccache R, et al. CdSe Quantum Dots for Two-Photon Fluorescence Thermal Imaging. Nano Lett [Internet]. 2010 Dec 8 [cited 2018 Aug 22];10(12):5109–15. Available from: http://pubs.acs.org/doi/abs/10.1021/nl1036098
142. Gavgani JN, Hasani A, Nouri M, Mahyari M, Salehi A. Highly sensitive and flexible ammonia sensor based on S and N co-doped graphene quantum dots/polyaniline hybrid at room temperature. Sensors Actuators B Chem [Internet]. 2016 Jun 28 [cited 2018 Aug

22];229:239–48. Available from: https://www.sciencedirect.com/science/article/pii/S0925400516300867
143. Li X, Wu Y, Zhang S, Cai B, Gu Y, Song J, et al. CsPbX 3 Quantum Dots for Lighting and Displays: Room-Temperature Synthesis, Photoluminescence Superiorities, Underlying Origins and White Light-Emitting Diodes. Adv Funct Mater [Internet]. 2016 Apr 1 [cited 2018 Aug 22];26(15):2435–45. Available from: http://doi.wiley.com/10.1002/adfm.201600109
144. Park CH, Yang H, Lee J, Cho H-H, Kim D, Lee DC, et al. Multicolor Emitting Block Copolymer-Integrated Graphene Quantum Dots for Colorimetric, Simultaneous Sensing of Temperature, pH, and Metal Ions. Chem Mater [Internet]. 2015 Aug 11 [cited 2018 Aug 22];27(15):5288–94. Available from: http://pubs.acs.org/doi/10.1021/acs.chemmater.5b01545
145. Albers AE, Chan EM, McBride PM, Ajo-Franklin CM, Cohen BE, Helms BA. Dual-Emitting Quantum Dot/Quantum Rod-Based Nanothermometers with Enhanced Response and Sensitivity in Live Cells. J Am Chem Soc [Internet]. 2012 Jun 13 [cited 2018 Aug 22];134(23):9565–8. Available from: http://pubs.acs.org/doi/10.1021/ja302290e
146. Pelton R. Temperature-sensitive aqueous microgels. Adv Colloid Interface Sci [Internet]. 2000 Feb 1 [cited 2018 Aug 22];85(1):1–33. Available from: https://www.sciencedirect.com/science/article/pii/S0001868699000238?via%3Dihub
147. Hayashi T, Fukuda N, Uchiyama S, Inada N. A Cell-Permeable Fluorescent Polymeric Thermometer for Intracellular Temperature Mapping in Mammalian Cell Lines. Blum R, editor. PLoS One [Internet]. 2015 Feb 18 [cited 2018 Aug 22];10(2):e0117677. Available from: http://dx.plos.org/10.1371/journal.pone.0117677
148. Qiao J, Hwang Y-H, Chen C-F, Qi L, Dong P, Mu X-Y, et al. Ratiometric Fluorescent Polymeric Thermometer for Thermogenesis Investigation in Living Cells. Anal Chem [Internet]. 2015 Oct 20 [cited 2018 Aug 22];87(20):10535–41. Available from: http://pubs.acs.org/doi/10.1021/acs.analchem.5b02791
149. Uchiyama S, Gota C, Tsuji T, Inada N. Intracellular temperature measurements with fluorescent polymeric thermometers. Chem Commun (Camb) [Internet]. 2017 Oct 5 [cited 2018 Aug 22];53(80):10976–92. Available from: http://www.ncbi.nlm.nih.gov/pubmed/28890966
150. Uchiyama S, Tsuji T, Ikado K, Yoshida A, Kawamoto K, Hayashi T, et al. A cationic fluorescent polymeric thermometer for the ratiometric sensing of intracellular temperature. Analyst [Internet]. 2015 Jun 15 [cited 2018 Aug 22];140(13):4498–506. Available from: http://xlink.rsc.org/?DOI=C5AN00420A
151. Seiichi Uchiyama *,†,‡, Yuriko Matsumura †, A. Prasanna de Silva ‡ and, Kaoru Iwai* †. Modulation of the Sensitive Temperature Range of Fluorescent Molecular Thermometers Based on Thermoresponsive Polymers. 2004 [cited 2018 Aug 22]; Available from: https://pubs.acs.org/doi/abs/10.1021/ac035248w
152. Okabe K, Inada N, Gota C, Harada Y, Funatsu T, Uchiyama S. Intracellular temperature mapping with a fluorescent polymeric thermometer and fluorescence lifetime imaging microscopy. Nat Commun [Internet]. 2012 Jan 28 [cited 2018 Aug 22];3(1):705. Available from: http://www.nature.com/articles/ncomms1714
153. Nakano M, Arai Y, Kotera I, Okabe K, Kamei Y, Nagai T. Genetically encoded ratiometric fluorescent thermometer with wide range and rapid response. Matsumoto T, editor. PLoS One [Internet]. 2017 Feb 17 [cited 2019 May 22];12(2):e0172344. Available from: http://www.ncbi.nlm.nih.gov/pubmed/28212432
154. Dunn CD. Some Liked It Hot: A Hypothesis Regarding Establishment of the Proto-Mitochondrial Endosymbiont During Eukaryogenesis. J Mol Evol [Internet]. 2017 Oct 15 [cited 2019 May 22];85(3–4):99–106. Available from: http://link.springer.com/10.1007/s00239-017-9809-5
155. Chrétien D, Bénit P, Ha H-H, Keipert S, El-Khoury R, Chang Y-T, et al. Mitochondria are physiologically maintained at close to 50 °C. Lane N, editor. PLoS Biol [Internet]. 2018 Jan 25 [cited 2019 May 22];16(1):e2003992. Available from: https://dx.plos.org/10.1371/journal.pbio.2003992
156. Bao G, Wong K-L, Jin D, Tanner PA. A stoichiometric terbium-europium dyad molecular thermometer: energy transfer properties. Light Sci Appl [Internet]. 2018 Dec 28 [cited 2019 May 22];7(1):96. Available from: http://www.nature.com/articles/s41377-018-0097-7
157. Tsuji T, Ikado K, Koizumi H, Uchiyama S, Kajimoto K. Difference in intracellular temperature rise between matured and precursor brown adipocytes in response to

uncoupler and β-adrenergic agonist stimuli. Sci Rep [Internet]. 2017 Dec 10 [cited 2019 May 22];7(1):12889. Available from: http://www.nature.com/articles/s41598-017-12634-7
158. Ferdinandus, Arai S. The ABC Guide to Fluorescent Toolsets for the Development of Future Biomaterials. Front Bioeng Biotechnol [Internet]. 2019 Jan 23 [cited 2019 May 22];7:5. Available from: https://www.frontiersin.org/article/10.3389/fbioe.2019.00005/full
159. Okabe K, Sakaguchi R, Shi B, Kiyonaka S. Intracellular thermometry with fluorescent sensors for thermal biology. Pflugers Arch [Internet]. 2018 May 4 [cited 2019 May 22];470(5):717–31. Available from: http://link.springer.com/10.1007/s00424-018-2113-4
160. Sekiguchi T, Sotoma S, Harada Y. Fluorescent nanodiamonds as a robust temperature sensor inside a single cell. Biophys physicobiology [Internet]. 2018 [cited 2019 May 22];15(0):229–34. Available from: https://www.jstage.jst.go.jp/article/biophysico/15/0/15_229/_article
161. Wilfred H. Stage incubator for microscopes. 1944 Sep 11 [cited 2018 Aug 29]; Available from: https://patents.google.com/patent/US2440472A/en?q=top&q=stage&q=incubator&oq=top+stage+incubator
162. Tsuchiya H. Incubator for observation by microscope. 2003 Mar 26 [cited 2018 Aug 29]; Available from: https://patents.google.com/patent/US20050248836A1/en?q=top&q=stage&q=incubator&q=microscope&oq=top+stage+incubator+microscope
163. Tam T, Boeschoten P, Gunderson A. Microscope stage-top incubator system. 2015 Sep 10 [cited 2018 Aug 29]; Available from: https://patents.google.com/patent/USD820987S1/en?q=top&q=stage&q=incubator&q=microscope&oq=top+stage+incubator+microscope
164. Lanzaro L, Caserta S, Guido S, Sabetta L, Sibillo V, Simeone M. Controlled temperature water (or other fluid)-jacket co2 microscope stage incubator. 2005 Mar 24 [cited 2018 Aug 29]; Available from: https://patents.google.com/patent/WO2005095576A2/en?q=top&q=stage&q=incubator&q=microscope&oq=top+stage+incubator+microscope
165. Controlled environment incubator for light microscopy. Fraser L Bak John H Baumann [Internet]. 1980 Apr 4 [cited 2018 Aug 29]; Available from: https://patents.google.com/patent/US4301252A/en?q=top&q=stage&q=incubator&q=microscope&oq=top+stage+incubator+microscope
166. French NA. Modeling Incubation Temperature: The Effects of Incubator Design, Embryonic Development, and Egg Size [Internet]. [cited 2018 Sep 11]. Available from: http://ps.oxfordjournals.org/
167. Seynhaeve ALB, Ten Hagen TLM. Using In Vitro Live-cell Imaging to Explore Chemotherapeutics Delivered by Lipid-based Nanoparticles. J Vis Exp [Internet]. 2017 [cited 2018 Aug 29];(129). Available from: http://www.ncbi.nlm.nih.gov/pubmed/29155748
168. Kulesa PM, Kasemeier-Kulesa JC. Construction of a Heated Incubation Chamber around a Microscope Stage for Time-Lapse Imaging. CSH Protoc [Internet]. 2007 Jul 1 [cited 2018 Aug 29];2007:pdb.prot4792. Available from: http://www.ncbi.nlm.nih.gov/pubmed/21357130
169. Bavister BD. A minichamber device for maintaining a constant carbon dioxide in ari atmosphere during prolonged culture of cells on the stage of an inverted microscope. Vitr Cell Dev Biol [Internet]. 1988 Aug [cited 2018 Aug 29];24(8):759–63. Available from: http://link.springer.com/10.1007/BF02623645
170. Jin W, Liu L, Yang T, Shen H, Zhu J, Xu W, et al. Exploring Peltier effect in organic thermoelectric films. Nat Commun [Internet]. 2018 Dec 4 [cited 2019 May 22];9(1):3586. Available from: http://www.nature.com/articles/s41467-018-05999-4
171. The use of the Peltier effect for simple and accurate calibration of thermoelectric devices. Proc R Soc London Ser B Biol Sci [Internet]. 1975 Aug 19 [cited 2019 May 22];190(1100):315–21. Available from: http://www.royalsocietypublishing.org/doi/10.1098/rspb.1975.0095
172. Drebushchak VA. The Peltier effect. J Therm Anal Calorim [Internet]. 2008 Jan 11 [cited 2019 May 22];91(1):311–5. Available from: http://link.springer.com/10.1007/s10973-007-8336-9
173. Thakor MD, Hadia SK, Kumar A. Precise temperature control through Thermoelectric Cooler with PID controller. In: 2015 International Conference on Communications and Signal Processing (ICCSP) [Internet]. IEEE; 2015 [cited 2018 Aug 29]. p. 1118–22.

Available from: http://ieeexplore.ieee.org/document/7322677/
174. Diller KR. Quantitative low temperature optical microscopy of biological systems. J Microsc [Internet]. 1982 Apr 1 [cited 2018 Aug 29];126(1):9–28. Available from: http://doi.wiley.com/10.1111/j.1365-2818.1982.tb00354.x
175. Hsu CC, Walsh AJ, Nguyen HM, Overcashier DE, Koning-Bastiaan H, Bailey RC, et al. Design and Application of a Low-Temperature Peltier-Cooling Microscope Stage. J Pharm Sci [Internet]. 1996 Jan 1 [cited 2018 Aug 29];85(1):70–4. Available from: http://linkinghub.elsevier.com/retrieve/pii/S0022354915499691
176. Seifert W, Pluschke V, Hinsche NF. Thermoelectric cooler concepts and the limit for maximum cooling. J Phys Condens Matter [Internet]. 2014 Jun 25 [cited 2018 Sep 11];26(25):255803. Available from: http://www.ncbi.nlm.nih.gov/pubmed/24899626
177. Mannella GA, La Carrubba V, Brucato V. Peltier cells as temperature control elements: Experimental characterization and modeling. Appl Therm Eng [Internet]. 2014 Feb 5 [cited 2018 Sep 11];63(1):234–45. Available from: https://www.sciencedirect.com/science/article/pii/S1359431113007886
178. Sigot V, Pellegrino JM, Guibert EE, Rodriguez JV. A modular perfused chamber for low- and normal- temperature microscopy of living cells. Biotechniques. 2011;50(4):251–4.
179. Heidemann SR, Lamoureux P, Ngo K, Reynolds M, Buxbaum RE. Open-dish incubator for live cell imaging with an inverted microscope. Biotechniques. 2003;35(4):708–16.
180. Petronis S, Stangegaard M, Bovöge Christensen C, Dufva M. Transparent polymeric cell culture chip with integrated temperature control and uniform media perfusion. Biotechniques [Internet]. 2006 Mar [cited 2018 Aug 29];40(3):368–76. Available from: https://www.future-science.com/doi/10.2144/000112122
181. Picard C, Hearnden V, Massignani M, Achouri S, Battaglia G, MacNeil S, et al. A micro-incubator for cell and tissue imaging. Biotechniques [Internet]. 2010 Feb [cited 2018 Aug 29];48(2):135–8. Available from: https://www.future-science.com/doi/10.2144/000113245
182. Miralles V, Huerre A, Malloggi F, Jullien M-C, Miralles V, Huerre A, et al. A Review of Heating and Temperature Control in Microfluidic Systems: Techniques and Applications. Diagnostics [Internet]. 2013 Jan 15 [cited 2018 Aug 30];3(1):33–67. Available from: http://www.mdpi.com/2075-4418/3/1/33
183. Bouhlel IB, Ohta M, Mayeux A, Bordes N, Dingli F, Boulanger J, et al. Cell cycle control of spindle pole body duplication and splitting by Sfi1 and Cdc31 in fission yeast. J Cell Sci [Internet]. 2015 Apr 15 [cited 2018 Aug 30];128(8):1481–93. Available from: http://www.ncbi.nlm.nih.gov/pubmed/9013342
184. Velve-Casquillas G, Costa J, Carlier-Grynkorn F, Mayeux A, Tran PT. A Fast Microfluidic Temperature Control Device for Studying Microtubule Dynamics in Fission Yeast. In: Methods in cell biology [Internet]. 2010 [cited 2018 Aug 30]. p. 185–201. Available from: http://www.ncbi.nlm.nih.gov/pubmed/20719272
185. Velve Casquillas G, Fu C, Le Berre M, Cramer J, Meance S, Plecis A, et al. Fast microfluidic temperature control for high resolution live cell imaging. Lab Chip [Internet]. 2011 Feb 7 [cited 2018 Aug 30];11(3):484–9. Available from: http://xlink.rsc.org/?DOI=C0LC00222D
186. Guijt RM, Dodge A, van Dedem GWK, de Rooij NF, Verpoorte E. Chemical and physical processes for integrated temperature control in microfluidic devices. Lab Chip [Internet]. 2003 Feb [cited 2018 Aug 30];3(1):1. Available from: http://www.ncbi.nlm.nih.gov/pubmed/15100796
187. Maltezos G, Rajagopal A, Scherer A. Evaporative cooling in microfluidic channels. 2006 [cited 2018 Aug 30]; Available from: http://www.hpl.hp.com/news/2003/oct_dec/
188. Dong L, Jiang H. Autonomous microfluidics with stimuli-responsive hydrogels. Soft Matter [Internet]. 2007 Sep 19 [cited 2019 May 22];3(10):1223. Available from: http://xlink.rsc.org/?DOI=b706563a
189. Miralles V, Huerre A, Malloggi F, Jullien M-C, Miralles V, Huerre A, et al. A Review of Heating and Temperature Control in Microfluidic Systems: Techniques and Applications. Diagnostics [Internet]. 2013 Jan 15 [cited 2019 May 22];3(1):33–67. Available from: http://www.mdpi.com/2075-4418/3/1/33
190. Issadore D, Humphry KJ, Brown KA, Sandberg L, Weitz DA, Westervelt RM. Microwave dielectric heating of drops in microfluidic devices. Lab Chip [Internet]. 2009 Jun 21 [cited 2019 May 22];9(12):1701. Available from: http://xlink.rsc.org/?DOI=b822357b
191. Bian H, Shan C, Chen F, Yang Q, Li Y, Li Q. Miniaturized 3-D Solenoid-Type Micro-Heaters in Coordination With 3-D Microfluidics. 2017;26(3):588–92.

192. Zheng C, Balasubramanian GPS, Tan Y, Maniatty AM, Hull R, Wen JT. Simulation, Microfabrication, and Control of a Microheater Array. IEEE/ASME Trans Mechatronics [Internet]. 2017 Aug [cited 2018 Aug 30];22(4):1914–9. Available from: http://ieeexplore.ieee.org/document/7811194/
193. Moschou D, Vourdas N, Kokkoris G, Papadakis G, Parthenios J, Chatzandroulis S, et al. All-plastic, low-power, disposable, continuous-flow PCR chip with integrated microheaters for rapid DNA amplification. Sensors Actuators B Chem [Internet]. 2014 Aug 1 [cited 2018 Aug 30];199:470–8. Available from: https://www.sciencedirect.com/science/article/pii/S0925400514004079
194. Son JM, Lee JH, Kim J, Cho YH. Temperature distribution measurement of Au micro-heater in microfluidic channel using IR microscope. Int J Precis Eng Manuf [Internet]. 2015 Feb 6 [cited 2018 Aug 30];16(2):367–72. Available from: http://link.springer.com/10.1007/s12541-015-0048-7
195. de Mello AJ, Habgood M, Lancaster NL, Welton T, Wootton RCR. Precise temperature control in microfluidic devices using Joule heating of ionic liquids. Lab Chip [Internet]. 2004 Oct [cited 2018 Aug 30];4(5):417. Available from: http://www.ncbi.nlm.nih.gov/pubmed/15472723
196. Pardy T, Tulp I, Kremer C, Rang T, Stewart R. Integrated self-regulating resistive heating for isothermal nucleic acid amplification tests (NAAT) in Lab-on-a-Chip (LoC) devices. Isalan M, editor. PLoS One [Internet]. 2017 Dec 21 [cited 2018 Aug 30];12(12):e0189968. Available from: http://dx.plos.org/10.1371/journal.pone.0189968
197. Rothbauer M, Charwat V, Ertl P. Cell Microarrays for Biomedical Applications. In Humana Press, New York, NY; 2016 [cited 2019 May 22]. p. 273–91. Available from: http://link.springer.com/10.1007/978-1-4939-3136-1_19
198. Mäki A-J, Verho J, Kreutzer J, Ryynänen T, Rajan D, Pekkanen-Mattila M, et al. A Portable Microscale Cell Culture System with Indirect Temperature Control. SLAS Technol Transl Life Sci Innov [Internet]. 2018 Dec 3 [cited 2019 May 22];23(6):566–79. Available from: http://journals.sagepub.com/doi/10.1177/2472630318768710
199. Kwok H, Lau P, Wu S, HO H, Gao M, Kwan Y, et al. Allergy Testing and Drug Screening on an ITO-Coated Lab-on-a-Disc. Micromachines [Internet]. 2016 Feb 27 [cited 2019 May 22];7(3):38. Available from: http://www.mdpi.com/2072-666X/7/3/38
200. Oyama K, Zeeb V, Kawamura Y, Arai T, Gotoh M, Itoh H, et al. Triggering of high-speed neurite outgrowth using an optical microheater. Sci Rep [Internet]. 2015 Dec 16 [cited 2019 May 22];5(1):16611. Available from: http://www.nature.com/articles/srep16611
201. Huang X, Ni J, Yan S, LeDuc PR, Yao J, Lin Q. Thermally Tunable Polymer Microlenses for Biological Imaging. J Microelectromechanical Syst [Internet]. 2010 Dec [cited 2019 May 22];19(6):1444–9. Available from: http://ieeexplore.ieee.org/document/5613132/
202. Català F, Marsà F, Montes-Usategui M, Farré A, Martín-Badosa E. Influence of experimental parameters on the laser heating of an optical trap. Sci Rep [Internet]. 2017 Dec 22 [cited 2018 Aug 30];7(1):16052. Available from: http://www.nature.com/articles/s41598-017-15904-6
203. Liu Y, Cheng DK, Sonek GJ, Berns MW, Chapman CF, Trombergt BJ. Evidence for Localized Cell Heating Induced by Infrared Optical Tweezers [Internet]. Vol. 68, Biophysical Journal. 1995 [cited 2018 Aug 31]. Available from: https://www.cell.com/biophysj/pdf/S0006-3495(95)80396-6.pdf
204. Urban P, Kirchner SR, Mühlbauer C, Lohmüller T, Feldmann J. Reversible control of current across lipid membranes by local heating. Sci Rep [Internet]. 2016 Sep 4 [cited 2018 Aug 30];6(1):22686. Available from: http://www.nature.com/articles/srep22686
205. Wang Z, Chen R, Zhu X, Liao Q, Ye D, Zhang B, et al. Control of the droplet generation by an infrared laser. AIP Adv [Internet]. 2018 Jan 4 [cited 2018 Aug 31];8(1):015302. Available from: http://aip.scitation.org/doi/10.1063/1.5007127
206. Remington BA, Drake RP, Ryutov DD. Experimental astrophysics with high power lasers and Z pinches. Rev Mod Phys [Internet]. 2006 Aug 8 [cited 2018 Aug 31];78(3):755–807. Available from: https://link.aps.org/doi/10.1103/RevModPhys.78.755
207. Wheeler EK, Baker BR, Piggott WT, Mabery SL, Hara CA, DeOtte J, et al. On-chip laser-induced DNA dehybridization. Analyst [Internet]. 2013 Jun 4 [cited 2018 Aug 31];138(13):3692. Available from: http://xlink.rsc.org/?DOI=c3an00288h
208. Wells J, Kao C, Mariappan K, Albea J, Jansen ED, Konrad P, et al. Optical stimulation of neural tissue in vivo. Opt Lett [Internet]. 2005 Mar 1 [cited 2018 Aug 31];30(5):504–6. Available from: http://www.ncbi.nlm.nih.gov/pubmed/15789717

209. Adler J, Pagakis SN. Reducing image distortions due to temperature-related microscope stage drift. J Microsc [Internet]. 2003 May 1 [cited 2019 May 23];210(2):131–7. Available from: http://doi.wiley.com/10.1046/j.1365-2818.2003.01160.x
210. Gayatri P, Menon GG, Suneel PR. Effect of Operating Microscope Light on Brain Temperature During Craniotomy. J Neurosurg Anesthesiol [Internet]. 2013 Jul [cited 2019 May 23];25(3):267–70. Available from: http://www.ncbi.nlm.nih.gov/pubmed/23459259
211. Zondervan R, Kulzer F, van der Meer H, Disselhorst JAJM, Orrit M. Laser-Driven Microsecond Temperature Cycles Analyzed by Fluorescence Polarization Microscopy. Biophys J [Internet]. 2006 Apr 15 [cited 2019 May 23];90(8):2958–69. Available from: https://www.sciencedirect.com/science/article/pii/S0006349506724766
212. EVANS J, ADLER J, MITCHELL J, BLANSHARD J, RODGER G. Use of Confocal Laser Scanning Microscope in Conjunction with a Conduction Heat Transfer Stage in Order to Observe Dynamically the Freeze–Thaw Cycle in an Autofluorescent Substance and to Measure Ice Crystal Sizein Situ. Cryobiology [Internet]. 1996 Feb 1 [cited 2019 May 23];33(1):27–33. Available from: https://www.sciencedirect.com/science/article/pii/S0011224096900036
213. Català F, Marsà F, Montes-Usategui M, Farré A, Martín-Badosa E. Influence of experimental parameters on the laser heating of an optical trap. Sci Rep [Internet]. 2017 Dec 22 [cited 2019 May 23];7(1):16052. Available from: http://www.nature.com/articles/s41598-017-15904-6
214. Holmstrom ED, Nesbitt DJ. Real-Time Infrared Overtone Laser Control of Temperature in Picoliter H(2)O Samples: "Nanobathtubs" for Single Molecule Microscopy. J Phys Chem Lett [Internet]. 2010 [cited 2019 May 23];1(15):2264–8. Available from: http://www.ncbi.nlm.nih.gov/pubmed/21814589
215. Neupane B, Jin T, Mellor LF, Loboa EG, Ligler FS, Wang G. Continuous-Wave Stimulated Emission Depletion Microscope for Imaging Actin Cytoskeleton in Fixed and Live Cells. Sensors (Basel) [Internet]. 2015 Sep 18 [cited 2019 May 23];15(9):24178–90. Available from: http://www.ncbi.nlm.nih.gov/pubmed/26393614
216. Laurent M, Johannin G, Gilbert N, Lucas L, Cassio D, Petit PX, et al. Power and limits of laser scanning confocal microscopy. Biol Cell [Internet]. 1994 Jan 1 [cited 2019 May 23];80(2):229–40. Available from: https://www.sciencedirect.com/science/article/pii/0248490094900469
217. Dietl A, Kieser C, Barends TRM, IUCr. A Peltier-cooled microscope stage for protein crystal post-crystallization treatment. J Appl Crystallogr [Internet]. 2017 Aug 1 [cited 2019 May 23];50(4):1208–11. Available from: http://scripts.iucr.org/cgi-bin/paper?S1600576717008755
218. Kawamoto N, Kakefuda Y, Mori T, Hirose K, Mitome M, Bando Y, et al. Nanoscale characterization of the thermal interface resistance of a heat-sink composite material by *in situ* TEM. Nanotechnology [Internet]. 2015 Nov 20 [cited 2019 May 23];26(46):465705. Available from: http://stacks.iop.org/0957-4484/26/i=46/a=465705?key=crossref.cbde2342dba57f50ef9c56d6794b044e
219. Malek A, Shabani SMA. Solving macroscopic and microscopic pin-fin heat sink problems by adapted spectral method. Comput Appl Math [Internet]. 2018 May 18 [cited 2019 May 23];37(2):1112–29. Available from: http://link.springer.com/10.1007/s40314-016-0386-9
220. Jia T, Gao D. Numerical Investigation of the Microscopic Heat Current Inside a Nanofluid System Based on Molecular Dynamics Simulation and Wavelet Analysis. Anal Chem [Internet]. 2018 Apr 3 [cited 2019 May 23];90(7):4297–302. Available from: http://pubs.acs.org/doi/10.1021/acs.analchem.7b05350
221. Kawamoto N, Kakefuda Y, Yamada I, Yuan J, Hasegawa K, Kimoto K, et al. Visualizing nanoscale heat pathways. Nano Energy [Internet]. 2018 Oct 1 [cited 2019 May 23];52:323–8. Available from: https://www.sciencedirect.com/science/article/pii/S2211285518305664
222. Dai Z, Fletcher DF, Haynes BS. Impact of tortuous geometry on laminar flow heat transfer in microchannels. Int J Heat Mass Transf [Internet]. 2015 Apr 1 [cited 2019 May 23];83:382–98. Available from: https://www.sciencedirect.com/science/article/pii/S0017931014011090
223. Lee DPDMI of T. Low-grade heat conversion into electricity by thermoelectric and electrochemical systems. 2018 [cited 2019 May 23]; Available from: https://dspace.mit.edu/handle/1721.1/120186
224. Tyagi P, Kumar A, Giri LI, Tuli S, Srivastava R. Conductive cooling in white organic light

emitting diode for enhanced efficiency and life time. Appl Phys Lett [Internet]. 2015 Jan 5 [cited 2019 May 23];106(1):013301. Available from: http://aip.scitation.org/doi/10.1063/1.4903800
225. Ma CJ, Steinfeld JB, Greene EC. Single-Stranded DNA Curtains for Studying Homologous Recombination. Methods Enzymol [Internet]. 2017 Jan 1 [cited 2019 May 23];582:193–219. Available from: https://www.sciencedirect.com/science/article/pii/S007668791630252X
226. Utzinger U, Baggett B, Weiss JA, Hoying JB, Edgar LT. Large-scale time series microscopy of neovessel growth during angiogenesis. Angiogenesis [Internet]. 2015 Jul 21 [cited 2019 May 23];18(3):219–32. Available from: http://link.springer.com/10.1007/s10456-015-9461-x
227. Wang W-H, Meng L, Hackett RJ, Oldenbourg R, Keefe DL. Rigorous thermal control during intracytoplasmic sperm injection stabilizes the meiotic spindle and improves fertilization and pregnancy rates. Fertil Steril [Internet]. 2002 Jun 1 [cited 2019 May 23];77(6):1274–7. Available from: https://www.sciencedirect.com/science/article/pii/S0015028202031175
228. Mamede JI, Hope TJ. Detection and Tracking of Dual-Labeled HIV Particles Using Wide-Field Live Cell Imaging to Follow Viral Core Integrity. In Humana Press, New York, NY; 2016 [cited 2019 May 23]. p. 49–59. Available from: http://link.springer.com/10.1007/978-1-4939-3046-3_4
229. Ho GH, Cheng A, Chen C-J, Fang CK, Li MC, Chang I-C, et al. Lens-heating-induced focus drift of I-line step and scan: correction and control in a manufacturing environment. In: Sullivan NT, editor. International Society for Optics and Photonics; 2001 [cited 2019 May 23]. p. 289. Available from: http://proceedings.spiedigitallibrary.org/proceeding.aspx?doi=10.1117/12.436722
230. Maltby L, Hills L. Spray drift of pesticides and stream macroinvertebrates: Experimental evidence of impacts and effectiveness of mitigation measures. Environ Pollut [Internet]. 2008 Dec 1 [cited 2019 May 23];156(3):1112–20. Available from: https://www.sciencedirect.com/science/article/pii/S0269749108002078
231. Lee SH, Baday M, Tjioe M, Simonson PD, Zhang R, Cai E, et al. Using fixed fiduciary markers for stage drift correction. Opt Express [Internet]. 2012 May 21 [cited 2019 May 23];20(11):12177. Available from: https://www.osapublishing.org/oe/abstract.cfm?uri=oe-20-11-12177
232. Cui Y. Fine-tune lens-heating-induced focus drift with different process and illumination settings. In: Progler CJ, editor. International Society for Optics and Photonics; 2001 [cited 2019 May 23]. p. 1369. Available from: http://proceedings.spiedigitallibrary.org/proceeding.aspx?doi=10.1117/12.435675
233. KREFT M, STENOVEC M, ZOREC R. Focus-Drift Correction in Time-Lapse Confocal Imaging. Ann N Y Acad Sci [Internet]. 2005 Jun 1 [cited 2019 May 23];1048(1):321–30. Available from: http://doi.wiley.com/10.1196/annals.1342.029
234. OOMEN LCJM, SACHER R, BROCKS HHJ, ZWIER JM, BRAKENHOFF GJ, JALINK K. Immersion oil for high-resolution live-cell imaging at 37°C: optical and physical characteristics. J Microsc [Internet]. 2008 Oct 31 [cited 2019 May 23];232(2):353–61. Available from: http://doi.wiley.com/10.1111/j.1365-2818.2008.02106.x
235. Peterson BM, Mermelstein PG, Meisel RL. Impact of immersion oils and mounting media on the confocal imaging of dendritic spines. J Neurosci Methods [Internet]. 2015 Mar 15 [cited 2019 May 23];242:106–11. Available from: http://www.ncbi.nlm.nih.gov/pubmed/25601477
236. The Why and How of Oil Immersion Microscopy - Bitesize Bio [Internet]. [cited 2019 May 23]. Available from: https://bitesizebio.com/23421/the-why-and-how-of-oil-immersion-microscopy/
237. Cargille JJ. Immersion Oil and the Microscope [Internet]. [cited 2019 May 23]. Available from: www.Cargille.com
238. Turner NA, Vulfson EN. At what temperature can enzymes maintain their catalytic activity? Enzyme Microb Technol [Internet]. 2000 Jul 1 [cited 2018 Jul 21];27(1–2):108–13. Available from: https://www.sciencedirect.com/science/article/pii/S0141022900001848
239. Unsworth LD, van der Oost J, Koutsopoulos S. Hyperthermophilic enzymes − stability, activity and implementation strategies for high temperature applications. FEBS J [Internet]. 2007 Aug [cited 2018 Jul 21];274(16):4044–56. Available from: http://doi.wiley.com/10.1111/j.1742-4658.2007.05954.x

240. Cao Y, Wang Y. Temperature-Mediated Regulation of Enzymatic Activity. ChemCatChem [Internet]. 2016 Sep 7 [cited 2018 Jul 21];8(17):2740–7. Available from: http://doi.wiley.com/10.1002/cctc.201600406
241. Peterson ME, Daniel RM, Danson MJ, Eisenthal R. The dependence of enzyme activity on temperature: determination and validation of parameters. Biochem J [Internet]. 2007 Mar 1 [cited 2018 Jul 21];402(2):331–7. Available from: http://www.ncbi.nlm.nih.gov/pubmed/17092210
242. Daniel RM, Danson MJ. Temperature and the catalytic activity of enzymes: A fresh understanding. FEBS Lett [Internet]. 2013 Sep 2 [cited 2018 Jul 21];587(17):2738–43. Available from: https://www.sciencedirect.com/science/article/pii/S0014579313004857
243. Hideyuki F. Arata *,†, Yannick Rondelez §, Hiroyuki Noji ‡ and, Fujita† H. Temperature Alternation by an On-Chip Microheater To Reveal Enzymatic Activity of β-Galactosidase at High Temperatures. 2005 [cited 2018 Aug 31]; Available from: https://pubs.acs.org/doi/abs/10.1021/ac050385%2B?journalCode=ancham
244. Kütemeyer C, Froeck M, Werlein H-D, Watkinson BM. The influence of salts and temperature on enzymatic activity of microbial transglutaminase. Food Control [Internet]. 2005 Oct [cited 2018 Aug 31];16(8):735–7. Available from: http://linkinghub.elsevier.com/retrieve/pii/S0956713504001318
245. Swarts JW, Kolfschoten RC, Jansen MCAA, Janssen AEM, Boom RM. Effect of diffusion on enzyme activity in a microreactor. Chem Eng J [Internet]. 2010 Aug 1 [cited 2018 Aug 31];162(1):301–6. Available from: http://linkinghub.elsevier.com/retrieve/pii/S1385894710003827
246. Rojek MJ, Walt DR. Observing Single Enzyme Molecules Interconvert between Activity States upon Heating. Sanchez-Ruiz JM, editor. PLoS One [Internet]. 2014 Jan 21 [cited 2018 Aug 31];9(1):e86224. Available from: http://dx.plos.org/10.1371/journal.pone.0086224
247. Guo M, Xu Y, Gruebele M. Temperature dependence of protein folding kinetics in living cells. Proc Natl Acad Sci U S A [Internet]. 2012 Oct 30 [cited 2018 Jul 22];109(44):17863–7. Available from: http://www.ncbi.nlm.nih.gov/pubmed/22665776
248. Hingorani KS, Gierasch LM. Comparing protein folding in vitro and in vivo: foldability meets the fitness challenge. Curr Opin Struct Biol [Internet]. 2014 Feb [cited 2018 Jul 22];24:81–90. Available from: http://www.ncbi.nlm.nih.gov/pubmed/24434632
249. Kumar S, Tsai CJ, Nussinov R. Thermodynamic differences among homologous thermophilic and mesophilic proteins. Biochemistry [Internet]. 2001 Nov 27 [cited 2018 Jul 22];40(47):14152–65. Available from: http://www.ncbi.nlm.nih.gov/pubmed/11714268
250. Somero GN. Proteins and Temperature. Annu Rev Physiol [Internet]. 1995 Oct [cited 2018 Jul 22];57(1):43–68. Available from: http://www.ncbi.nlm.nih.gov/pubmed/7778874
251. Kiyonaka S, Sakaguchi R, Hamachi I, Morii T, Yoshizaki T, Mori Y. Validating subcellular thermal changes revealed by fluorescent thermosensors. Nat Methods [Internet]. 2015 Sep 1 [cited 2018 Aug 31];12(9):801–2. Available from: http://www.nature.com/articles/nmeth.3548
252. Baffou G, Quidant R, García de Abajo FJ. Nanoscale Control of Optical Heating in Complex Plasmonic Systems. ACS Nano [Internet]. 2010 Feb 23 [cited 2018 Aug 31];4(2):709–16. Available from: http://pubs.acs.org/doi/10.1021/nn901144d
253. Zhu M, Baffou G, Meyerbröker N, Polleux J. Micropatterning Thermoplasmonic Gold Nanoarrays To Manipulate Cell Adhesion. ACS Nano [Internet]. 2012 Aug 28 [cited 2018 Aug 31];6(8):7227–33. Available from: http://pubs.acs.org/doi/10.1021/nn302329c
254. Baffou G, Quidant R, Girard C. Thermoplasmonics modeling: A Green's function approach. Phys Rev B [Internet]. 2010 Oct 13 [cited 2018 Aug 31];82(16):165424. Available from: https://link.aps.org/doi/10.1103/PhysRevB.82.165424
255. Nakano M, Arai Y, Kotera I, Okabe K, Kamei Y, Nagai T. Genetically encoded ratiometric fluorescent thermometer with wide range and rapid response. PLoS One. 2017;12(2):1–14.
256. American Society of Biological Chemists., Rockefeller Institute for Medical Research., American Society for Biochemistry and Molecular Biology. The Journal of biological chemistry. [Internet]. American Society for Biochemistry and Molecular Biology; [cited 2019 Jun 11]. Available from: http://www.jbc.org/content/262/17/8360.short
257. Detrich HW, Neighbors BW, Sloboda RD, Williams RC. Microtubule-associated proteins from antarctic fishes. Cell Motil Cytoskeleton [Internet]. 1990 Jan 1 [cited 2019 Jun 11];17(3):174–86. Available from: http://doi.wiley.com/10.1002/cm.970170305

258. Billger M, Wallin M, Williams RC, Detrich HW. Dynamic instability of microtubules from cold-living fishes. Cell Motil Cytoskeleton [Internet]. 1994 Jan 1 [cited 2019 Jun 11];28(4):327–32. Available from: http://doi.wiley.com/10.1002/cm.970280406
259. Delphin C, Bouvier D, Seggio M, Couriol E, Saoudi Y, Denarier E, et al. MAP6-F is a temperature sensor that directly binds to and protects microtubules from cold-induced depolymerization*. 2012 [cited 2018 Aug 31]; Available from: http://www.jbc.org/cgi/doi/10.1074/jbc.M112.398339
260. Myachina F, Bosshardt F, Bischof J, Kirschmann M, Lehner CF. Drosophila β-Tubulin 97EF is upregulated at low temperature and stabilizes microtubules. Development [Internet]. 2017 Oct 15 [cited 2018 Aug 31];144(24):4573–87. Available from: http://www.ncbi.nlm.nih.gov/pubmed/29084803
261. Hong W, Takshak A, Osunbayo O, Kunwar A, Vershinin M. The Effect of Temperature on Microtubule-Based Transport by Cytoplasmic Dynein and Kinesin-1 Motors. Biophys J [Internet]. 2016 Sep 20 [cited 2018 Aug 31];111(6):1287–94. Available from: https://www.sciencedirect.com/science/article/pii/S0006349516306646
262. Bachand GD, Jain R, Ko R, Bouxsein NF, VanDelinder V. Inhibition of Microtubule Depolymerization by Osmolytes. Biomacromolecules [Internet]. 2018 Jul 9 [cited 2018 Aug 31];19(7):2401–8. Available from: http://pubs.acs.org/doi/10.1021/acs.biomac.7b01799
263. Higa T, Hasegawa S, Hayasaki Y, Kodama Y, Wada M. Temperature-dependent signal transmission in chloroplast accumulation response. J Plant Res [Internet]. 2017 Jul 18 [cited 2018 Aug 31];130(4):779–89. Available from: http://link.springer.com/10.1007/s10265-017-0938-0
264. Bollinger JA, Stevens MJ. Catastrophic depolymerization of microtubules driven by subunit shape change. Soft Matter [Internet]. 2018 Mar 7 [cited 2018 Aug 31];14(10):1748–52. Available from: http://xlink.rsc.org/?DOI=C7SM02033C
265. Möller MN, Li Q, Chinnaraj M, Cheung HC, Lancaster JR, Denicola A. Solubility and diffusion of oxygen in phospholipid membranes. Biochim Biophys Acta - Biomembr [Internet]. 2016 Nov 1 [cited 2018 Aug 31];1858(11):2923–30. Available from: https://www.sciencedirect.com/science/article/pii/S0005273616302929
266. Weng L, Ellett F, Edd J, Wong KHK, Uygun K, Irimia D, et al. A highly-occupied, single-cell trapping microarray for determination of cell membrane permeability. Lab Chip [Internet]. 2017 Nov 21 [cited 2018 Aug 31];17(23):4077–88. Available from: http://xlink.rsc.org/?DOI=C7LC00883J
267. De Gier J, Mandersloot JG, Van Deenen LLM. Lipid composition and permeability of liposomes. Biochim Biophys Acta - Biomembr [Internet]. 1968 Jun 11 [cited 2018 Aug 31];150(4):666–75. Available from: https://www.sciencedirect.com/science/article/pii/0005273668900564
268. Papahadjopoulos D, Jacobson K, Nir S, Isac I. Phase transitions in phospholipid vesicles Fluorescence polarization and permeability measurements concerning the effect of temperature and cholesterol. Biochim Biophys Acta - Biomembr [Internet]. 1973 Jul 6 [cited 2018 Aug 31];311(3):330–48. Available from: https://www.sciencedirect.com/science/article/pii/0005273673903143
269. Blicher A, Wodzinska K, Fidorra M, Winterhalter M, Heimburg T. The Temperature Dependence of Lipid Membrane Permeability, its Quantized Nature, and the Influence of Anesthetics. Biophys J [Internet]. 2009 Jun 3 [cited 2018 Aug 31];96(11):4581–91. Available from: https://www.sciencedirect.com/science/article/pii/S000634950900664X
270. Bischof JC, Padanilam J, Holmes WH, Ezzell RM, Lee RC, Tompkins RG, et al. Dynamics of cell membrane permeability changes at supraphysiological temperatures. Biophys J [Internet]. 1995 Jun 1 [cited 2018 Aug 31];68(6):2608–14. Available from: https://www.sciencedirect.com/science/article/pii/S0006349595804455
271. Dolan EB, Haugh MG, Tallon D, Casey C, Mcnamara LM. Heat-shock-induced cellular responses to temperature elevations occurring during orthopaedic cutting. [cited 2019 May 23]; Available from: http://rsif.royalsocietypublishing.org.
272. full-text.
273. Chang C-H, Chiang M-L, Chou C-C. The effect of temperature and length of heat shock treatment on the thermal tolerance and cell leakage of Cronobacter sakazakii BCRC 13988. Int J Food Microbiol [Internet]. 2009 Sep 15 [cited 2019 May 23];134(3):184–9. Available from: http://www.ncbi.nlm.nih.gov/pubmed/19625097
274. Sorensen JG, Loeschcke V, Kristensen TN. Cellular damage as induced by high temperature is dependent on rate of temperature change - investigating consequences of

ramping rates on molecular and organismal phenotypes in Drosophila melanogaster. J Exp Biol [Internet]. 2013 Mar 1 [cited 2019 May 23];216(5):809–14. Available from: http://www.ncbi.nlm.nih.gov/pubmed/23155086
275. Elegans C, Briggsae Graphical C, Begasse ML, Grill SW, Hyman AA, Leaver M, et al. Temperature Dependence of Cell Division Timing Accounts for a Shift in the Thermal Limits of Temperature Dependence of Cell Division Timing Accounts for a Shift in the Thermal Limits of C. elegans and C. briggsae. CellReports [Internet]. 2015 [cited 2019 May 23];10:647–53. Available from: http://dx.doi.org/10.1016/j.celrep.2015.01.006http://dx.doi.org/10.1016/j.celrep.2015.01.006
276. LeCun Y, Bengio Y, Hinton G. Deep learning. Nat 2015 5217553 [Internet]. 2015 May 27 [cited 2019 May 24];521(7553):436. Available from: http://www.nature.com/articles/nature14539
277. Jordan MI, Mitchell TM. Machine learning: Trends, perspectives, and prospects. Science [Internet]. 2015 Jul 17 [cited 2019 May 24];349(6245):255–60. Available from: http://www.ncbi.nlm.nih.gov/pubmed/26185243
278. Arel I, Rose DC, Karnowski TP. Deep Machine Learning - A New Frontier in Artificial Intelligence Research [Research Frontier]. IEEE Comput Intell Mag [Internet]. 2010 Nov [cited 2019 May 24];5(4):13–8. Available from: http://ieeexplore.ieee.org/document/5605630/
279. Bengio Y. Learning Deep Architectures for AI. Found Trends® Mach Learn [Internet]. 2009 Nov 15 [cited 2019 May 24];2(1):1–127. Available from: http://www.nowpublishers.com/article/Details/MAL-006
280. Krizhevsky A, Sutskever I, Hinton GE. ImageNet Classification with Deep Convolutional Neural Networks [Internet]. [cited 2019 May 24]. Available from: http://code.google.com/p/cuda-convnet/
281. Szegedy C, Liu W, Jia Y, Sermanet P, Reed S, Anguelov D, et al. Going Deeper with Convolutions [Internet]. [cited 2019 Apr 25]. Available from: https://www.cs.unc.edu/~wliu/papers/GoogLeNet.pdf
282. He K, Zhang X, Ren S, Sun J. Deep Residual Learning for Image Recognition. 2015 Dec 10 [cited 2019 May 24]; Available from: http://arxiv.org/abs/1512.03385
283. Liu G, Guo L, Liu C, Wu Q. Evaluation of different calibration equations for NTC thermistor applied to high-precision temperature measurement. Measurement [Internet]. 2018 May 1 [cited 2019 Jun 4];120:21–7. Available from: https://www.sciencedirect.com/science/article/pii/S0263224118300939
284. Steinhart JS, Hart SR. Calibration curves for thermistors. Deep Sea Res Oceanogr Abstr [Internet]. 1968 Aug 1 [cited 2019 Jun 4];15(4):497–503. Available from: https://www.sciencedirect.com/science/article/pii/0011747168900570?via%3Dihub
285. Eastman ED. THEORY OF CERTAIN ELECTROMETRIC AND CONDUCTIMETRIC TITRATIONS. J Am Chem Soc [Internet]. 1925 Feb [cited 2019 Jun 4];47(2):332–7. Available from: http://pubs.acs.org/doi/abs/10.1021/ja01679a008
286. Holmes HN, Williams HA. IODINE AS AN EMULSIFYING AGENT. J Am Chem Soc [Internet]. 1925 Feb [cited 2019 Jun 4];47(2):323–5. Available from: http://pubs.acs.org/doi/abs/10.1021/ja01679a006
287. Dusen MS Van. PLATINUM-RESISTANCE THERMOMETRY AT LOW TEMPERATURES [1]. J Am Chem Soc [Internet]. 1925 Feb [cited 2019 Jun 4];47(2):326–32. Available from: http://pubs.acs.org/doi/abs/10.1021/ja01679a007
288. Microfluidic chip support and system for thermally regulating a speciman in a spatially controlled and rapid manner [Internet]. Yong Chen Maël LE BERRE Guilhem Velve Casquillas Adrien Plecis. 2011 [cited 2019 Jun 6]. Available from: https://patents.google.com/patent/WO2011138748A1/en?inventor=Guilhem+Velve+Casquillas
289. Tran PT, Marsh L, Doye V, Inoué S, Chang F. A Mechanism for Nuclear Positioning in Fission Yeast Based on Microtubule Pushing 7. J Cell Biol [Internet]. 2001 [cited 2019 Jun 13];153(2):397–411. Available from: http://www.jcb.org/cgi/content/full/153/2/397
290. Krüger LK, Sanchez J-L, Paoletti A, Tran PT. Kinesin-6 regulates cell-size-dependent spindle elongation velocity to keep mitosis duration constant in fission yeast. Elife [Internet]. 2019 Feb 26 [cited 2019 Jun 13];8. Available from: https://elifesciences.org/articles/42182
291. Vela-Corcía D, Romero D, de Vicente A, Pérez-García A. Analysis of β-tubulin-

carbendazim interaction reveals that binding site for MBC fungicides does not include residues involved in fungicide resistance. Sci Rep [Internet]. 2018 May 8 [cited 2019 Jun 26];8(1):7161. Available from: http://www.ncbi.nlm.nih.gov/pubmed/29740047
292. WALKER GM. Cell Cycle Specificity of Certain Antimicrotubular Drugs in Schizosaccharomyces pombe. Microbiology [Internet]. 1982 Jan 1 [cited 2019 Jun 26];128(1):61–71. Available from: http://www.ncbi.nlm.nih.gov/pubmed/7086393
293. Vernos I, Heasman J, Wylie C. Multiple Kinesin-like Transcripts in Xenopus Oocytes. Dev Biol [Internet]. 1993 May [cited 2019 Jun 13];157(1):232–9. Available from: http://www.ncbi.nlm.nih.gov/pubmed/8482413
294. Meunier S, Timón K, Vernos I. Aurora-A regulates MCRS1 function during mitosis. Cell Cycle [Internet]. 2016 Jul 2 [cited 2019 Jun 13];15(13):1779–86. Available from: http://www.tandfonline.com/doi/full/10.1080/15384101.2016.1187342
295. Amargant F, Barragan M, Vassena R, Vernos I. Insights of the tubulin code in gametes and embryos: from basic research to potential clinical applications in humans†. Biol Reprod [Internet]. 2019 Mar 1 [cited 2019 Jun 13];100(3):575–89. Available from: https://academic.oup.com/biolreprod/article/100/3/575/5105747
296. Sedwick C. Isabelle Vernos: Motoring around the mitotic spindle. J Cell Biol [Internet]. 2010 [cited 2019 Jun 13];188(5):616. Available from: https://www.ncbi.nlm.nih.gov/pmc/articles/PMC2835938/
297. Bakhoum SF, Genovese G, Compton DA. Deviant Kinetochore Microtubule Dynamics Underlie Chromosomal Instability. Curr Biol [Internet]. 2009 Dec [cited 2019 Jun 27];19(22):1937–42. Available from: https://linkinghub.elsevier.com/retrieve/pii/S0960982209017680
298. Nixon FM, Gutiérrez-Caballero C, Hood FE, Booth DG, Prior IA, Royle SJ. The mesh is a network of microtubule connectors that stabilizes individual kinetochore fibers of the mitotic spindle. Elife [Internet]. 2015 Jun 19 [cited 2019 Jun 27];4. Available from: https://elifesciences.org/articles/07635
299. Hood FE, Williams SJ, Burgess SG, Richards MW, Roth D, Straube A, et al. Coordination of adjacent domains mediates TACC3–ch-TOG–clathrin assembly and mitotic spindle binding. J Cell Biol [Internet]. 2013 Aug 5 [cited 2019 Jun 27];202(3):463–78. Available from: http://www.jcb.org/lookup/doi/10.1083/jcb.201211127
300. Forth S, Kapoor TM. The mechanics of microtubule networks in cell division. J Cell Biol [Internet]. 2017 Jun 5 [cited 2019 Jun 27];216(6):1525–31. Available from: http://www.ncbi.nlm.nih.gov/pubmed/28490474
301. Mora-Bermúdez F, Matsuzaki F, Huttner WB. Specific polar subpopulations of astral microtubules control spindle orientation and symmetric neural stem cell division. Elife [Internet]. 2014 Jul 4 [cited 2019 Jun 27];3. Available from: http://www.ncbi.nlm.nih.gov/pubmed/24996848
302. Tolić IM. Mitotic spindle: kinetochore fibers hold on tight to interpolar bundles. Eur Biophys J [Internet]. 2018 Apr 19 [cited 2019 Jun 27];47(3):191–203. Available from: http://link.springer.com/10.1007/s00249-017-1244-4
303. Mitchison TJ, Wühr M, Nguyen P, Ishihara K, Groen A, Field CM. Growth, interaction and positioning of microtubule asters in extremely large vertebrate embryo cells. Cytoskeleton (Hoboken) [Internet]. 2012 Oct [cited 2019 Jun 27];69(10):738. Available from: http://www.ncbi.nlm.nih.gov/pubmed/22786885
304. Holy TE, Dogterom M, Yurke B, Leibler S. Assembly and positioning of microtubule asters in microfabricated chambers. Proc Natl Acad Sci U S A [Internet]. 1997 Jun 10 [cited 2019 Jun 27];94(12):6228–31. Available from: http://www.ncbi.nlm.nih.gov/pubmed/9177199
305. Tio M, Zavortink M, Yang X, Chia W. A functional analysis of inscuteable and its roles during Drosophila asymmetric cell divisions. J Cell Sci [Internet]. 1999 May 1 [cited 2019 Jun 27];112 (Pt 10)(10):1541–51. Available from: http://www.ncbi.nlm.nih.gov/pubmed/10212148
306. Magiera MM, Singh P, Janke C. SnapShot: Functions of Tubulin Posttranslational Modifications. Cell [Internet]. 2018 [cited 2019 Jun 13];173(10):1552-1552.e1. Available from: https://doi.org/10.1016/j.cell.2018.05.032
307. Magiera MM, Singh P, Gadadhar S, Janke C. Tubulin Posttranslational Modifications and Emerging Links to Human Disease. Cell [Internet]. 2018 May 31 [cited 2019 Jun 13];173(6):1323–7. Available from: http://www.ncbi.nlm.nih.gov/pubmed/29856952
308. Souphron J, Bodakuntla S, Jijumon AS, Lakisic G, Gautreau AM, Janke C, et al. Purification of tubulin with controlled post-translational modifications by polymerization–

depolymerization cycles. Nat Protoc [Internet]. 2019 May 17 [cited 2019 Jun 13];14(5):1634–60. Available from: http://www.nature.com/articles/s41596-019-0153-7
309. Dickson M, Gagnon JP. Key factors in the rising cost of new drug discovery and development. Nat Rev Drug Discov [Internet]. 2004 May 1 [cited 2018 Apr 23];3(5):417–29. Available from: http://www.nature.com/doifinder/10.1038/nrd1382
310. DiMasi JA, Grabowski HG, Hansen RW. The Cost of Drug Development. N Engl J Med [Internet]. 2015 May 14 [cited 2018 Apr 23];372(20):1972–1972. Available from: http://www.nejm.org/doi/10.1056/NEJMc1504317
311. Robuck PR, Wurzelmann JI, Merrick M. Understanding the drug development process. Inflamm Bowel Dis [Internet]. 2005;11(SUPPL. 1):S13–6. Available from: http://ovidsp.ovid.com/ovidweb.cgi?T=JS&CSC=Y&NEWS=N&PAGE=fulltext&D=emed7&AN=2005500309
312. Kaitin KI. Deconstructing the drug development process: The new face of innovation. Clin Pharmacol Ther. 2010;87(3):356–61.
313. Baldini E, Tuccilli C, Arlot-Bonnemains Y, Chesnel F, Sorrenti S, De Vito C, et al. Deregulated expression of VHL mRNA variants in papillary thyroid cancer. Mol Cell Endocrinol [Internet]. 2017 Mar [cited 2019 Jun 13];443:121–7. Available from: https://linkinghub.elsevier.com/retrieve/pii/S0303720717300230
314. Chesnel F, Hascoet P, Gagné JP, Couturier A, Jouan F, Poirier GG, et al. The von Hippel–Lindau tumour suppressor gene: uncovering the expression of the pVHL172 isoform. Br J Cancer [Internet]. 2015 Jul 2 [cited 2019 Jun 13];113(2):336–44. Available from: http://www.nature.com/articles/bjc2015189
315. Lenglet M, Robriquet F, Schwarz K, Camps C, Couturier A, Hoogewijs D, et al. Identification of a new *VHL* exon and complex splicing alterations in familial erythrocytosis or von Hippel-Lindau disease. Blood [Internet]. 2018 Aug 2 [cited 2019 Jun 13];132(5):469–83. Available from: http://www.ncbi.nlm.nih.gov/pubmed/29891534
316. Institution of Engineering and Technology. Y. Micro & nano letters. [Internet]. Vol. 13, Micro & Nano Letters. Institution of Engineering and Technology; 2006 [cited 2019 Jun 17]. 1367–1372 p. Available from: https://digital-library.theiet.org/content/journals/10.1049/mnl.2018.5169
317. Gravesen P, Branebjerg J, Jensen OS. Microfluidics-a review. J Micromechanics Microengineering [Internet]. 1993 Dec 1 [cited 2019 Jun 17];3(4):168–82. Available from: http://stacks.iop.org/0960-1317/3/i=4/a=002?key=crossref.b937fbfa327ffcb4bee296d7459f34fc
318. Terry SC, Jerman JH, Angell JB. A gas chromatographic air analyzer fabricated on a silicon wafer. IEEE Trans Electron Devices [Internet]. 1979 Dec [cited 2019 Jun 17];26(12):1880–6. Available from: http://ieeexplore.ieee.org/document/1480369/
319. Selecting the Best Microfluidics Device Material for Your In Vitro Diagnostic [Internet]. 2017 [cited 2019 Jun 17]. Available from: www.imtag.ch
320. Roy E, Pallandre A, Zribi B, Horny M-C, Delapierre FD, Cattoni A, et al. Overview of Materials for Microfluidic Applications. In: Advances in Microfluidics - New Applications in Biology, Energy, and Materials Sciences [Internet]. InTech; 2016 [cited 2019 Jun 17]. Available from: http://www.intechopen.com/books/advances-in-microfluidics-new-applications-in-biology-energy-and-materials-sciences/overview-of-materials-for-microfluidic-applications
321. Qin D, Xia Y, Whitesides GM. Soft lithography for micro- and nanoscale patterning. Nat Protoc [Internet]. 2010 Mar 18 [cited 2019 Jun 17];5(3):491–502. Available from: http://www.nature.com/articles/nprot.2009.234
322. Sackmann EK, Fulton AL, Beebe DJ. The present and future role of microfluidics in biomedical research. Nature [Internet]. 2014 Mar 12 [cited 2019 Jun 17];507(7491):181–9. Available from: http://www.nature.com/articles/nature13118
323. Berthier E, Young EWK, Beebe D. Engineers are from PDMS-land, Biologists are from Polystyrenia. Lab Chip [Internet]. 2012 Mar 7 [cited 2019 Jun 17];12(7):1224. Available from: http://xlink.rsc.org/?DOI=c2lc20982a
324. Auner AW, Tasneem KM, Markov DA, McCawley LJ, Hutson MS. Chemical-PDMS binding kinetics and implications for bioavailability in microfluidic devices. Lab Chip [Internet]. 2019 Feb 26 [cited 2019 Jun 18];19(5):864–74. Available from: http://xlink.rsc.org/?DOI=C8LC00796A
325. Gokaltun A, Yarmush ML, Asatekin A, Usta OB. Recent advances in nonbiofouling PDMS surface modification strategies applicable to microfluidic technology. Technology

[Internet]. 2017 Mar [cited 2019 Jun 18];5(1):1. Available from: http://www.ncbi.nlm.nih.gov/pubmed/28695160
326. Hard-soft microfluidic device bypasses drawbacks of PDMS. [cited 2019 Jun 18]; Available from: https://pubs.acs.org/doi/10.1021/ac900866n.
327. Halldorsson S, Lucumi E, Gómez-Sjöberg R, Fleming RMT. Advantages and challenges of microfluidic cell culture in polydimethylsiloxane devices. Biosens Bioelectron [Internet]. 2015 Jan 15 [cited 2019 Jun 18];63:218–31. Available from: https://www.sciencedirect.com/science/article/pii/S0956566314005302
328. Crivello J V., Lam JHW. Photoinitiated cationic polymerization with triarylsulfonium salts. J Polym Sci Polym Chem Ed [Internet]. 1979 Apr 1 [cited 2019 Jun 18];17(4):977–99. Available from: http://doi.wiley.com/10.1002/pol.1979.170170405
329. Anhoj TA, Jorgensen AM, Zauner DA, Hübner J. The effect of soft bake temperature on the polymerization of SU-8 photoresist. J Micromechanics Microengineering [Internet]. 2006 Sep 1 [cited 2019 Jun 18];16(9):1819–24. Available from: http://stacks.iop.org/0960-1317/16/i=9/a=009?key=crossref.083acb714bd962f34858cc5ba13156c5
330. Martinez-Duarte R, Madou MJ. 8 SU-8 Photolithography and Its Impact on Microfluidics [Internet]. [cited 2019 Jun 18]. Available from: https://pdfs.semanticscholar.org/ac6a/495d309f93a08746f7dc7957dd85b71fc7c1.pdf
331. Shamsi A, Amiri A, Heydari P, Hajghasem H, Mohtashamifar M, Esfandiari M. Low cost method for hot embossing of microstructures on PMMA by SU-8 masters. Microsyst Technol [Internet]. 2014 Oct 15 [cited 2019 Jun 18];20(10–11):1925–31. Available from: http://link.springer.com/10.1007/s00542-013-2000-z
332. Mohammed MI, Haswell S. Lab-on-a-chip or Chip-in-a-lab: Challenges of Commercialization Lost in Translation. Procedia Technol [Internet]. 2015 Jan 1 [cited 2019 Jun 18];20:54–9. Available from: https://www.sciencedirect.com/science/article/pii/S2212017315001875
333. Arscott S. SU-8 as a material for lab-on-a-chip-based mass spectrometry. Lab Chip [Internet]. 2014 Jul 16 [cited 2019 Jun 18];14(19):3668. Available from: http://xlink.rsc.org/?DOI=C4LC00617H
334. Chang C-W, Cheng Y-J, Tu M, Chen Y-H, Peng C-C, Liao W-H, et al. A polydimethylsiloxane-polycarbonate hybrid microfluidic device capable of generating perpendicular chemical and oxygen gradients for cell culture studies. Lab Chip [Internet]. 2014 Oct 7 [cited 2019 Jun 18];14(19):3762–72. Available from: http://www.ncbi.nlm.nih.gov/pubmed/25096368
335. Li H, Fan Y, Kodzius R, Foulds IG. Fabrication of polystyrene microfluidic devices using a pulsed CO2 laser system. Microsyst Technol [Internet]. 2012 Mar 29 [cited 2019 Jun 18];18(3):373–9. Available from: http://link.springer.com/10.1007/s00542-011-1410-z
336. Tran R, Ahn B, Myers DR, Qiu Y, Sakurai Y, Moot R, et al. Simplified prototyping of perfusable polystyrene microfluidics. Biomicrofluidics [Internet]. 2014 Jul [cited 2019 Jun 18];8(4):046501. Available from: http://www.ncbi.nlm.nih.gov/pubmed/25379106
337. DU L, Chang H, Song M, Liu C. The effect of injection molding PMMA microfluidic chips thickness uniformity on the thermal bonding ratio of chips. Microsyst Technol [Internet]. 2012 Jun 27 [cited 2019 Jun 18];18(6):815–22. Available from: http://link.springer.com/10.1007/s00542-012-1514-0
338. Jena RK, Yue CY. Cyclic olefin copolymer based microfluidic devices for biochip applications: Ultraviolet surface grafting using 2-methacryloyloxyethyl phosphorylcholine. Biomicrofluidics [Internet]. 2012 [cited 2019 Jun 18];6(1):012822. Available from: https://www.ncbi.nlm.nih.gov/pmc/articles/PMC3365341/
339. Aghvami SA, Opathalage A, Zhang ZK, Ludwig M, Heymann M, Norton M, et al. Rapid prototyping of cyclic olefin copolymer (COC) microfluidic devices. Sensors Actuators B Chem [Internet]. 2017 Aug 1 [cited 2019 Jun 18];247:940–9. Available from: https://www.sciencedirect.com/science/article/pii/S0925400517304318
340. Jena RK, Yue CY, Lam YC. Micro fabrication of cyclic olefin copolymer (COC) based microfluidic devices. Microsyst Technol [Internet]. 2012 Feb 18 [cited 2019 Jun 18];18(2):159–66. Available from: http://link.springer.com/10.1007/s00542-011-1366-z
341. Young EWK, Berthier E, Guckenberger DJ, Sackmann E, Lamers C, Meyvantsson I, et al. Rapid Prototyping of Arrayed Microfluidic Systems in Polystyrene for Cell-Based Assays. Anal Chem [Internet]. 2011 Feb 15 [cited 2019 Jun 18];83(4):1408–17. Available from: https://pubs.acs.org/doi/10.1021/ac102897h
342. Fan Y, Liu Y, Li H, Foulds IG. Printed wax masks for 254 nm deep-UV pattering of PMMA-

based microfluidics. J Micromechanics Microengineering [Internet]. 2012 Feb 1 [cited 2019 Jun 18];22(2):027001. Available from: http://stacks.iop.org/0960-1317/22/i=2/a=027001?key=crossref.0ffc41b6f99355a866b8c5fda39ea142
343. Lei KF, Chang C-H, Chen M-J. Paper/PMMA Hybrid 3D Cell Culture Microfluidic Platform for the Study of Cellular Crosstalk. ACS Appl Mater Interfaces [Internet]. 2017 Apr 19 [cited 2019 Jun 18];9(15):13092–101. Available from: http://pubs.acs.org/doi/10.1021/acsami.7b03021
344. Shamsi A, Shamloo A, Mohammadaliha N, Hajghassem H, Mehrabadi JF, Bazzaz M. High throughput blood plasma separation using a passive PMMA microfluidic device. Microsyst Technol [Internet]. 2016 Oct 25 [cited 2019 Jun 18];22(10):2447–54. Available from: http://link.springer.com/10.1007/s00542-015-2664-7
345. Fan A, Tofangchi A, De Venecia M, Saif T. A simple microfluidic platform for the partial treatment of insuspendable tissue samples with orientation control. Lab Chip [Internet]. 2018 [cited 2019 Jun 18];18(5):735–42. Available from: http://www.ncbi.nlm.nih.gov/pubmed/29362759
346. Thian SCH, Fuh JYH, Wong YS, Loh HT, Gian PW, Tang Y. Fabrication of microfluidic channel utilizing silicone rubber with vacuum casting. Microsyst Technol [Internet]. 2008 Aug 4 [cited 2019 Jun 18];14(8):1125–35. Available from: http://link.springer.com/10.1007/s00542-008-0640-1
347. Langelier SM, Livak-Dahl E, Manzo AJ, Johnson BN, Walter NG, Burns MA. Flexible casting of modular self-aligning microfluidic assembly blocks †. [cited 2019 Jun 18]; Available from: http://pubs.rsc.org
348. Gencturk E, Mutlu S, Ulgen KO. Advances in microfluidic devices made from thermoplastics used in cell biology and analyses. Biomicrofluidics [Internet]. 2017 Sep [cited 2019 Jun 18];11(5):051502. Available from: http://www.ncbi.nlm.nih.gov/pubmed/29152025
349. Lachaux J, Salmon H, Loisel F, Arouche N, Ochoa I, Fernandez LL, et al. Soft Thermoplastic Elastomer for Easy and Rapid Spin-Coating Fabrication of Microfluidic Devices with High Hydrophilization and Bonding Performances. Adv Mater Technol [Internet]. 2019 Feb 1 [cited 2019 Jun 18];4(2):1800308. Available from: http://doi.wiley.com/10.1002/admt.201800308
350. Jake S, Jiang K. Elastomer Application in Microsystem and Microfluidics. In: Advanced Elastomers - Technology, Properties and Applications [Internet]. InTech; 2012 [cited 2019 Jun 18]. Available from: http://www.intechopen.com/books/advanced-elastomers-technology-properties-and-applications/elastomer-application-in-microsystem-and-microfluidics
351. Gale B, Jafek A, Lambert C, Goenner B, Moghimifam H, Nze U, et al. A Review of Current Methods in Microfluidic Device Fabrication and Future Commercialization Prospects. Inventions [Internet]. 2018 Aug 28 [cited 2019 Jun 18];3(3):60. Available from: http://www.mdpi.com/2411-5134/3/3/60
352. Ren K, Zhou J, Wu H. Materials for Microfluidic Chip Fabrication. Acc Chem Res [Internet]. 2013 Nov 19 [cited 2019 Jun 18];46(11):2396–406. Available from: http://pubs.acs.org/doi/10.1021/ar300314s
353. Faustino V, Catarino SO, Lima R, Minas G. Biomedical microfluidic devices by using low-cost fabrication techniques: A review. J Biomech [Internet]. 2016 Jul 26 [cited 2019 Jun 18];49(11):2280–92. Available from: http://www.ncbi.nlm.nih.gov/pubmed/26671220
354. Nguyen H-T, Thach H, Roy E, Huynh K, Perrault CM-T. Low-Cost, Accessible Fabrication Methods for Microfluidics Research in Low-Resource Settings. Micromachines [Internet]. 2018 Sep 12 [cited 2019 Jun 18];9(9). Available from: http://www.ncbi.nlm.nih.gov/pubmed/30424394
355. Xia Y, Whitesides GM. SOFT LITHOGRAPHY. Annu Rev Mater Sci [Internet]. 1998 Aug 28 [cited 2019 Jun 18];28(1):153–84. Available from: http://www.annualreviews.org/doi/10.1146/annurev.matsci.28.1.153
356. Browne AW, Rust MJ, Jung W, Lee SH, Ahn CH. A rapid prototyping method for polymer microfluidics with fixed aspect ratio and 3D tapered channels. Lab Chip [Internet]. 2009 Oct 21 [cited 2019 Jun 18];9(20):2941. Available from: http://www.ncbi.nlm.nih.gov/pubmed/19789747
357. Synergy of 3D printing and injection molding: A new prototyping method for rapid design optimization and manufacturing of microfluidic devices - SINTEF [Internet]. [cited 2019 Jun 18]. Available from:

https://www.sintef.no/en/publications/publication/?pubid=CRIStin+1509305
358. Giboz J, Copponnex T, Mélé P. Microinjection molding of thermoplastic polymers: a review. J Micromechanics Microengineering [Internet]. 2007 Jun 1 [cited 2019 Jun 18];17(6):R96–109. Available from: http://stacks.iop.org/0960-1317/17/i=6/a=R02?key=crossref.1433df5680278d815a739a8d69ab45b2
359. Wu J, Gu M. Microfluidic sensing: state of the art fabrication and detection techniques. J Biomed Opt [Internet]. 2011 Aug [cited 2019 Jun 18];16(8):080901. Available from: http://www.ncbi.nlm.nih.gov/pubmed/21895307
360. Heckele M, Schomburg WK. Review on micro molding of thermoplastic polymers. J Micromechanics Microengineering [Internet]. 2004 Mar 1 [cited 2019 Jun 18];14(3):R1–14. Available from: http://stacks.iop.org/0960-1317/14/i=3/a=R01?key=crossref.f56c7699751909a49cadd9e505b9d776
361. Çoğun F, Yıldırım E, Sahir Arikan MA. Investigation on replication of microfluidic channels by hot embossing. Mater Manuf Process [Internet]. 2017 Dec 10 [cited 2019 Jun 18];32(16):1838–44. Available from: https://www.tandfonline.com/doi/full/10.1080/10426914.2017.1317795
362. Yang S, DeVoe DL. Microfluidic Device Fabrication by Thermoplastic Hot-Embossing. In: Methods in molecular biology (Clifton, NJ) [Internet]. 2013 [cited 2019 Jun 18]. p. 115–23. Available from: http://www.ncbi.nlm.nih.gov/pubmed/23329439
363. Yeo LP, Ng SH, Wang ZF, Xia HM, Wang ZP, Thang VS, et al. Investigation of hot roller embossing for microfluidic devices. J Micromechanics Microengineering [Internet]. 2010 Jan 1 [cited 2019 Jun 18];20(1):015017. Available from: http://stacks.iop.org/0960-1317/20/i=1/a=015017?key=crossref.6e72a9e5f951306686736ed601292326
364. da Costa ET, Santos MFS, Jiao H, do Lago CL, Gutz IGR, Garcia CD. Fast production of microfluidic devices by CO_2 laser engraving of wax-coated glass slides. Electrophoresis [Internet]. 2016 Jul [cited 2019 Jun 19];37(12):1691–5. Available from: http://www.ncbi.nlm.nih.gov/pubmed/27028724
365. Serhatlioglu M, Ortaç B, Elbuken C, Biyikli N, Solmaz ME. CO_2 laser polishing of microfluidic channels fabricated by femtosecond laser assisted carving. J Micromechanics Microengineering [Internet]. 2016 Nov 1 [cited 2019 Jun 19];26(11):115011. Available from: http://stacks.iop.org/0960-1317/26/i=11/a=115011?key=crossref.656d692420b3e4a875cc89f879bd9f2a
366. Chung CK, Chang HC, Shih TR, Lin SL, Hsiao EJ, Chen YS, et al. Water-assisted CO2 laser ablated glass and modified thermal bonding for capillary-driven bio-fluidic application. Biomed Microdevices [Internet]. 2010 Feb 15 [cited 2019 Jun 19];12(1):107–14. Available from: http://www.ncbi.nlm.nih.gov/pubmed/19830566
367. Spicar-Mihalic P, Toley B, Houghtaling J, Liang T, Yager P, Fu E. CO_2 laser cutting and ablative etching for the fabrication of paper-based devices. J Micromechanics Microengineering [Internet]. 2013 Jun 1 [cited 2019 Jun 19];23(6):067003. Available from: http://stacks.iop.org/0960-1317/23/i=6/a=067003?key=crossref.5ece8ad6c6feea3b865ce255b3dd4dfa
368. Prakash S, Kumar S. Fabrication of microchannels on transparent PMMA using CO2 Laser (10.6 μm) for microfluidic applications: An experimental investigation. Int J Precis Eng Manuf [Internet]. 2015 Feb 6 [cited 2019 Jun 19];16(2):361–6. Available from: http://link.springer.com/10.1007/s12541-015-0047-8
369. Gaal G, Mendes M, de Almeida TP, Piazzetta MHO, Gobbi ÂL, Riul A, et al. Simplified fabrication of integrated microfluidic devices using fused deposition modeling 3D printing. Sensors Actuators B Chem [Internet]. 2017 Apr 1 [cited 2019 Jun 19];242:35–40. Available from: https://www.sciencedirect.com/science/article/pii/S0925400516317373
370. Salentijn GI, Oomen PE, Grajewski M, Verpoorte E. Fused Deposition Modeling 3D Printing for (Bio)analytical Device Fabrication: Procedures, Materials, and Applications. Anal Chem [Internet]. 2017 Jul 5 [cited 2019 Jun 19];89(13):7053–61. Available from: http://pubs.acs.org/doi/10.1021/acs.analchem.7b00828
371. Kanai T, Tsuchiya M. Microfluidic devices fabricated using stereolithography for preparation of monodisperse double emulsions. Chem Eng J [Internet]. 2016 Apr 15 [cited 2019 Jun 19];290:400–4. Available from: https://www.sciencedirect.com/science/article/pii/S1385894716300328
372. He Y, Wu W, Fu J. Rapid fabrication of paper-based microfluidic analytical devices with desktop stereolithography 3D printer. RSC Adv [Internet]. 2015 Dec 8 [cited 2019 Jun 19];5(4):2694–701. Available from: http://xlink.rsc.org/?DOI=C4RA12165A

373. Au AK, Huynh W, Horowitz LF, Folch A. 3D-Printed Microfluidics. Angew Chemie Int Ed [Internet]. 2016 Mar 14 [cited 2019 Jun 19];55(12):3862–81. Available from: http://www.ncbi.nlm.nih.gov/pubmed/26854878
374. Waheed S, Cabot JM, Macdonald NP, Lewis T, Guijt RM, Paull B, et al. 3D printed microfluidic devices: enablers and barriers. Lab Chip [Internet]. 2016 [cited 2019 Jun 19];16(11):1993–2013. Available from: http://www.ncbi.nlm.nih.gov/pubmed/27146365
375. Bhattacharjee N, Urrios A, Kang S, Folch A. The upcoming 3D-printing revolution in microfluidics. Lab Chip [Internet]. 2016 [cited 2019 Jun 19];16(10):1720–42. Available from: http://www.ncbi.nlm.nih.gov/pubmed/27101171
376. Romanov V, Samuel R, Chaharlang M, Jafek AR, Frost A, Gale BK. FDM 3D Printing of High-Pressure, Heat-Resistant, Transparent Microfluidic Devices. Anal Chem [Internet]. 2018 Sep 4 [cited 2019 Jun 19];90(17):10450–6. Available from: http://pubs.acs.org/doi/10.1021/acs.analchem.8b02356
377. Bressan LP, Adamo CB, Quero RF, de Jesus DP, da Silva JAF. A simple procedure to produce FDM-based 3D-printed microfluidic devices with an integrated PMMA optical window. Anal Methods [Internet]. 2019 Feb 21 [cited 2019 Jun 19];11(8):1014–20. Available from: http://xlink.rsc.org/?DOI=C8AY02092B
378. Rusling JF. Developing Microfluidic Sensing Devices Using 3D Printing. ACS Sensors [Internet]. 2018 Mar 23 [cited 2019 Jun 19];3(3):522–6. Available from: http://pubs.acs.org/doi/10.1021/acssensors.8b00079
379. Zips S, Wenzel OJ, Rinklin P, Grob L, Terkan K, Adly NY, et al. Direct Stereolithographic 3D Printing of Microfluidic Structures on Polymer Substrates for Printed Electronics. Adv Mater Technol [Internet]. 2019 Mar 1 [cited 2019 Jun 19];4(3):1800455. Available from: http://doi.wiley.com/10.1002/admt.201800455
380. Waheed S, Cabot JM, Macdonald NP, Lewis T, Guijt RM, Paull B, et al. 3D printed microfluidic devices: enablers and barriers. Lab Chip [Internet]. 2016 May 24 [cited 2019 Jun 19];16(11):1993–2013. Available from: http://xlink.rsc.org/?DOI=C6LC00284F
381. Brimmo A, Goyette P-A, Alnemari R, Gervais T, Qasaimeh MA. 3D Printed Microfluidic Probes. Sci Rep [Internet]. 2018 Dec 20 [cited 2019 Jun 19];8(1):10995. Available from: http://www.nature.com/articles/s41598-018-29304-x
382. Khashayar P, Amoabediny G, Larijani B, Hosseini M, Van Put S, Verplancke R, et al. Rapid prototyping of microfluidic chips using laser-cut double-sided tape for electrochemical biosensors. J Brazilian Soc Mech Sci Eng [Internet]. 2017 May 22 [cited 2019 Jun 19];39(5):1469–77. Available from: http://link.springer.com/10.1007/s40430-016-0684-6
383. Nath P, Fung D, Kunde YA, Zeytun A, Branch B, Goddard G. Rapid prototyping of robust and versatile microfluidic components using adhesive transfer tapes. Lab Chip [Internet]. 2010 Sep 7 [cited 2019 Jun 19];10(17):2286. Available from: http://www.ncbi.nlm.nih.gov/pubmed/20593077
384. Gerber LC, Kim H, Riedel-Kruse IH. Microfluidic assembly kit based on laser-cut building blocks for education and fast prototyping. Biomicrofluidics [Internet]. 2015 Nov [cited 2019 Jun 19];9(6):064105. Available from: http://www.ncbi.nlm.nih.gov/pubmed/26634013
385. Patko D, Mártonfalvi Z, Kovacs B, Vonderviszt F, Kellermayer M, Horvath R. Microfluidic channels laser-cut in thin double-sided tapes: Cost-effective biocompatible fluidics in minutes from design to final integration with optical biochips. Sensors Actuators B Chem [Internet]. 2014 Jun 1 [cited 2019 Jun 19];196:352–6. Available from: https://www.sciencedirect.com/science/article/pii/S0925400514001324
386. Walsh DI, Kong DS, Murthy SK, Carr PA. Enabling Microfluidics: from Clean Rooms to Makerspaces. Trends Biotechnol [Internet]. 2017;35(5):383–92. Available from: http://dx.doi.org/10.1016/j.tibtech.2017.01.001
387. Gao B, Wang L, Han S, Pingguan-Murphy B, Zhang X, Xu F. Engineering of microscale three-dimensional pancreatic islet models *in vitro* and their biomedical applications. Crit Rev Biotechnol [Internet]. 2015 Feb 11 [cited 2019 Jun 19];1–11. Available from: http://www.tandfonline.com/doi/full/10.3109/07388551.2014.1002381
388. Cui P, Wang S. Application of microfluidic chip technology in pharmaceutical analysis: A review. J Pharm Anal [Internet]. 2018 Dec 6 [cited 2019 Jun 19]; Available from: https://www.sciencedirect.com/science/article/pii/S2095177918305094#bib42
389. Cosson S, Lutolf MP. Hydrogel microfluidics for the patterning of pluripotent stem cells. Sci Rep [Internet]. 2015 May 25 [cited 2019 Jun 19];4(1):4462. Available from: http://www.nature.com/articles/srep04462

390. Houshmand M, Soleimani M, Atashi A, Saglio G, Abdollahi M, Nikougoftar Zarif M. Mimicking the Acute Myeloid Leukemia Niche for Molecular Study and Drug Screening. Tissue Eng Part C Methods [Internet]. 2017 Feb 1 [cited 2019 Jun 19];23(2):72–85. Available from: https://www.liebertpub.com/doi/10.1089/ten.tec.2016.0404
391. Ronaldson-Bouchard K, Vunjak-Novakovic G. Cell Stem Cell Review Organs-on-a-Chip: A Fast Track for Engineered Human Tissues in Drug Development. Stem Cell [Internet]. 2018 [cited 2019 Jun 19];22:310–24. Available from: https://doi.org/10.1016/j.stem.2018.02.011
392. Sosa-Hernández JE, Villalba-Rodríguez AM, Romero-Castillo KD, Aguilar-Aguila-Isaías MA, García-Reyes IE, Hernández-Antonio A, et al. Organs-on-a-Chip Module: A Review from the Development and Applications Perspective. Micromachines [Internet]. 2018 Oct 22 [cited 2019 Jun 19];9(10). Available from: http://www.ncbi.nlm.nih.gov/pubmed/30424469
393. Konar D, Devarasetty M, Yildiz D V, Atala A, Murphy S V. Lung-On-A-Chip Technologies for Disease Modeling and Drug Development. Biomed Eng Comput Biol [Internet]. 2016 [cited 2019 Jun 19];7(Suppl 1):17–27. Available from: http://www.ncbi.nlm.nih.gov/pubmed/27127414
394. Beckwitt CH, Clark AM, Wheeler S, Taylor DL, Stolz DB, Griffith L, et al. Liver 'organ on a chip.' Exp Cell Res [Internet]. 2018 Feb 1 [cited 2019 Jun 19];363(1):15–25. Available from: http://www.ncbi.nlm.nih.gov/pubmed/29291400
395. Zheng F, Fu F, Cheng Y, Wang C, Zhao Y, Gu Z. Organ-on-a-Chip Systems: Microengineering to Biomimic Living Systems. Small [Internet]. 2016 May [cited 2019 Jun 19];12(17):2253–82. Available from: http://doi.wiley.com/10.1002/smll.201503208
396. Balijepalli A, Sivaramakrishan V. Organs-on-chips: research and commercial perspectives. Drug Discov Today [Internet]. 2017 Feb [cited 2019 Jun 19];22(2):397–403. Available from: https://linkinghub.elsevier.com/retrieve/pii/S1359644616304275
397. Wilmer MJ, Ng CP, Lanz HL, Vulto P, Suter-Dick L, Masereeuw R. Kidney-on-a-Chip Technology for Drug-Induced Nephrotoxicity Screening. Trends Biotechnol [Internet]. 2016 Feb 1 [cited 2019 Jun 19];34(2):156–70. Available from: http://www.ncbi.nlm.nih.gov/pubmed/26708346
398. Lee J, Kim S. Kidney-on-a-Chip: A New Technology for Predicting Drug Efficacy, Interactions, and Drug-induced Nephrotoxicity. Curr Drug Metab [Internet]. 2018 Jul 9 [cited 2019 Jun 19];19(7):577–83. Available from: http://www.ncbi.nlm.nih.gov/pubmed/29521220
399. Deng J, Qu Y, Liu T, Jing B, Zhang X, Chen Z, et al. Recent organ-on-a-chip advances toward drug toxicity testing. Microphysiological Syst [Internet]. 2018 [cited 2019 Jun 19];1:1–1. Available from: http://mps.amegroups.com/article/view/4798/5575
400. Hooper L V., Macpherson AJ. Immune adaptations that maintain homeostasis with the intestinal microbiota. Nat Rev Immunol [Internet]. 2010 Mar [cited 2019 Jun 19];10(3):159–69. Available from: http://www.nature.com/articles/nri2710
401. Trujillo-de Santiago G, Lobo-Zegers MJ, Montes-Fonseca SL, Zhang YS, Alvarez MM. Gut-microbiota-on-a-chip: an enabling field for physiological research. Microphysiological Syst [Internet]. 2018 [cited 2019 Jun 19];1:1–1. Available from: http://mps.amegroups.com/article/view/4777/5555
402. Bein A, Shin W, Jalili-Firoozinezhad S, Park MH, Sontheimer-Phelps A, Tovaglieri A, et al. Microfluidic Organ-on-a-Chip Models of Human Intestine. Cell Mol Gastroenterol Hepatol [Internet]. 2018 Jan 1 [cited 2019 Jun 19];5(4):659–68. Available from: https://www.sciencedirect.com/science/article/pii/S2352345X17301893
403. Wang G, Das C, Ledden B, Sun Q, Nguyen C, Kumar S. Evaluation of disposable microfluidic chip design for automated and fast Immunoassays. Biomicrofluidics [Internet]. 2017 Jan [cited 2019 Jun 19];11(1):014115. Available from: http://www.ncbi.nlm.nih.gov/pubmed/28344726
404. Yao P, Liu Z, Tung S, Dong Z, Liu L. Fully Automated Quantification of Insulin Concentration Using a Microfluidic-Based Chemiluminescence Immunoassay. J Lab Autom. 2016;21(3):387–93.
405. Yoon J-Y, Kim B. Lab-on-a-Chip Pathogen Sensors for Food Safety. Sensors [Internet]. 2012 Aug 6 [cited 2019 Jun 19];12(8):10713–41. Available from: http://www.ncbi.nlm.nih.gov/pubmed/23112625
406. Neethirajan S, Kobayashi I, Nakajima M, Wu D, Nandagopal S, Lin F. Microfluidics for food, agriculture and biosystems industries. Lab Chip [Internet]. 2011 May 7 [cited 2019

Jun 19];11(9):1574. Available from: http://xlink.rsc.org/?DOI=c0lc00230e
407. Escarpa A. Lights and shadows on Food Microfluidics. Lab Chip [Internet]. 2014 Jul 31 [cited 2019 Jun 19];14(17):3213–24. Available from: http://xlink.rsc.org/?DOI=C4LC00172A
408. Neethirajan S, Kobayashi I, Nakajima M, Wu D, Nandagopal S, Lin F. Microfluidics for food, agriculture and biosystems industries. Lab Chip [Internet]. 2011 May 7 [cited 2019 Jun 19];11(9):1574. Available from: http://www.ncbi.nlm.nih.gov/pubmed/21431239
409. Fanous M, Ozhikandathil J, Badilescu S, Packirisamy M. Evaluation of optical properties and biocompatibility of polymer materials for microfluidic applications. In: 2015 Photonics North [Internet]. IEEE; 2015 [cited 2019 Jun 21]. p. 1–4. Available from: http://ieeexplore.ieee.org/document/7292461/
410. Ogilvie IRG, Sieben VJ, Floquet CFA, Zmijan R, Mowlem MC, Morgan H. Reduction of surface roughness for optical quality microfluidic devices in PMMA and COC. J Micromechanics Microengineering [Internet]. 2010 Jun 1 [cited 2019 Jun 21];20(6):065016. Available from: http://stacks.iop.org/0960-1317/20/i=6/a=065016?key=crossref.e2fbcc86fc1545219235e745b992ee14
411. Jeon JS, Chung S, Kamm RD, Charest JL. Hot embossing for fabrication of a microfluidic 3D cell culture platform. Biomed Microdevices [Internet]. 2011 Apr 27 [cited 2019 Jun 21];13(2):325–33. Available from: http://www.ncbi.nlm.nih.gov/pubmed/21113663
412. Mair DA, Geiger E, Pisano AP, Fréchet JMJ, Svec F. Injection molded microfluidic chips featuring integrated interconnects. Lab Chip [Internet]. 2006 Sep 26 [cited 2019 Jun 21];6(10):1346–54. Available from: http://xlink.rsc.org/?DOI=B605911B
413. Jena RK, Yue CY. Cyclic olefin copolymer based microfluidic devices for biochip applications: Ultraviolet surface grafting using 2-methacryloyloxyethyl phosphorylcholine. Biomicrofluidics [Internet]. 2012 Mar 15 [cited 2019 Jun 21];6(1):012822. Available from: http://aip.scitation.org/doi/10.1063/1.3682098
414. Serra M, Pereiro I, Yamada A, Viovy J-L, Descroix S, Ferraro D. A simple and low-cost chip bonding solution for high pressure, high temperature and biological applications. Lab Chip [Internet]. 2017 Feb 14 [cited 2019 Jun 21];17(4):629–34. Available from: http://xlink.rsc.org/?DOI=C6LC01319H
415. Monat C, Domachuk P, Eggleton BJ. Integrated optofluidics: A new river of light. Nat Photonics [Internet]. 2007 Feb 1 [cited 2019 Jun 21];1(2):106–14. Available from: http://www.nature.com/articles/nphoton.2006.96
416. Keller N, Nargang TM, Runck M, Kotz F, Striegel A, Sachsenheimer K, et al. Tacky cyclic olefin copolymer: a biocompatible bonding technique for the fabrication of microfluidic channels in COC. Lab Chip [Internet]. 2016 Apr 26 [cited 2019 Jun 21];16(9):1561–4. Available from: http://xlink.rsc.org/?DOI=C5LC01498K
417. Tang NH, Fong CS, Masuda H, Jourdain I, Yukawa M, Toda T. Generation and characterisation of temperature sensitive mutants of genes encoding the fission yeast spindle pole body. 2017 Oct 27 [cited 2019 Jun 25]; Available from: https://peerj.com/preprints/3377/
418. Zigova T, Sanberg PR, Sanchez-Ramos JR, Jourdain I, Toda T. Neural stem cells : methods and protocols [Internet]. Humana Press; 2002 [cited 2019 Jun 25]. 381 p. Available from: https://ore.exeter.ac.uk/repository/handle/10871/26077
419. Glatz A, Pilbat A-M, Németh GL, Vince-Kontár K, Jósvay K, Hunya Á, et al. Involvement of small heat shock proteins, trehalose, and lipids in the thermal stress management in Schizosaccharomyces pombe. Cell Stress Chaperones [Internet]. 2016 Mar 2 [cited 2019 Jun 25];21(2):327–38. Available from: http://link.springer.com/10.1007/s12192-015-0662-4
420. Gómez EB, Angeles VT, Forsburg SL. A screen for Schizosaccharomyces pombe mutants defective in rereplication identifies new alleles of rad4+, cut9+ and psf2+. Genetics [Internet]. 2005 Jan [cited 2019 Jun 25];169(1):77–89. Available from: http://www.ncbi.nlm.nih.gov/pubmed/15466421
421. Bonatti S, Simili M, Abbondandolo A. Isolation of Temperature-Sensitive Mutants of Schizosaccharomyces pombe. J Bacteriol [Internet]. 1972 [cited 2019 Jun 25];109(2):484. Available from: https://www.ncbi.nlm.nih.gov/pmc/articles/PMC285166/
422. Hagan IM, Grallert A, Simanis V. Synchronizing Progression of *Schizosaccharomyces pombe* Cells from G 2 through Repeated Rounds of Mitosis and S Phase with *cdc25-22* Arrest Release. Cold Spring Harb Protoc [Internet]. 2016 Aug 1 [cited 2019 Jun 25];2016(8):pdb.prot091264. Available from:

http://www.ncbi.nlm.nih.gov/pubmed/27480720
423. Norris SR, Jung S, Singh P, Strothman CE, Erwin AL, Ohi MD, et al. Microtubule minus-end aster organization is driven by processive HSET-tubulin clusters. Nat Commun [Internet]. 2018 [cited 2019 Aug 8];9(1):2659. Available from: http://www.ncbi.nlm.nih.gov/pubmed/29985404
424. Foe VE, von Dassow G. Stable and dynamic microtubules coordinately shape the myosin activation zone during cytokinetic furrow formation. J Cell Biol [Internet]. 2008 Nov 3 [cited 2019 Aug 8];183(3):457–70. Available from: http://www.ncbi.nlm.nih.gov/pubmed/18955555
425. Holy TE, Dogterom M, Yurke B, Leibler S. Assembly and positioning of microtubule asters in microfabricated chambers. Proc Natl Acad Sci U S A [Internet]. 1997 Jun 10 [cited 2019 Aug 8];94(12):6228–31. Available from: http://www.ncbi.nlm.nih.gov/pubmed/9177199
426. Skoufias DA, DeBonis S, Saoudi Y, Lebeau L, Crevel I, Cross R, et al. *S* -Trityl-L-cysteine Is a Reversible, Tight Binding Inhibitor of the Human Kinesin Eg5 That Specifically Blocks Mitotic Progression. J Biol Chem [Internet]. 2006 Jun 30 [cited 2019 Aug 8];281(26):17559–69. Available from: http://www.ncbi.nlm.nih.gov/pubmed/16507573
427. Rupali M, Amit P. A Review Paper on General Concepts of "Artificial Intelligence and Machine Learning" Int Adv Res J Sci [Internet]. 2017 [cited 2019 Aug 8];4. Available from: https://iarjset.com/upload/2017/si/NCIARCSE-2017/IARJSET-NCIARCSE 22.pdf
428. Mathieu M, Henaff M, LeCun Y. Fast Training of Convolutional Networks through FFTs. 2013 Dec 20 [cited 2019 Aug 8]; Available from: http://arxiv.org/abs/1312.5851
429. Rovce WW. MANAGING THE DEVELOPMENT OF LARGE SOFTWARE SYSTEMS [Internet]. [cited 2019 Jul 12]. Available from: http://www-scf.usc.edu/~csci201/lectures/Lecture11/royce1970.pdf